THE EFFECTS OF ALLOY CHEMISTRY ON THE ELECTROCHEMICAL AND HYDRIDING PROPERTIES OF NI-SUBSTITUTED $LaNi_5$

Thesis by

Charles K. Witham

In Partial Fulfillment of the Requirements
for the Degree of
Doctor of Philosophy

California Institute of Technology
Pasadena, California

2000
(Submitted August 24th, 1999)

Acknowledgments

There were many people who were instrumental in the completion of my graduate work and this thesis who I would like to thank here. These are by no means listed in order of importance, as I could not have accomplished as much as I did without each of them. My advisor Prof. Fultz has been of utmost utility in training me in the use of laboratory equipment, in applying my own insight, both in and out of the classroom, and in familiarizing me with the mechanisms of successfully maneuvering in both the University setting and the current academic funding environment.

Dr. Bob Bowman was particularly helpful in freely transferring to me his vast knowledge of metal hydride systems, and a bit of his cynicism. He also helped to expose me to the scientific community and a side of the metal hydride community that I might never have seen without his introductions.

In regards to the electrochemical tests, I must acknowledge and show my great appreciation to Dr. Ratnakumar Bugga of the Jet Propulsion Laboratory Electrochemical Technologies Group and Adrian Hightower of Caltech. Dr. Bugga trained me on all of the equipment relevant to the testing of metal hydride alloys in alkaline batteries, and imparted to me much of what I know about electrochemistry. My fellow graduate student Adrian Hightower performed some of the tests of the alloys' electrochemical kinetics.

The work presented in this thesis was carried out under funding by the Department of Energy, grant DE-FG03-94ER14493.

And I cannot forget my undergraduate professors, John Hack, Bob Weber, Dave Keenes, and Alessandro Gomez, who all encouraged me to attend graduate school and helped give me the courage to achieve.

Finally, I truly appreciate that all of the people who were involved in my work have also extended to me their friendship.

Abstract

The primary goal of this work was to verify the hypothesis that alloying $LaNi_5$ with ternary elements that have a large heat of formation with La (and secondarily, with Ni) would slow the kinetics of metal (La) atom diffusion. This would have the effect of stabilizing the Haucke phase crystal structure of $LaNi_5$ during electrochemical and gas-phase hydrogen absorption/desorption cycling, and extending the material's useful lifetime.

To test this hypothesis, I prepared a variety of single-phase alloys of composition $LaNi_{5-x}M_x$, $0 \leq x \leq 0.5$, $M \in \{Al, Si, Ga, Ge, In, Sn\}$. Each alloy was annealed to insure equilibrium starting conditions. The lifetimes of these alloys were tested by charge-discharge cycling as the anode of an alkaline Ni-MH rechargeable cell. By characterizing the lifetimes of the alloys as an exponential capacity decay, I was able to determine a trend between the capacity decay and the heat of formation of an average 'B' element with La

The alloys were further characterized by obtaining gas-phase isotherms and, in the case of the Ge_x alloys, the thermodynamics of metal hydride formation and decomposition. X-ray diffraction was used to measure the effect of substitution on the alloy and its hydride phase. By examining the data obtained at Caltech as well as data published in the literature, several trends were noted. There is a fairly linear relationship between the solute's expansion of the $LaNi_5$ unit cell and its radius. The total volume expansion an alloy experienced upon absorption of hydrogen was found to decrease with substituted composition. The discrete lattice expansion of Ge_x alloys was found to decrease substantially for $0 < x < 0.2$, but subsequent substitution had little effect on the volume expansion.

The electrode electrochemical kinetice of charge transfer were investigated for each MH alloy. Measurements of the charge transfer exchange current by micropolarization and AC impedance were similar, while those measured by Tafel polarization did not have a clear relationship.

Table of Contents

Lists of Tables and Illustrations

Chapter 2: Background

Chapter 3: Methods

Chapter 4: X-Ray Diffraction

Chapter 5: Isotherms

Chapter 6: Electrochemical Kinetics

Chapter 7: Electrochemical Cycling

I. Introduction

This section will briefly describe the organization of the thesis.

The reader will note that the "background" section (§II) is quite large, 1/3 the length of the text. In writing my thesis, I felt it necessary to describe the context within which my work would exist. The short "History" (§II.A) and "Applications" (§II.B) sections allude to the technological and scientific importance of metal hydrides. The great volume of applications of this class of material is argument enough that continued research into the scientific nature of hydrogen absorption in metals will be valuable.

The academic setting for my thesis begins to appear in "$LaNi_5$" (§II.C) and is expanded upon in "Alloy Modifications" (§II.D). These sections describe what is currently known about how $LaNi_5$ and its alloys react in the presence of hydrogen. The specific dilemma that my work attempts to address is presented in "Alloy Degradation" (§II.F). Included in this section are the attempts of researchers to prevent $LaNi_5$ from deteriorating while it works. Sections § II.C.1, § II.C.3, § II.C.5, § II.D, and § II.F will be most useful in interpreting my work.

"§ IV. X-Ray Diffraction" investigates the physical changes that occur when $LaNi_5$ is alloyed by Ni-substitution, and when these alloys absorb hydrogen. "§ VII. Electrochemical Cycling" explores the phase change that takes place during electrochemical cycling and its dependency on alloy properties. These two sections are integral to reaching the goal of my thesis. "§ V. Isotherms" and "§ IV. Electrochemical Kinetics" are useful in gaining further understanding into the hydriding and bulk electrode properties of Ni-substituted $LaNi_5$, but their understanding is not essential in increasing the alloys' lifetimes during cycling.

In completing this work, I concur with Bob Bowman's statement that we know a great deal about $LaNi_5$ and other metal hydrides, but what we understand is a much smaller realm. I hope that the work I have completed will advance our understanding of the fundamentally interesting natural phenomenon of hydrogen absorption in metal hydrides.

II. Background

A. Short History of Metal Hydrides

1. Palladium

In 1866, T. Graham reported the first observation of the absorption of hydrogen by a metal, namely Pd.[1] He followed this work with experiments measuring the variation of several physical properties, including lattice expansion, electrical resistivity, and magnetic susceptibility, with hydrogen composition.[2] This discovery of the ability of Pd to absorb large amounts of hydrogen has been followed by many years of research into the science and application of this relationship between one of the periodic table's most interesting elements and this most versatile class of materials.

A pressure-composition-isotherm, commonly called an *isotherm*, of PdH at room temperature is shown in **Figure II-1**.[3] Pd reversibly absorbs hydrogen up to a composition of 1.0 H/Pd at a pressure that rises gradually with hydrogen content.

2. Intermetallic Hydrides

The first hydride of an intermetallic compound, cubic $ZrNiH_3$, was discovered in 1958 by Libowitz, *et al.*[4] This finding was particularly auspicious because the properties of hydride forming intermetallic compounds can be controlled. Intermetallic alloys which form hydrides are traditionally generalized by the chemical formula AB_n, where A refers to the strongly hydride forming element, usually a rare earth (*RE*) or early transition metal, and B usually refers to a late transition metal. Other types of intermetallic hydrides are FeTi (b.c.c. AB type),[5] Mg_2Ni (A_2B type),[6] $(Zr,Ti)(Mn,Cr,V)_2$ (C14 or C15 Laves phase AB_2),[7,8] and $LaNi_5$ (Haucke phase AB_5), the latter of which is the subject of this thesis.

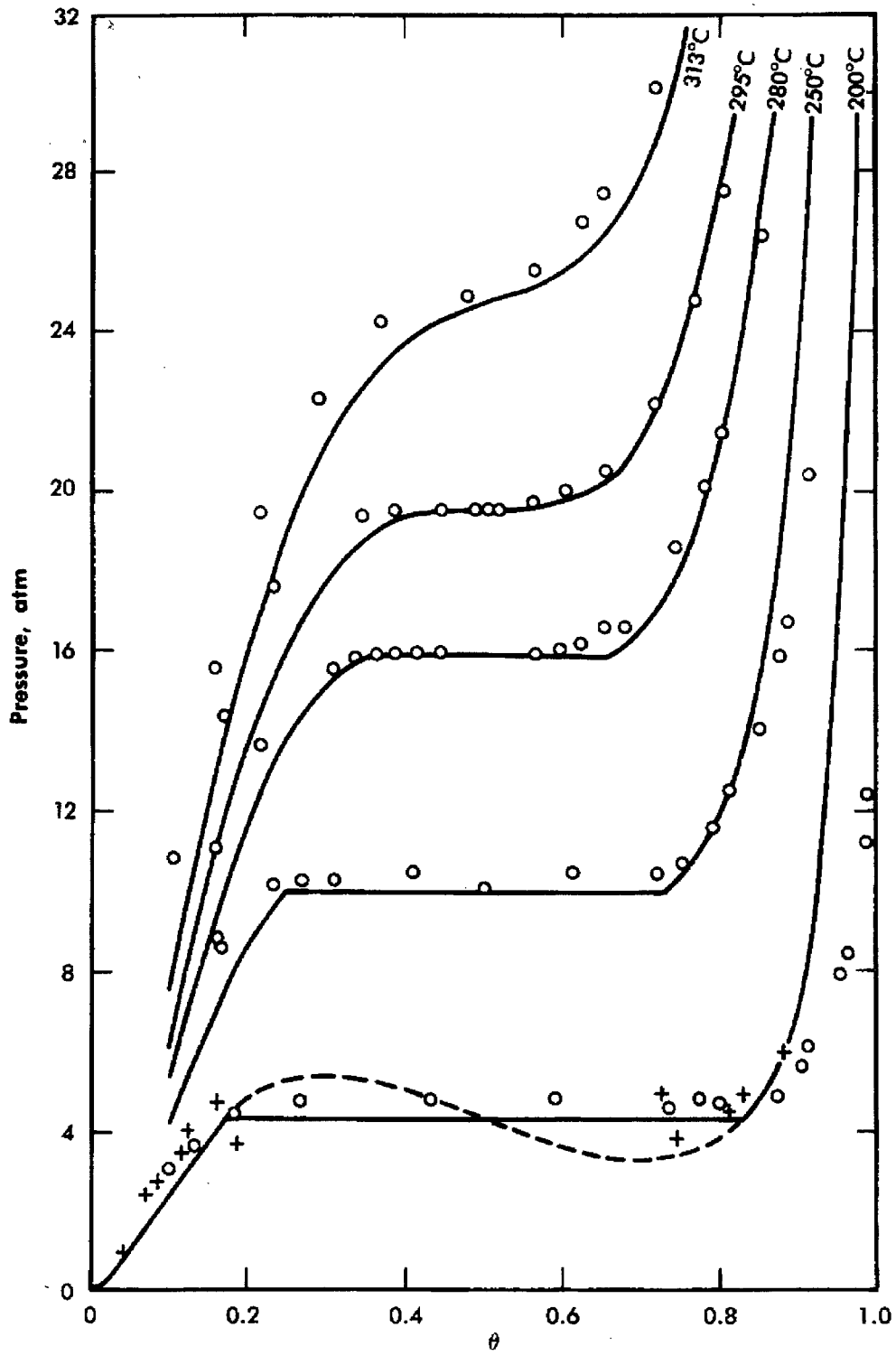

Figure II-1 Gas-phase isotherm of PdH, θ = H/M. (reprinted from J.R. Lacher, *Proc. Roy. Soc. (London), Ser. A*, **161** (1937): 526.)

The hydriding properties of the compound $SmCo_5$ were first noticed by Zijlstra and Westendorp.[9] They were studying a change in the material's magnetic properties with hydrogen content, and were surprised to find a large reduction in coercivity with a correspondingly large increase in hydrogen content, both of which were reversible. Neumann conducted the first studies of the hydrogen absorption properties of $LaNi_5$,[10] but the importance of this material was not recognized until the work of van Vucht, *et al.*, who explored the discovery of Zijlstra and Westendorp with a variety of AB_5 materials.[11] As stated by van Vucht, *et al.*, these metal hydrides are "exceptional in that they absorb hydrogen at room temperature quickly and reversibly, dependent only on hydrogen-gas pressure."[11] The density of hydrogen in $LaNi_5$ at full capacity, ~6.7 H atoms per $LaNi_5$ formula unit (*f.u.*), is 7.6×10^{22} atoms/cm^3, or ~1000 cc hydrogen gas per cc $LaNi_5$ at STP. This is much greater than that of liquid hydrogen, 784 cc/cc at –273° C, or hydrogen in high-pressure storage tanks, ~200cc/cc at 200 atm.

Isotherms of some of these archetype materials are shown in **Figure II-2.**[13] We can see that these materials operate at a variety of pressures at room temperature, making them useful for different applications. They also have a range of volumetric and gravimetric densities as hydrogen storage materials, seen in **Table II-1**. The aspect of intermetallic hydrides that makes them particularly useful and attractive for applications is that their isotherms, and hence operating pressures as well as several other properties of these materials, can be modified by alloying them with other metals.

Although intermetallic compound hydrides are distinct from metal hydrides, I will call all AB_5 intermetallic alloys *metal hydrides* (*MH*).

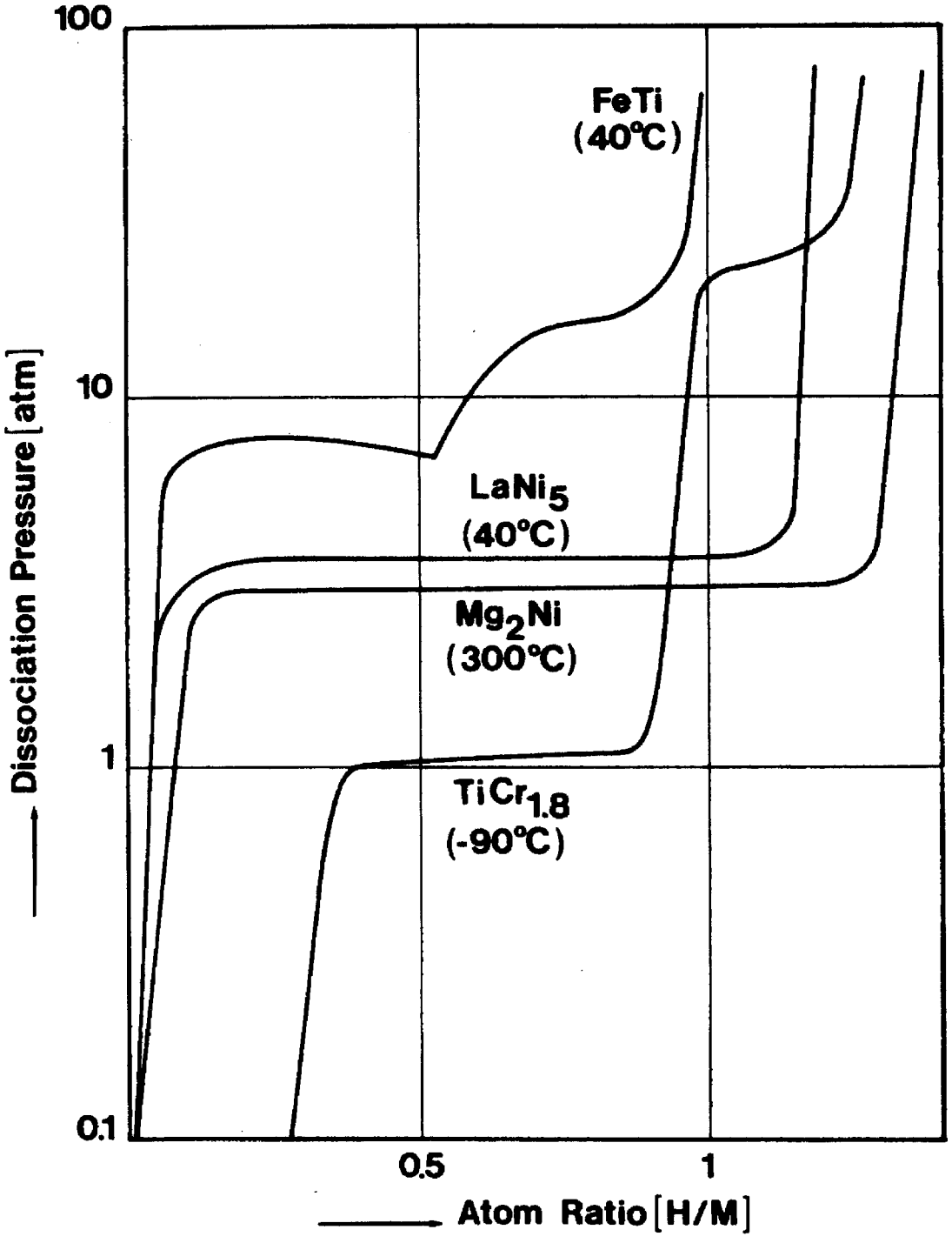

Figure II-2 Gas-phase isotherm of archetypal AB_n alloys. (reprinted from a. Percheron-Guégan and J.-M. Welter in *Topics in Applied Physics: Hydrogen in Intermetallic Compounds I*, Chapter 2, L. Schlapbach, ed., Springer Verlag (Berlin: 1988).)

Material	Molar mass [g]	C_H [wt.%]	$V_{Unit\ Cell}$ [Å^3]	ρ_H [g H_2/cc]	$P_{desorption}$ [atm.]
ZrNiH $ZrNiH_3$	149.930	0.66 2.0	542.08 405.224		<0.001 0.25 (@ 250° C)[4]
FeTiH $FeTiH_2$	103.747	0.95 1.9	88.3 288.8	0.056 0.104	4 8 (@ 25° C)[5]
Mg_2NiH_4	107.334	3.6	293.9	0.093	3.2 (@ 26° C)[6]
$AB_2H_{\sim 3}$	~150.0	1.8 - 2.0			0.1 - 20 (@ 25° C)[8]
$LaNi_5H_6$	432.456	1.5	126.6	0.0787	2.5 (@ 25° C)[12]

Table II-1 Volumetric and gravimetric densities of AB_n intermetallic hydrides.

[1] T. Graham, *Phil. Trans. Roy. Soc.*, **156** (1866): 399.

[2] T. Graham, *Proc. Roy. Soc. (London),* **17** (1869): 212, 500; *C. R. Acad. Sci.,* **68** (1869): 101, 1511; *Ann. Chim. Phys. (Paris),* **16** (1869): 188; *Ann. Chem. Pharm.,* **150** (1869): 353; **152** (1869): 168.

[3] J.R. Lacher, *Proc. Roy. Soc. (London), Ser. A*, **161** (1937): 526.

[4] G.G. Libowitz, H.F. Hayes, and T.R.P. Gibb, *J. Phys. Chem.* **62** (1958): 76.

[5] J.J. Reilly and R.H. Wiswall, *Inorg. Chem.*, **13** (1974): 218; see references for earlier work on FeTi-H.

[6] J.J. Reilly and R.H. Wiswall, *Inorg. Chem.*, **7** (1968): 2254.

[7] A. Pebler and E.A. Gulbransen, *Electrochem. Technology*, **4 (5-6)** (1966): 211.

[8] D. Shaltiel, I. Jacob, and D. Davidov, *J. Less-Common Met.*, **53** (1977): 117.

[9] H. Zijlstra and F.F. Westendorp, *Sol. State Comm.*, **7** (1969): 857.

[10] H.-H. Neumann: "Lõslichkeit von Wasserstoff und Deuterium in $LaNi_5$; Ph.D. Thesis, Faculty of Chemistry, Technische Hochschule Darmstadt, 1969.

[11] J.H.N. van Vucht, F.A. Kuijpers, and H.C.A.M. Bruning, *Philips Res. Rep.*, **25** (1970): 133.

[12] K.H.J. Buschow and H.H. van Mal, *J. Less-Common Met.*, **29** (1972): 203.

[13] A. Percheron-Guégan and J.-M. Welter in *Topics in Applied Physics: Hydrogen in Intermetallic Compounds I*, Chapter 2, L. Schlapbach, ed., Springer Verlag (Berlin: 1988).

B. Applications

Despite the early discovery of metal hydrides, widespread application of this phenomenon was not pursued until the 1970's. That decade heralded a small explosion in metal hydride research that continues today. This renewed interest is exemplified by the publication of many texts about the science and technology of metal and intermetallic hydrides, such as the *Topics in Applied Physics (TAP)* volumes *Hydrogen in Metals I & II* (1978) [1,2] *Hydrogen in Intermetallic Compounds I* (1988) *& II* (1992),[3,4] and *III* (1997).[5]

1. Gas-Phase

There are many characteristics of metal hydrides that are of scientific and technological interest. Some examples include crystal structure, thermodynamics and phase diagrams, electronic and magnetic properties, the lattice dynamics of hydrogen and the host metal, surface properties, and elastic interactions. These properties can be harnessed in unique ways to create heat pumps and refrigerators, hydrogen purifiers and isotope separators, temperature sensors, steam generation plants, chilled water production plants,[6-8] hydrogen sorption cooling for air conditioners,[8] cryocoolers,[9] and many, many other technological applications. J. J. Reilly provided an extensive, although early, description of possible technological uses for metal hydrides.[10] I have transcribed some of his descriptions to give the reader an idea of the usefulness of MH heat pumps:

> The rather large latent heat effects of metal-hydrogen systems can be exploited to design novel heat pump cycles. In essence, the device consists of two metal hydride beds, an evaporator bed and a condenser bed as shown in Fig. 13. Gruen *et al.*[11] have designed and built a demonstration facility (HYCSOS) to test various alloy hydride and bed configurations. Initial designs incorporated a heat storage capability which was later eliminated because of its high cost. Present designs specify two different AB_5 alloy hydride beds having matched pressure-temperature characteristics to give optimum performance. The beds are cycled very rapidly to reduce alloy inventory to a minimum. A mechanical compressor is not required.

Most recently Alefeld [12] has proposed a heat pump topping cycle for power generation using a high temperature Mg alloy hydride and low temperature ferrotitanium or AB_5 alloy hydride. The author envisages an increase in power generation efficiency from 37 - 49%. The cycle is rather complicated and for a full discussion the reader is referred to the references cited.

The hydriding and dehydriding reactions of a number of unstable metal-hydrogen systems are rapid enough to consider their use as hydrogen compressors or pumps. The pumping action is derived from the alternate decomposition and reformation of a metal hydride using low grade heat and a heat sink to provide the driving force. The first such pump using an unstable hydride was built in 1971 [13] for laboratory use and is still in operation. The pumping action was obtained by the alternate decomposition and reformation of VH_2 using hot (50° C) and cold (18° C) water. A more sophisticated and higher capacity compressor has recently been built using $LaNi_5H_x$ and its operation is described by van Mal.[14]

An interesting variant has been suggested by Powell *et al.*[15] who are concerned with highly efficient power conversion systems. It is based on using a low temperature heat source in combination with a high temperature heat source in a closed Brayton cycle where hot compressed gas is expanded through a turbine. The novel feature of the system is the use of an unstable hydride and low temperature heat to effect the compression of the gas, thereby eliminating mechanical compressor work and substantially increasing the efficiency of the use of the high temperature heat.

A later overview of MH applications can be found in TAP v67, chapter 5, written by Gary Sandrock, S. Suda, and L. Schlapbach.[16] This compilation adds liquid hydrogen, catalytic, electrochemical, and permanent magnet production to the long list of MH technologies. The most recent description of MH applications was written by P. Dantzer for TAP v73, chapter 7.[17] One especially useful aspect of this review is that it addresses the properties of MH alloys that are relevant, generally and in particular, to technological applications.

Of course, one of the most important applications of metal hydrides is simply the storage of hydrogen gas for use as a fuel, whether for combustion in a turbine engine or electrochemical oxidation in a fuel cell. The fossil fuel crisis in the early seventies brought about a search for alternative fuels, and hydrogen was a prime candidate.[18] This

prompted in 1974 discussion of the world's transforming from a fossil fuel to a "Hydrogen Economy" at the first international conference on Hydrogen Energy, the Hydrogen Economy Miami Energy Conference.[19] This seminal conference was soon followed with the formation in the same year of the International Association for Hydrogen Energy.[20]

The properties of significance to hydrogen storage, whether portable or stationary, are capacity, sorption temperature-pressure relationship, and cyclic lifetime. These are depicted by the hydrogen isotherm, the van't Hoff plot, and capacity-lifetime curves. The high capacity and convenient sorption pressures of $LaNi_5$ makes it the most attractive system for terrestrial applications. At room temperature, the pressure above $LaNi_5$ at full capacity, ~6.7 H/f.u., is ~2.5 atm. The equipment necessary to store and transport hydrogen in $LaNi_5$ is much simpler, more reliable, and less expensive than that necessary to store hydrogen compressed at very high pressures or liquid hydrogen at very low temperatures. One drawback to using $LaNi_5$ as a hydrogen storage medium, however, is its low specific density. The 1.5 wt.% hydrogen density attained by $LaNi_5$ is reduced to a practical value of 1.2 wt.% when the container and regulating equipment are added to the material weight.[21]

2. Electrochemical

Another aspect of metal hydrides of great interest to society is their ability to act as the anode material in an alkaline rechargeable battery. The concept of a MH cell is rather young, and was first attempted by Lewis, *et al.* in 1967 with PdH as the anode material.[22] Not long after Lewis made his PdH cell, IMCHs were investigated as hydride electrodes.[23] When $LaNi_5$ was first used as the anode material in an alkaline rechargeable cell, the researchers could attain a capacity of only 100 mAh/g.[24] This is ~25% of the material's theoretical capacity of 372 mAh/g, corresponding to $LaNi_5H_6$. Percheron, *et al.*, were able to achieve higher capacities with substituted $LaNi_5$ alloys, obtaining

capacities as high as 325 mAh/g for $LaNi_{4.75}Al_{0.25}$, 340 mAh/g for $LaNi_{4.98}Ti_{0.02}$, and 390 mAh/g with $LaNi_{4.5}Mn_{0.5}$.[25] Subsequent work designing AB_5 alloys for nickel metal-hydride (*Ni-MH*) batteries has been summarized in a recent review by Sakai where he states, "A tremendous R&D effort has been conducted on the MH electrode and the Ni-MH battery since 1985, leading to prominent progress in every area of performance."[26] The state-of-the-art, commercially produced nickel metal-hydride battery has a practical energy density of ~175 mAh/g and can make up to 2000 cycles at 100% depth of discharge (DOD) before the capacity of the anode dips substantially below that of the cathode.[26] Over 200 million Ni-MH cells were manufactured in 1994, and "extensive research on large Ni-MH batteries is in progress for EV application."[26]

The Ni-MH cell commonly has a metal-hydride anode and a pasted $Ni(OH)_2$/NiOOH cathode. Each electrode material is wrapped in nickel mesh, which serves as the current collector, and enclosed in some separator material, e.g., woven nylon. A 6 molar KOH solution serves as the electrolyte to transport the reaction species, OH^- and H_2O. A schematic of the charging and discharging processes is shown in **Figure II-3.**

There are several aspects of Ni-MH batteries that make them attractive for commercial use. These properties will all be compared with Nickel Cadmium (*Ni-Cd*) batteries, which are considered the current commercial standard as well as being prevalent in technological circles. First, the cell components are almost identical to those in Ni-Cd's, the only difference being the anode, where Cd is replaced by the MH alloy and the associated conductive and binder materials. Second, the cell potential is slightly higher than that of Ni-Cd batteries, giving them greater power densities as well as making them more resistant to the well known "memory-effect." (The memory effect is caused by a reversible phase change in the $Ni(OH)_2$/NiOOH cathode which is affected by the charging potential.[27]) Although $Cd/Cd(OH)_2$ anodes have theoretical densities reportedly as great as 365 mAh/g,[26] the practical energy density of Ni-MH batteries is still 20-30 wt.% and 50-100 vol.% greater than that of Ni-Cd's. The graph shown in **Figure II-4**

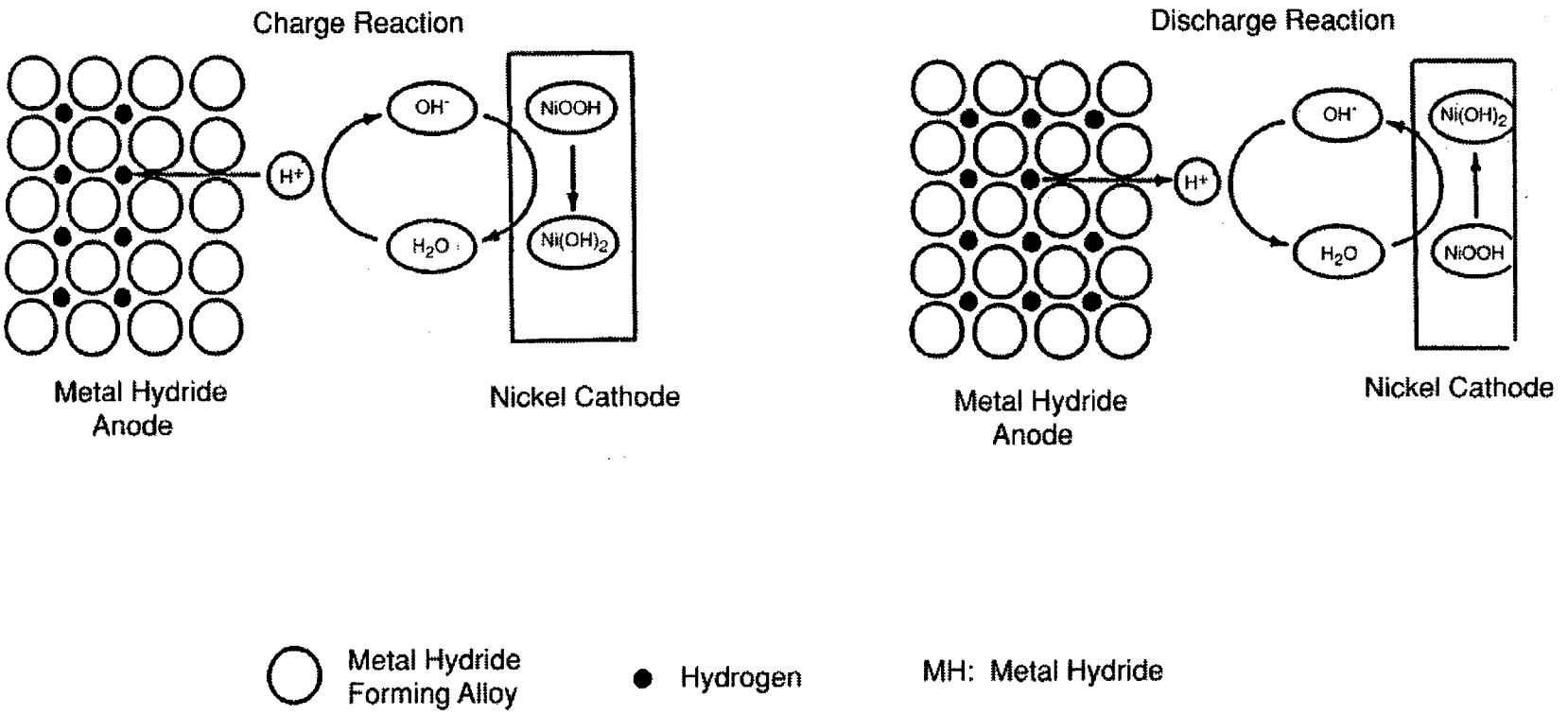

$$LaNi_5 + 6Ni(OH)_2 \leftrightarrow LaNi_5H_6 + 6NiOOH$$

Figure II-3 Schematic of MH charging process.

COMPARISON OF Wh/l OF SEALED RECHARGEABLE CELLS

NIKKEL ELECTRONICS 1989. 3. 20

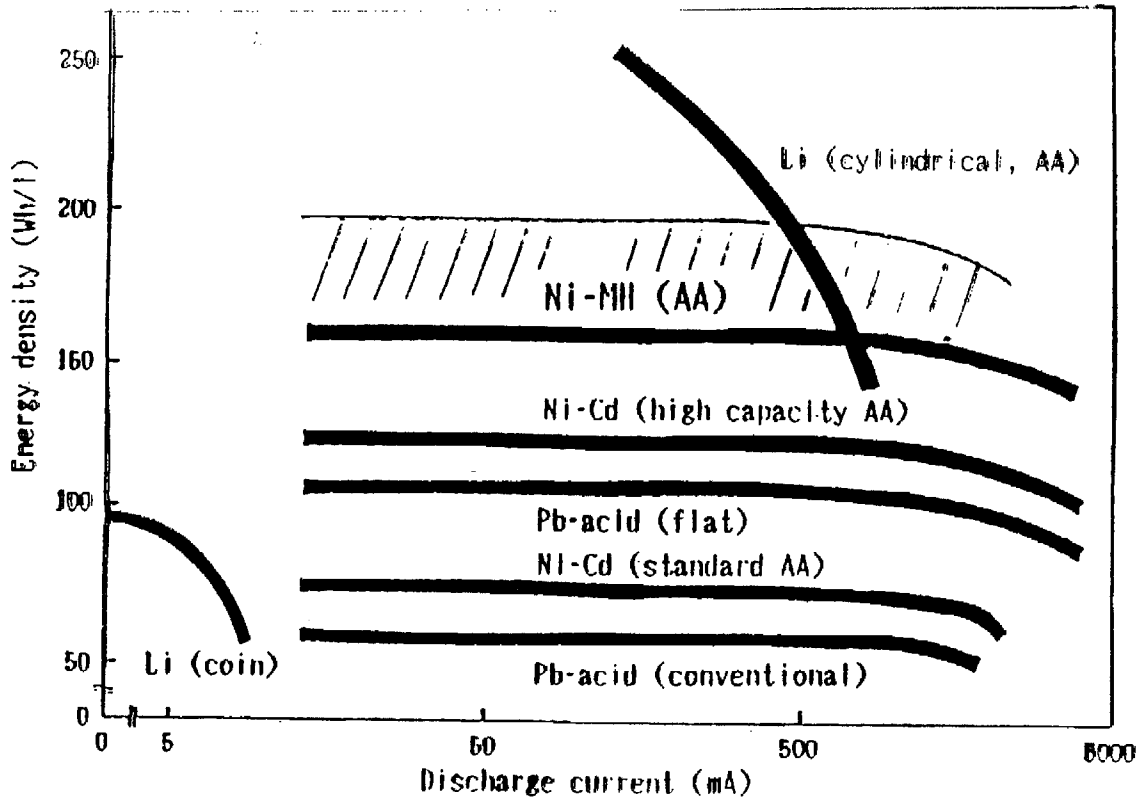

- **Highest energy densities especially at high discharge currents**

Figure II-4 Power densities of various rechargeable batteries.

displays the ranges of power density that a variety of rechargeable battery technologies can achieve *vs* discharge current density (with the discharge energies normalized by the anode active material mass). The gas recombination mechanisms available to Ni-MH batteries make them resistant to the problems associated with overcharge and discharge.[26] Finally, there are little or no environmental or human health hazards associated with the materials used in Ni-MH batteries, in contrast with the well known hazards associated with the production and processing of the metal cadmium.

[1] *Topics in Applied Physics v. 28 Hydrogen in Metals I: Basic Properties*, G. Alefeld and J. Volkl, eds., Springer-Verlag, Berlin. 1978.

[2] *Topics in Applied Physics v. 29 Hydrogen in Metals II: Application-Oriented Properties*, G. Alefeld and J. Volkl, eds., Springer-Verlag, Berlin. 1978.

[3] *Topics in Applied Physics v. 63 Hydrogen in Intermetallic Compounds I: Electronic, Thermodynamic, and Crystallographic Properties, Preparation*, L. Schlapbach, ed., Springer-Verlag, Berlin. 1988.

[4] *Topics in Applied Physics v. 67 Hydrogen in Intermetallic Compounds I: Surface and Dynamic Properties, Applications*, L. Schlapbach, ed., Springer-Verlag, Berlin. 1992.

[5] *Topics in Applied Physics v. 73: Hydrogen in Metals III*, H. Wipf, ed., Springer-Verlag, Berlin, 1997.

[6] S. Suda, *J. Less-Common Met.*, **104** (1984): 211.

[7] M. Ron, *J. Less-Common Met.*, **104** (1984): 259.

[8] I. Sheft, D.M. Gruen, G.J. Lamich, L.W. Carlson, A.E. Knox, J.M. Nixon, and M.H. Mendelsohn, in *Proc. Int. Symp. on Hydrides for Energy Storage, Geilo, August 14-19, 1977*, Pergamon, New York, 1978, p. 551.

[9] B.D. Freeman, E.L. Ryba, R.C. Bowman, Jr., and J.R. Phillips, *Int. J. Hydrogen Energy*, **22 (12)** (1997): 1125; R.C. Bowman, Jr., P.B. Karlmann, and S. Bard, *Advances in Cryogenic Engineering*, **43** (1998): 1017.

[10] J.J. Reilly, *Zeitschrift für Physikalische Chemie Neue Folge*, **117** (1979): 155.

[11] D.M. Gruen, T.L. McBeth, M. Mendelsohn, J.M. Nixon, F. Schreiner, and I. Sheft, *Proc. 11th Intersociety Energy Conversion Eng. Conf.,* Stateline, Nevada, American Institute of Chemical Engineers, N.Y., 1976.

[12] G. Alefeld in *Topics in Applied Physics: Hydrogen in Metals II*, Springer, Berlin-Heidelberg-New York, 1978.

[13] J.J. Reilly, A. Holtz, and R.H. Wiswall, Jr., *Rev. Sci. Instrum.*, **42** (1972) 10: 1495.

[14] H. H. van Mal, *Proc. Int. Symp. on Hydrides for Energy Storage*, Geilo, Norway, 1977, A.F. Andresen and A.J. Maeland, eds., pp. 251-261, Pergamon Press, London 1978.

[15] J.R. Powell, F.J. Salzano, Wen-Shi Yu, and J.S. Milau, USERDA Report, BNL 50447, Brookhaven National Laboratory, Upton, N.Y., 1975.

[16] Gary Sandrock, S. Suda, and L. Schlapbach, in L. Schlapbach, ed. *Topics in Applied Physics v. 67 Hydrogen in Intermetallic Compounds I: Surface and Dynamic Properties, Applications*, Springer-Verlag, Berlin. 1992, chapter 5.

[17] P. Dantzer in *Topics in Applied Physics v. 73: Hydrogen in Metals III*, H. Wipf, ed., Springer-Verlag, Berlin, 1997, p. 279.

[18] D.P. Gregory, *Scientific American*, **228** (Jan. 1973): 13.

[19] *Hydrogen Energy: proc. the Hydrogen Economy Miami Energy (THEME) Conference*, Miami Beach, FL, March 18-20, 1974, T. Nehat Veziroglu, ed.(New York : Plenum Press, 1975).

[20] T. Nehat Veziroglu, *International Journal of Hydrogen Energy*, **20** (1994): 1.

[21] R.L. Cohen, and J.H. Wernick, *Science*, **214** (1981): 1081.

[22] F.A. Lewis, *The Palladium Hydrogen System*, (Academic London 1967).

[23] E.W. Justi, H.H. Ewe, A.W. Kalberlah, N.M. Saridakis, and M.H. Schaefer, *Energy Conversion*, **10** (1970): 183.

[24] H.H. Ewe, E.W. Justi, and K. Stephan, *Energy Conversion*, **13** (1973): 109.

[25] A. Percheron-Guégan, L. Schlapbach, J.C. Achard, J. Sarradin, and G. Bronoël, *Journées de l'état solide,* Société Chimique de France, Paris, Sept. 1974; G. Bronoël, J. Sarradin, M. Bonnemay, A. Percheron, J.C. Achard, and L. Schlapbach, *Int. J. of Hydrogen Energy*, **1** (1976): 251; G. Bronoël, J. Sarradin, M. Bonnemay, A. Percheron, and J.C. Achard, *Mater. Res. Bulletin*, **13** (1978): 1265.

[26] T. Sakai, M. Matsuoka, and C. Iwakura, in *Handbook on the Physics and Chemistry of Rare Earths*, eds. K.A. Gschneidner, Jr. and L. Eyring, **21** (1995): 133.

[27] H. Bode, K. Dehmelt, and J. Witte, *Electrochim. Acta.*, **11** (1966): 1079.

C. $LaNi_5$

1. Phase Diagram and Crystal Structure of $LaNi_5$

The La-Ni phase diagram, shown in **Figure II-5**, was first determined experimentally by Vogel.[1] He expressed uncertainty about the compositions of several phases, and several researchers have since reinvestigated the phase diagram,[2,3] with the most recent study done by D. Zhang, *et al.*[4] As seen in the phase diagram, the alloy $LaNi_5$ is a stoichiometric compound below a temperature of ~950° C.

The original X-ray diffraction (*XRD*) study of the structure of $LaNi_5$ and many other RE AB_5 materials was performed by Nowotny in 1942.[5] It was correctly indexed as Haucke phase ($CaCu_5$ structure),[6] but later work by Wernick and Geller in 1959 showed that Nowotny's determination of the lattice parameters was in error.[7] The alloy unit cell shown in **Figure II-6** is hexagonal with lattice parameters a = 5.017 Å and c = 3.987 Å.[3] The lanthanum atom lies on the basal plane of the unit cell, and the atoms in its first two nearest neighbor shells (CN = 18) are all Ni atoms, $d_{La\text{-}Ni}$ = 2.896 Å and 3.204 Å. The Ni atom in the 2c location also lies on the basal plane and has 6 Ni atoms in the 1st nearest neighbors shell, $d_{Ni\text{-}Ni}$ = 2.464 Å. The second nearest neighbor shell, lying 17% farther away ($d_{Ni\text{-}Ni}$ = 2.883 Å), is occupied by 3 La atoms and 3 Ni atoms. The 3g Ni atom location lies in the z = 1/2 plane and has 8 Ni atoms in the first two nearest neighbor shells (1% separation, $d_{Ni\text{-}Ni}$ = 2.464 Å and 2.509 Å). Its third nearest neighbor shell, lying 30% farther away than the first ($d_{La\text{-}Ni}$ = 3.2 Å) contains 4 La atoms.

Above ~950° C, this hP6 ordered alloy is stable for a range of stoichiometry $LaNi_{5+x}$ that increases with temperature to $-0.15 \leq x \leq 0.40$ at 1200° C, returning to $LaNi_5$ at the melting temperature, 1350° C.[3] Buschow and van Mal performed an evaluation of the alloy structure in this range and found that the lattice parameters depend on the

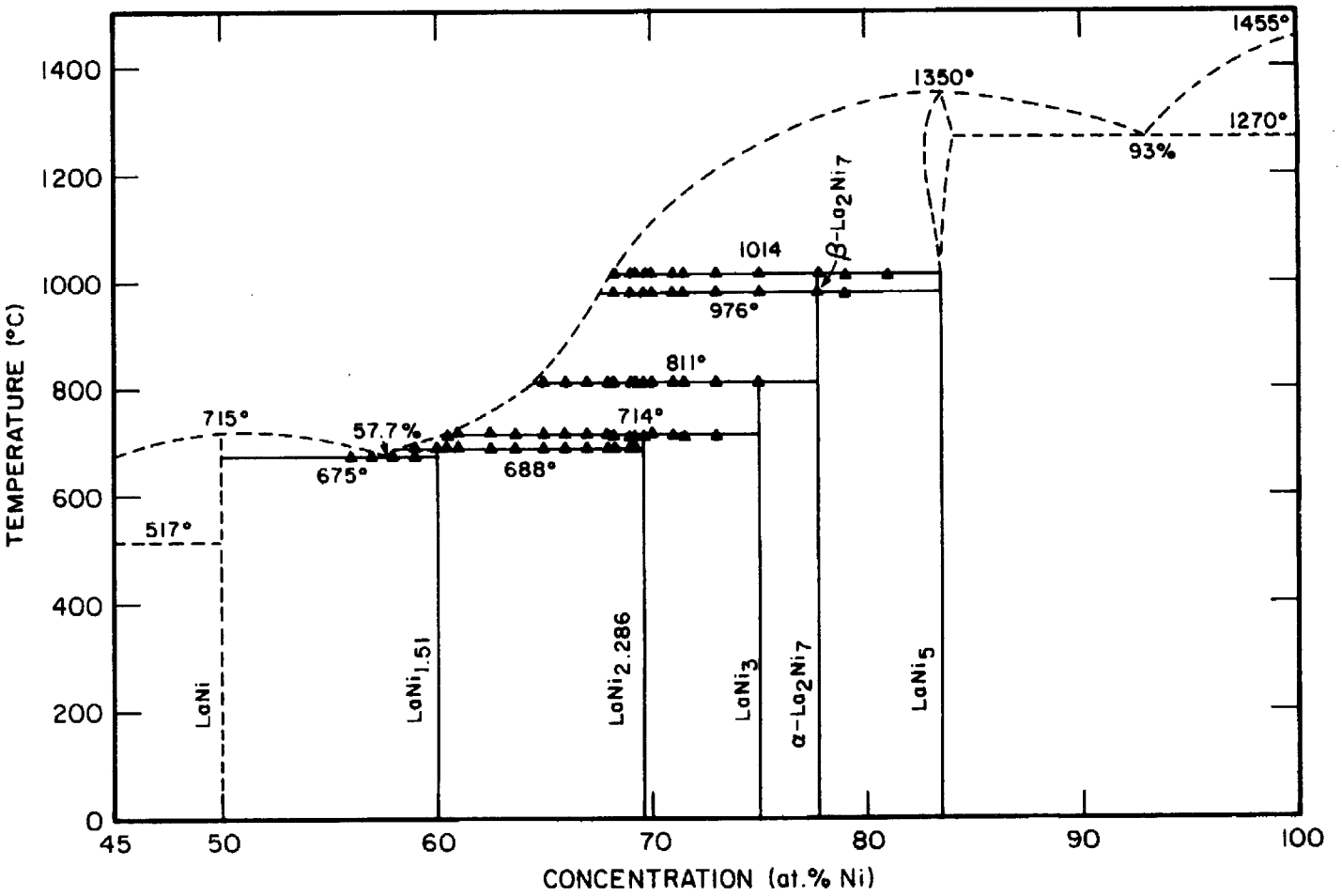

Figure II-5 Detail of Ni-rich half of La-Ni Phase diagram. (reprinted from D. Zhang, J. Tang, and K.A. Gschneidner, Jr., *J. Less-Common Met.*, **169** (1991): 45.)

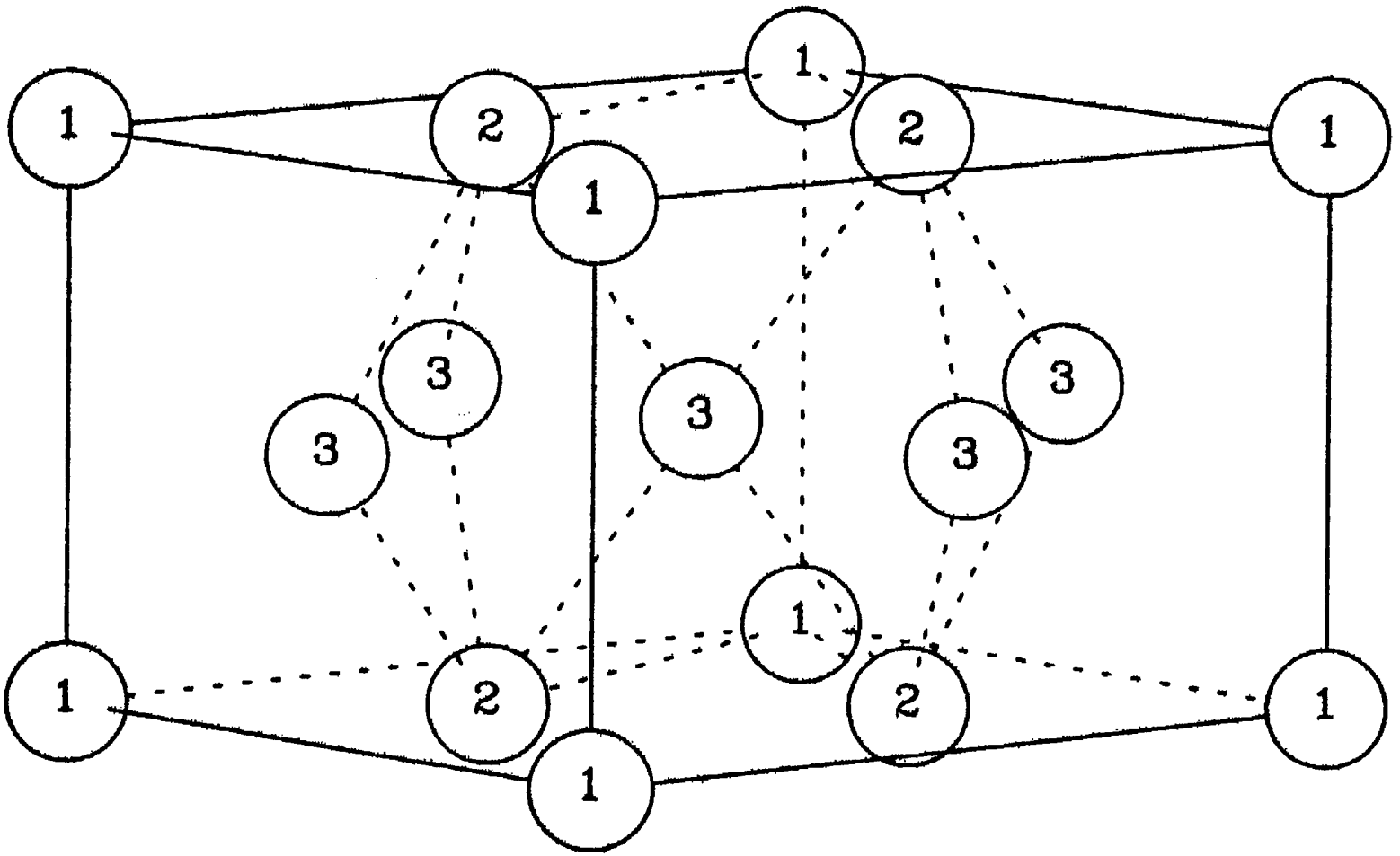

Figure II-6 Unit cell of $LaNi_5$. 1 = La, 2 = 2c Ni, 3 = 3g Ni. (reprinted from J.L.C. Daams, P. Villars, and J.H.N. van Vucht, *Atlas of Crystal Structure Types for Intermetallic Phases* (Newbury, OH: ASM International, 1991).)

stoichiometry as shown in **Figure II-7**, reprinted from ref. 3. The nature of the resulting disorder was later investigated by Coene, *et al.*[8] The results of their transmission electron microscopy (*TEM*) experiments show that for $x < 0$, there is a simple substitutional replacement of the 3g Ni atoms with La. When $x > 0$, La atoms are replaced by 2 Ni atoms in a dumbbell configuration with the connecting axis along the crystallographic z-direction.[8]

2. Gas-Phase p-c-isotherm

When $LaNi_5$ metal is in the presence of hydrogen, the hydrogen is absorbed into the metal lattice at a hydrogen partial pressure (equivalent to chemical potential) determined by the temperature and the heat of formation of the metal hydride. This reaction follows **equation II.1**:

$$LaNi_5 + y/2\ H_2 \rightarrow LaNi_5H_y. \qquad [II.1]$$

The relationship between hydrogen composition in the metal hydride and hydrogen pressure in the gas phase is usually depicted as a hydrogen pressure-composition-isotherm, or *isotherm*. A room temperature isotherm of binary $LaNi_5$ can be seen in **Figure II-8**. There are three sections of note in this diagram. In the first, the hydrogen pressure and composition are both quite low, and the pressure rises rather steeply with composition. Here, the hydrogen gas is in equilibrium with hydrogen in solution in the metal lattice, which is called the *α-phase*. In the α-phase, the hydrogen pressure is proportional to the square root of the hydrogen stoichiometry, following what is known as Sievert's law.[9] As the hydrogen composition increases, attractive hydrogen-hydrogen interactions begin to dominate, and the hydrogen begins to cluster in the metal lattice. These regions of high hydrogen composition are called the *hydride*, or *β-phase*. In the portion of the isotherm called the *plateau* region, the α- and β-phases are in equilibrium

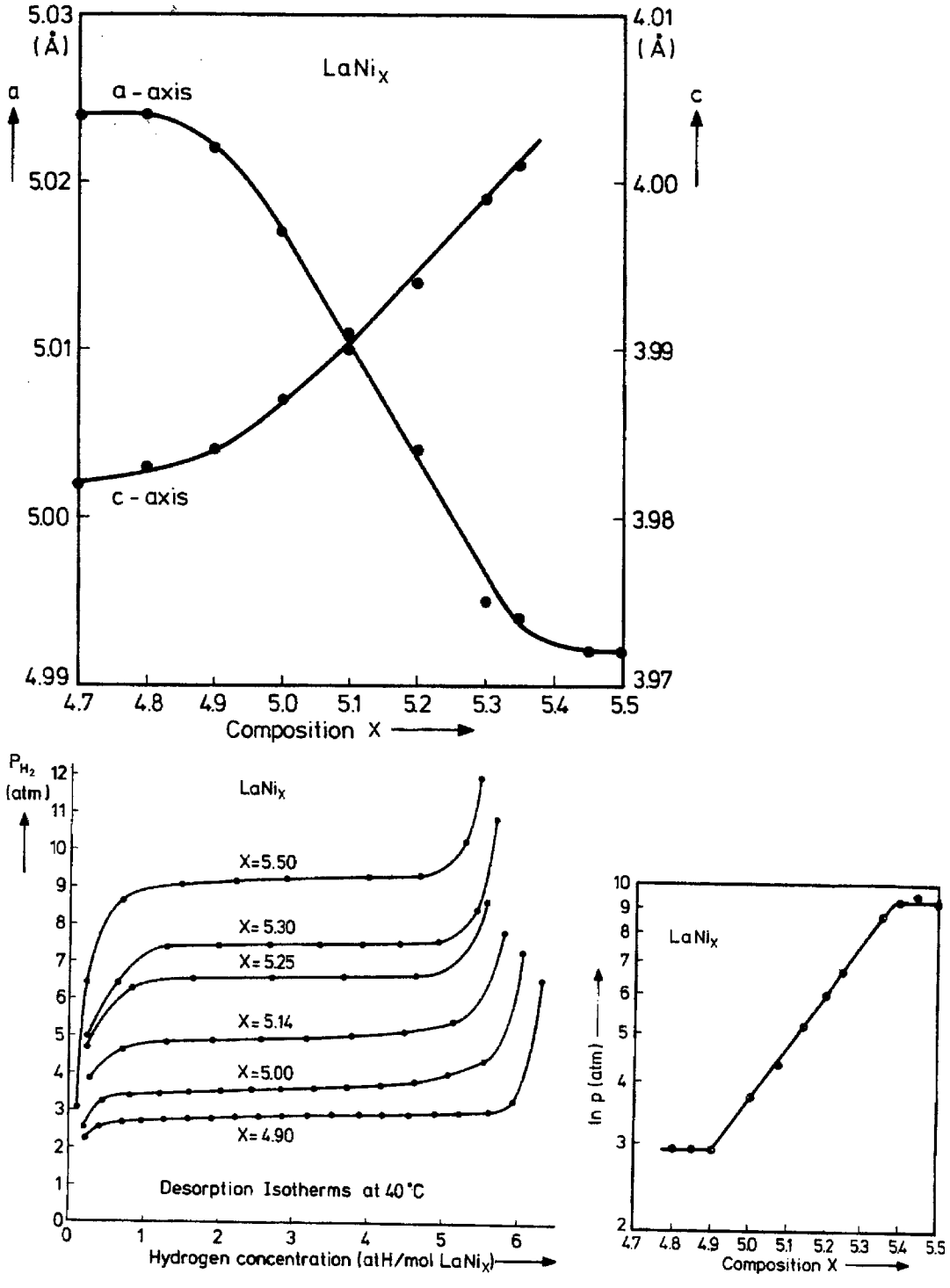

Figure II-7 Dependence of $LaNi_x$ lattice parameters and isotherm characteristics on alloy stoichiometry. (reprinted from K.H.J. Buschow, and H.H. van Mal, *J. Less-Common Met.*, **29** (1972): 203.)

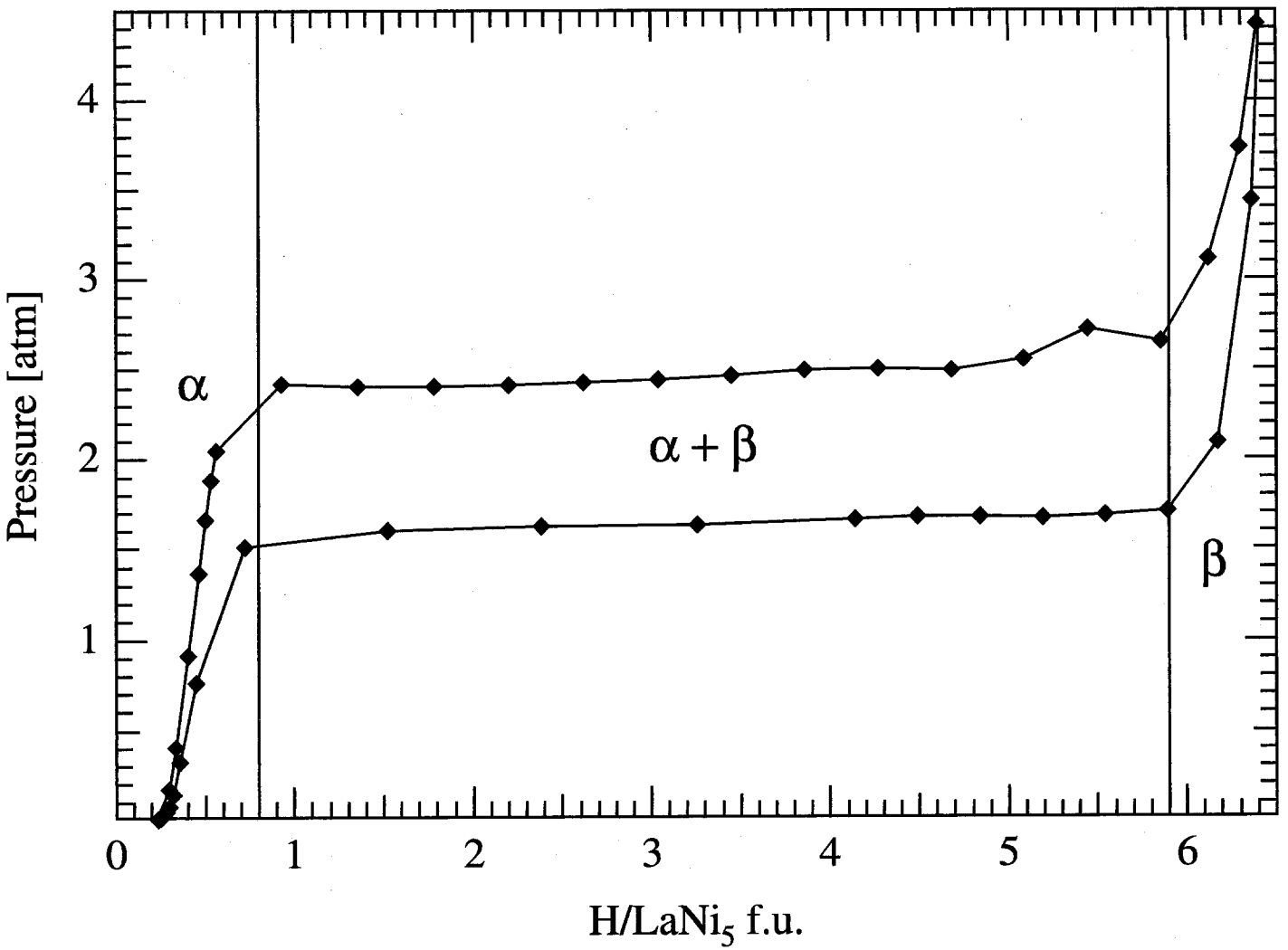

Figure II-8 Room temperature gas-phase isotherm of $LaNi_5$.

with each other and with hydrogen in the gas-phase. When both the α- and β-phase hydrides are present, the additional variable of the relative phase fractions removes one degree of freedom from the system, a consequence of Gibbs' phase rule. In a closed, isothermal homogeneous system, the variation of the phase fractions is allowed because the pressure in the 2-phase region becomes constant. The end of the plateau region in the room temperature isotherm corresponds to a β-phase metal hydride holding approximately 5.9 hydrogen atoms per $LaNi_5$ formula unit.[10] Finally, when all of the metal hydride in the α-phase has been converted to the β-phase, the hydrogen-hydrogen interactions begin to be repulsive, and the pressure rises. Isotherms of $LaNi_5$ have been measured to a pressure of 1650 atm. Corresponding to a composition of $LaNi_5H_{8.35}$.[11]

The effect of increasing temperature is shown schematically in **Figure II-9**.[12] The plateau pressure increases and the width of the plateau decreases, a result of the narrowing of the miscibility gap between the α- and β-phases. At some critical temperature for β-phase formation, the miscibility gap and plateau disappear and the α-phase transforms continuously into the β-phase. An interesting phenomenon that can sometimes be seen in the $LaNi_5$ isotherm is the appearance of a second plateau that appears between 3 and 3.5 H/f.u.[13] This has been attributed to the existence of a second hydride phase. This γ-hydride phase was first noted in the isotherm of the metal hydride [13] and later confirmed by *in-situ* XRD.[14,15] Recent isotherm measurements confirm that the plateau splitting is stabilized at higher temperatures (60 - 90° C) and by cycling.[16]

a. Thermodynamics

The functional relationship between the free energy of hydrogen in the metal lattice and the absorption or desorption pressures is easily determined by equilibrium thermodynamics. The hydrogen in the hydride phase is in equilibrium with hydrogen in

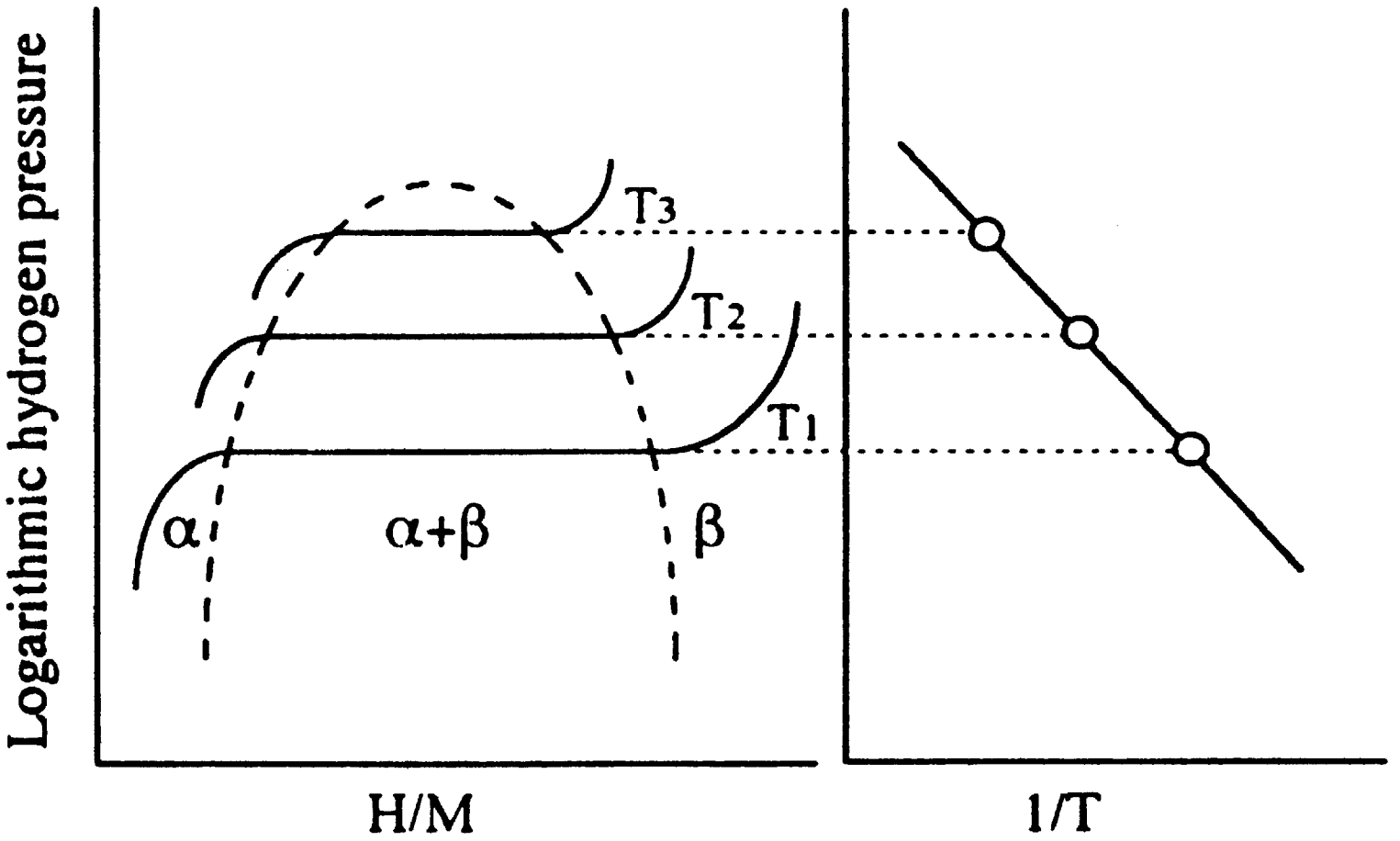

Figure II-9 Schematic of multiple T isotherms and van't Hoff plot of MH alloy. (reprinted from L. Schlapbach in *Topics in Applies Physics: Hydrogen in Intermetallic Compounds I*, Chapter 1, L. Schlapbach, ed., Springer Verlag (Berlin: 1988).)

the gas phase, so the free energy of hydrogen in each phase is equal. At room temperature, the chemical potential of an ideal gas is $\mu = \mu_0 + kT \ln p$. The thermodynamic relationships $N\mu = G$ and $\Delta G = \Delta H - T\Delta S$ make it possible to find the enthalpy and entropy of hydride formation by plotting $R \ln p$ *vs* $1/T$ in a van't Hoff plot, shown schematically in **Figure II-9**.[12] The heat of formation of the intermetallic hydride of $LaNi_5$ is ~31.6 kJ/mol H_2, and the entropy loss associated with this phase change is ~108 J/°C/mol H_2.

Entropy changes in reaction [**II.1**] are almost entirely dominated by the reduction of the entropy of gaseous hydrogen from 130.8 J/°C/mol H_2 [17] to that of essentially metallic hydrogen. The contribution of H atoms to the lattice vibrational entropy of the solid AB_5 hydride is probably quite small near room temperature, the main effect being the addition of an optical phonon branch at fairly high frequencies.

b. Hysteresis

A pressure hysteresis can be noted between the absorption and desorption plateaus in the isotherm of $LaNi_5$, as seen in **Figure II-8**. To some degree, hysteresis accompanies all first-order phase transitions. In metal hydrides, the transformation from the α-phase (hydrogen in solution in the MH lattice) to the β-phase MH (hydrogen ordering on the MH lattice at a composition of ~1 H/metal atom) is a first-order phase transition. A first-order phase transition is characterized by a discontinuity in the first derivative of the free energy at the transition point. Evidence of this in the hydride transition can be seen in the volume discontinuity (explained in §II.C.3.). Above the critical point for the hydride transition (see **Figure II-9**), the volume discontinuity and hysteresis disappear. The magnitude of the energy dissipated (or entropy produced) in one hysteresis cycle is:

$$1/2\ RT \ln (p_a/p_d) \qquad [II.2]$$

Reviews of hysteresis in metal hydrides are available by Qian and Northwood [18] and by Flanagan and Park,[19] among others. Ever since hysteresis was first noticed in the Pd-H system by Lambert and Gates, [20] researchers have formulated models to explain the cause of this effect. The magnitude of the hysteresis has been empirically correlated to the discontinuity in the volume expansion and the width of the pressure plateau $c^{\beta} - c^{\alpha}$,[19] and we have found a correlation to the density of crystalline defects as determined by XRD. Justification has been given for using as the equilibrium hydriding pressure the desorption pressure, the arithmatic mean of the absorption and desorption pressures, and the geometric mean of the pressures.[18] Recent experiments to determine the nature of hysteresis in $LaNi_5$ indicate that an equilibrium pressure between the absorption and desorption plateaus does not exist, rather that the metal hydride exhibits a thermodynamically important difference during absorption and desorption.[21] Their neutron powder diffraction (*NPD*) measurements of lattice parameter variation during and after activation indicate that α- and β-phases coexist in $LaNi_5$ particles, implying that the hysteresis is caused by misfit stresses at the α/β interface.[22] Existing theories adequately describe some aspects of hysteresis in some MHs, but there is no theory that sufficiently explains all of the experimentally observed behavior in each MH system.

3. Hydride Structure and Lattice Expansion

When $LaNi_5$ absorbs hydrogen, the crystal lattice must expand to accommodate the hydrogen. At room temperature, the unit cell volume of activated $LaNi_5$ first expands isotropically and continuously ~1.5%. The lattice then experiences a discontinuous, near-isotropic volume expansion of 21.5% when it transforms from the α- to the β-phase. In **Figure II-10**, showing *in-situ* XRD by Notten, *et al.*,[23] the shift in diffraction peak positions associated with the lattice expansion can be seen. This figure also explicates the 2-phase nature of $LaNi_5$. It can be seen that the diffraction peak positions, and hence the lattice parameters, do not increase continuously when the system absorbs hydrogen,

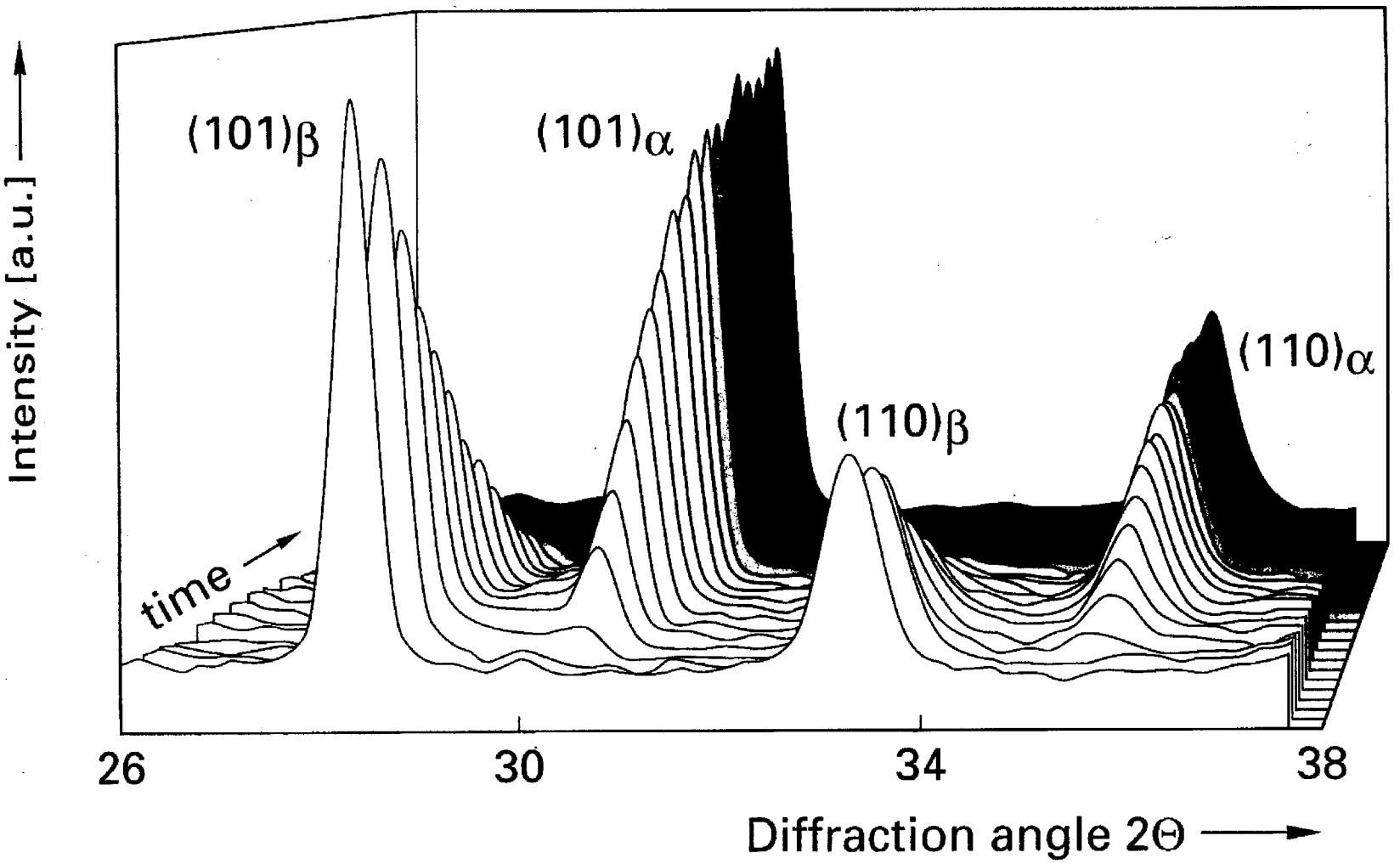

Figure II-10 In-situ XRD Of $LaNi_5H_y$ during hydrogen desorption. (reprinted from P.H.L. Notten, et al., *J. Alloys Comp.*, **209** (1994): 85.)

but material in the α-phase changes discontinuously to the β-phase.[23] When all the available α-$LaNi_5$ has been hydrided to the lower limit of the β-phase, the unit cell volume expands continuously with hydrogen composition. **Figure II-11** depicts lattice expansion as β-$LaNi_5H_{y>5}$ absorbs hydrogen. The a-axis expansion is initially greater than the c-axis expansion, but subsequent absorption makes the expansion isotropic. At the largest hydrogen concentration measured, 6.7 H/f.u., the lattice has isotropically expanded 25.75%.[10]

Under certain circumstances (elevated temperature, microstrain), the unit cell volume of α-$LaNi_5$ expands 11.8% discontinuously and anisotropically ($\Delta a/a$ = 5.2%, $\Delta c/c$ = 1.3%) to the limit of a third phase called the γ-phase, and subsequent expansion is continuous with hydrogen composition. The nature of the volume expansion has been empirically linked to characteristics of the plateau in the isotherm. A particularly flat plateau is indicative of the discontinuous volume expansion associated with the miscibility gap of the first-order phase transition. A sloping nature to regions of the plateau indicates the alloy-hydrogen system is not in a 2-phase region, and the resulting volume expansion will be continuous. This can be interpreted as the alloy having higher temperature and hydrogen composition than the critical temperature and composition for hydrogen ordering on the Haucke-phase lattice.

The structure of the β-phase hydride is a complex question, and was for some time a point of contention in the metal-hydride community. Geometric considerations by Westlake and Switendick determined that hydrogen atoms would occupy interstitial sites with a minimum radius of 0.4 Å [24] and a minimum separation of 2.1 Å from another hydrogen atom.[25] The best methods to probe hydrogen utilize coherent scattering of neutrons by deuterium and their large incoherent scattering by hydrogen.[26] Neutron diffraction is used to determine the locations of deuterium in $LaNi_5D_y$ compounds and quasi-elastic neutron scattering from deuterium or incoherent inelastic scattering from hydrogen is used to measure the dynamics of hydrogen motion in the alloys. These data

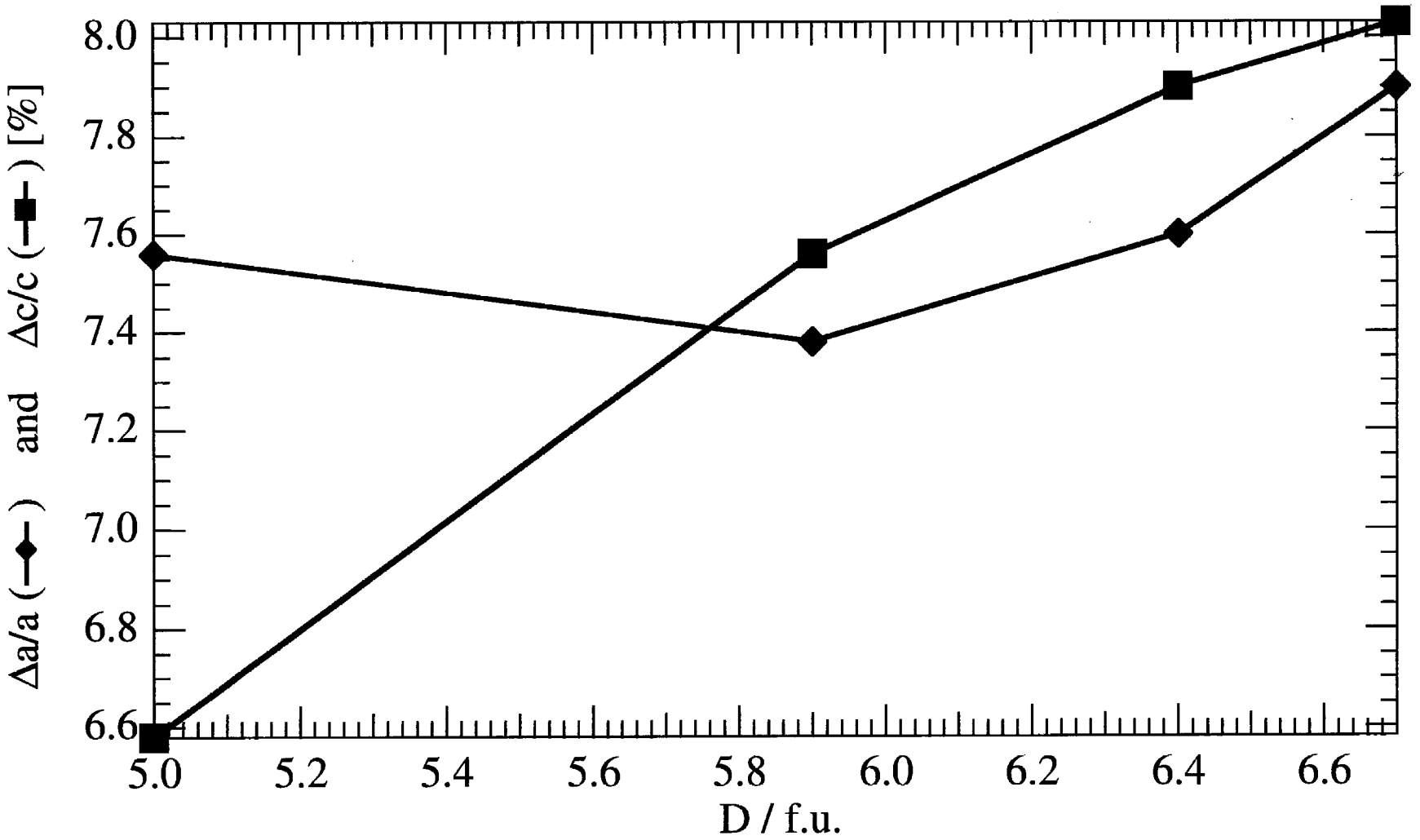

Figure II-11 β-phase lattice expansion of $LaNi_5$.
(from C. Lartigue, *et al., J. Less-Common Met.* , **113** (1985): 127.)

can also be reinforced by proton NMR measurements which investigate the time scales of hydrogen motion in the hydride.[27] An extensive review of H locations in $LaNi_5$ and its substituted alloys $LaNi_{5-x}M_x$ was performed by Percheron-Guégan, *et al.*[26]

The first neutron powder diffraction (NPD) pattern of $LaNi_5D_{6.6}$ was recorded and analyzed by Bowman, *et al.*[28] The pattern was indexed to the P31*m* space group, and hydrogen atoms were determined to fully occupy 3g ($z \approx 0.1$) sites and partially occupy 6d ($z \approx 0.5$) sites, a model later confirmed by other groups.[29-31] When Percheron-Guégan, *et al.* performed Rietveld refinement on a high-resolution neutron diffraction patterns taken on the D1B instrument at the Institut Max von Laue-Paul Langevin, Grenoble, they saw no evidence of a symmetry reduction and concluded that the deuteride structure was in the P6/*mmm* symmetry group.[32] In this model, hydrogen partially occupies 5 sites: 3f (1/2 0 0), 12n (1/2- δ_2 0 δ_3), 4h (1/3 2/3 1/2-δ_1), 6m (x 2x 1/2), and 12o (x 2x 1/2- δ_4), where δ_i is a small quantity. **Figure II-12** shows the $LaNi_5$ crystal structure with hydrogen locations of both models. The models are similar, but while the 2-site model utilizes anisotropic thermal parameters to describe the regions of deuterium occupation, the 5-site model creates/describes 2 "cages" containing multiple deuterium sites. In this way, the 5-site model gives more information on the structure of the potential wells nearby the 3c (corresponding to the 3f, 12n cage) and 6d clusters (corresponding to the 6m, 4h, 12o cage).

Further study by Percheron, *et al.* on NPD patterns of $LaNi_5D_y$, $5.0 < y < 6.7$, noted a small diffraction peak at the d = 1.805Å reflection position in their experiments as well as in previously published diffraction patterns,[29,31,32] the intensity of which seemed to decrease with decreasing D composition. Including this and two other {(201) and (205)} superlattice reflections in the refinement of their diffraction patterns required a doubling of the $LaNi_5$ unit cell along the c-axis, reducing the crystal symmetry to $P6_3mc$. As seen in table II-2, it was determined that in this range of D composition, the ratio of deuterium in the 3c cluster of sites to that in the 6d cluster stays approximately constant. However,

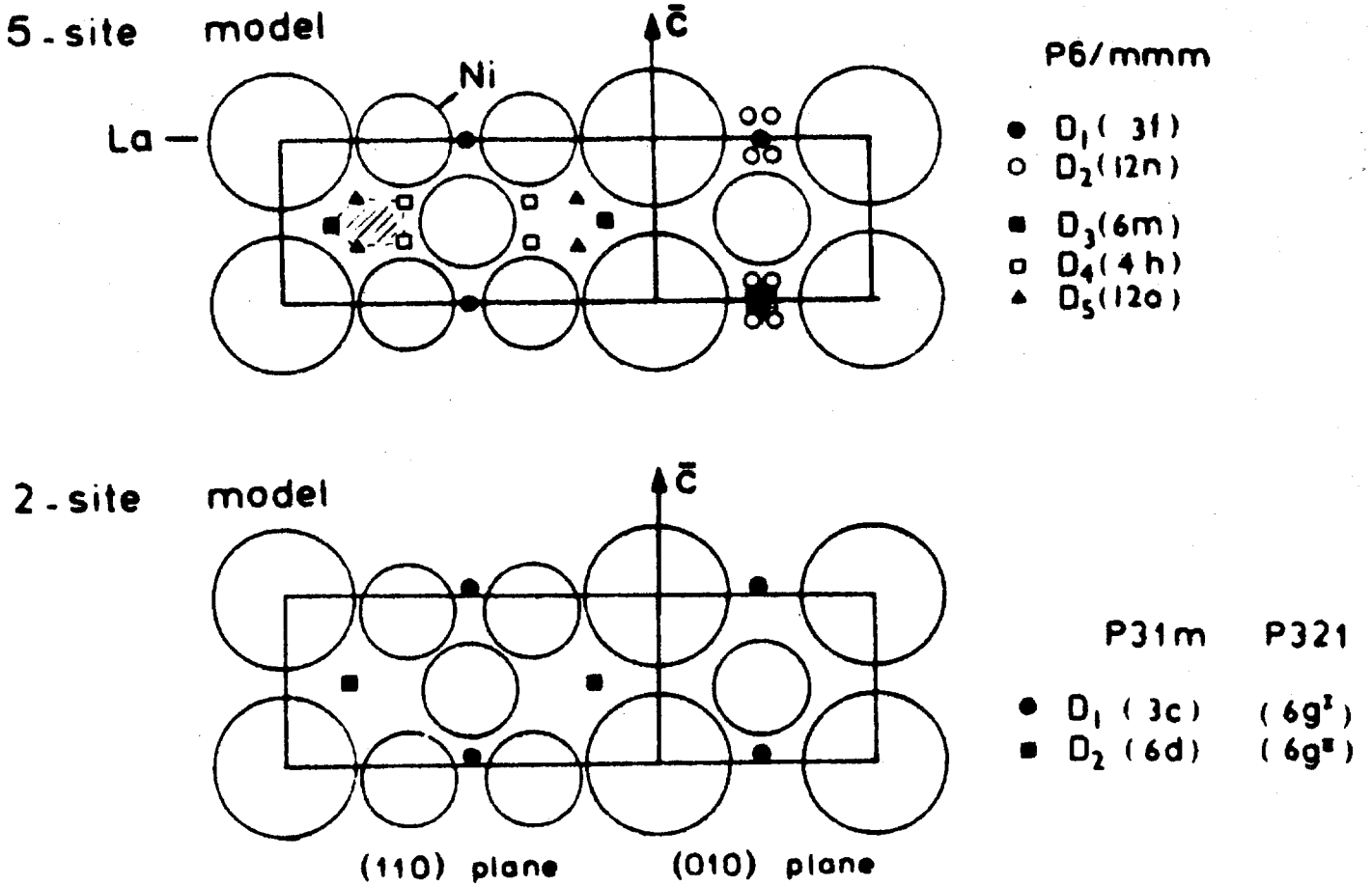

Figure II-12 Deuterium site-occupancy in $LaNi_5H_y$. 2-site and 5-site models. (reprinted from C. Lartigue, et al., *J. Less-Common Met.*, **113** (1985): 127.)

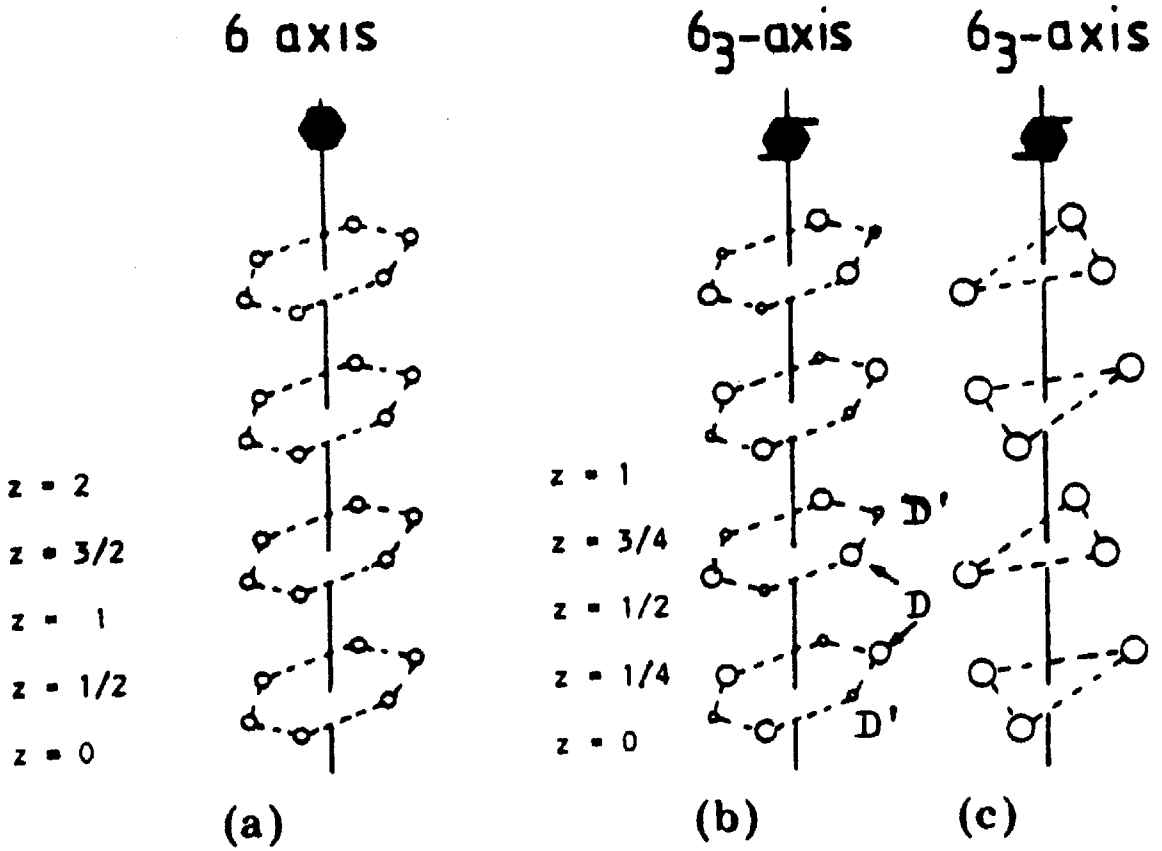

Figure II-13 D ordering in $LaNi_5H_y$ for $y \geq 5$. (reprinted from C. Lartigue, et al., *J. Less-Common Met.*, **113** (1985): 127.)

D Sites [a]	D_5	$D_{5.9}$	$D_{6.4}$	$D_{6.7}$	$(D_{7.0})^b$
2b (4h)	0.2	0.58	0.75	0.83	1.0
% of hex	8%	17%	20%	22%	25%
$6c^I$ (6m)	1.78	1.4	1.34	0.88	1.0
% of hex	67%	42%	35%	24%	25%
$6c^{II}$ (12o)	0.68	1.37	1.59	1.99	2.0
% of hex	26%	41%	43%	54%	50%
12d (12n)	2.34	2.56	2.71	3.0	3.0
% of total	47%	43%	42%	45%	43%

a Pearson symmetry notation, sites in $P6_3mc$ cell with reduced symmetry, () – sites in P6/*mmm* cell.

b Hypothetical fully ordered compound.

Table II-2 Deuterium site occupancy in β-$LaNi_5H_y$.

ordering does occur within the 6d cluster as the D composition increases. Repulsive interactions between D atoms in adjacent cells forces them out of high symmetry 6m positions to 4h and 12o positions in order to maximize the H-H separation. The ordering parameter α corresponds to $n' = (1-\alpha)n$, n = (x, 2x, z) occupation, $n' = (x, 2x, z+1/4)$ occupation. **Figure II-13** from ref. 10 shows a schematic representation of the ordering of the D atoms on (x, 2x, z) positions. In this new model, occupation of the 3f site has been abandoned. This study was soon followed by an investigation by P. Thompson, *et al.*, who utilized the different NPD scattering lengths of Ni and ^{60}Ni to discover a similar deuterium ordering and symmetry reduction consistent with the 2-site model.[33]

Statistical thermodynamic calculations have also been used to support both the 2- and 5-site models.[34-38] The entropy loss upon hydride phase formation is dominated by the entropy of gaseous hydrogen, 130.8 J/°C/mol H. Early calculations of the configurational part of this entropy loss neglected to consider the constraints caused by the interaction between protons in β-$LaNi_5$.[34,35] Percheron, *et al.* calculated entropy and enthalpy changes for hydrogen absorption using both the 2- and 5-site models in which the geometric considerations of Westlake are used to provide constraints to a statistical mechanical partition function for occupation of a multiple interstitial site structural model. Their conclusions showed support for the 5-site model: "The calculated configurational entropies for both structures are very close: 3.6 cal (mol H_2)$^{-1}$ and 2.6 cal (mol H_2)$^{-1}$ for the P6/*mmm* and the P31*m* space groups respectively.[35] However, the calculation of the enthalpy change ΔH_H (-11 kcal (mol H_2)$^{-1}$ and -8.6 kcal (mol H_2)$^{-1}$ for P6/*mmm* and P31*m* respectively) shows that hydrogen absorption is more favourable in the structure with space group P6/*mmm*."[38]

Other support for structural determinations of $LaNi_5H_y$ comes from hydrogen diffusion and lattice dynamics measurements. Quasielastic neutron scattering [40] and nuclear magnetic resonance [41] experiments have determined two time scales for hydrogen motion in $LaNi_5H_y$. Hydrogen diffusion with low activation energy and diffusion

coefficients measured to be on the order of 10^{-11} cm^2/s have been assigned to short range hydrogen motion within the cages and between the z = 1/2 cages forming a hexagonal ring. Long-range hopping between the two sets of interstices has higher activation energies and corresponds to a diffusion coefficient of ~10^{-8} cm^2/s.[42] Although these measurements do not distinguish between the 2-site or 5-site models, they do give general information about the hydrogen occupation in the hydride phase.

As mentioned above, the lattice parameters of the intermediate γ-hydride phase have been studied by XRD [14,15] and NPD [16]. The most recent work by Gray, *et al.*, shows that the lattice expansion between the α- and γ-hydride phases is discontinuous and anisotropic ($\Delta a/a > \Delta c/c$) at all temperatures studied. The γ- to β-hydride phase transition, however, is discontinuous at 30° C and continuous at 65° C and 100° C. "There appears to be a thermodynamic critical temperature for the β + γ system in our sample in desorption between 30 and 65° C." The existence of the γ-hydride phase and information about its structure imply that the stability of one of the hydrogen environments in the $LaNi_5$ cell is particularly sensitive to temperature and structure changes.[16]

4. Basic Electrochemical Properties

$LaNi_5$ is particularly attractive for use in alkaline rechargeable cells because it is simple to design a $LaNi_5$-based alloy with a plateau pressure below 1 atm., which can then be easily used in sealed cells. The electrochemical potential of the metal hydride cell at room temperature is related to the hydrogen partial pressure by the Nernst equation:

$$E_{Eq}(\mathrm{H})(\textbf{vs. HgO/Hg}) = [E^0(\mathrm{H}) - E^0(\mathrm{HgO/Hg})] + \frac{RT}{2F}\ln\left(\frac{a(\mathrm{H_2O})}{a(\mathrm{H_2})}\right)$$

$$= [E^0(\mathrm{H}) - E^0(\mathrm{HgO/Hg})] + \frac{RT}{2F}\ln\left(\frac{a(\mathrm{H_2O})}{\gamma(H_2)P_{eq}(\mathrm{H})}\right)$$

$$= -0.9324 - 0.0291 \log (P_{H2}).^{43} \qquad \text{[II.3]}$$

$E^0(H)$ = standard electrode potential of the H_2O/H couple.

$E^0(HgO/Hg)$ = standard electrode potential of the HgO/Hg couple.

$a(i)$ = activity of species *i*. $\gamma(H_2)$ = fugacity coefficient of water.

R = gas constant. T = cell temperature [K].

F = Faraday constant.

Because a change of one order of magnitude in hydrogen pressure only corresponds to a potential change of 29 mV, Ni-MH batteries have a very stable voltage profile over their capacity range. In electrochemical isotherms, the cell potential is commonly converted to pressure by the Nernst equation, and hydrogen composition is displayed as an electrochemical capacity in mAh/g. As in gas-phase isotherms, electrochemical isotherms are quasi-equilibrium, usually pulse charged with a waiting period of 20-60 min to allow the potential to reach its rest value before measurement. Electrochemical isotherms of a Ni-MH rechargeable battery using AB_5 as the anode material are shown in **Figure II-14.**

A hydrogen composition of 6.7 $H/LaNi_5$ would give the anode material a maximum capacity of 372 mAh/g. Because of the weight of the cathode, electrolyte, casing, and other inactive components, the largest energy density that can be realized in a battery is approximately 175 mAh/g.[44] This, combined with a cell potential in the range of 1.2 - 1.5V gives the Ni-MH battery a fairly high power density when compared to other types of rechargeable battery technologies.[44] The voltage and specific power of Ni-MH rechargeables makes them attractive for use in many applications. The similarity in voltage and benefits in specific energy and environmental compatibility makes Ni-MH the number one choice for replacement of Ni-Cd batteries for single cell (AAA - D sizes) and battery pack (camcorder, power tools) applications. For low current applications, such as laptop computers and portable phones, Li-ion rechargeables will be optimal once

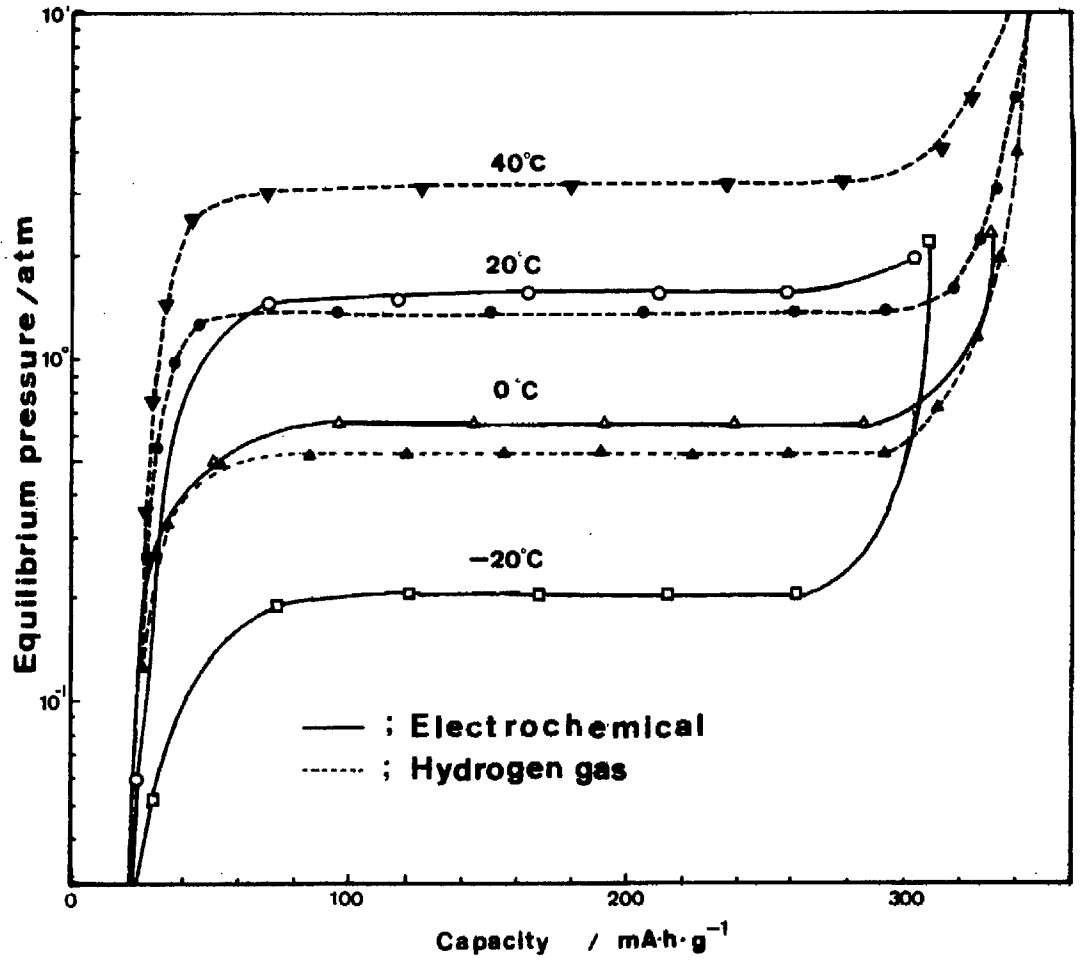

Figure II-14 Electrochemical and gas-phase isotherms of $LaNi_5$. (reprinted from T. Sakai, M. Matsuoka, and C. Iwakura, in *Handbook on the Physics and Chemistry of Rare Earths*, eds. K.S. Gschneidner, Jr., and L. Eyring, **21** (1995): 133.)

they are more developed, but Ni-MH batteries are more attractive for high current applications such as electric vehicles.

5. Microstrains

It is well known that the discontinuous lattice expansion accompanying hydrogen absorption in metal hydrides creates great stress at the interface between the α- and β-phases because of the misfit in the lattice parameters of the 2 phases. This misfit strain provides the activation energy to nucleate dislocations and induce planar defects in the Haucke phase crystalline lattice.[29] An obvious macroscopic result of the misfit strains is the *decrepitation* of ingots of $LaNi_5$ to fine powders.

The microstructural effects of the misfit strains are clearly evident in the XRD pattern of a $LaNi_5$ sample which has been *activated* by gas-phase hydrogen absorption, as seen in **Figure II-15**. The diffraction peaks of activated $LaNi_5$ are broadened anisotropically, with large lorentzian (crystallite size) and gaussian (microstrain) components to the broadening in all directions and additional gaussian broadening in directions orthogonal to (00l). This broadening was first interpreted using the simple method of Williamson and Hall.[45] For each family *l* of reflections (*hkl*), the broadening in K-space (integral breadth, $\beta\cos\theta$) was plotted *vs* the K-vector of the diffraction peak ($2\sin\theta/\lambda$). An example of this anisotropy can be seen in **Figure II-16**, showing Williamson-Hall plots of peak broadening in an activated sample of $LaNi_5$. The apparent crystallite size in each family/direction is given by λ/β_0 and the microstrain $\Delta d/d$ in that direction is given by the slope of this plot.[32] (For further explanation of microstrain and the Williamson-Hall technique, see III.C.b.) Subsequent works implemented modifications of the Rietveld method to refine the severe anisotropic strain seen in diffraction patterns of hydrogen activated $LaNi_5$ alloys.[46-48]

There have been a number of TEM studies of activated $LaNi_5$ alloys undertaken to

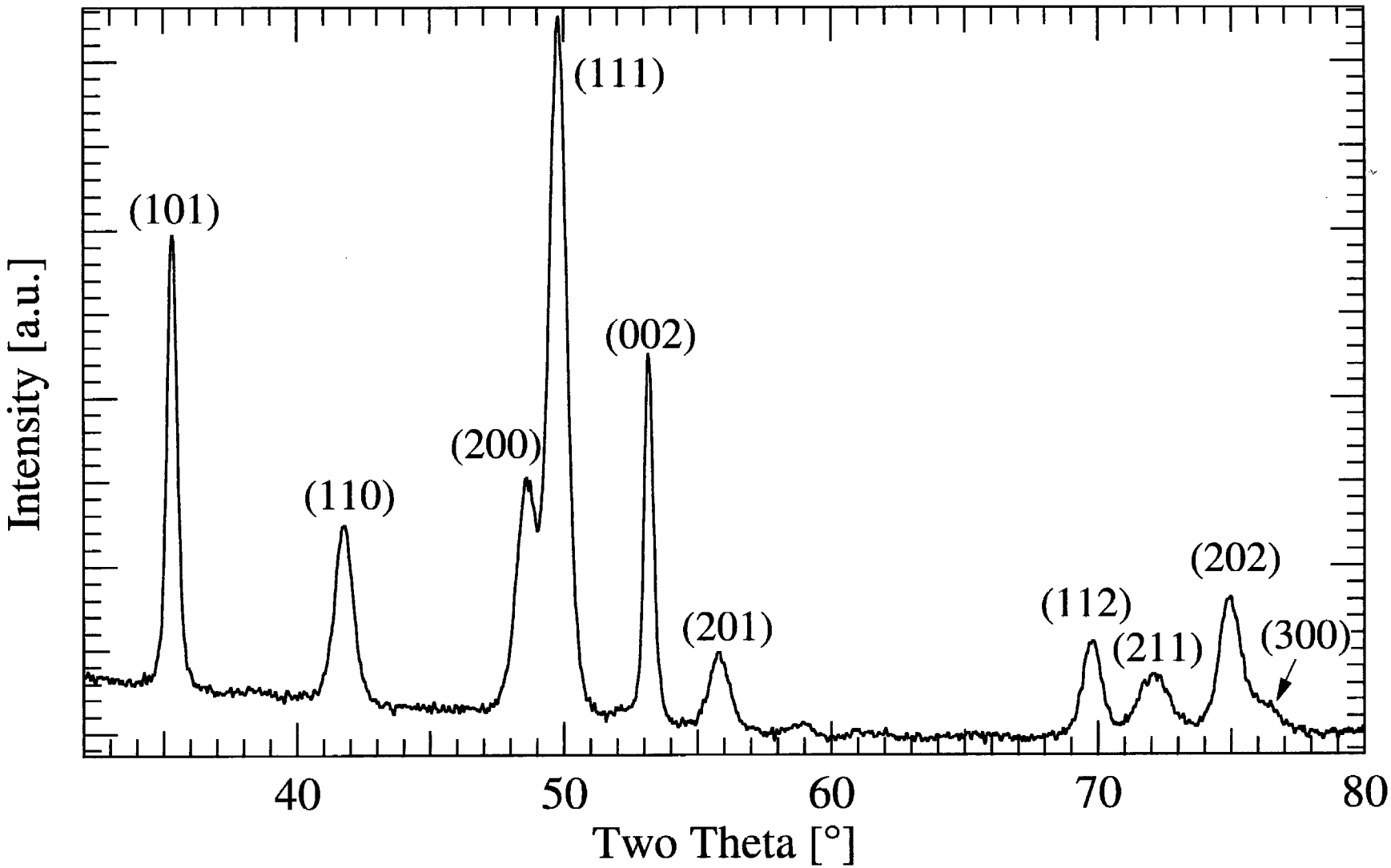

Figure II-15 XRD pattern of activated $LaNi_5$ depicting anisotropic line broadening.

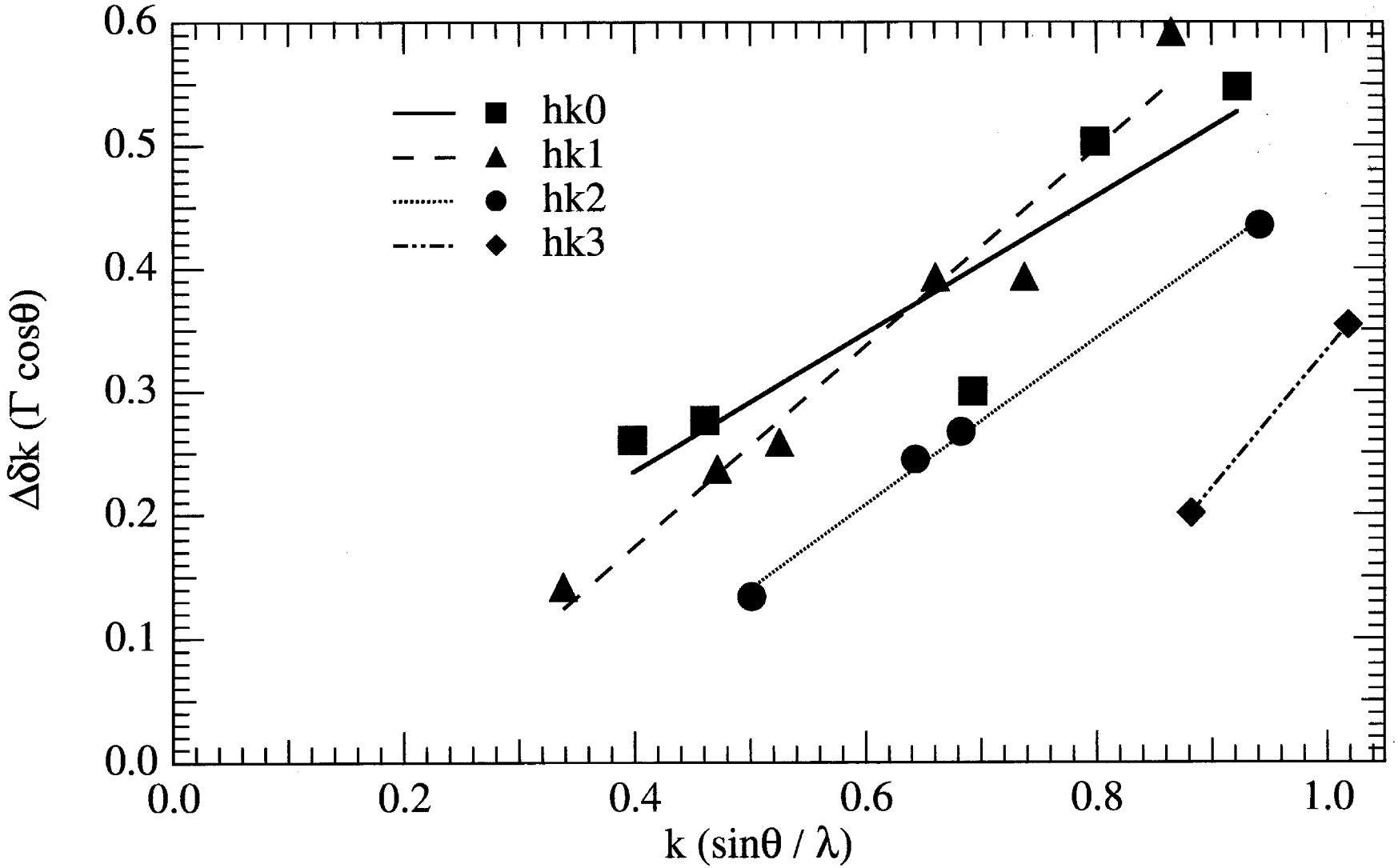

Figure II-16 Williamson-Hall plots depicting $LaNi_5$ XRD anisotropic line broadening.

determine the microstructural defects responsible for the diffraction broadening. Kisi, *et al.*[48] attempted a TEM study on bulk $LaNi_5$ powder particles, but the severe distortion defects and lack of sample preparation prevented them from identifying the types of defects present in activated $LaNi_5$. G.-H. Kim, *et al.*[49] used TEM on $LaNi_5$ powders embedded in epoxy and ion beam milled to study the change in the surface of $LaNi_5$ induced by hydrogen activation. They found regions of $LaNi_5$ crystals containing microtwins near the surface of the grains and the decomposition products. Notten, *et al.*[50] studied similarly prepared samples of unhydrided and dehydrided $LaNi_5$ and found sets of planar defects in the dehydrided powders. The displacement vectors of the defects were determined to be in the (001) plane, which is consistent with the anisotropic diffraction broadening seen in powder diffraction patterns. In addition, the average spacing between the defects was consistent with mean particle sizes obtained by Williamson-Hall analysis of NPD,[51] rather than the average grain size obtained by SEM. High-resolution TEM (*HRTEM*) images showed further that the habit planes of planar defects were actually stepped (100) plane interfaces having an average inclination of 10° to the (100) plane. The 180° C cure of the TEM specimens might have modified the defect structures of the activated powders. However, similar treatments do not affect the severe diffraction peak broadening mentioned above, so correlations with these measurements should be consistent.

Further work by G.-H. Kim, *et al.*[52,53] and H. Inui, *et al.*[54] have identified dislocation structures in hydrogen activated $LaNi_5$. In $LaNi_5$ hydrided to the limit of the α-phase, they detected <hkl> "ripple" dislocations thought to be produced by the lattice distortion during hydrogen penetration into the matrix. In addition, they found <00l> dislocation loops that could have been produced by the lattice misfit accompanying hydride precipitation. After complete hydride formation, <hk0> misfit super dislocations were found to pile up, sometimes forming hexagonal grid twist boundaries. These types of dislocations are consistent with the maximum strain to the <hk0> plane and minimum

strain to <00l> plane measured by powder diffraction techniques. They also found some structural disorder and micro-twins.[53] Inui, *et al.* found <00l> dislocations formed at cracks and equal fractions of <hk0> and <00l> grown in dislocations. Observation of the facile motion of only the c-type dislocations led them to conclude that the a-type dislocations contribute to decrepitation in $LaNi_5$.[54] These determinations of dislocation direction and burgers vectors are consistent with the anisotropic broadening seen in powder diffraction patterns.

1 R. Vogel, *Z. Metallkd.*, **38** (1947): 97.

2 A. V. Virkar and A. Raman, *J. Less-Common Met.*, **18** (1969): 59; K.A. Gschneidner, Jr., *Rare Earth Alloys*, D.D. van Nostrand, New York, 1961, p.221.

3 K.H.J. Buschow and H.H. van Mal, *J. Less-Common Met.*, **29** (1972): 203.

4 D. Zhang, J. Tang, and K.A. Gschneidner, Jr., *J. Less-Common Met.*, **169** (1991): 45.

5 H. Nowotny, *Zeitschrift Für Metallkunde*, **34** (1947): 247.

6 J.L.C. Daams, P. Villars, and J.H.N. van Vucht, *Atlas of crystal structure types for intermetallic phases* (Newbury, OH : ASM International, 1991).

7 J.H. Wernick and S. Geller, *Acta Crystallogr.*, **12** (1959): 662.

8 W. Coene, P.H.L. Notten, F. Hakkens, R.E.F. Einerhand, and J.L.C. Daams, *Phil. Mag. A*, **65 (6)** (1992): 1485.

9 R. Speiser in *Metal Hydrides*, W.M. Mueller, J.P. Blackledge, and G.G. Libowitz, eds. (Academic Press, New York: 1968), p. 72.

10 C. Lartigue, A. Percheron-Guégan, J.C. Achard, and J.L. Soubeyroux, *J. Less-Common Met.*, **113** (1985): 127.

11 J.F. Lakner, F.S. Uribe, and S.A. Steward, *J. Less-Common Met.*, **74** (1980): 13.

12 L. Schlapbach in *Topics in Applied Physics: Hydrogen in Intermetallic Compounds I*, Chapter 1, L. Schlapbach, ed., Springer Verlag (Berlin: 1988).

13 P.D. Goodell, *J. Less-Common Met.*, **99** (1984): 1.

[14] S. Ono, K. Nomura, E. Akiba, and H. Uruno, *J. Less-Common Met.*, **113** (1985): 113.

[15] T. Matsumoto and A. Matsushita, *J. Less-Common Met.*, **123** (1986): 135.

[16] S. Luo, J.D. Clewley, T.B. Flanagan, R.C. Bowman Jr., and J.S. Cantrell, *J. Alloys Comp.*, **253-254** (1997): 226.

[17] R. Griessen and T. Riesterer, chapter 6 in *Topics in Applied Physics v. 63 Hydrogen in Intermetallic Compounds I: Electronic, Thermodynamic, and Crystallographic Properties, Preparation*, L. Schlapbach, ed. Springer-Verlag, Berlin. 1988, p. 219.

[18] S. Qian and D.O. Northwood, *Int. J. Hydrogen Energy*, **13(1)** (1988): 25.

[19] T. Flanagan and C.-N. Park, *Mat. Sci. Forum*, **341** (1988): 297; T.B. Flanagan, C.-N. Park, and W.A. Oates, *Prog. Solid St. Chem..*, **23(4)** (1995): 291.

[20] B. Lambert and S.F. Gates, *Proc. Roy. Soc., Ser. A*, **108** (1925): 456.

[21] E.MacA. Gray, E.H. Kisi, and R.I. Smith, *J. Alloys Comp.*, in press.

[22] M.P. Pitt, E.MacA. Gray, E.H. Kisi, and B.A. Hunter, *J. Alloys Comp.*, in press.

[23] P.H.L. Notten, J.L.C. Daams, A.E.M. De Veirman, and A.A. Staals, *J. Alloys Comp.*, **209** (1994): 85.

[24] D.G. Westlake, *J. Less-Common Met.*, **90** (1983): 251; **91** (1983) 1.

[25] A.C. Switendick, *Theoretical Study of Hydrogen in Metals; Current Status and Further Prospects Report, Sandia Lab*, SAND 78-0250 (1978).

[26] A. Percheron-Guégan and C. Lartigue, *Materials Science Forum*, **31** (1988): 125.

[27] D. Richter, R. Hempelmann, and R.C. Bowman, Jr. in *Topics in Applied Physics: Hydrogen in Intermetallic Compounds II*, Chapter 3, L. Schlapbach, ed., Springer Verlag (Berlin: 1988), p. 97.

[28] A.L. Bowman, J.L. Anderson, and N.G. Nereson, in *Proc. 10th Rare Earth Research Conf., Carefree, AZ, 1973*, C.J. Kevane and T. Moeller (eds.), p. 485.

[29] P. Fischer, A. Furrer, G. Busch, and L. Schlapbach, *Helv. Phys. Acta*, **50** (1977): 421.

[30] A.F. Andresen, in *Proc. Int. Symp. on Hydrides for Energy Storage*, Geilo, Norway, 1977, A.F. Andresen and A.J. Maeland, eds., Pergamon Press, London 1978, p. 61.

[31] D. Noréus, L.G. Olsson, and P.E. Werner, *J. Phys. F: Met. Phys.*, **13** (1983): 715.

[32] A. Percheron-Guégan, C. Lartigue, J.C. Achard, P. Germi, and F. Tasset, *J. Less-Common Met.*, **74** (1980): 1.

[33] P. Thompson, J.J. Reilly, L.M. Corliss, J.M. Hastings, and R. Hempelmann, *J. Phys. F: Met. Phys.*, **16** (1986): 675.

[34] D.M. Gruen and M. Mendelsohn, *J. Less-Common Met.*, **55** (1977): 149.

[35] W.E. Wallace, H.E. Flotow, and D. Ohlendorf, *J. Less-Common Met.*, **79** (1981): 157.

[36] J.C. Achard, C. Lartigue, A. Percheron-Guégan, J.C. Mathieu, A. Pasturel, and F. Tasset, *J. Less-Common Met.*, **79** (1981): 161.

[37] A. Pasturel, B. Brion, P. Hicter, A. Percheron-Guégan, and J.C. Achard, *J. Less-Common Met.*, **86** (1982): 19.

[38] A. Pasturel, B. Brion, P. Hicter, A. Percheron-Guégan, and J.C. Achard, *J. Less-Common Met.*, **88** (1982): 442.

[39] D. Ohlendorf and H.E. Flotow, *J. Chem Phys.*, **73** (1980): 2937.

[40] C. Lartigue, A. Percheron-Guégan, J.C. Achard, M. Bee, and A.J. Dianoux, *J. Less-Common Met.*, **101** (1984): 403.

[41] R.C. Bowman, D.M. Gruen, and M.H. Mendelsohn, *Solid State Commun.*, **32** (1979): 501.

[42] F.E. Spada, H. Oesterreicher, R.C. Bowman, Jr., and M.P. Guse, *Phys. Rev. B*, **30** (1984): 4909.

[43] C. Iwakura, T. Asaoka, H. Yoneyama, T. Sakai, H. Ishikawa, and K. Oguro, *Nippon Kagaku Kaishi*, **8** (1988): 1482.

[44] T. Sakai, M. Matsuoka, and C. Iwakura, in *Handbook on the Physics and Chemistry of Rare Earths*, eds. K.A. Gschneidner, Jr. and L. Eyring, **21** (1995): 133.

[45] G.K. Williamson and W.H. Hall, *Acta Metall.*, **1** (1953): 22.

[46] C. Lartigue, A. Le Bail, and A. Percheron-Guégan, *J. Less-Common Met.*, **129** (1987): 65.

[47] P. Thompson, J.J. Reilly, and J.M. Hastings, *J. Less-Common Met.*, **129** (1987): 105.

[48] E.H. Kisi, C.E. Buckley, and E.Mac A. Gray, *J. Alloys Comp.*, **185** (1992): 369.

[49] G.-H. Kim, C.-H. Chun, S.-G. Lee, and J.-Y. Lee, *Scripta Met. et Mat.*, **29** (1993): 485.

[50] A.E.M. De Veirman, A.A. Staals, and P.H.L. Notten, *Phil. Mag. A.*, **70** (1994): 837.

[51] E. Wu, E.H. Kisi, and E.MacA. Gray, *J. Appl. Cryst.*, **31** (1998): 363.

[52] G.-H. Kim, C.-H. Chun, S.-G. Lee, and J.-Y. Lee, *Acta Met. Mat.*, **42** (1994): 3157.

[53] G.-H. Kim, S.-G. Lee, K.-Y. Lee, C.-H. Chun, and J.-Y. Lee, *Acta Met. Mat.*, **43** (1995): 2233.

[54] H. Inui, T. Yamamoto, Z. Di, and M. Yamaguchi, *J. Alloys Comp.*, **269** (1998): 294.

D. Alloy Modifications

One aspect of $LaNi_5$ that makes it very attractive for reversible gas-phase and electrochemical hydrogen storage is that its hydriding and cycling stability are easily altered by alloying substitutions for both La and Ni. Even in the first examinations of the reversible hydriding of $LaNi_5$ by van Vucht, *et al.*, attempts were made to change its sorption properties by partial substitution of La with other metals.[1] They studied the variations of the plateau pressures and lattice parameters of $La_{1-x}Ce_xNi_5$ with Ce composition. The desorption rate of $LaNi_5$ was also studied at various temperatures and was compared to that of $La_{0.9}Zr_{0.1}Ni_5$.[1] While many investigations have been performed on the alloying of $LaNi_5$, systematic variations of alloy composition were not routinely performed, and it is still difficult to extract trends from published data that can be used in designing $LaNi_5$ alloys for use in alkaline rechargeable batteries. The alloys used in my research were prepared by systematically varying the chemical composition of the solute element. In all cases, third element substitutions were made for Ni.

1. Phase Diagram and Metal-Atom Crystal Structure

Many metal elements have a range of solubility in which they can be substituted for Ni in equilibrium $LaNi_5$ alloys, and some (Co, Cu) form solid solutions with Ni in the $CaCu_5$ lattice. A good review of the preparation of substituted $LaNi_5$ alloys was written by A. Percheron-Guégan and J.-M. Welter.[2] Phase composition and crystallographic states of order have proven to be sensitive to preparation and subsequent heat-treatment conditions. This fact complicates comparison of published results because alloys of nominally identical composition but different heat treatment (resulting, e.g., from batch size) can have different physical properties. Researchers have empirically determined solubility limits for some elements by the presence of other phases in a $CaCu_5$ matrix. No

one has examined the nature of the solubility limits to determine guidelines such as a Hume-Rothery rule.[3]

The most immediate effect of substitution on the crystal structure of the alloy is a change in the lattice parameters and hence the unit cell volume. This is fairly easy to measure with diffraction methods, and it has been shown that lattice expansion (or contraction) is in most cases linear with solute composition x. Simple geometrical considerations outlined by J. Shinar, *et al.* show that in $LaNi_5$, the z = 0 lattice plane is close packed while the z = 1/2 plane is not.[4] As a result, elements with metallic radii larger than Ni should have a steric preference to occupy the 3g Ni sites on the z = 1/2 plane.

The hydriding properties and crystal structures of the systems $LaNi_{5-x}Co_x$ and $LaNi_{5-x}Cu_x$ have been studied by van Mal, *et al.*[5] and J. Shinar, *et al.*,[4] respectively . Each system is isostructural with $CaCu_5$ for the entire range of substitution. The lattice parameters of $LaNi_{5-x}Cu_x$ follow Vegard's law, but those of $LaNi_{5-x}Co_x$ do not. The discontinuity in the $LaNi_{5-x}Co_x$ lattice parameters with x has been attributed to magnetic effects [5,6] and a preferential ordering of Co.[7] A variety of researchers have confirmed that Co atoms do indeed favor the 3g sites, e.g., 88%/12% [7] or 75%/25% [8] occupation of the 3g/2c sites, rather than the statistical 60%/40%. Cu, however, has been found to have a slight preference for the 2c site.[9]

Refinement of the crystal structures of $LaNi_{5-x}M_x$ alloys has been performed by NPD and XRD, and by Mössbauer spectroscopy in the case of Fe. Metal atom site occupation has been determined for Mn,[10,11] Fe,[12] Co,[7,8] Cu,[9] Al,[9,10] Si,[9] and Sn.[13] Mn was found to substitute on both the 2c and 3g sites with a preference for the 3g sites,[11] while Fe occupies almost exclusively (95%) the 3g site.[12] Noble, or p-shell, metals show strong preference for the 3g sites, occupying them almost exclusively.[9,10,13] **Figures II-17** and **II-18**, reprinted from ref. 14, show the unit cell volume and metal site occupancy of some substituted $LaNi_{5-x}M_x$ compounds.

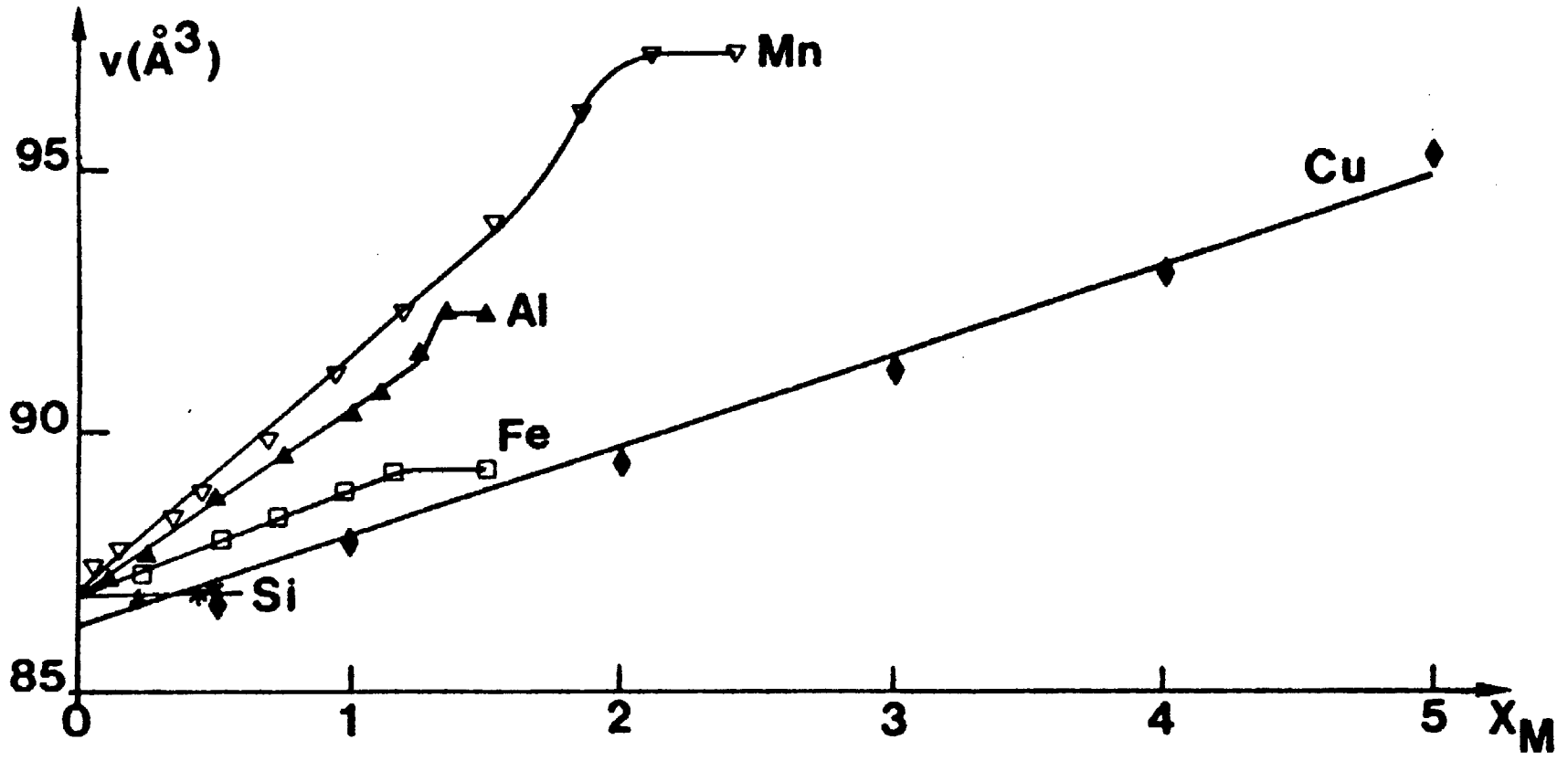

Figure II-17 Unit cell volume *vs* x for $LaNi_{5-x}M_x$ alloys. (reprinted from A. Percheron-Guégan, et al., *J. Less-Common Met.*, **109** (1985): 287.)

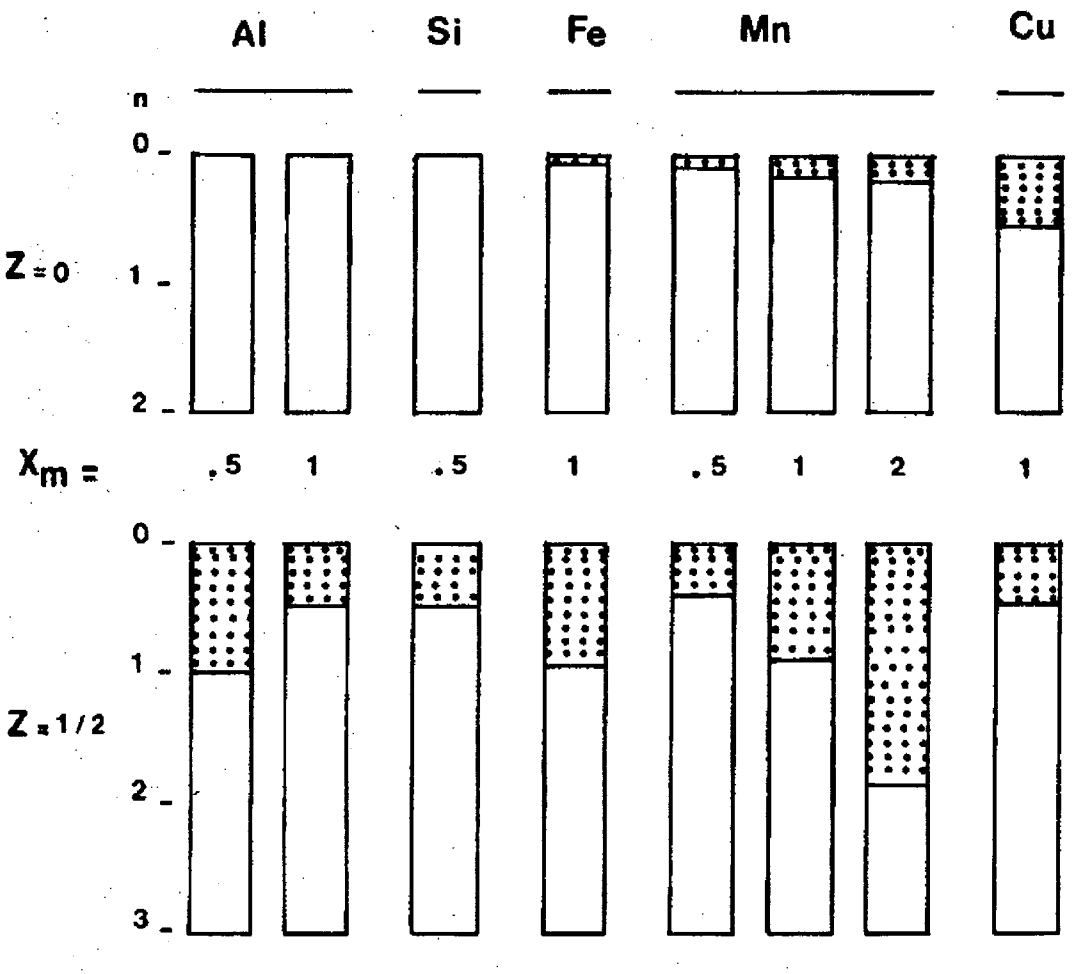

Figure II-18 Metal atom site occupancy of $LaNi_{5-x}M_x$ alloys. (reprinted from A. Percheron-Guégan, et al., *J. Less-Common Met.*, **109** (1985): 287.)

2. Isotherm

Ternary substitutions for Ni affect the isotherm in four ways: (i) change in plateau pressure, (ii) reduction of total H capacity, (iii) change in pressure hysteresis, and (iv) change in shape (reduction of plateau width or increase in slope). These effects are important in gas phase applications such as heat pumps and cryocoolers, and less so in rechargeable batteries. For most gas-phase hydride applications, for example, a near-zero plateau slope is desirable and the pressure-temperature relationship should be precisely controlled throughout the MH lifetime.[15] In rechargeable batteries, the plateau pressure affects the cell potential, self-discharge characteristics, and the ease of testing in the slightly pressurized configuration often used in the laboratory environment. Of course, alloys with plateau pressures greater than a few atmospheres can not easily be made into commercial sealed cells. The total capacity affects the alloy charge capacity, usually measured in mAh/g. The pressure hysteresis seems to be connected to the alloy's volume expansion and cyclic stability. A sloping nature in the isotherm characteristics will affect the cell potential, but because 1 order of magnitude change in the plateau pressure corresponds to a potential difference of only 29 mV, Ni-MH cell potentials are rather stable. The plateau width does seem to be related to the size of the miscibility gap and corresponding discrete volume change between the α-and β-phases, and this has an effect on the alloy cyclic stability. Isotherms of $LaNi_{5-x}Co_xH_y$ are unique in the splitting of the pressure plateau at $y = 3.5$ for $x = 0.5$.[5]

Many models have been proposed to predict the relative stability of MH compounds, or more precisely the hydride phase heat of formation.[16] A particularly useful trend that is used to design AB_5 metal hydrides is the linear dependence of the hydride heat of formation,[17-19] and thereby the logarithm of the alloy plateau pressure,[20] on the size of the interstices occupied by hydrogen in the cell [18,19] and the alloy's unit cell volume.[17,20] There are many examples of how this has been exploited to prepare complex alloy hydrides

having predictable and desirable temperature-pressure characteristics for specific applications.[18,20] Other effects of substitution on the isotherm are discussed in the following sections.

3. Hydride Structure and Lattice Expansion

The decrease in hydrogen storage capacity mentioned above (§II.D.2) is a result of the blocking of hydrogen occupation in specific interstitial sites. Most of the work on hydrogen (deuterium) site occupation in ternary substituted alloys has been performed by Percheron-Guégan, *et al.*, and is summarized in **Table II-3**.[20] The D-site occupation of $LaNi_{5-x}M_xH_y$ alloys exhibit characteristics similar to that of $LaNi_5H_{5<y<7}$. The ratio of occupied sites in the 3c cluster to those occupied in the 6d cluster stays approximately constant. However, deuterides of Ni-substituted $LaNi_5$ do not exhibit the deuterium ordering observed in $LaNi_5D_{y>5}$. The 4h, 12o, and 3f sites are found to have progressively lower occupations, dependant upon substituent and substituted composition, while the 6m and 12n sites do not experience much decrease in hydrogen occupation. Again, what is happening is that D is prevented from occupying high symmetry positions in the 6d clusters. Therefore, the D-D spacing is not allowed to be maximized between adjacent unit cells. The 6m and 12n interstitial sites are larger than the other sites, and would therefore be less likely to become too small to be occupied by protons when Ni is substituted by a larger element. Hydrogen occupation has also been postulated to be affected by the electron state of the substituting metal. The 12o and 4h interstitial sites are in close contact with at least two metal atoms in the 3g sites, where Ni substitution usually takes place. These interstitial sites would be more strongly affected by the number of valence electrons of the substitutional atoms as suggested by Gschneidner, *et al.*[22] This exclusion of hydrogen sites also precludes the hydrogen ordering found in $LaNi_5H_y$, $y \geq 5$. Other than that, the hydrides of Ni-substituted $LaNi_5$ alloys have been found to retain the P6/*mmm* symmetry for all substituents but Co,[5] as explained below.[21]

Another effect of Ni substitution is a change in the lattice expansion of the alloy upon hydrogen absorption. In all cases, substitution reduces the *total* volume expansion of the alloy. This is consistent with a reduction in hydrogen capacity, except in the case of Mn where there is little or no capacity reduction for $x \leq 0.7$.[11] The molar volume of hydrogen in the hydride phase is also often reduced. While the lattice expansion of $LaNi_5$ is approximately isotropic, the substitution of Ni with other metals often induces anisotropy in the lattice expansion in which the expansion in the direction of the a-axis is greater than in the direction of the c-axis. This anisotropy is consistent, though more pronounced, with the anisotropy in lattice expansion seen in $LaNi_5H_5$. In $LaNi_{4.5}Si_{0.5}H_{4.3}$, for example, the a-axis expands 6.4% while the c-axis expands only 2.1%.[9] As mentioned above, the reduction in volume expansion is accompanied by a reduction in pressure hysteresis.

The lattice expansion and crystal structures of $LaNi_{5-x}Co_xH_y$ alloys were studied by XRD for $0 \leq x \leq 5$ by van Mal, *et al.*[5] $LaNi_4CoD_y$ was studied by NPD by Gurewitz, *et al.* [7] and Latroche, *et al.* [8,23] at a variety of D compositions. The diffraction patterns of Gurewitz, *et al.* exhibited the presence of both the α- and β-phase hydrides.[7] The hydride structures were found to be hexagonal for $0 \leq x \leq 3$ and orthorhombic for $3 \leq x \leq 5$, with $LaNi_2Co_3H_y$ changing from orthorhombic to hexagonal for $y = 3.2$.[5] An additional phase intermediate between the α- and β-phases appears that is coincident with the second plateau in the isotherm. The lattice expansion caused by hydrogen absorption in the $LaNi_{5-x}Co_xH_y$ system is depicted in **Figure II-19**. In this figure, open symbols denote discontinuous volume expansion and closed symbols denote lattice expansion continuous from the previous discontinuous expansion value. When an intermediate hydride phase does appear, its lattice expansion is anisotropic, $\Delta a/a > \Delta c/c$. As the hydrogen composition increases, the anisotropy becomes less pronounced, but it does not disappear. NPD measurements have determined that in $LaNi_4CoD_{4.4}$, which is where the

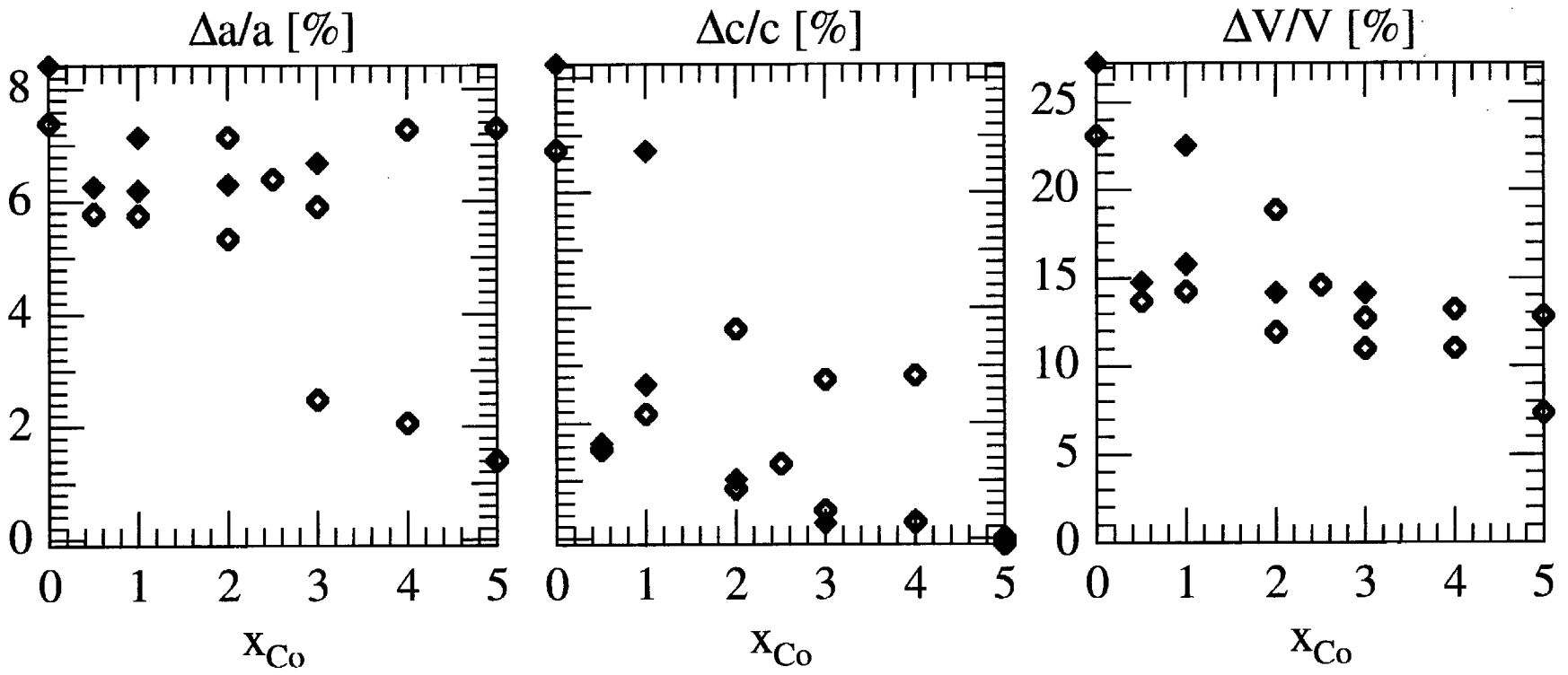

Figure II-19 Lattice expansion in $LaNi_{5-x}Co_x$ system. (from H.H. van Mal, K.H.J. Buschow, and F.A. Kuijpers, *J. Less-Common Met.* , **32** (1973): 298.)

intermediate phase appears, D atoms are spread approximately equally between 6m and 12n sites, with minor occupation of the 4h sites.[23] Further deuterium loading does not change the relative occupation of these sites, but does induce the ordering mentioned above (§II.C.3), displacing deuterium from 6m to 12o sites.[8]

NPD and XRD measurements have rarely been performed on Ni-substituted $LaNi_5$ alloys at intermediate stages of hydrogen (deuterium) occupation, but there are enough measurements available to get a good idea of how the lattice behaves when it absorbs hydrogen. The results of these studies, shown in **Table II-4**, will be discussed below. All lattice expansion values are with respect to the dehydrided lattice parameters, unless otherwise stated. Latroche, *et al.* performed in-situ NPD on an electrode of $LaNi_{4.5}Al_{0.5}$ during charge-discharge cycling. The initial lattice expansion was found to be anisotropic ($\Delta a/a:\Delta c/c::5:1$) as was the discontinuous lattice expansion ($\Delta a/a:\Delta c/c::8:5$). Subsequent continuous expansion was greater in the c-direction than in the a-direction. The volume expansion is reduced appreciably from that of $LaNi_5$, but we do not see discontinuous expansion being replaced by continuous expansion.[24]

Latroche, *et al.* also measured lattice expansion in $LaNi_4CoD_y$ and multi-component $LaNi_{3.55}Mn_{0.4}Al_{0.3}Co_{0.75}D_y$.[8,23] These measurements were not performed in-situ, but were taken at several deuterium compositions. As seen before, the initial and "discontinuous" lattice expansions are anisotropic, and subsequent expansion reduces the anisotropy. The volume of the α-phase at maximum hydrogen composition was not measured, but assuming ~1% expansion in the α-phase and <1% expansion in the β-phase before the $y = 4.4$ measurement, this corresponds to a discontinuous volume expansion of ~14%, which is consistent with measurements by Gurewitz, *et al.*[7] It is not clear whether subsequent expansion to 22.4% is continuous or discontinuous. The flat plateau of the isotherm implies that the volume expansion is discontinuous. However, the in-situ measurements by Ono, *et al.*[25] and Gray, *et al.*[26] show that $LaNi_5H_y$ can have a flat plateau for $y > 4.0$ and still expand continuously in that range, implying that $LaNi_4CoH_y$ will

Alloy	Δa/a [%]	Δc/c [%]	ΔV/V [%]
$LaNi_{4.5}Al_{0.5}D_{\alpha}$ [20]	0.5	0.1	1.1
$LaNi_{4.5}Al_{0.5}D_{\beta}$ [20]	5.5	3.4	+ 13.8
$LaNi_{4.5}Al_{0.5}D_{\beta+}$ [20]	5.9	4.5	+ 2.4
$LaNi_4CoD_{\alpha}$			α_{Co1}
$LaNi_4CoD_{4.0}$ [4]	5.7	2.2	+ 14.2 - α_{Co1}
$LaNi_4CoD_{4.4}$ [21]	6.2	2.7	+ 1.5
$LaNi_4CoD_{6.11}$ [22]	7.1	6.7	+ 6.7 - α_{Co1}
$LaNi_{3.55}Mn_{0.4}Al_{0.3}Co_{0.75}D_{0.6}$ [21]	0.7	0.4	1.9
$LaNi_{3.55}Mn_{0.4}Al_{0.3}Co_{0.75}D_{3.4}$ [21]	4.1	2.5	+ 9.1
$LaNi_{3.55}Mn_{0.4}Al_{0.3}Co_{0.75}D_{4.6}$ [21]	5.4	4.2	+ 4.7
$LaNi_{3.55}Mn_{0.4}Al_{0.3}Co_{0.75}D_{5.57}$ [22]	6.2	5.8	+ 3.7
$LaNi_{4.8}Fe_{0.2}D_{\alpha}$ [23]			$\alpha_{Fe0.2}$
$LaNi_{4.8}Fe_{0.2}D_{\beta}$ [23]	6.9	5.8	+ 20.9
$LaNi_{4.8}Fe_{0.2}D_{\beta+}$ [23]			+ 1.4 - $\alpha_{Fe0.2}$
$La_{0.7}Sm_{0.3}Ni_4Fe_1D_{\alpha}$ [23]			α_{Fe1}
$La_{0.7}Sm_{0.3}Ni_4Fe_1D_{\beta}$ [23]	4.9	2.4	+ 12.9
$La_{0.7}Sm_{0.3}Ni_4Fe_1D_{\beta+}$ [23]			+ 3.8 - α_{Fe1}

Table II-3 Lattice expanding behavior of Ni-substituted $LaNi_5$ alloys with hydrogen absorption. (α denotes no measurement of expanded α-phase was given.)

D Sites[a]	$Si_{0.5}D_{4.3}$	$Al_{1.0}D_{4.8}$	$Al_{0.5}D_{5.4}$	$MnD_{5.9}$	$Mn_{0.5}D_{6.6}$
2b (4h)	0.25		0.23	0.20	0.34
% of hex	21%		8%	7%	9%
$6c^{I}$ (6m)	1.93	2.06	1.91	2.06	2.21
% of hex	79%	100%	69%	67%	58%
$6c^{II}$ (12o)			0.64	0.81	1.28
% of hex			23%	26%	33%
12d (12n)	2.11	2.74	2.62	2.83	2.78
% of total	49%	57%	49%	48%	42%

a Pearson symmetry notation, sites in $P6_3mc$ cell with reduced symmetry, () – sites in P6/*mmm* cell.

Table II-4 Deuterium site occupancy in β-$LaNi_{5-x}M_xH_y$.

expand continuously between y = 4.4 and y = 6.11. This being the case, we do see discontinuous lattice expansion being replaced by continuous expansion for these two alloys. In $LaNi_4Co$, the discontinuous volume expansion is large, but is only 63% of the total volume expansion. The discontinuous lattice expansion is reduced in $LaNi_{3.55}Mn_{0.4}Al_{0.3}Co_{0.75}$ and because total volume expansion is large, it accounts for only 47% of the total volume expansion.

Nakamura, *et al.* performed in-situ XRD on $La_{0.7}Sm_{0.3}Ni_{4.0}Fe_{1.0}$ and $LaNi_{4.8}Fe_{0.2}$. They measured a slightly anisotropic ($\Delta a/a$ = 6.9%, $\Delta c/c$ = 5.8%), discontinuous volume expansion of 20.9% in $LaNi_{4.8}Fe_{0.2}$ followed by a continuous expansion of 1.4%. They made no mention of α-phase expansion, but if we presume a 1% α-phase expansion, the discontinuous expansion is 19.9%, 89% of the total. Overall, the lattice expanding behavior of $LaNi_{4.8}Fe_{0.2}$ was not unlike from that of $LaNi_5$. The $La_{0.7}Sm_{0.3}Ni_{4.0}Fe_{1.0}$ sample showed more pronounced changes. The discontinuous volume expansion was found to be quite reduced (12.9%, 77% of the total) and much more anisotropic ($\Delta a/a$ = 4.9%, $\Delta c/c$ = 2.4%), and the total volume expansion (16.7%) is one-third smaller than that of $LaNi_5$. In this sample, some discontinuous lattice expansion is replaced by continuous expansion, but it is not as prominent as in even the $LaNi_4Co$ alloy. Fe is known to preferentially occupy the crystallographic 3g-site, but it does not induce a second plateau in the isotherm as Co does.[5] It is more likely that Fe-substitution promotes the exclusion of hydrogen sites, and hence reduces lattice expansion, rather than slightly changing the occupation energies of hydrogen sites.[27] The latter situation would be consistent with a lattice expansion continuous with hydrogen composition.

Another outcome of the reduction in hydriding volume expansion is a reduction in the microstrain and the associated diffraction peak broadening. Oddly enough, the anisotropy in the diffraction peak broadening of dehydrided alloys disappears at moderate substitution levels.[10] This will be further discussed with the results.

J.H.N. van Vucht, F.A. Kuijpers, H.C.A.M. Bruning, *Philips Res. Rep.*, **25** (1970): 133.

[2] A. Percheron-Guégan and J.-M. Welter in *Topics in Applied Physics: Hydrogen in Intermetallic Compounds I*, Chapter 2, L. Schlapbach, ed., Springer Verlag (Berlin: 1988).

[3] William Hume-Rothery and G.V. Raynor, *The Structure of Metals and Alloys*, (Institute of Metals: London) 1962.

[4] J. Shinar, D. Shaltiel, D. Davidov, and A. Grayevsky, *J. Less-Common Met.*, **60** (1978): 209.

[5] H.H. van Mal, K.H.J. Buschow, and F.A. Kuijpers, *J. Less-Common Met.*, **32** (1973): 289.

[6] M. Brouha and K.H.J. Buschow, *J. Phys. F*, **5** (1975): 543.

[7] E. Gurewitz, H. Pinto, M.P. Dariel, and H. Shaked, *J. Phys. F: Met. Phys.*, **13** (1983): 545.

[8] M. Latroche, J. Rodríguez-Carvajal, A. Percheron-Guégan, and F. Bourée-Vigneron, *J. Alloys Comp.*, **218** (1995): 64.

[9] J.C. Achard, A.J. Dianoux, C. Lartigue, A. Percheron-Guégan, and F. Tasset, in *The Rare Earths in Modern Science and Technology*, vol. 3, eds. G.J. McCarthy, Silber, and J.J. Rhyne (Plenum Press, New York, 1982), p. 481.

[10] A. Percheron-Guégan, C. Lartigue, J.C. Achard, P. Germi, and F. Tasset, *J. Less-Common Met.*, **74** (1980): 1.

[11] C. Lartigue, A. Percheron-Guégan, J.C. Achard, and F. Tasset, *J. Less-Common Met.*, **75** (1980): 23.

[12] J. Lamloumi, A. Percheron-Guégan, J.C. Achard, G. Jehanno, and D. Givord, *J. Physique*, **45** (1984): 1643.

[13] J.-M. Joubert, M. Latroche, R. Cerby, R.C. Bowman, Jr., A. Percheron-Guégan, and K. Yvon, , *J. Alloys Comp.*, in press.

[14] A. Percheron-Guégan, C. Lartigue, and J.C. Achard, *J. Less-Common Met.*, **109** (1985): 287.

[15] Gary Sandrock, S. Suda, and L. Schlapbach, in L. Schlapbach, ed. *Topics in Applied Physics v. 67 Hydrogen in Intermetallic Compounds I: Surface and Dynamic Properties, Applications*, Springer-Verlag, Berlin. 1992, chapter 5.

[16] R. Griessen and T. Riesterer, chapter 6 in *Topics in Applied Physics v. 63 Hydrogen in Intermetallic Compounds I: Electronic, Thermodynamic, and Crystallographic Properties, Preparation*, L. Schlapbach, ed. Springer-Verlag, Berlin. 1988, p. 219.

[17] J.C. Achard, A. Percheron-Guégan, H. Diaz, and F. Briaucourt, in F. Demany (ed.), *Proc. 2nd Int. Cong. on Hydrogen In Metals, Paris, June 1977*, Vol. 3, Pergamon, Oxford, 1978, Paper 1E12.

[18] C.E. Lundin, F.E. Lynch, and C.B. Magee, *J. Less-Common Met.*, **56** (1977): 19.

[19] D.G. Westlake, *J. Less-Common Met.*, **91** (1983) 1.

[20] M.H. Mendelsohn, D.M. Gruen, and A.E. Dwight, *J. Less-Common Met.*, **63** (1979) 193; D.M. Gruen, M.H. Mendelsohn, and A.E. Dwight, *Advances in Chemistry Series 167 Transition Metal Hydrides*, R. Bau, ed., American Chemical Society, Wash. DC, (1978): 327.

[21] A. Percheron-Guégan and C. Lartigue, *Materials Science Forum*, **31** (1988): 125.

[22] K.A. Gschneidner, Jr., T. Takeshita, Y. Chung, and O.D. McMasters, *J. Phys. F*, **12** (1982): L1.

[23] M. Latroche, A. Percheron-Guégan, and F. Bourée-Vigneron, *J. Alloys Comp.*, **265** (1998): 209.

[24] M. Latroche, A. Percheron-Guégan, Y. Chabre, C. Poinsignon, and J. Pannetier, *J. Alloys Comp.*, **189** (1992): 59.

[25] S. Ono, K. Nomura, E. Akiba, and H. Uruno, *J. Less-Common Met.*, **113** (1985): 113.

[26] E.MacA. Gray, E.H. Kisi, and R.I. Smith, *J. Alloys Comp.*, in press.

[17] Y. Nakamura, K. Sato, S. Fujitani, K. Nishio, K. Oguro, and I. Uehara, *J. Alloys Comp.*, **267** (1998): 205.

E. Electronic Structure

There has been speculation about the influence of the electron structure of $LaNi_5$ on its hydriding properties since work on this material began. Van Vucht hypothesized that that La "induces nickel to become also a hydrogen-bonding element."[1] The capacity of the hydride phase has been associated with the valence electrons of the alloy.[2] Griessen and Driessen have developed a semi-empirical band-structure model correlating the heat of formation of the hydride and a characteristic band-structure energy parameter.[3]

There have only been three band-structure calculations of $LaNi_5$ alloys, and only two of these include their hydrides. Malik, *et al.*[4] used the augmented plane wave (APW) method [5] to calculate energy bands and densities of states for $LaNi_5$ and the isoelectronic $GdNi_5$. M. Gupta used a tight-binding recursion scheme for the calculations, and included calculations for $LaNi_5H_7$.[6] Later calculations by Gupta used the density functional theory in the local density approximation, using the self-consistent linear muffin tin orbital method within the atomic sphere approximation. The latter work included $LaNi_4M$, $M \in \{Fe, Co, Mn, Cu, Al\}$, $LaNi_{4.5}Sn_{0.5}$, and $LaNi_4CoH_4$.[7] Results from both authors match well with experimental data.

Experimental results on the electronic structure of $LaNi_5$ include measurements of heat capacity [8-10] and magnetic susceptibility,[11] as well as direct DOS measurements by core-level [12-13] and valence band [13-15] photoemission spectra. Heat capacity [10,16] and magnetic susceptibility [11,17] measurements have been made for β-$LaNi_5H_y$. However, the tendency of AB_5 MH alloys to desorb hydrogen in vacuum has made direct measurements of their electronic structure impossible. Therefore, the best information available about the hydrides of these alloys comes from band-structure calculations.

Band structure calculations and core-level photoemission spectroscopic measurements confirm that there is little or no charge transfer between Ni and La in the binary alloy. The band structure looks very similar to those of metallic Ni and La, with the major differences resulting from the decrease in metal-atom coordination and increase in Ni-Ni and La-La distances. The Fermi energy E_F falls close to the end of the Ni 3d bands, leaving them unfilled. Substitutions for Ni with metals having s-p valence electrons leads to a decrease of the DOS at E_F associated with a progressive filling of the Ni-d states.[7] In these ternary alloys ($Sn_{0.5}$ and Al_1), low energy structures are found at ~-9 eV (Sn) and ~-7 eV (Al) that are attributed to the s states of the substituent.[7]

In the hydride, calculations predict a charge transfer between La and H, inducing a hybridization of the Ni-d and H-s states. The metal-hydrogen bonding states appear 5-10 eV below E_F. The Fermi is found at a higher energy than in the alloy, and the DOS is found to be smaller at E_F than in the alloy.[7] It is possible that the s-derived states block the metal-bonding states by filling the DOS at that energy.

1 J.H.N. van Vucht, F.A. Kuijpers, and H.C.A.M. Bruning, *Philips Res. Rep.*, **25** (1970): 133.

2 K.A. Gschneidner, Jr., T. Takeshita, Y. Chung, and O.D. McMasters, *J. Phys. F*, **12** (1982): L1.

3 R. Griessen and T. Riesterer, chapter 6 in *Topics in Applied Physics v. 63 Hydrogen in Intermetallic Compounds I: Electronic, Thermodynamic, and Crystallographic Properties, Preparation*, L. Schlapbach, ed. Springer-Verlag, Berlin. 1988, p. 219.

4 S.K. Malik, F.J. Arlinghaus, and W.E. Wallace, *Physical Review B*, **25** (1982): 6488.

5 F.J. Arlinghaus, *Physical Review*, **186** (1969): 609.

6 M. Gupta, *J. Less-Common Met.*, **130** (1987): 219; M. Gupta and L. Schlapbach, chapter 5 in *Topics in Applied Physics v. 63 Hydrogen in Intermetallic Compounds I:*

Electronic, Thermodynamic, and Crystallographic Properties, Preparation, L. Schlapbach, ed. Springer-Verlag, Berlin. 1988, p. 139.

[7] M. Gupta, in *Hydrogen in Semiconductors and Metals*, eds. N.H. Nickel, W.B. Jackson, R.C. Bowman, and R.G. Leisure (Materials Research Society, Warrendale, PA 1998) 79.

[8] S. Nasu, H.H. Neumann, N. Marzouk, R.S. Craig, and W.E. Wallace, *J. Phys. Chem. Solids*, **32** (1971): 2779.

[9] T. Takeshita, G. Dublon, O.D. McMasters, and K.A. Gschneidner, Jr., in *The Rare Earths in Mod. Sci. and Technol.*, ed. G.J. McCarthy, J.J. Rhyne, and H.B. Silber (Plenum Press, New York 1980) p. 563; T. Takeshita, K.A. Gschneidner, Jr., D.K. Thome, and O.D. McMaster, *Phys. Rev. B*, **21** (1980): 5636.

[10] D. Ohlendorf and H.E. Flotow, *J. Chem. Phys.*, **73** (7980): 2973.

[11] L. Schlapbach, *J. Phys. F.*, **10** (1980): 2477; L. Schlapbach, C. Pina-Perez, and T. Siegrist, *Solid State Commun.*, **41** (1982): 135.

[12] L. Schlapbach, *Solid State Commun.*, **38** (1981): 117.

[13] F.U. Hillebrecht, J.C. Fuggle, P.A. Bennet, Z. Zolnierek, and Ch. Frieburg, *Phys. Rev. B*, **27** (1983): 2179.

[14] J.C. Fuggle, F.U. Hillebrecht, R. Zeller, Z. Zolnierek, P.A. Bennet, and Ch. Frieburg, *Phys. Rev. B*, **27** (1982): 2145.

[15] J.H. Weaver, A. Franciosi, D.J. Peterman, T. Takeshita, and K.A. Gschneidner, Jr., *J. Less-Common Met.*, **86** (1982): 195.

[16] Y. Chung, T. Takeshita, O.D. McMasters, and K. A. Gschneidner, Jr., *J. Less-Common Met.*, **74** (1980): 217.

[17] J. Palleau and G. Chouteau, *J. de Phys. Lett.*, **41** (1980): L227.

F. Alloy Degradation

1. Disproportionation

One of the main barriers to the widespread use of $LaNi_5$ for reversible hydrogen storage is the fast degradation of the active material with cycling. The hydride of $LaNi_5$, or any intermetallic hydride, is not in thermodynamic equilibrium. The heat of formation of H with La is great, causing the reaction

$$LaNi_5H_6 \rightarrow LaH_2 + 5Ni + 2\,H_2 \qquad [II.4]$$

called a *disproportionation reaction*, to be thermodynamically favorable. The heat of formation of this reaction is -224.6 kJ (mol H_2)$^{-1}$,[1] compared with $\Delta H^f_{LaNi_5}$ = -273 kJ (mol $LaNi_5$)$^{-1}$ [2] and $\Delta H^f_{hydride}$ = -15.6 kJ (mol H)$^{-1}$. With extended cycling, $LaNi_5$ disproportionates into LaH_y, $2 < y < 3$, and Ni metal. This can also take place during thermal aging of the hydride, when β-phase material is kept at high temperatures for extended periods.

Disproportionation was described by P. D. Goodell as follows:

> Alloy disproportionation is the result of the metastable character of many pseudobinary hydride phases.[3] It is a separation of alloy components which is induced by hydrogen: the more electropositive alloy elements (lanthanum, calcium, titanium, etc.) tend to form regions of increased hydride stability. This leaves the less electropositive alloy elements (nickel, cobalt, iron, etc.) as regions of decreased hydride stability. The regions in question may be of atomic dimensions as in lattice disorder or clustering, or they may be much larger if phase separation occurs. The hydriding properties may be expected to vary accordingly, but a general result is the loss of useful reversible hydrogen storage capacity. In some cases the capacity can be recovered by removing the hydrogen during mild thermal treatment.[4]

The first experimental verification of the disproportionation of $LaNi_5$ was obtained by Cohen, *et al.* The hydrogen content and residual hydrogen over $La_{0.9}Eu_{0.1}Ni_{4.6}Mn_{0.4}$ during 1500 thermally induced hydrogen absorption-desorption cycles were found to be

consistent with reaction II.4. In addition, Eu Mössbauer spectroscopic measurements of the cycled sample found a stable phase containing divalent Eu that did not return to Eu^{3+} upon hydrogen desorption. This "fixed" europium hydride coexisted with the reversibly hydrided material.[1] Subsequent experiments including ^{61}Ni Mössbauer [5] and magnetization [6] measurements of thermally cycled $LaNi_5$ confirmed the existence of Ni microprecipitates. The presence of trapped hydrogen in thermally cycled $LaNi_5$ was later confirmed by inelastic neutron scattering, but there was not strong evidence for the presence of LaH_2.[7] It was not until Bowman, *et al.* performed XRD and TEM on thermally cycled $LaNi_5$ that evidence of the LaH_x product of the disproportionation reaction was found.[8] XRD patterns of alloys degraded over 50% in reversible H capacity contained diffraction clearly indicating the presence of LaH_x. Dark-field TEM images using the (111) and (200) f.c.c. diffraction rings revealed diffractions from regions only a few nanometers in size.[8]

The fact that $LaNi_5$ does not immediately decompose in the presence of hydrogen gas rests on the large energy barrier that must be overcome to dissociate the Haucke phase $CaCu_5$ structure. For a hydrogen atom to bond with La, a free La atom must be present. Because no unbonded La atoms are present in $LaNi_5$, the first atoms to disproportionate will be those in the least stable environments, at the alloy surface.

When the La atoms at the alloy surface have left the alloy and bonded with hydrogen, a La depleted region is created near the surface. This concentration gradient drives more La atoms to diffuse to the surface, continuing the disproportionation reaction. A schematic of this process is depicted in **Figure II-20**, reprinted from L. Schlapbach, *et al.*[9] Once an appreciable amount of La has left the lattice, the large concentration of vacancies will destabilize the remaining Ni structures. The added strain associated with lattice dilatation and La atom diffusion will break these structures off, exposing fresh alloy surface to hydrogen. The rate limiting step in this process should involve the kinetics of metal-atom diffusion.

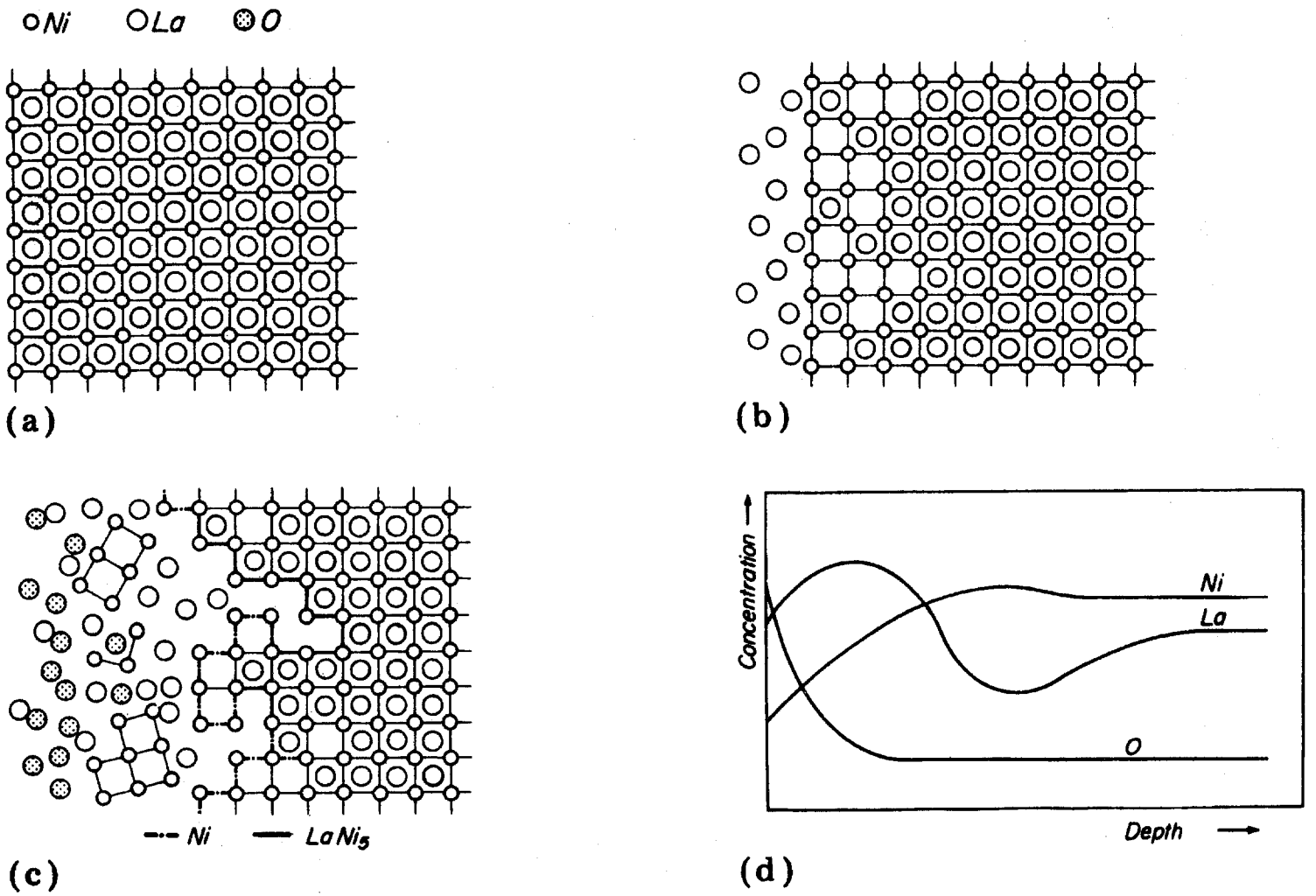

Figure II-20 Schematic of $LaNi_5$ disproportionation. (reprinted from L. Schlapbach, et al., *J. Less-Common Met.*, **73** (1980): 145.)

Metal-atom diffusion should follow Fick's First law:

$$J = -D\frac{dc}{dx} \qquad \text{[II.5]}$$

That is to say that atoms in a potential gradient, in this case a gradient in chemical potential caused by the concentration gradient of the species, will diffuse in a direction that will oppose the concentration gradient. There are several ways in which the flux of La atoms to the alloy surface can be enhanced. Increasing either the diffusion coefficient D or the potential gradient $d\phi/dx$ will enhance the diffusion of lanthanum.

In $LaNi_5$ La has a lower surface energy than Ni, providing a driving force for La diffusion to the alloy surface.[9,10] Therefore the situation described here is that of diffusion in a potential field. Evidence of this has been given in the form of Auger Electron Spectroscopy (AES) depth profiling.[11] In this experiment a sample of polycrystalline $LaNi_5$ previously exposed to air was introduced to an ultrahigh vacuum of 10^{-8} torr. The sample was then sputter cleaned until the surface composition was approximately equal to that of $LaNi_5$. Immediately after sputter cleaning, the surface concentrations of La and O were found to increase while the Ni concentration decreased slowly. After 20 minutes, the La to Ni concentration ratio at the surface was ~1:1.7.[11]

> "Surface segregation is a well known phenomenon in intermetallic compounds.[12,13] The free energy of an intermetallic compound is minimized if the surface concentration of the element with the smaller surface energy is increased. In $LaNi_5$ stability increases if La segregates to the surface..." [11]

The second factor enhancing the diffusion of La to the surface of $LaNi_5$ is the presence of large strains at the interface between the region of hydrogen in solution in the metal lattice and the metal hydride. As discussed in §.II.C.3, $LaNi_5$ experiences strains of up to 7.5% during hydrogen absorption. The presence of such large strains during hydriding will facilitate the atom movements required during La diffusion, thereby creating a larger, "dynamic" diffusion coefficient. For the large (1.83Å radius) La atom to hop from its lattice position to a possible vacancy position, the Ni atoms separating the

two locations must move far from their equilibrium positions. The largest hole in the equilibrium $LaNi_5$ lattice has a radius of 0.75 Å. Each Ni atom would have to move ~1.1 Å to accommodate the La atoms. This corresponds to an activation energy of ~10 eV/atom. At the interface between the α- and β-phase, the lattice misfit strains should be large enough to enhance the diffusion of La atoms. In addition, the strains induce microstructural defects such as dislocations and stacking faults, as explained above (§ II.C.5). The presence of dislocations is known to enhance the kinetics of metal diffusion,[14] so the high concentration of such defect structures in activated $LaNi_5$ will enhance the diffusion of La.

2. Corrosion

If hydride disproportionation limits the attractiveness of $LaNi_5$ for consumer hydrogen storage applications, corrosion by OH^- ions in an alkaline electrolyte almost prevents its usefulness in Ni-MH rechargeable batteries. During cycling in the 6 molar KOH solution electrolyte of Ni-MH batteries, $LaNi_5$ corrodes according to:

$$LaNi_5 + 3\ OH^- \rightarrow La(OH)_3 + 5Ni + 3e^- \qquad [II.6]$$

$$LaNi_5 + 3\ H_2O \rightarrow La(OH)_3 + 5Ni + 3H \qquad [II.6]$$

The free enthalpy of formation of this reaction is -472 kJ (mol $LaNi_5$)$^{-1}$, [15] which is ~4.4 times the heat of hydride formation assuming 7 H (mol $LaNi_5$)$^{-1}$ and almost 2 times the formation enthalpy of the compound $LaNi_5$, -273 kJ H (mol $LaNi_5$)$^{-1}$ [2]. It is likely that the very large heat of formation driving the transformation to $La(OH)_3$ means that the kinetics of the alloy degradation is no longer simply controlled by metal atom diffusion.

Hydroxide ions quickly form a La depletion layer that may be thick enough to spall or crack with each new hydriding cycle. This decrepitation prevents the non-conducting hydroxide films from inducing a charge transfer resistance at the particle surface. If

$La(OH)_3$ developed more slowly, it might not spall off during subsequent cycles. The charge transfer resistance would then create an over-potential on discharge, preventing active hydrogen storage capacity from being utilized, and the corrosion layer would be enhanced. It is ironic that the fast corrosion of $LaNi_5$ in KOH is partially responsible for its usefulness in a battery.

The corrosion is thought to take place during discharge, and mostly when the hydrogen content of the anode is low. It is then that the potential of the anode is lowered, thermodynamically favoring corrosion, and the kinetically favorable reaction of OH^- with H^+ is hindered by the low concentration of H at the anode. The corrosion products $La(OH)_3$, and Ni have been identified by Sakai, *et al.* in cycled electrodes.[2] Boonstra, *et al.* detected $Ni(OH)_2$ as well, and proposed a corrosion mechanism whereby $LaNi_5$ corrodes to $La(OH)_3$ and $Ni(OH)_2$, followed by a reaction of $LaNi_5$ with $Ni(OH)_2$.[16]

3. Approaches to Suppress Degradation

Many approaches have been explored to slow the degradation of $LaNi_5$ during hydrogen absorption/desorption cycling. These have included microencapsulation of the $LaNi_5$ powder with Ni or Cu, [17-19] altering the concentration [19] or composition [20] of the electrolyte, pretreatment of the alloy powder, [21] changing the alloy microstructure, [22-24] alloying substitutions for Ni and La, [2,15,25-28] and optimizing the alloy stoichiometry.[29] The lifetime stabilizing mechanisms associated with many of these methods have been proposed, and sometimes refuted, and some of these will be discussed below.

a. Alloy Composition

As stated in the introduction, Willems, *et al.* decreased the capacity fade of $LaNi_5$-based MH rechargeable batteries by alloying substitutions for Ni and for La. To quantify the improvements in lifetime, they used the parameter S_{400}, the relative fraction of the residual storage capacity left after 400 electrochemical cycles. **Figure II-21**, reprinted

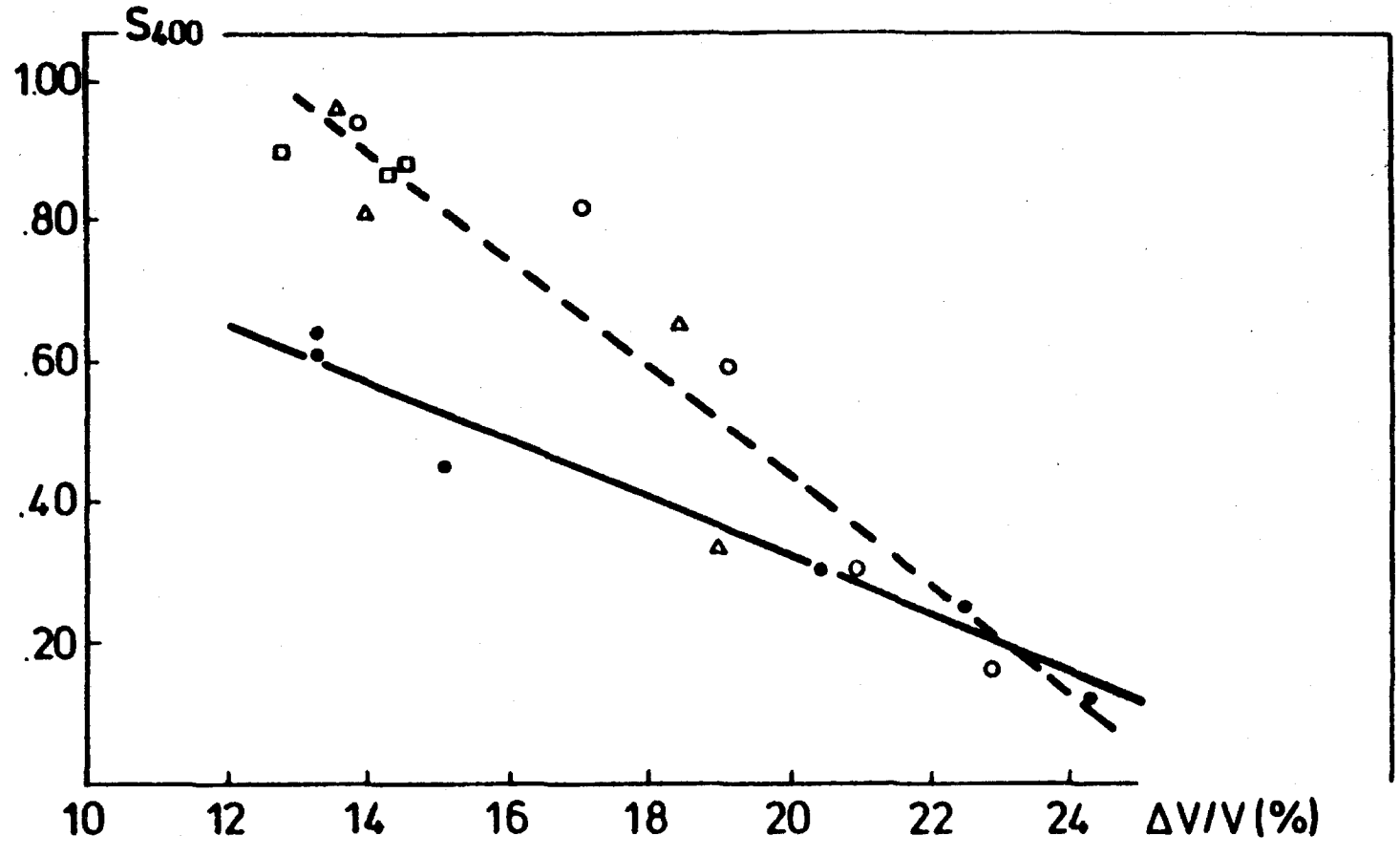

Figure II-21 S_{400} *vs* % volume expansion upon hydriding. (reprinted from J.J.G. Willems and K.H.J. Buschow, *J. Less-Common Met.*, **129** (1987): 13.)

from ref. 15, shows S_{400} *vs* % volume expansion upon hydriding. They noticed that reduced volume expansion in $LaNi_{5-x}Co_x$ alloys containing small amounts of silicon or aluminum (dashed line) was twice as effective in promoting electrochemical stability as the same reduction in $LaNi_{5-x}Co_x$ alloys (solid line). (It should be noted that although they did differentiate between discontinuous and continuous volume expansion, the expansion values in **Figure II-21** refer to total volume expansion.) To put this another way, adding small amounts of Si or Al to the Co-substituted compounds did not appreciably change the nature of the volume expansion, but did increase the stability of the compounds during electrochemical cycling. To justify this difference, they hypothesized that, "[t]he beneficial influence of small amounts of aluminum or silicon on the electrode stability was interpreted as being due to the formation of a more or less closed surface layer surrounding the fine particles, which gives them additional protection against the electrolyte. This surface layer can be thought to be built up of islands of cobalt or nickel interspersed with aluminium- or silicon-containing oxides. The protective effect of the surface layer will be present only when the volume expansion is not too large." Their final alloy, $La_{0.8}Nd_{0.2}Ni_{2.5}Co_{2.4}Si_{0.1}$, retained a residual storage capacity of 88% of the initial capacity of 292 mAh/g after 400 cycles. They did find more stable compounds, but the low initial capacity of these alloys was considered to limit their use.[30]

T. Sakai, *et al.* tested $LaNi_{4.5}M_{0.5}$ and $LaNi_4M$ alloys, $M \in \{Mn, Cu, Cr, Al\}$ and $LaNi_{2.5}Co_{2.5}$ and determined that their effectiveness in improving the cycle life increased in the order Mn, Ni, Cu, Cr, Al, and Co.[31] They found some correlation between the capacity fade and the total volume expansion, but this was clearly not the only effect. Correlations were also found between capacity fade and both the alloy hardness, and its BET surface area after cycling.

Reducing the volume expansion upon hydride formation has been followed by many researchers in the pursuit of long-lived MH alloys.[27,28] It is clear that the problem is not the volume expansion itself. A uniform and gradual dilatation will not produce

decrepitation and defect structures. It is the sharp strain gradient at the α-/β- interface associated with the discontinuous volume expansion that causes lattice misfit strains. One method used to extend MH lifetimes is not to reduce the total volume expansion, which often reduces the total hydrogen capacity, but rather to reduce the discontinuous volume expansion. As explained above (§ II.D.3) alloys of $LaNi_5$ will often continue to expand in the β-phase, absorbing more hydrogen as they expand. In this way, the misfit strain at the interface between the α- and β-phases will correspond to the smaller discontinuous lattice expansion while the total lattice expansion continues to be large.

Notten, *et al.* found that a reduction in the discrete volume expansion was more important than a reduction in the alloy's maximum volume expansion. In-situ XRD determined that the volume expansion of $LaNi_{4+x}CuH_{\sim 6}$ alloys were all approximately equivalent, but the difference in unit cell volumes between the α- and β-phases of these alloys varied greatly.[32] On electrochemical cycling of these and $LaNi_{5.4-x}Cu_x$ alloys, they found that alloys with the smallest discrete volume expansions had the longest lifetimes.[29]

b. Mischmetal

In addition to altering the energetics or time scale of the phase decomposition during cycling, the possibility of alloying $LaNi_5$ increases the likelihood of consumer use of AB_5 Ni-MH batteries from an economic standpoint. La is a relatively abundant metal, the least expensive of the rare earths at $150/kg 1994 prices (99.9% purity),[33] but the purification of La from mischmetal (Mm) is an energy intensive and costly processing step. Mischmetal is a naturally occurring ore containing a mixture of the 4f rare earth metals. Mischmetal ores from different mines contain different proportions of the rare earths present in the purified mischmetal. As of 1993, China was thought to hold 51% of the world's store of RE ores. The predominant RE minerals found there, bastnaesite and monazite, have La:Ce:other RE ratios of 23:47:30 and 32:50:18.[34]

The large amount of Ce present in mischmetal raises the plateau pressure of the metal hydride by slightly less than an order of magnitude, depending on the Ce composition.[35] This effect can easily be offset by alloying with metals such as Mn, Al, or Sn.[36] The lanthanide ratio,[37] alloy stoichiometry,[38,39] chemical composition,[40] and solidification technique (and resulting microstructure) [41] of Mm-based alloys have all been varied to optimize their lifetimes during electrochemical cycling. The alloy composition commonly used in the commercial production of Ni-MH cells is $MmNi_{3.55}Co_{0.75}Mn_{0.4}Al_{0.3}$,[2] often denoted MmB_5, ($B = Ni_{3.55}Co_{0.75}Mn_{0.4}Al_{0.3}$). Cells made with these alloys experience a capacity reduction of only 10% after 2000 cycles.[2]

The volume expanding behaviors of LaB_5 and MmB_5 alloys have also been measured. LaB_5 alloys have a miscibility gap between y = 0.6 D/f.u. and y = 3.4 D/f.u. and corresponding discrete volume expansion of 9.1%.[42] The isotherms of MmB_5 alloys have almost no plateau region, and therefore a smaller miscibility gap, but well-annealed alloys still experience a discrete volume expansion of ~9.5%.[40] Lichtenberg, *et al.* [43] and Züttel, *et al.* [40] measured discrete volume expansion in a number of multicomponent MmB_5 alloys. They found a general trend linking cyclic stability to low volume expansion, but the substituted elements used and their compositions had an equally large effect. Solidification techniques such as gas atomization or melt spinning can have the effect of further reducing the miscibility gap.[40]

The increased lifetimes of these alloys is likely not only due to chemical effects from the alloying elements. Including a variety of elements in the alloy will create configurational disorder on the $LaNi_5$ lattice. Disorder on the crystalline lattice would create disorder in the α- to β-hydride transition by creating a continuum of chemical environments for H to occupy in the Haucke phase lattice. This would replace the singularity in hydrogen concentration at the alloy/hydride interface with a hydrogen concentration gradient. This effect could be produced with many metal elements, exclusive of their other effects on the hydriding properties of the alloy. Creating

configurational disorder as outlined here would thus lower the critical temperature for hydrogen ordering, reducing the miscibility gap between the α- and β-hydride phases.

There are several ways to lower the critical temperature for hydrogen ordering. All of the possible methods involve changing the regularity of the sites available for hydrogen occupation. This can be performed by alloying substitutions for Ni and/or La, by quenching in atomic disorder in the lattice, and by preparation of a non-stoichiometric alloy. The third method, preparing non-stoichiometric alloys, is actually a combination of the other two methods. Changing the La:Ni ratio means that La is a substituent for Ni, or Ni (a pair of Ni atoms actually) is a substituent for La. $LaNi_5$ is a stoichiometric compound at room temperature. This means that non-stoichiometric alloys must be quenched below the alloys' glass transition temperature so that the additional stoichiometry will not precipitate out of the $LaNi_5$ matrix. The precipitate would be Ni in the case of Ni-rich alloys, or a lanthanum-rich binary compound (La_2Ni_7 or $LaNi_3$) in the case of La-rich alloys. Alloying different metals for Ni creates disorder in the hydrogen sublattice, but sometimes it changes the environment of the hydrogen sites too drastically. This may result in the loss of hydrogen capacity instead of resulting in a region of the isotherm that is outside the 2-phase region.

c. Thesis Approach

The methods of reducing the volume dilatation and lowering the critical temperature for hydride formation both help extend the lifetimes of AB_5 alloys during cyclic hydrogen absorption/desorption. However, these are both mainly mechanical effects. If these results can be generated with alloying elements that also increase the chemical stability of the alloy (i.e., through the thermodynamics or kinetics of phase transformation), the lifetimes of the MH alloys would be greatly enhanced. There has been some evidence of these chemical effects in the literature, but the sources of these effects are extremely hard to extract from other causes. Most chemical differences will be associated with mechanical

effects that result from the substitution of a metal with a different metallic radius than Ni. This will change the plateau pressure, volume expansion, and H environments, each of which may affect the cyclic lifetime.

Willems, *et al.* saw evidence of chemical effects with Al and Si substitutions in $LaNi_{2.4}Co_{2.5}$, but incorrectly attributed the effects to the formation of structures on the alloy surface.[15] XPS experiments by Schlapbach, *et al.* determining surface compositions have refuted the existence of an Al or Si rich surface layer in similarly substituted alloys.[9] Sakai, *et al.* correlated an increase in lifetime with a decrease in the alloy hardness.

To determine the chemical effects of Ni substitution with respect to the cyclic lifetimes of $LaNi_5$ MH alloys, trends in cyclic lifetime of Ni-substituted $LaNi_5$ alloys were extracted from the pre-1993 literature. The lifetime effect of each Ni substitution was quantified by taking the ratio of the number of cycles the substituted alloy completed before 50% degradation to the number of cycles the binary alloy from the same publication/research group completed before 50% degradation. This ratio was plotted *vs* a variety of parameters that described the alloy, such as hardness or total volume expansion, or the substituting element, such as metallic radius or the heat of formation of the element M with La, ΔH_{LaM}. Two examples of these correlations are shown in **Figure II-22**, *vs* metallic radius, and **Figure II-23**, *vs* ΔH_{LaB}. The best trend was found in the case of ΔH_{LaB}.

Because the $\Delta H^{decomp.}$ of reactions II.4 and II.6 are much larger than $\Delta H^{f}_{LaNi_5}$, it is not likely that the alloying will appreciably affect the thermodynamics of the degradation of $LaNi_5$ during cycling. Indeed, calorimetry by Pasturel, *et al.* has shown for $LaNi_4M$ alloys $M \in \{Mn, Cu, Fe\}$, $(\Delta H^{f}_{LaNi_4M} - \Delta H^{f}_{LaNi_5})/ \Delta H^{f}_{LaNi_5} = 8.6\%$.[44] To understand this correlation, we borrowed insight from work on the kinetics of metal atom diffusion.

Our approach to reducing the alloy degradation is to reduce the kinetics of metal-atom diffusion by substituting for Ni metals which have a large heat of formation with La. Dr.

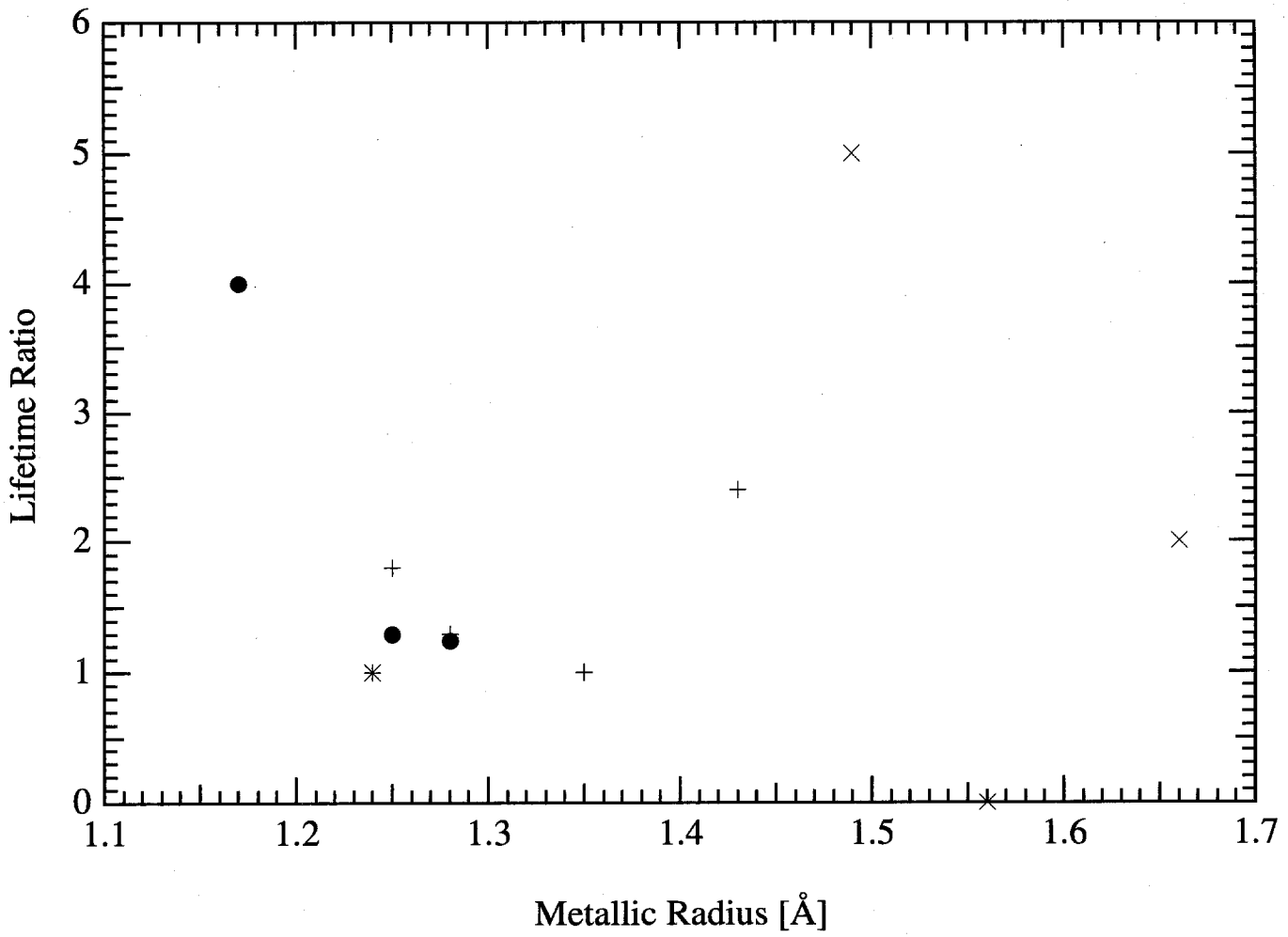

Figure II-22 Correlation of AB_5 alloy cyclic lifetime with metallic radius of solute atom.

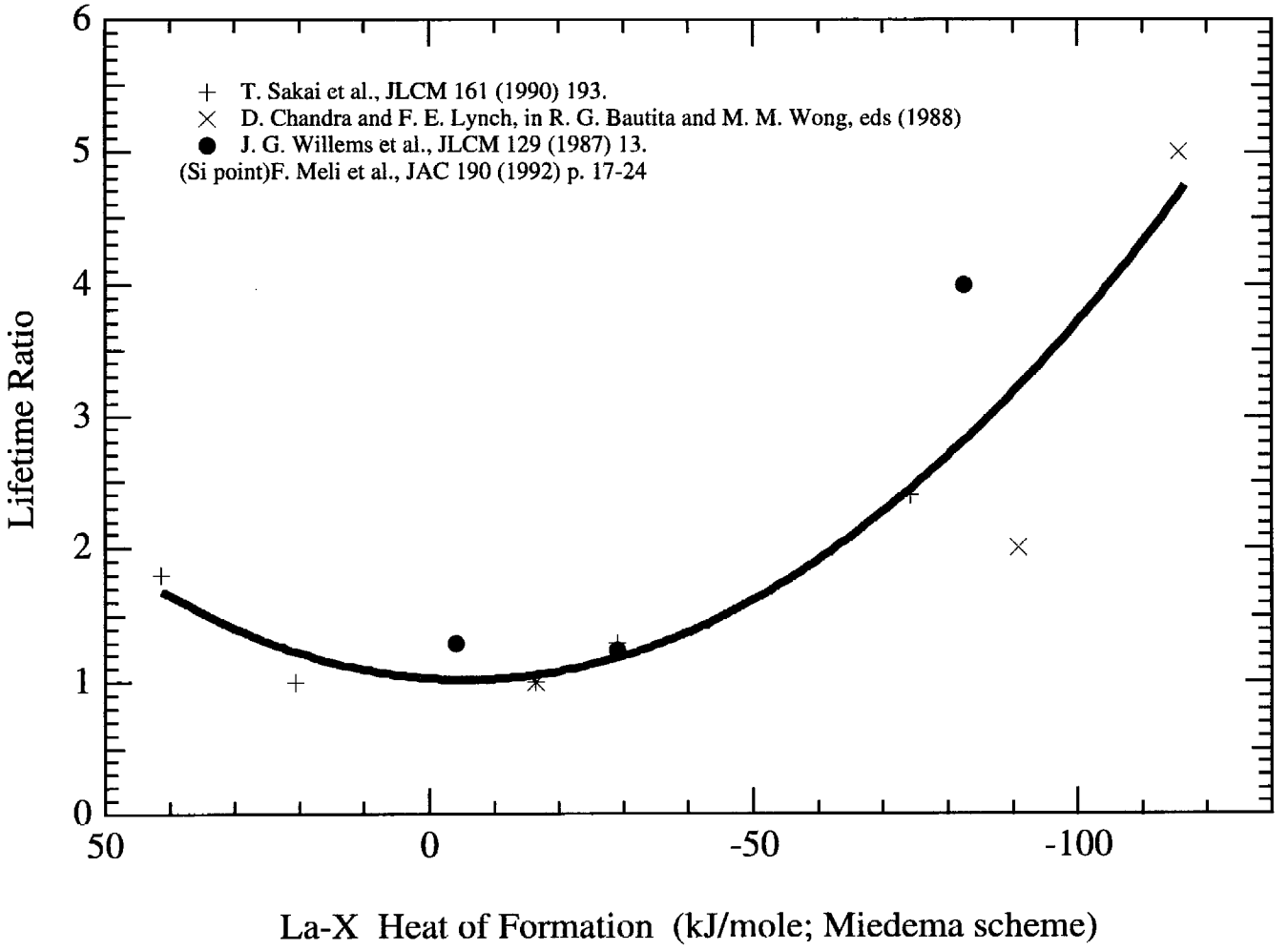

Figure II-23 Correlation of AB_5 alloy cyclic lifetime with ΔH_{LaM}.

B. Fultz used Monte Carlo simulations to study the kinetics of short- and long-range ordering in binary and ternary alloys.[45,46] He found that small substitutions with a ternary element could affect the activation barrier for metal atom diffusion and the time scales for order-disorder transitions.[46]

This was first tested in the $LaNi_5$ system by thermally cycling $LaNi_5$, $LaNi_{4.9}Sn_{0.1}$, and $LaNi_{4.8}Sn_{0.2}$ alloys from room temperature to greater than 200° C. It was found that even these dilute substitutions of Sn for Ni provide dramatic improvements to the cyclic lifetime of the alloys.[8] However, a recent measurement by Joubert, *et al.* shows that the total volume expansion of $Sn_{0.2}$ is 22.4%, a reduction of only 2.2% from that of $LaNi_5$.[47] In addition, the wide plateau of $Sn_{0.2}$ ($\Delta y = 5.3$) implies that almost all of the volume expansion is discontinuous. It is reasonable to think that this small reduction in lattice expansion and the associated misfit strains alone should not produce such a marked improvement in cyclic lifetime. This positive result encouraged us to test this hypothesis with other metal elements. Because we used electrochemical cycling, the faster degradation mentioned above enabled us to test many alloys.

1 R.L. Cohen, K. W. West, and J. H. Wernick, *J. Less-Common Met.*, **70** (1980): 229.

2 T. Sakai, M. Matsuoka, and C. Iwakura, in *Handbook on the Physics and Chemistry of Rare Earths*, eds. K.A. Gschneidner, Jr., and L. Eyring, **21** (1995): 133.

3 K.H.J. Buschow and A.R. Miedema, in *Proc. Int. Symp. On Hydrides for Energy Storage, Geilo*, A.F. Andresen and A.J. Maeland, eds., (Pergamon Press: Oxford, 1978), p. 235.

4 P. D. Goodell, *J. Less-Common Met.*, **99** (1984): 1.

5 H. Rummel, R.L. Cohen, P. Gutlich, and K.W. West, *Appl. Phys. Lett.*, **40 (6)** (1982): 477.

6 R.L. Cohen, R.C. Sherwood, and K.W. West, *Appl. Phys. Lett.*, **41 (10)** (1982): 999.

[7] M.J. Benham and D.K. Ross, *Zeitschrift für Physikalische Chemie Neue Folge, Bd.*, **147** (1986): 219.

[8] R.C. Bowman, Jr., C.H. Luo, C.C. Ahn, C.K. Witham, and B. Fultz, *J. Alloys Comp.*, **217** (1995): 185.

[9] L. Schlapbach, A. Seiler, F. Stucki, and H.C. Siegmann, *J. Less-Common Met.*, **73** (1980): 145.

[10] L. Schlapbach, chapter 2 in *Topics in Applied Physics v. 67 Hydrogen in Intermetallic Compounds II: Surface and Dynamic Properties, Applications*, L. Schlapbach, ed. Springer-Verlag, Berlin. 1992, p. 72.

[11] L. Schlapbach, A. Seiler, H.C. Siegmann, T. van Waldkirch, and P. Zürcher, *Int. J. Hydrogen Energy*, **4** (1979): 21.

[12] S. H. Overbury, P.A. Bertrand, and G. A. Somorjai, *Chem. Rev.*, **75** (1975): 547.

[13] J. J. Burton, E. Hymann, and D. G. Fedak, *J. Catalysis*, **37** (1975): 106.

[14] A.D. Vasilyev, *Thin Solid Films,* **289**: (1996) 205.

[15] J.J.G. Willems and K.H.J. Buschow, *J. Less-Common Met.*, **129** (1987): 13.

[16] A.H. Boonstra and T.N.M. Bernards, *J. Less-Common Met.*, **155** (1989): 119.

[17] H. Ishikawa, K. Oguro, A. Kato, H. Suzuki, and E. Ishii, *J. Less-Common Met.*, **107** (1985): 105; **120** (1986): 123.

[18] T. Sakai, H. Ishikawa, K. Oguro, C. Iwakura, and H. Yoneyama, *J. Electrochem. Soc.*, **134 (3)** (1987): 558.

[19] A.H. Boonstra and T.N.M. Bernards, *J. Less-Common Met.*, **161** (1990): 355.

[20] S. Mukerjee, J. McBreen, G. Adzic, J.R. Johnson, J.J. Reilly, M.R. Marrero, M.P. Soriaga, M.S. Alexander, A. Visintin, and S. Srinivasan, *J. Electrochem. Soc.*, **144** (1997): L258.

[21] N. Kuriyama, T. Sakai, H. Miyamura, H. Tanaka, I. Uehara, F. Meli, and L. Schlapbach, *J. Alloys Comp.*, **238**: (1996): 128.

[22] L. Zhang, T.J. O'Hara, and G.M. Michal, in *Hydrogen and Metal Hydride Batteries*, P.D. Bennett and T. Sakai, Ed., **PV 94-27**, p 45, The Electrochem. Soc. Proceedings Series, Pennington, NJ (1994).

[23] W.K. Hu, *J. Alloys Comp.*, **279** (1998): 295.

[24] R.C. Bowman, C. Witham, B. Fultz, B.V. Ratnakumar, T.W. Ellis, and I.E. Anderson, *J. Alloys Comp.*, **253** (1997): 613.

[25] B.V. Ratnakumar, C. Witham, R.C. Bowman, Jr., A. Hightower, and B. Fultz, *J Electrochem. Soc.*, **143** (1996): 2578.

[26] C. Witham, A. Hightower, B. Fultz, B.V. Ratnakumar, and R.C. Bowman, Jr., *J Electrochem. Soc.*, **144** (1997): 3758.

[27] M.P. Sridhar Kumar, K. Petrov, W. Zhang, A.A. Rostami, S. Srinivasan, G.D. Adzic, J.R. Johnson, J.J. Reilly, and H.S. Lim, *J. Electrochem. Soc.*, 142 (1995): 3424.

[28] F. Meli, A. Züttel, and L. Schlapbach, *J. Alloys Comp.*, **231** (1995): 639.

[29] P.H.L. Notten, R.E.F. Einerhand, and J.L.C. Daams, *J. Alloys Comp.*, **210** (1994): 221.

[30] J.J.G. Willems, *Philips J. Research*, **39 (1)** (1984): 1.

[31] T. Sakai, K. Oguro, H. Miyamura, N. Kuriyama, A. Kato, and H. Ishikawa, *J. Less-Common Met.*, **161**, 193 (1990).

[32] P.H.L. Notten, J.L.C. Daams, and R.E.F. Einerhand, *J. Alloys Comp.*, **210** (1994): 233.

[33] J.B. Hedrick, *J. Alloys and Comp.*, **250** (1997): 471.

[34] P. Falconnet, *J. Alloys and Comp.*, **192** (1993): 114.

[35] K.R. Clay, A.J. Goudy, R.G. Schweibenz, and A. Zarynow, *J. Less-Common Met.*, **166** (1990): 153.

[36] R. Balasubramaniam, M.N. Mungole, and K.N. Rai, *J. Alloys Comp.*, **196** (1993): 63.

[37] G.D. Adzic, J.R. Johnson, J.J. Reilly, J. McBreen, S. Mukerjee, M.P.S. Kumar, W. Zhang, and S. Srinivasan, *J. Electrochem. Soc.*, **142** (1995): 3429.

[38] T. Sakai, H. Miyamura, H. Kuriyama, H. Ishikawa, and I. Uehara, *J. Alloys Comp.*, **192** (1993): 155.

[39] Y. Fukumoto, M. Miyamoto, H. Inoue, M. Matsuoka, and C. Iwakura, *J. Alloys Comp.*, **231**.(1995): 562.

[40] A. Züttel, D. Chartouni, K. Gross, P. Spatz, M. Bächler, F. Lichtenberg, A. Fölzer, and N.J.E. Adkins, *J. Alloys Comp.*, **253** (1997): 626.

[41] T. Sakai, H. Miyamura, N. Kuriyama, H. Ishikawa, and I. Uehara, *Zeitschrift für Physikalische Chemie, Bd.*, **183** (1994): 333.

[42] J. Latroche, A. Percheron-Guégan, and G. Bourée-Vigneron, *J. Alloys Comp.*, **365** (1998): 209.

[43] F. Lichtenberg, U. Köhler, A. Fölzer, N.J.E. Adkins, and A. Züttel, *J. Alloys Comp.*, **253-254** (1997): 570.

[44] A. Pasturel, C. Chatillon-Colinet, A. Percheron-Guégan, and J.C. Achard, *J. Less-Common Met.*, **84** (1982): 73.

[45] B. Fultz, *J. Chem. Phys.*, **87 (3)**: (1987): 1604.

[46] B. Fultz, *J. Mater. Res.*, **7 (4)** (1992): 946.

[47] J.-M. Joubert, M. Latroche, R. Cerby, R.C. Bowman, Jr., A. Percheron-Guégan, and K. Yvon, *J. Alloys Comp.*, in press.

III. Methods: Experimental Techniques, Equipment, and Data Analysis

A. Alloy Preparation

Alloys were made by melting in a silver-boat induction furnace stoichiometric amounts of La (99.99%), Ni (99.999%), and one of the solute elements Sn, Ge, In, Al, Si, Ga, Sb, or Bi (99.999%) purchased from Alfa-Aesar, in an argon atmosphere. Alloy ingots were then sealed in quartz ampoules that had been purged and back-filled with argon. Annealing was performed at a temperature of 900° C for 3 days, after which the alloys were allowed to slowly cool inside the furnace. Alloys were then activated by gas-phase hydrogen absorption. Some alloys were further activated by the measurement of gas-phase isotherms or by thermally driven absorption/desorption cycling. All handling after annealing was performed in an argon glove box, except electrode preparation which was done in air. In the text, alloys of composition $LaNi_{5-x}M_x$ will be denoted as M_x.

B. Gas-Phase p-c-isotherms

Unless otherwise noted, the isotherms shown here were measured with an automated Sievert's apparatus designed, constructed, and operated at Caltech. The equipment was also used for hydrogen sorption activation, thermally induced hydrogen cycling, and hydrogen charging of the alloys before poisoning the alloy surface with CO. It has experienced several design as well as mechanical changes, and I will only describe the most recent version here.

A picture of the Sievert's apparatus appears in **Figure III-1**, and a schematic drawing in **Figure III-2**. All tubing and fittings used were 1/4" 316 stainless steel with Swagelok VCR fittings unless otherwise noted. Manual valves were Nupro bellows valves, VS-

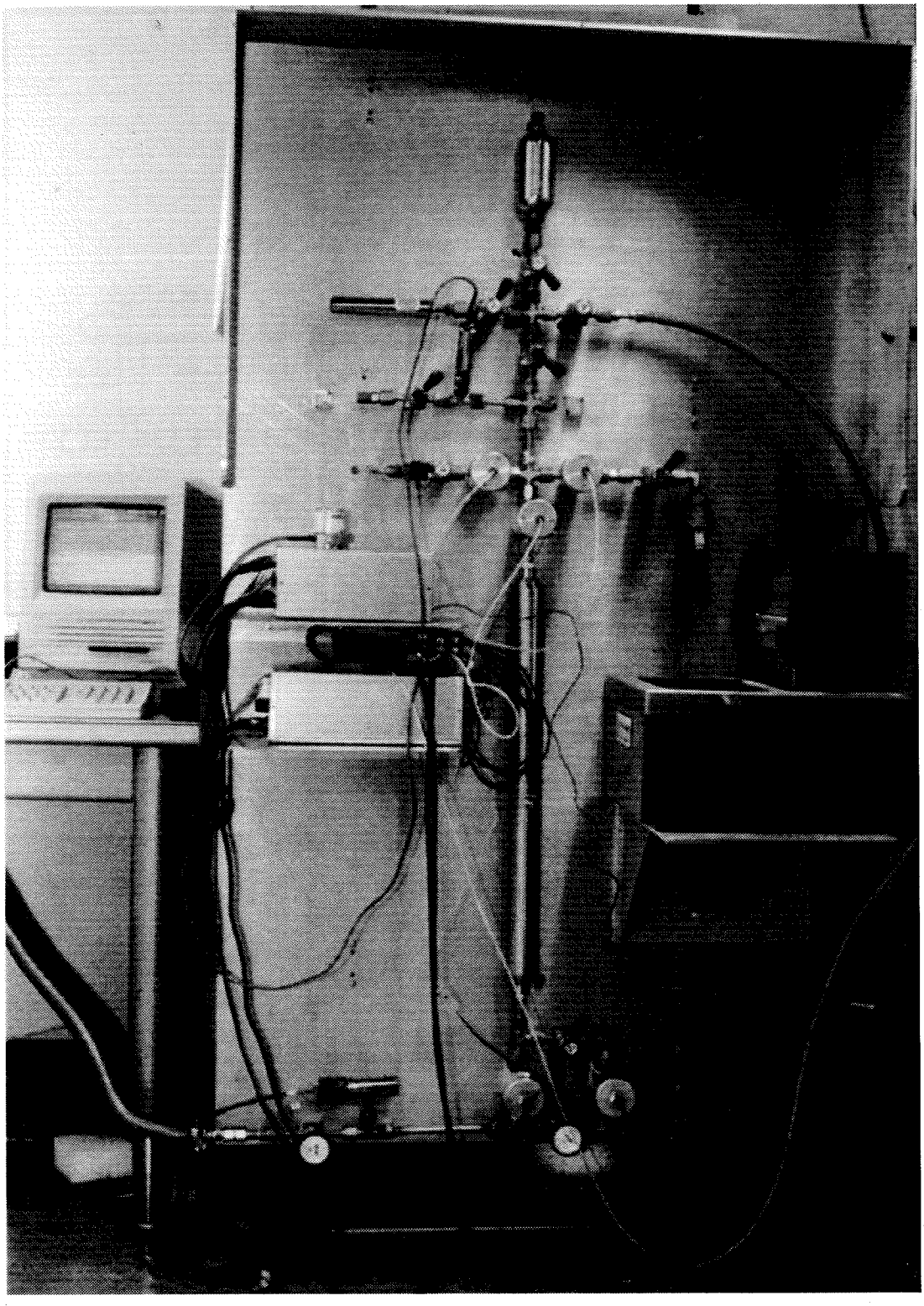

Figure III-1 Picture of Sievert's apparatus.

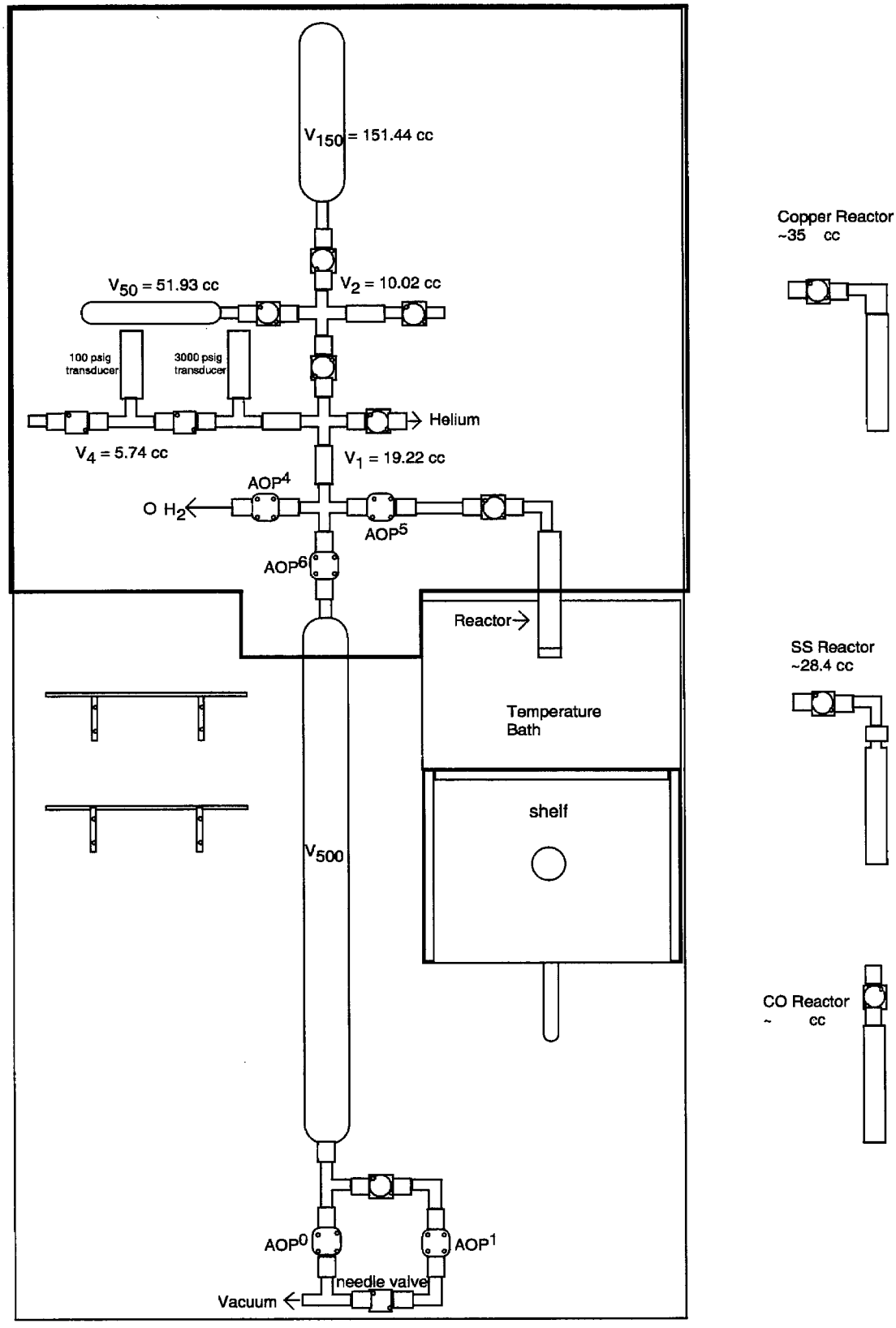

Figure III-2. Schematic of Caltech Sievert's apparatus.

51C. Pneumatic valves were actuated by small solenoid valves. Pressure measurements were made with SETRA pressure gauges. Isotherms could be measured at high pressures (up to 500 psia) at 0.1 psi accuracy or at low pressures (100 psig) at 0.01 psi accuracy. These gauges were calibrated by mounting a 600 psig manual Heise gauge on the system. Zero pressure was read by a Granville-Philips convectron gauge, giving a zero reading of $< 1 \times 10^{-4}$ torr. Reactor and room temperatures were monitored by K-type thermocouples from Omega. Isotherms at elevated temperatures were measured with the sample reactor immersed in water in a Polystat Model 1268-44 Circulator, accurate to ±0.5° C.

The manifold and reactor volumes were calibrated with high-purity argon or helium gas. V_{150} was initially calibrated at Aerojet Aerospace Corp. and was used as the reference volume in gas-expansion volume measurements. It was possible to vary the manifold volume by opening manual valves isolating calibrated volumes. The hydrogen used for measurements was Matheson ULSI hydrogen (99.9999%). It was connected to the Sievert's apparatus with electropolished SS tubing to a brass regulator. A Tribodyn oil-free shaft driven mechanical pump manufactured by Danielson was used to evacuate gas from the system. A hot air gun was used to heat the sample reactor to a maximum of 300° C for sample bake-out.

The analog readings from the pressure and temperature gauges were converted by a Strawberry Tree PCI board. This was interfaced to a Macintosh SE computer. The SE read and recorded the pressure data and operated the relay-solenoid-pneumatic-valve chain used to control the pressure of the hydrogen gas in the apparatus. The program used to operate and read the equipment was written in C.

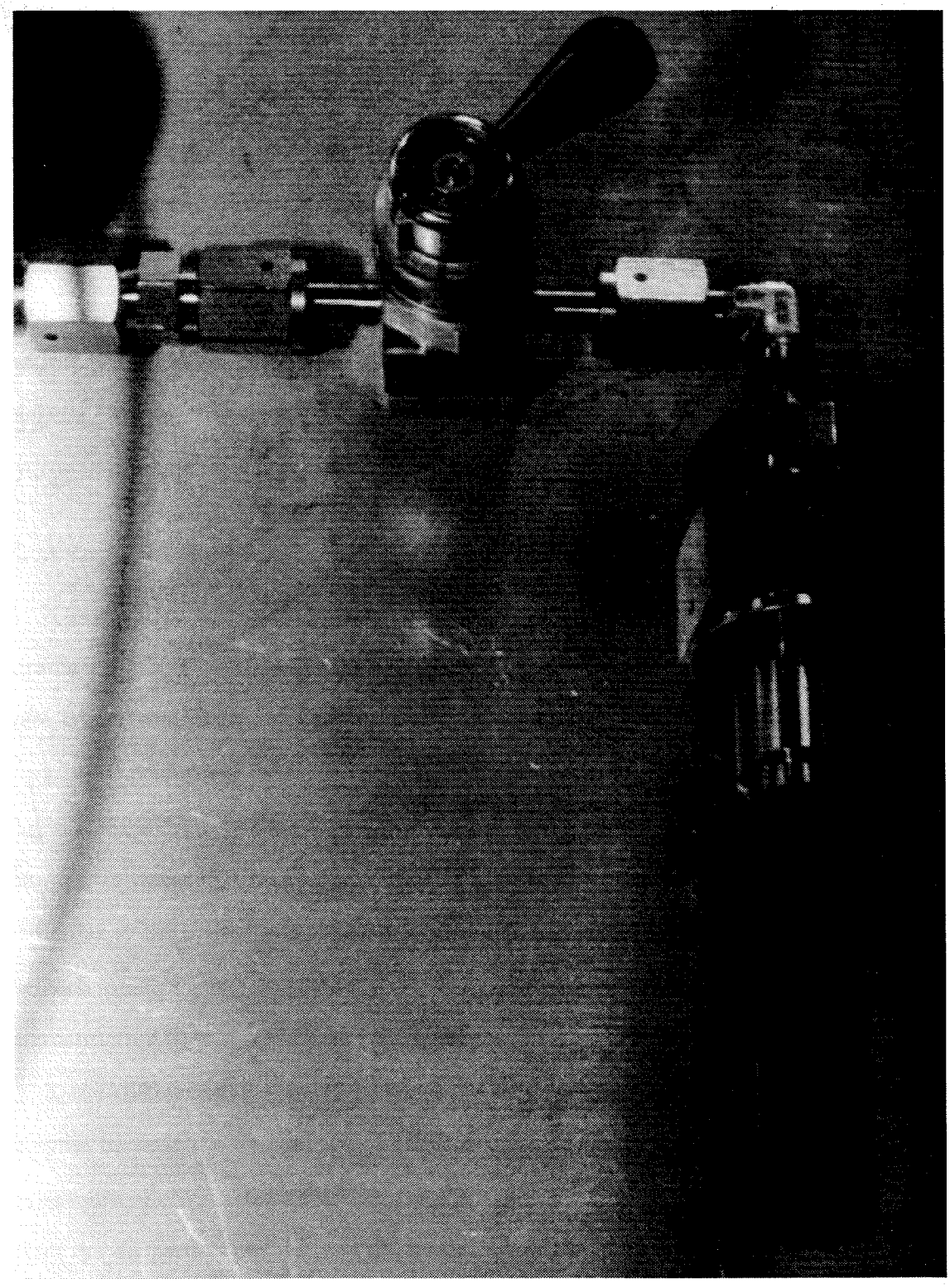

Figure III-3 Sample reaction chamber.

The sample reactor, shown in **Figure III-3**, was a double walled tube made of 1/16" copper pipe electron-beam welded to a 3/4" 316 stainless steel male Swagelok VCR flange. Several VCR porous metal filter gaskets with pore size 0.5 μm were used to prevent the sample from migrating into the system and contaminating the valves. Although the copper reactor has much better thermal conductivity than previous stainless steel sample reactors, the kinetics of hydrogen sorption in this system was dominated by thermal transport in the metal hydride particles and gas diffusion through the filter gaskets. When measuring isotherms, sufficient time (20-40 min) was allowed for the hydrogen pressure in contact with the sample to equilibrate before recording the pressure.

C. X-ray Diffraction

X-ray diffraction (*XRD*) was used to obtain information about alloy lattice parameters, phase composition, grain size, and retained lattice strain. Diffraction patterns were taken from activated samples and electrochemically cycled materials. Most of the work was performed with an Inel CPS-120 diffractometer using Co Kα radiation (λ_{α_1} = 1.788965Å). In the following section, I will discuss some of the physics that goes into the intrinsic diffraction profile. Then I will explain the characteristics that are particular to the diffractometer used in the work shown here. Finally, I will discuss the methods of data analysis I used to extract information about the sample structure and microstructure from the diffraction patterns.

X-ray diffraction is one of the most powerful techniques available to the materials scientist because the amount of information gained is relatively high when compared to the amount of effort put forth to analyze the material. However, many physical processes affect the diffraction pattern, and these must be taken into account when interpreting the resulting data.

An experimentally measured XRD pattern h(x) is considered to be the convolution of two components, the intrinsic diffraction profile f(x) and the instrumental factors g(x):

$$h(x) = f(x) \bullet g(x). \qquad [III.1]^{1}$$

1. Pure diffraction profile

When a monochromatic, unpolarized electric field is incident on a crystalline lattice, the scattered wave can be calculated as:

$$\psi\ (\Delta k) = \sum_{r_g}^{lattice} \exp(-i\ 2\pi\Delta k \bullet r_g) \sum_{r_k}^{basis} g_{atom}(r_k) f_{atom}(r_k) \exp(-i\ 2\pi\Delta k \bullet r_k), \qquad [III.2]^{2}$$

This is the diffraction equation, and can be separated into a structure factor:

$$F\ (\Delta k) = \sum_{r_k}^{basis} g_{atom}(r_k) f_{atom}(r_k) \exp(-i\ 2\pi\Delta k \bullet r_k), \qquad [III.3]^{2}$$

and a shape factor:

$$S\ (\Delta k) = \sum_{r_g}^{lattice} \exp(-i\ 2\pi\Delta k \bullet (r_g - s)) \ . \qquad [III.4]^{2}$$

Δk = diffraction vector (hkl).

r_k = unit cell basis vector ($x_{atom} y_{atom} z_{atom}$).

g_{atom} = occupancy of unit cell site at r_k.

f_{atom} = atomic scattering factor of atom at r_k.

r_g covers all unit cell positions in the defect-free crystal.

s = deviation, or defect, vector.

In XRD, the structure factor controls the magnitude and peak positions of the diffracted intensity, while the shape factor describes the distribution of the diffracted intensity in k-space.

a. Structure

Information about the atomic structure of a crystalline sample can be extracted from the positions and intensities of a set of diffraction peaks. The wavelength of the radiation used and the unit cell basis vectors determine the locations of the diffracted intensity. From the locations, θ, of the peaks, the spacing of the diffraction grating generating these peaks can be calculated using Bragg's Law:

$$\lambda / 2 = d_{hkl} * \sin(\theta), \qquad \text{[III.5]}$$

where λ = x-ray wavelength and d_{hkl} = crystalline lattice spacing. In a hexagonal lattice, the lattice spacing for a particular set of planes (hkl) is calculated from the unit cell parameters as:

$$d_{hkl}^{\ 2} = (h^2 + h*k*\sqrt{3}/2 + k^2)\, a^2 + c^2. \qquad \text{[III.6]}$$

When the intensities of the scattered wave are measured by an X-ray diffractometer, a variety of geometric factors must be included to calculate the measured intensity of the scattered wave: [3]

$$I_{hkl} = S * |F_{hkl}|^2 * T * LP * J * P \qquad \text{[III.7]}$$

S = scaling factor (incident beam intensity, time length of pattern, etc.)

F_{hkl} = structure factor

g_n = lattice site occupation factor

f_n = atomic scattering factor

T = temperature factor $= \exp(-B/\sin\theta/\lambda)$

LP = Lorentz-polarization factor $= \dfrac{1 + \cos^2(2\theta)\cos(2\theta_m)}{\sin^2\theta\cos\theta}$

J = multiplicity of crystal plane

P = Preferred orientation (factor)

The atomic scattering factor, temperature factor and the Lorentz-polarization factor all induce asymmetries in the resulting peak profiles.

i. Lattice parameter extrapolation

The effect of errors in the diffraction peak position on the calculated lattice parameter can be determined by taking the derivative of [III.5]:

$$-d_{hkl} * \cos(\theta) * \Delta\theta = \Delta d_{hkl} * \sin(\theta)$$

$$-\cot(\theta) * \Delta\theta = \Delta d_{hkl} / d_{hkl}. \qquad [III.8]$$

So, $\lim_{\theta \to \pi/2} \Delta d_{hkl} = 0$. In a well-aligned asymmetric diffractometer, the largest error in 2θ position results from sample displacement and transparency (see § III.C.2.e), $\Delta 2\theta = s * \sin(2\theta)$, so [III.8] becomes:

$$-\cot(\theta) * 2s \sin(\theta)\cos(\theta) = -2s \cos^2(\theta) = \Delta a_{hkl}/a_{hkl}. \qquad [III.9]$$

by extrapolating values of d_{hkl} *vs* $\cos^2(\theta)$, we should obtain a line whose intercept with $\cos^2(\theta) = 0$ is the lattice parameter a_{hkl}.

b. Microstructure

> The kinematic theory of x-ray scattering shows that particle size and lattice distortion are diffraction order independent and dependent, respectively, enabling the separation of the two effects...
>
> T. Ungár, A Borbély, *Appl. Phys. Lett.*, **69** (21) (1996): 3173.

I open the section on microstructure with this optimistic statement because that is the approach that I took when I began the analysis of the XRD patterns included here. Unfortunately, I had neither the experience nor equipment with enough precision necessary to analyze the MH samples tested here to this extent. I did accomplish some crystallite size/microstrain analysis, so I will include the formalism here.

The formalism of diffraction broadening resulting from crystallite size and microstrain is easily seen through manipulation of Bragg's law. Taking the derivative of [III.5],

$$0 = \Delta d \sin\theta - d\cos\theta .$$

$$\frac{\Delta d}{d} = \Delta\theta \cot\theta \qquad \text{[III.10]}$$

and

$$\frac{\Delta d}{d^2} = \frac{\Delta\theta\cos\theta}{d\sin\theta} = \frac{\cos\theta}{\frac{\lambda}{2}} = \frac{\Delta 2\theta\cos\theta}{\lambda} \qquad \text{[III.11]}$$

In this case, Δ stands for the breadth of a parameter, not the deviation from its true value, as in [III.8]. Strain broadening can be directly related through $\Delta d/d$, while size broadening must involve the shape function of the diffraction equation, eq III.4.

i. Crystallite Size

Scherrer first pointed out that as crystallite size decreased below about 1μm, the integral breadth (β) of the diffraction profile would increase according to

$$\beta_{2\theta} = \frac{\lambda}{\tau\cos\theta} . \qquad \text{[III.12]}$$

where τ is the apparent X-ray crystallite size.[4]

ii. Microstrain

There are many methods to measure crystallite size and strain in polycrystalline materials by X-ray and neutron powder diffractometry. The first measurements of strain by XRD peak broadening were performed by Scherrer [4] and Warren.[5] The understanding of lattice strain and size broadening effects were later simplified and expanded by Williamson and Hall.[6]

It is now routine to determine lattice strain by Rietveld refinement of diffraction patterns. The most important step in determining strain from powder diffraction patterns is to create a physical model by which lattice strain can be connected to diffraction peak broadening. Small crystallite size broadens diffraction peaks by reducing the size of the coherent domain that scatters X-rays. The effect of crystallite size on diffraction patterns can be seen in **equation [III.8]**. The extent of this microstructural damage can be measured with XRD by plotting the peak broadening in k-space (dΔk) of diffraction peaks *vs* the diffraction vector Δk.

Microstrain also broadens the specimen profile according to

$$\beta = k\varepsilon \tan\theta \qquad \text{[III.13]}$$

where ε represents the microstrain and k is a constant whose value depends on the definition of microstrain used.

2. Inel CPS-120 Instrument Broadening Effects

Several characteristics inherent to the Inel diffractometer, shown in **Figure III-4**, make acquisition and analysis of its diffraction patterns different from those of patterns recorded with a conventional Bragg-Brentano diffractometer. Some of the differences that will be addressed here include: the effects of absorption by the sample, sample displacement, and the lack of a focusing or even a parafocusing geometry.

a. Background for Curved Position Sensitive detectors

To date, many attempts have been reported to build cylindrical or curved position-sensitive gaseous detectors for X-ray crystallography.[7-12] Of these, Ballon, *et al.*[11] were the first to employ a thin metal blade as anode, which has the advantage of being rigid and relatively easy to construct. Their detector, of 20 cm radius of curvature 60° angular opening, works in 'self-quenching streamer' mode in place of the normal proportional

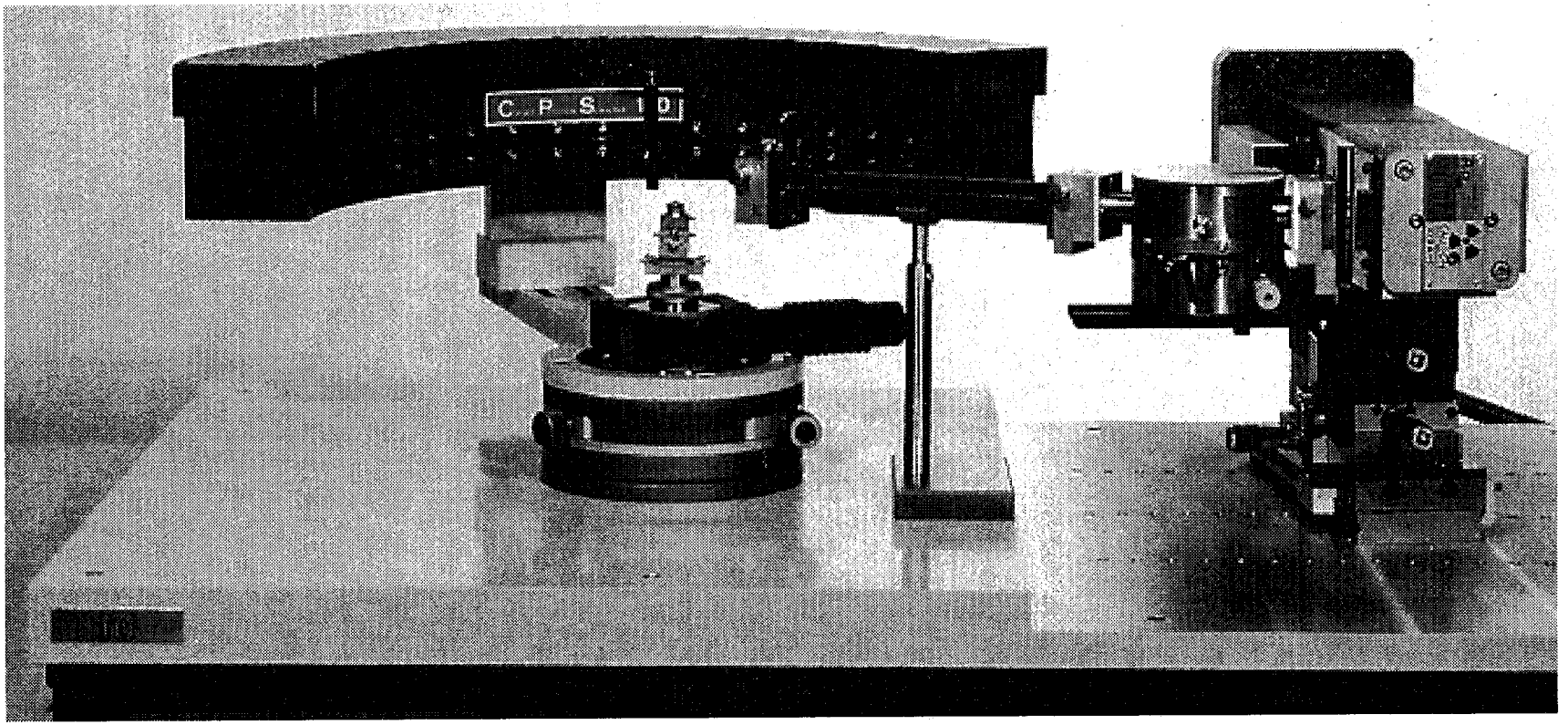

Figure III-4 Picture of Inel diffractometer.

mode as in other examples.[13,14] A good signal-to-noise ratio obtainable in this mode of gas ionization has provided a high angular resolution of some hundredths of a degree.[15]

b. Speed of acquisition

The gas-filled proportional counter used to detect diffracted photons allows data to be collected simultaneously over 120 degrees 2θ.[11] This means that diffraction patterns can be acquired in a fraction of the time necessary with traditional θ-2θ diffractometers. This is particularly useful for ascertaining what phases are present in a sample and qualitatively examining variations in microstructure within a set of similar samples. In addition, the Inel is rather versatile. Changing sample configuration is elementary, and changing source radiation only slightly more complicated. However, the Inel also introduces several uncertainties and instrument effects that make quantitative analysis of XRD patterns quite difficult.

c. 2θ calibration

The detector has 4096 electrical bins or *channels* within its ~120° 2θ range. This gives it an approximately constant step size of 0.032 °2θ/channel. Unfortunately, the spacing of the channels on the detector knife edge is not constant, and varies from detector to detector. This means there is some deviation from linearity in the 2θ calibration. To determine this deviation, I used a LaB_6 standard, NIST SRM 660, to calibrate the 2θ range. An example of the LaB_6 raw data is shown in **Figure III-5**.

The first step in the 2θ calibration is to fit the diffraction peaks to gaussian profiles *vs* channel number. The LaB_6 peak positions in 2θ angle as determined by Bragg's law with $\lambda \frac{Co}{K_\alpha}$ = 1.79026 Å are then fit *vs* peak position in channel to a sixth order polynomial. This was used as an initial 2θ calibration and Rietveld refinement was performed. Once the instrument function (including X-ray incident angle and monochromator setting $\frac{K_{\alpha 2}}{K_{\alpha 1}}$, discussed in § III.C.2.d.i and § III.C.2.f) and sample microstructure were determined, an XRD pattern was calculated using these parameters. The peaks in this calculated pattern

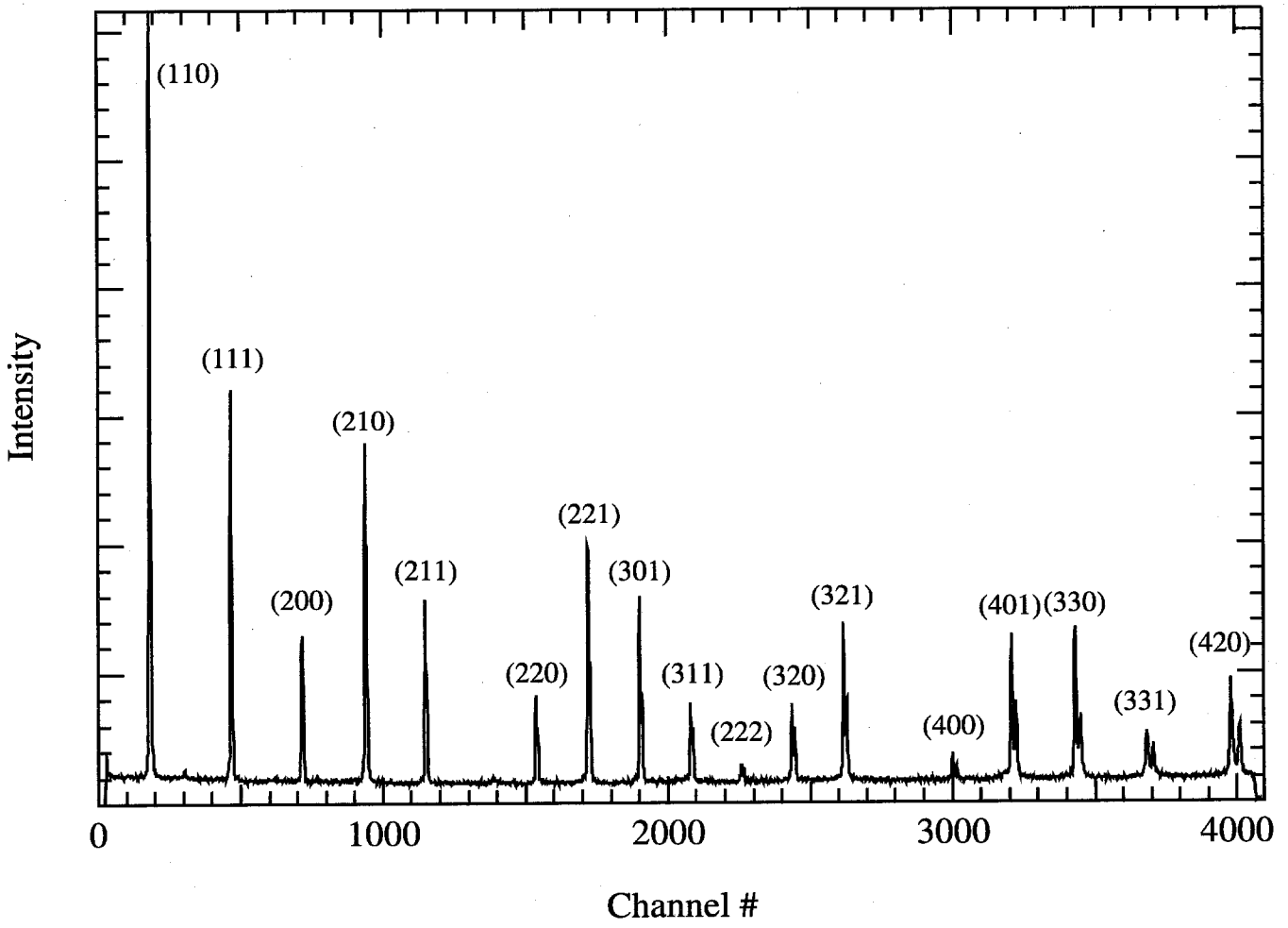

Figure III-5 XRD pattern of LaB_6.

were fit to gaussian profiles to determine their experimental peak positions in 2θ angle. These peak positions were plotted *vs* the previously obtained positions in channel, and a final 2θ calibration curve was determined. This process was repeated if the diffractometer alignment was changed. This procedure was a bit lengthy, and was automated by code written in the programming environment of the Mac application Igor v. 3.13. I should stress that this only need be followed for the extraction of quantitative results from the XRD patterns.

Figure III-6a shows the deviation from linearity of the 2θ values of the Inel used in this work, and **Figure III-6b** shows a published example of Inel detector non-linearity.[16] The 2θ scaling wave is approximated well by the sixth order polynomial:

$$2\theta = 0.52 - 1.1 \times 10^{-6}x^2 + 6.8 \times 10^{-10}x^3 - 1.5 \times 10^{-13}x^4 + 1.1 \times 10^{-17}x^5, \qquad [III.14]$$

but a higher order polynomial was often used. This shape is preserved when the 2θ range of the detector is changed.

d. 2θ geometry

i. absorption correction

The sample goniometer of the Inel is in a 2θ geometry. As seen in **Figure III-7**, the angle of incidence, α, is fixed, while the direction of the diffracted beam, 2θ, is variable. One effect of this is that the path length of radiation through the sample, absorption of the radiation, and hence the intensity of the diffracted beam, has a functional relationship on the incident angle of the source radiation and on the direction of the diffracted beam.

Figure III-8 shows the radiation path for a beam diffracted at angle 2θ. The volume irradiated in an element of thickness dz at a depth z is $\Delta V = (A/\sin\alpha)*dz$, where A is the area of the incident beam. Absorption along the path length $z/\sin\alpha$ reduces the incident intensity at z to $I_0\exp(-\mu z/\sin\alpha)$, where μ = sample absorbance. The diffracted beam path length is $z/\sin(2\theta-\alpha)$, so the diffracted beam intensity is further attenuated by the factor $\exp(-\mu z/\sin(2\theta-\alpha))$. If b denotes the fraction of the incident beam that is diffracted, the

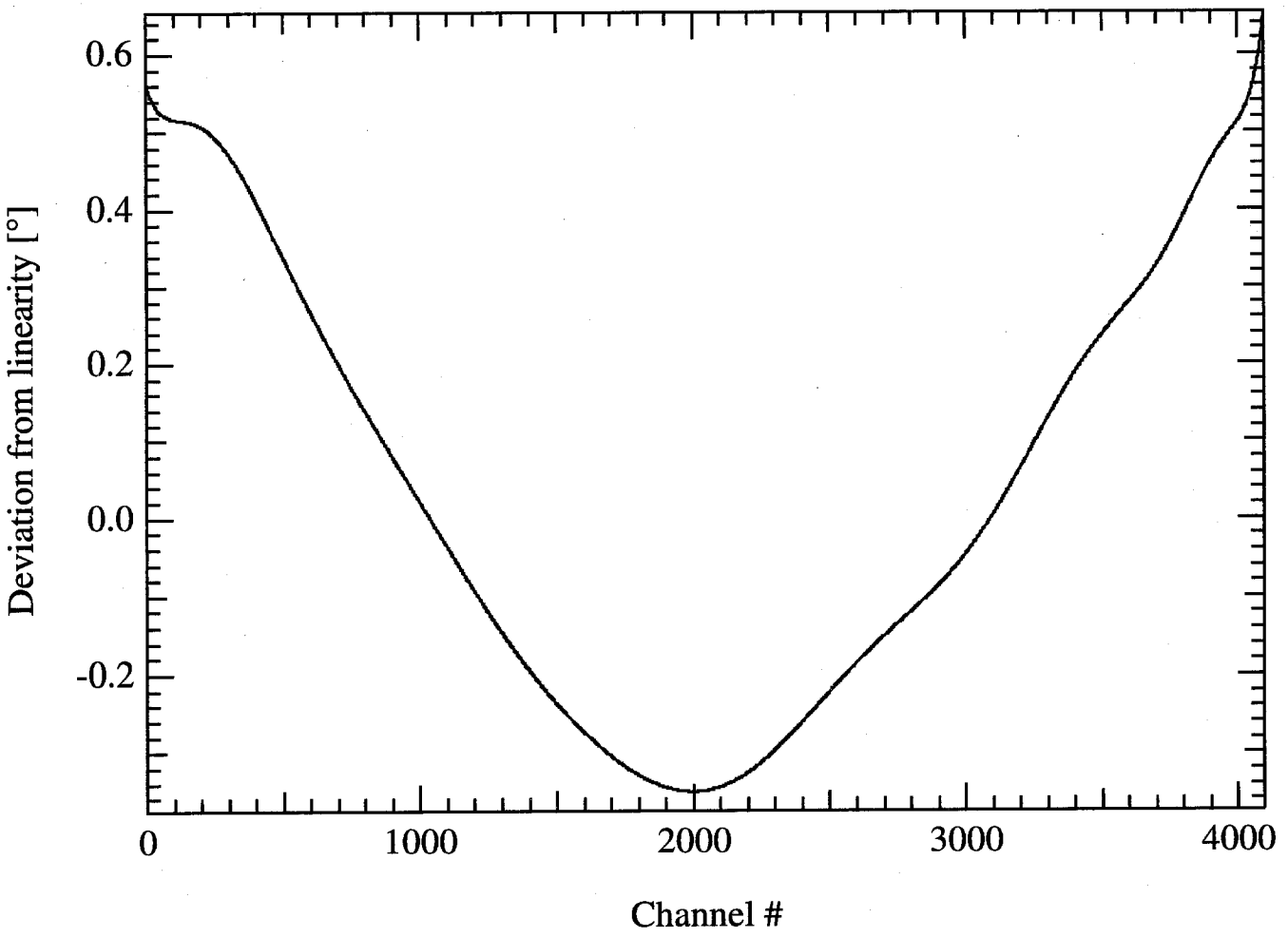

Figure III-6a Non-linearity of channel spacing for Caltech Inel detector.

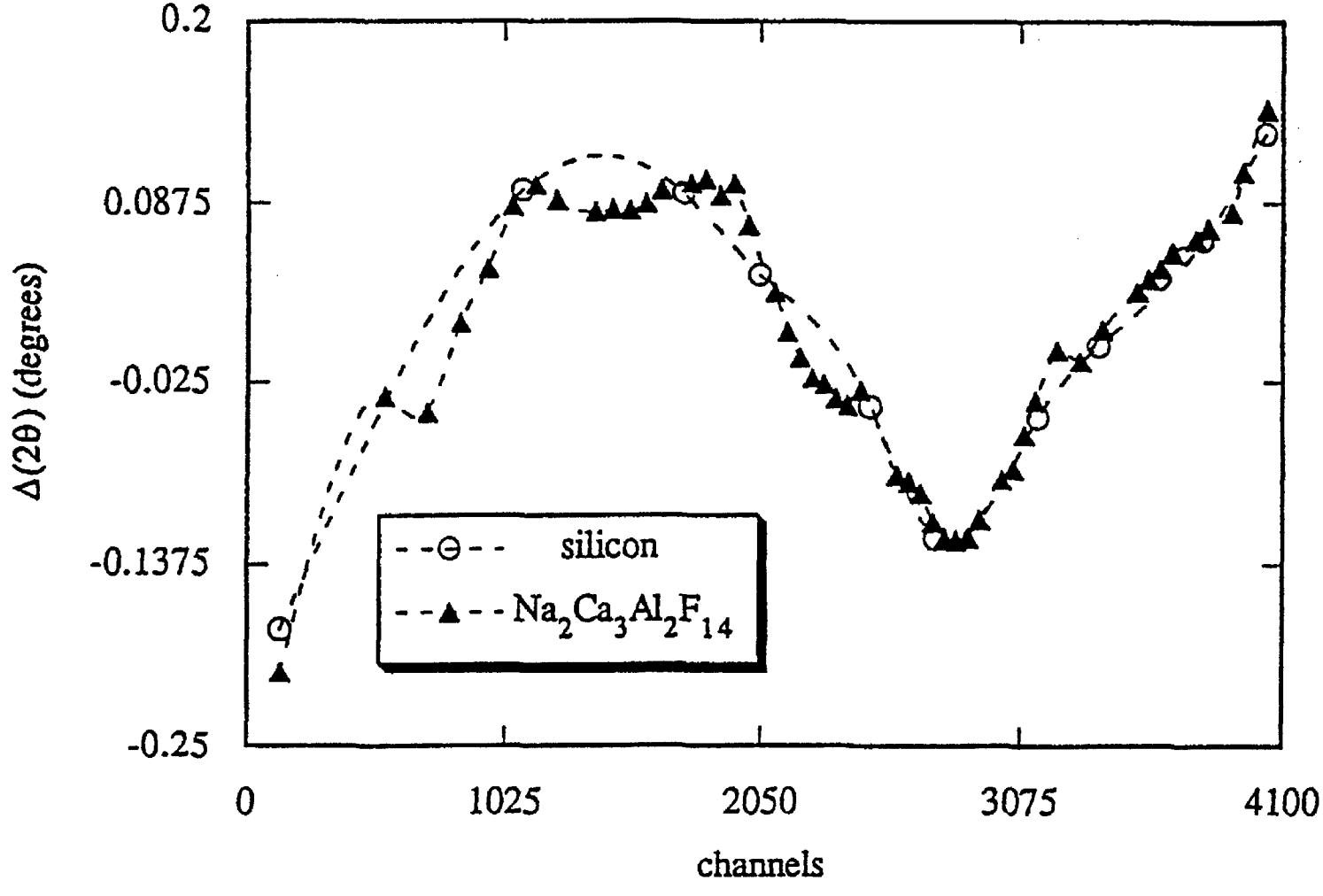

Figure III-6b Published Inel channel spacing non-linearity. (reprinted from M. Evain, P. Deniard, A. Jouanneaux, and R. Brec, *J. Appl. Cryst.*, **26** (1993): 563.)

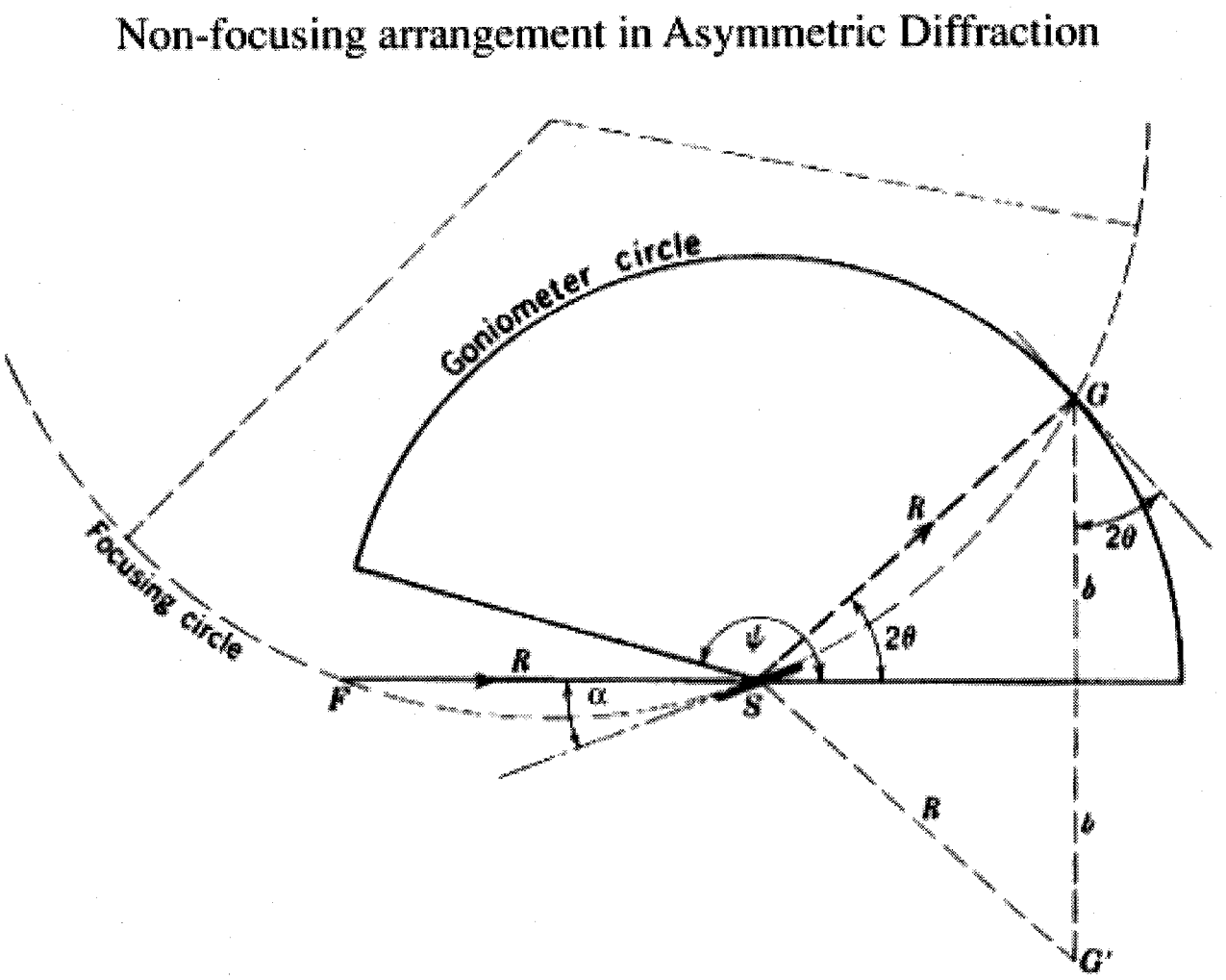

Figure III-7 Diffractometer 2θ geometry, fixed α.

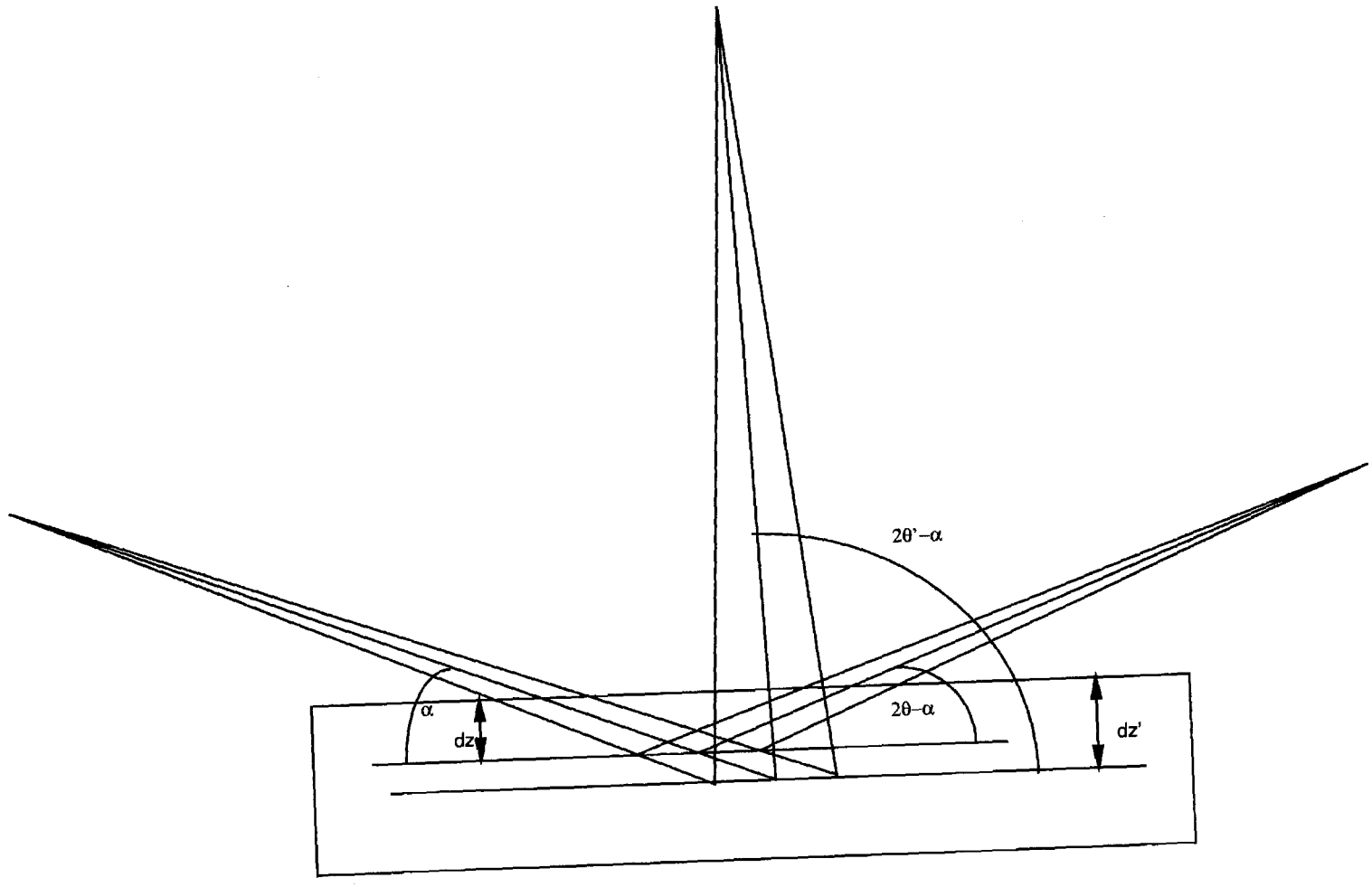

Figure III-8 Radiation path in sample for 2θ geometry.

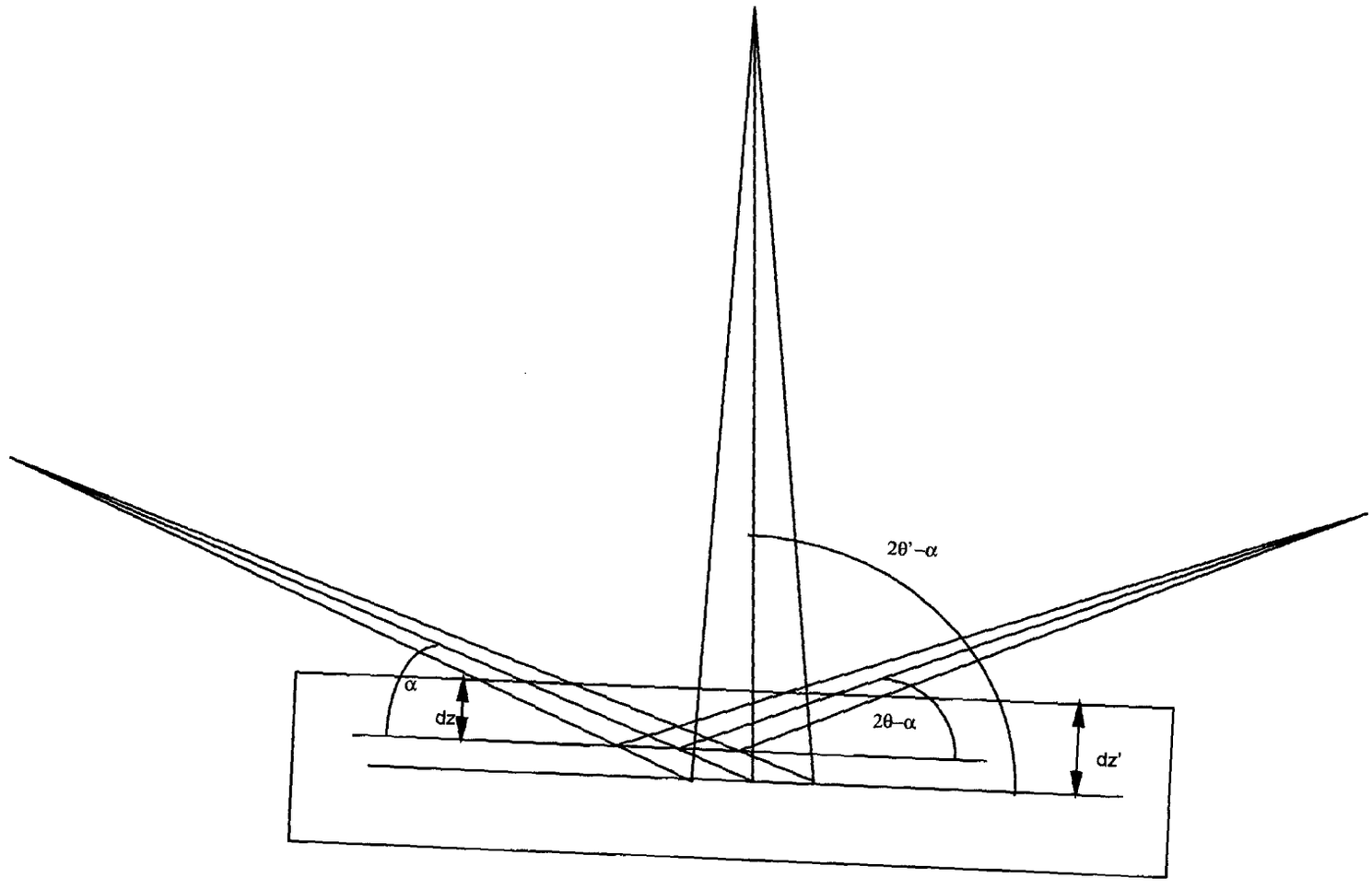

Figure III-8 Radiation path in sample for 2θ geometry.

intensity of the radiation diffracted from volume element ΔV at a depth z at the diffraction angle 2θ is then:

$$I_D = bI_0 \exp\left(\frac{-\mu z}{\sin\alpha}\right)\exp\left(\frac{-\mu z}{\sin(2\theta-\alpha)}\right)dz. \qquad \text{[III.15]}$$

If the sample thickness is much larger than the X-ray extinction length, we can let $t \rightarrow \infty$. The effect of sample absorbance can be found by integrating the diffracted intensity from $z = 0 \rightarrow \infty$:

$$I_D = I_0 b \int_0^{\infty} \frac{A}{\sin\alpha}\exp\left[-\mu z\left(\frac{1}{\sin\alpha}+\frac{1}{\sin(2\theta-\alpha)}\right)\right]dz\ , \qquad \text{[III.17]}$$

$$I_D = \frac{I_0 A b}{\mu}\left(\frac{\sin(2\theta-\alpha)}{\sin\alpha+\sin(2\theta-\alpha)}\right). \qquad \text{[III.18]}$$

The effect of absorption in the 2θ sample geometry can be seen by plotting the absorption correction factor

$$A(\theta,\alpha) = \left(\frac{\sin(2\theta-\alpha)}{\sin\alpha+\sin(2\theta-\alpha)}\right) \qquad \text{[III.19]}$$

vs 2θ. **Figure III-9** displays the absorption correction factors for several glancing angles.

ii. peak broadening from reflection asymmetric geometry with flat-plate sample

Because α, the angle of incidence, does not change (~15°), the diffractometer is not in a parafocusing geometry. Instead, the geometry is what is known as *reflection asymmetric*. As shown in **Figure III-10**, radiation that is diffracted at angles less than α is focused in front of the detector and that diffracted at greater angles is focused behind the detector. This adds an additional instrumental peak broadening function, shown in **Figure III-11** in the parafocusing approximation, to be convoluted with the sample intrinsic diffraction profile. There are no Rietveld refinement codes that include this type of instrument effect, and I did not attempt to change any code to offer this capability.

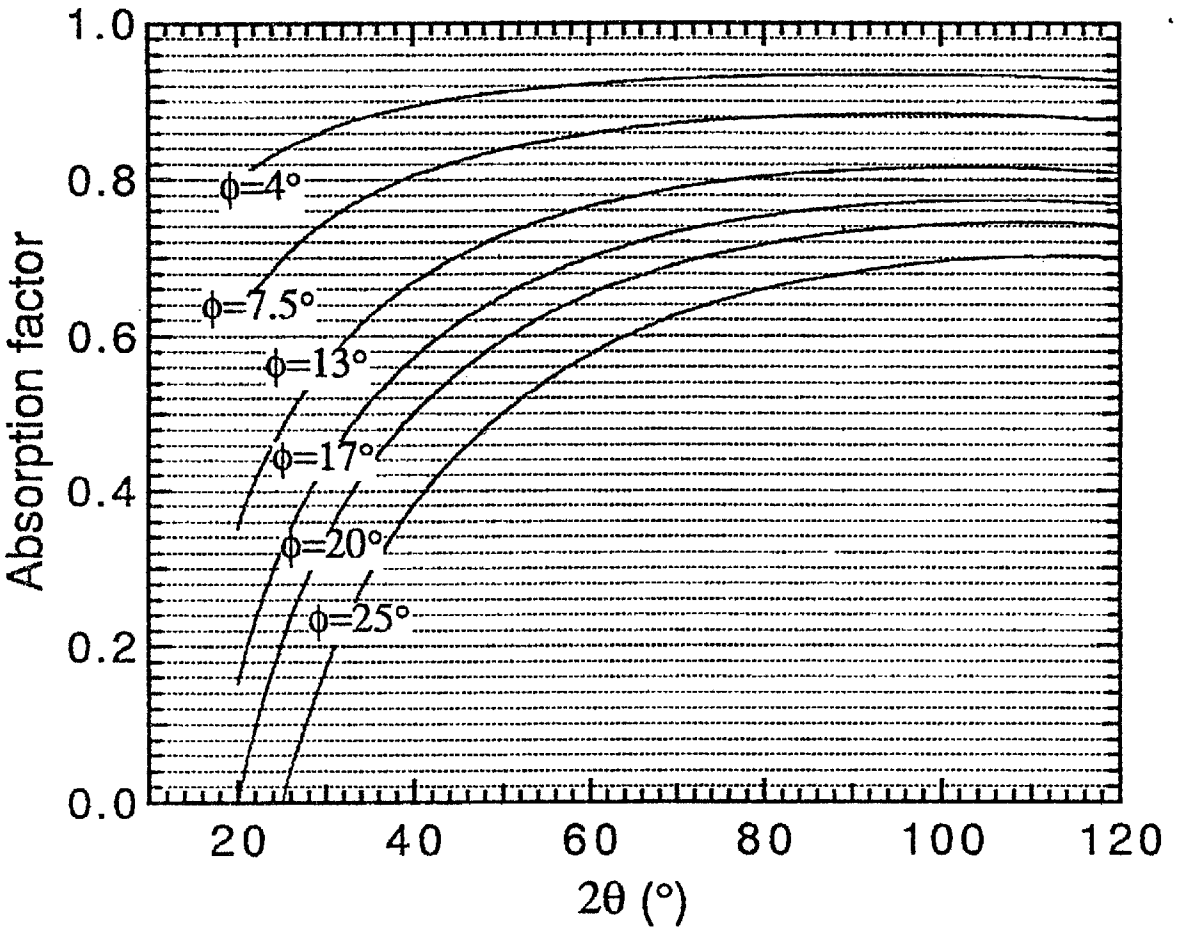

Figure III-9 Absorption correction in 2θ geometry for several incident angles. (reprinted from Z.-Q. Gao, The Kinetics of Ordering, Grain Growth, and Chemical Segregation in Nonequilibrium Fe_3X alloys (X = Al, Si, and Ge). Caltech Thesis UM#94-31,832.)

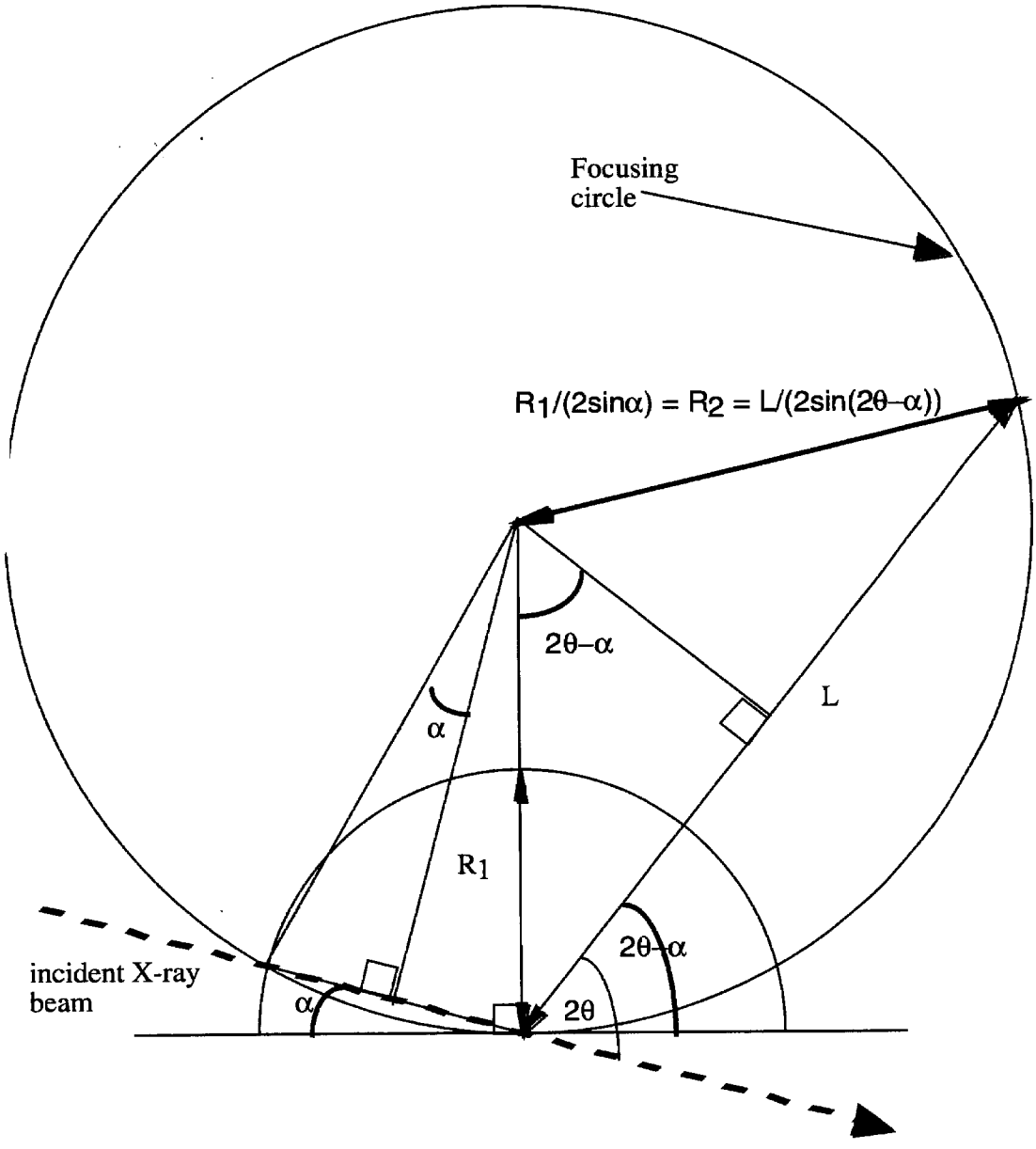

Figure III-10 Focusing circle of 2θ diffractometer.

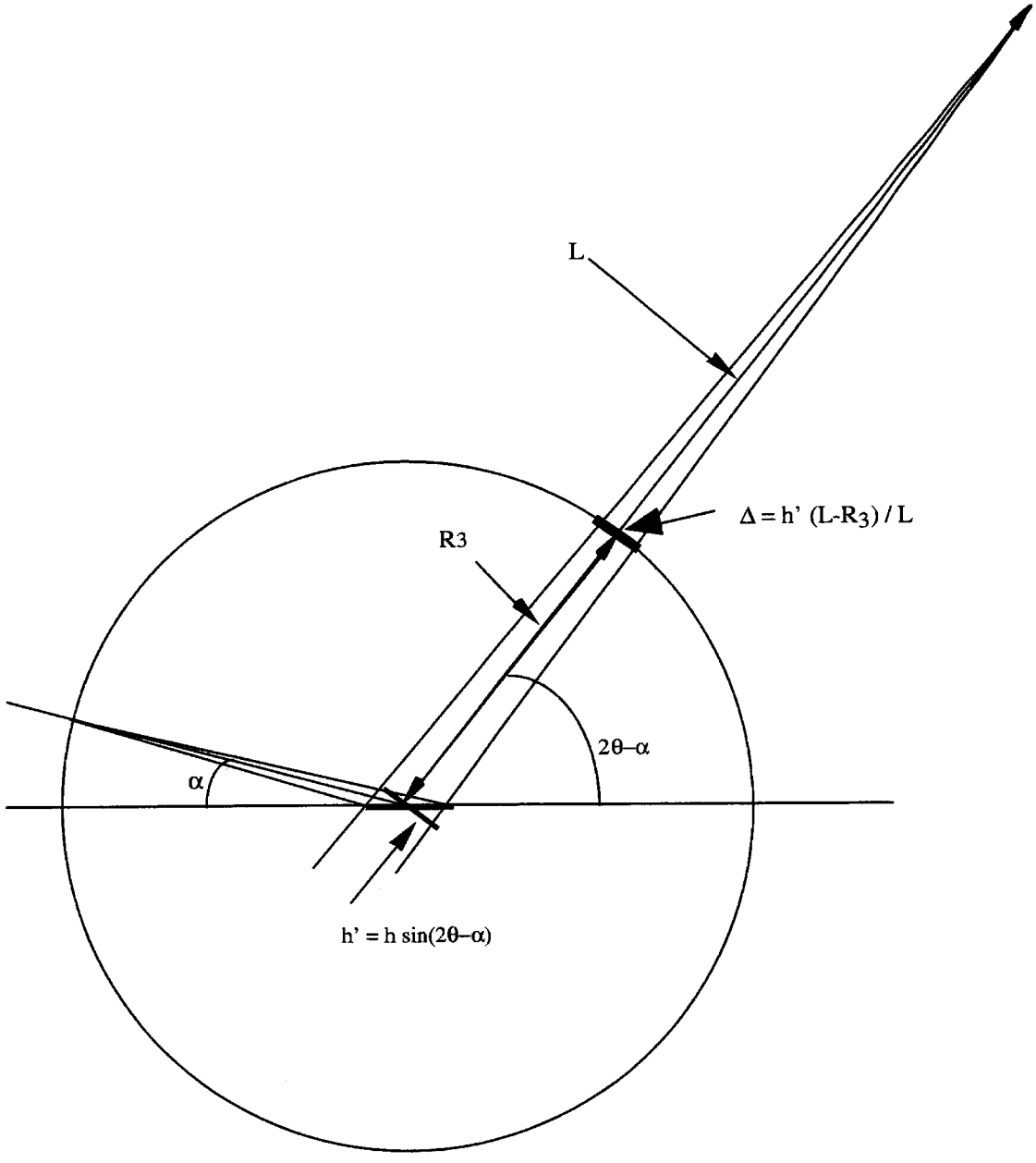

Figure III-11 Peak broadening of 2θ diffractometer.

However, it is reasonable to assume that this effect can be taken care of by its inclusion in the instrumental broadening function.

e. flat-plate Bragg-Brentano sample orientation.

The flat plate approximation to the Bragg-Brentano orientation was chosen as the best sample configuration for this work. There are several outcomes of this arrangement that will change the positions and shapes of the diffracted lines. Sample transparency and displacement from the goniometer center will both increase the path length of the incident radiation before diffraction, resulting in a 2θ offset of the diffraction peaks that is proportional to $\sin(2\theta)$, as can be seen in **Figure III-12.** Axial divergence contributes to an asymmetric broadening of the diffraction peaks that will have a small effect on the position of the diffraction peak. The first effect is easily treated in Rietveld refinements by refinement of a sample displacement parameter. Axial divergence is related to the vertical divergence of the incident and diffracted beams, and is best treated by a first principles approach. Larry W. Finger, *et al.* have developed an analytical approximation to the convolution of the axial divergence with a diffraction profile which is available in some Rietveld refinement codes.[17]

f. monochromator

In this section I will discuss the horizontal and spectral divergence of the incident beam. The incident beam monochromator on the Inel is pyrolytic graphite, which has a mosaic spread of ~0.5°. This is useful for separating the K_α radiation from the Bremstrahlung and K_β energies, but the K_{α_1} radiation cannot be separated from the K_{α_2} radiation. This results in a horizontal divergence of the radiation. This addition to the peak broadening is included in the instrument function. The $K_{\alpha_2}/K_{\alpha_1}$ intensity ratio is dependant upon the monochromator setting, and is not necessarily equivalent to the theoretical value. This value was refined from the LaB_6 calibration pattern and the refined value was fixed in subsequent data refinement.

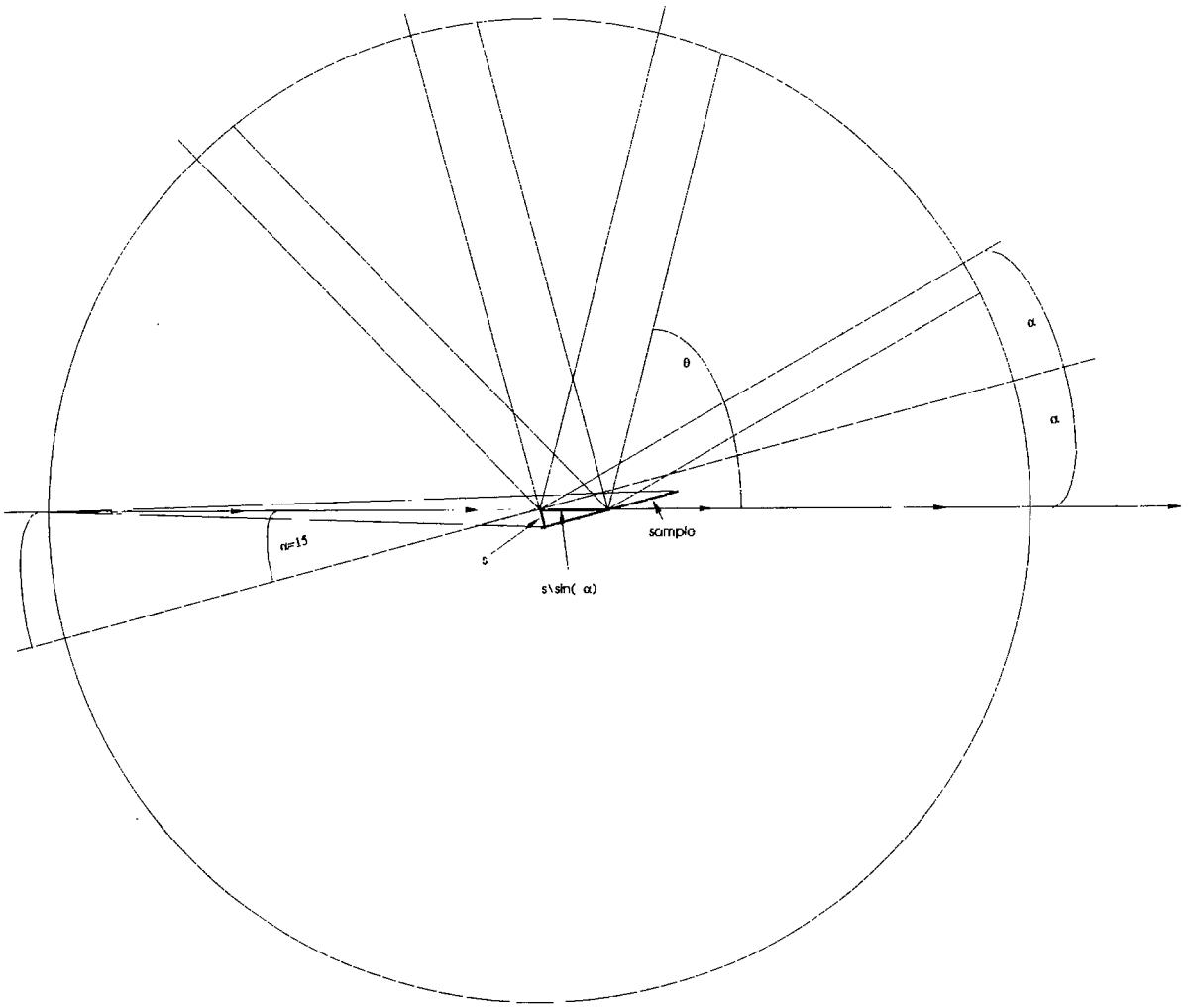

Figure III-12 Peak position errors from sample displacement and transparency for 2θ diffractometer.

3. CO Poisoning

An important property of the alloys studied here is the volume expansion upon hydrogen absorption. Unfortunately, equipment that would allow measurement of XRD patterns at high hydrogen pressures was not available. To measure the volume expansion, the method of Johnson and Reilly [19] was used to "poison" the surface layers of hydrided alloys with CO. This creates a lanthanum carbonate film on the powder surface, allowing the alloys to retain their hydrogen composition when exposed to air. After the poisoning treatment, the alloys lost hydrogen slowly so that diffraction patterns could be recorded at various hydrogen compositions.

Poisoning the alloys was performed by first activating them by hydrogen absorption, then desorbing hydrogen from the samples to specific compositions. The sample chamber was then removed from the Sievert's and relocated to the poisoning stand, shown in **Figure III-13**. There it was immersed in liquid nitrogen. While the sample cooled, the dead space of the poisoning apparatus was back-filled and purged with CO at ~5 atm. After sufficient cooling, the sample was exposed to the 300cc volume filled with CO at 5 atm. The sample chamber was closed when the CO was done condensing, decreasing the effective volume by a factor of 10. The l-N_2 was allowed to boil off, slowly bringing the sample back to room temperature. When the sample had reached room temperature, the pressure of CO in the chamber was 40-45 atm.

When the sample had achieved room temperature, XRD patterns were taken. The samples lost hydrogen gradually, and many quick diffraction patterns were initially taken after air exposure to ensure that hydrogen was not being lost during measurement. This would have the effect of changing the position of the diffraction peak during measurement, making it broader than the sample intrinsic profile.

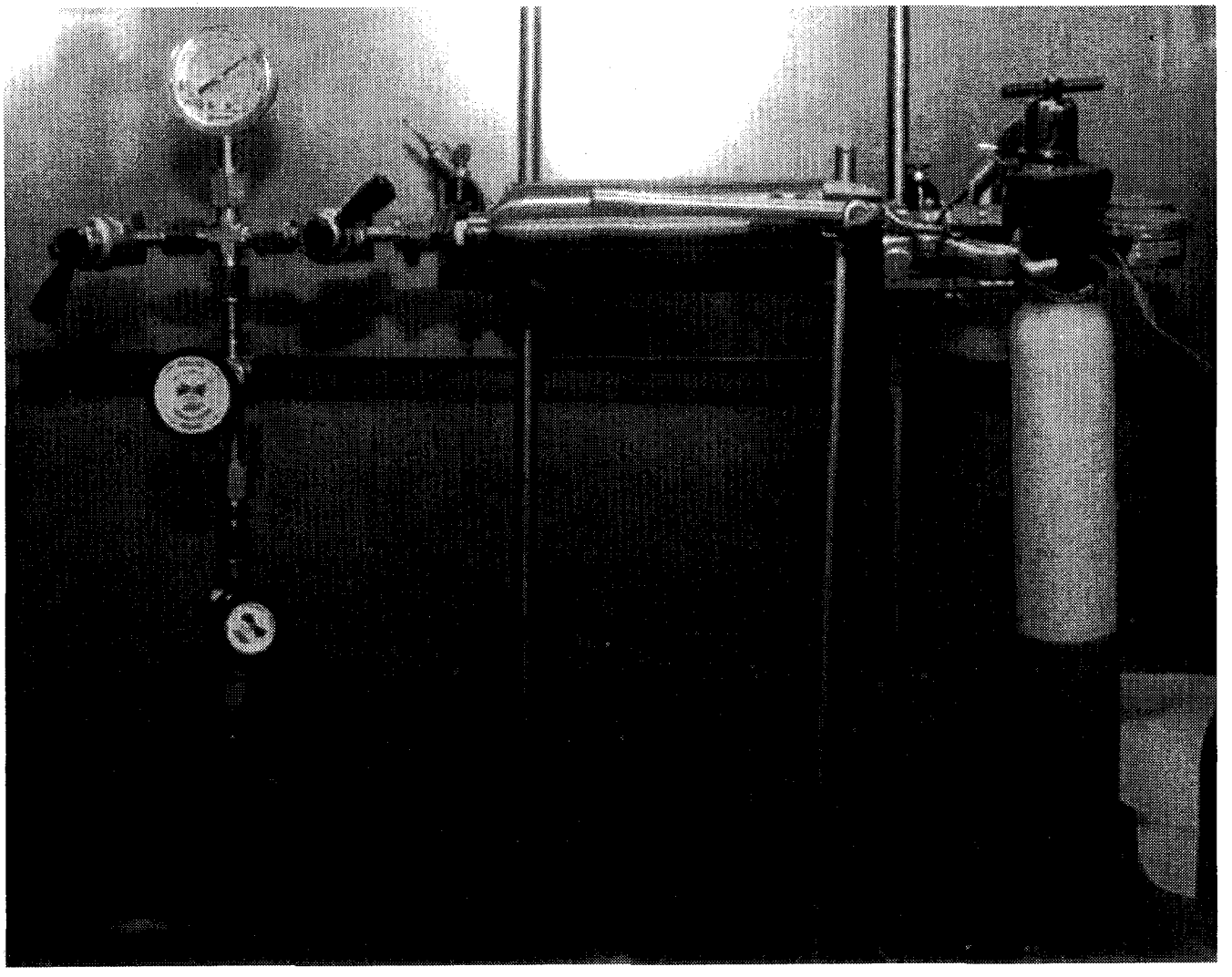

Figure III-13 CO poisoning stand.

4. Data Analysis

Most of the data were analyzed by hand, by fitting the diffraction peaks to gaussians to determine their peak positions, half-widths, and intensities. Lattice parameters were obtained by performing a extrapolating *vs* $\cos^2(\theta)$. The uncertainties mentioned above prevent quantitative phase analyses from being performed, but peak intensities could be extracted to determine the growth of the hydride or other phases.

The program Rietan [18] was used to determine the lattice parameters of hydrided samples. The variation in hydrogen composition in the sample prevented other microstructural information from being extracted, but I have confidence in the lattice parameters obtained.

The Macintosh application "Igor" was used to fit the diffraction peaks to Voigt functions and to perform subsequent analyses on peak positions and shapes. The native Igor peak-fitting procedure was extensively modified and linked with compiled c-code to facilitate the fitting of XRD patterns. Lattice parameters were determined by the standard extrapolation technique of plotting d_{hkl} *vs* $\cos^2\theta_{hkl}$. Lattice parameters were determined to be the y-intercept of a linear fit to these data.

Because $LaNi_5$-based alloys have a hexagonal lattice, an iterative procedure was used to determine the lattice parameters: First, (hk0) peaks were used to calculate the a-lattice parameter. This value was then used with (hkl) peaks to calculate the c-lattice parameter. When the c-parameter was then used to calculate the a-parameter, it was found that the original estimate was over- or under-estimated. The new a-parameter was used to correct the original estimate, and a new c-parameter calculated. This continued for several iterations and the final lattice parameter was determined by fitting successive estimates to an exponential decay. These final lattice parameters were used to calculate their complement to insure consistency.

H.P. Klug and L.E. Alexander, X-Ray Diffraction Procedures, (John Wiley & Sons, New York; 1974) p. 618.

[2] B. Fultz and J. Howe, Transmission Electron Microscopy and Diffractometry of Materials, (in preparation).

[3] The Rietveld Method, ed. R.A. Young, (Oxford University Press, New York: 1995).

[4] P. Scherrer, *Nachr. Ges. Wiss. Göttingen*, 26 September (1918): 98; Zsigmondy Kolloidchemie, 3rd edn., (1920) p. 387.

[5] B.L. Averbach and B.E. Warren, *J. Appl. Phys.*, **20** (1949): 1060.

[6] G.K. Williamson and W.H. Hall, *Acta Metall.*, **1** (1953): 22.

[7] S.K. Byram, B. Han, G.B. Rothbart, R.N. Samdahl, and R.A. Sparks, *Advances in X-ray Analysis*, **20** (1977): 529.

[8] D. Ortendahl, V. Perez-Mendez, and J. Stoker, *Nucl. Inst. and Methods*, **156** (1978): 53.

[9] T. Izumi, *Nucl. Inst. and Methods*, **177** (1980): 405.

[10] E.R. Woelfel, *J. Appl. Cryst.*, **16** (1983): 341.

[11] J. Ballon, V. Comparat, and J. Pouxe, *Nucl. Inst. and Methods*, **217** (1983): 213.

[12] J.H. Dujin, C.W.E. van Ejik, R.W. Hollander, and R. Marx, *Trans. IEEE Nucl. Sci.*, **33** (1986): 388.

[13] G.D. Alekseev, N.A. Kalinina, V.V. Karpukhin, D.M. Khazins, and V.V. Kruglov, *Nucl. Inst. and Methods*, **177** (1980): 385.

[14] M. Atac, A.V. Tollestrup, and D. Potter, *Nucl. Inst. and Methods*, **200 (2-3)** (1982): 345.

[15] S. Shishiguchi, I. Minato, and H. Hashizume, *J. Appl. Cryst.*, **19** (1986): 420.

[16] M. Evain, P. Deniard, A. Jouanneaux, and R. Brec, *J. Appl. Cryst.*, **26** (1993): 563.

[17] L.W. Finger, D.E. Cox, and A.P. Jephcoat, *J. Appl. Cryst.*, **27** (1994): 892.

[18] F. Izumi, The Rietveld Method, ed. R.A. Young, (Oxford University Press, New York: 1995), Chapter 13.

[19] J.R. Johnson and J.J. Reilly, *Inorganic Chemistry*, **17**: 3103 (1978).

D. Microprobe Analysis

Microprobe analysis was performed on some alloys in the Geology department at Caltech by Paul Carpenter and myself. Small ingots were embedded in epoxy and polished in air before inserting into the SEM. Chemical analyses were performed with a JEOL Superprobe 733 electron microprobe.

E. Electrochemical Tests

The electrochemical cell is a unique place to test chemical environments because the polarization behavior of an electrode gives important information about the chemical reactions taking place. Chemical reaction rates are strong functions of electrochemical potential, and the current resulting from a reaction is proportional to the net rate of the reaction. Interpretation of this information is complicated by the fact that several reactions can be taking place simultaneously at different rates, but we can still extract useful information about the chemical reactions taking place at the electrode. Several researchers have developed kinetic models for the MH electrode.[1-6]

As mentioned in the introduction, an alkaline rechargeable battery is also a useful place to study the stability of MH alloys during hydrogen absorption/desorption cycling. $LaNi_5$ degrades much faster during electrochemical cycling in an alkaline electrolyte than in a gaseous hydrogen based environment. However, the mechanisms involved in hydride formation and decomposition in the two situations seem to be the same. In each case, hydrogen absorption at the alloy surface is a function of its chemical potential. Electrochemical isotherms whose potentials have been converted to pressures via the Nernst equation are equivalent to gas-phase isotherms.[7] Hydrogen diffusion coefficients measured by electrochemical methods are of the same order of magnitude as those measured by proton NMR.[8] The faster degradation in the electrochemical environment is

a result of the much larger heats of formation of La with the OH^- ion than with hydrogen. We can therefore obtain information about the durability of alloys much more quickly by cycling them electrochemically than by either thermal or pressure induced hydrogen absorption desorption cycling.

Unless otherwise noted, all electrochemical testing was done on the following mixture including the MH alloy. After gas-phase activation, 76 weight % (w%) MH alloy powder was mixed with 19 w% INCO 255 filamentary nickel powder (<1 μm) as a conductive diluent and 5 w% PTFE as binder material. This will be called the anode mixture. Because Hg/HgO reference electrodes were used in all electrochemical tests, all potentials given in this text will be with respect to Hg/HgO. Conversion to potentials with respect to a standard hydrogen electrode can be performed by adding 320mV.

1. Kinetics

The half-cell is often used to make electrochemical measurements because it eliminates or decreases effect from reactions at the cathode. This is accomplished by using a cathode with an electrochemical capacity several times that of the anode, placing the two electrodes far enough apart that the anode experiences a homogeneous potential from the cathode, and using a stable reference electrode to measure the potential of the anode.

a. Half-cell construction

A picture of the half-cell used for the measurements of kinetic parameters is shown in **Figure III-14**. To construct this cell, ~100mg of the anode mixture was pressed into the cylindrical cavity of a BAS (Bio-Analytical Systems) electrode. This electrode was positioned as close as possible to the tip of a Luggin capillary connected to the Hg/HgO reference electrode. The cathode was flight quality NiOOH from Eagle-Picher wrapped in Ni ExMet (expanded metal screen). This cathode was placed at an appreciable

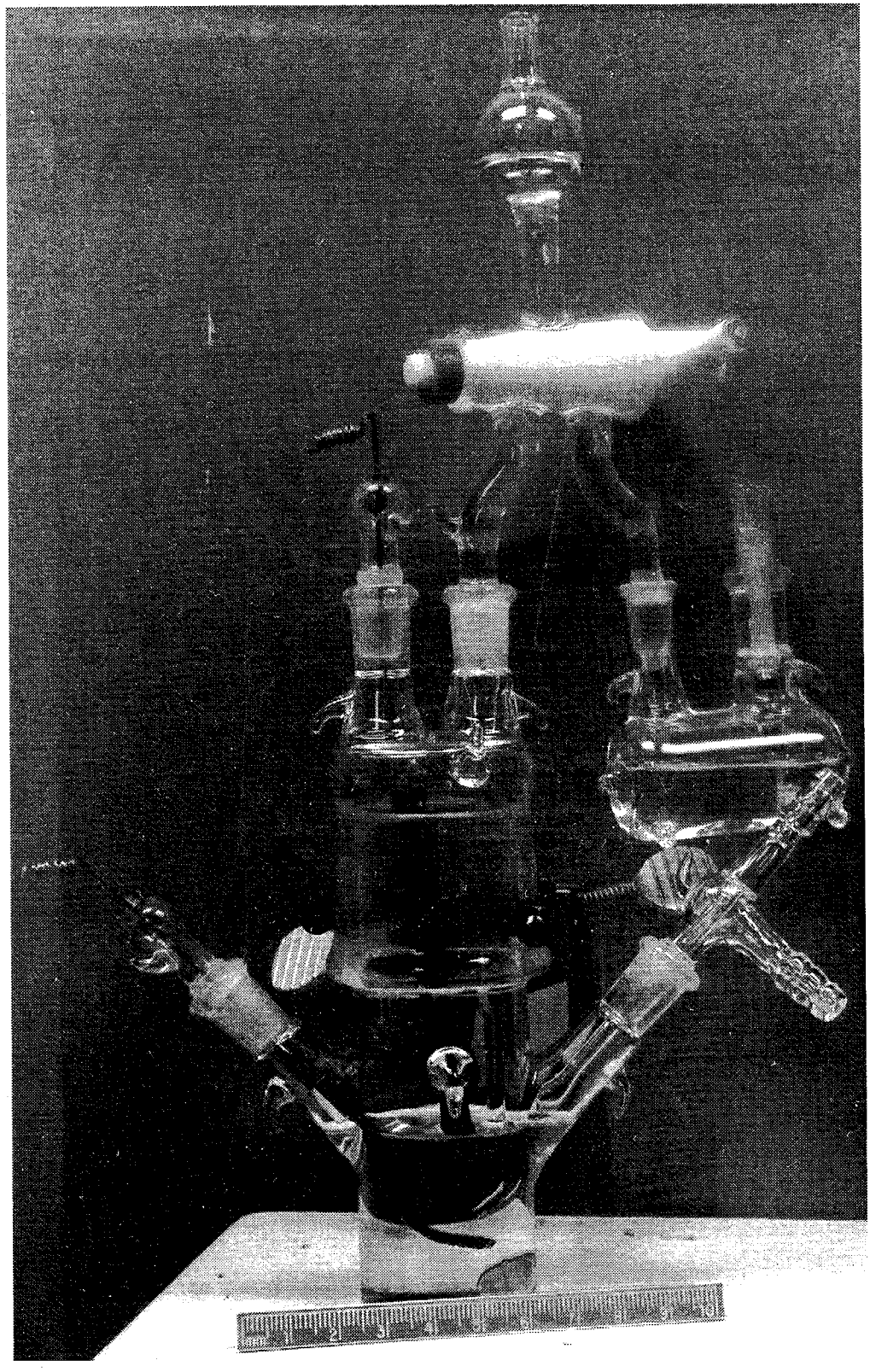

Figure III-14 Picture of half-cell.

distance from the anode so that the anode would see a uniform counter potential. A stirring bar was inserted into the half-cell and it was filled with 31 w% KOH. The half-cell was positioned above an active stirring plate during testing to reduce concentration gradients and so that bubbles from evolving gasses did not affect the measurements by interference with the MH/electrolyte interface.

b. Kinetics

In studying the kinetics of Ni-MH batteries, we are investigating the reactions that take place at the anode and their individual time constants. To begin, it is instructive to examine the steps that take place during charge transfer to (and from) the MH anode:

1. Ionic transport (OH^-) in the electrolyte and electronic transport (e^-) in the solid phase (electrode).
2. Charge-transfer and hydrogen transfer reactions at the surface of the MH particles:

$$M^S + e^- + H_2O \rightarrow M^SH_{ads} + OH^-. \qquad \text{[III.E.1]}$$

The reduction of hydrogen from water at the alloy surface creates a concentration gradient that drives hydrogen diffusion into the particle, leading to

3. A surface to bulk hydrogen atom transfer:

$$M^SH_{ads} + M^B \rightarrow M^S + M^BH_{abs}, \qquad \text{[III.E.2]}$$

where M^S and M^B are the surface and bulk species of the MH.

4. The diffusion of hydrogen in metal, involving nucleation and growth of the β-phase from the α-phase:

$$M^BH^{\alpha}_{abs} \rightarrow M^BH^{\beta}_{abs}. \qquad \text{[III.E.3]}$$

Secondary reactions that are not usually included in kinetic analyses are:

5. MH alloy corrosion or disproportionation:

$$LaNi_5 + 3\ OH^- \rightarrow La(OH)_3 + 5Ni + 3e^-, \qquad \text{[III.E.4]}$$

$$Ni + 2\,OH^- \rightarrow Ni(OH)_2 + 2e^-. \qquad [III.E.5]$$

6. *Hydrogen evolution reactions:*

$$2H_2O + 2e^- \rightarrow H_2 + 2\,OH^-, \qquad [III.E.6]$$

$$2\,M^SH_{ads} \rightarrow 2M + H_2. \qquad [III.E.7]$$

It is generally accepted that the rate limiting step under most conditions is charge-transfer at the MH alloy surface. Because of the high concentration of OH^- ions, charge transport in the electrolyte will only become important at very high currents. The transfer of surface adsorbed hydrogen to bulk absorbed hydrogen is not well understood. However, because the activation energy for hydrogen absorption in the α-phase (~ -61 kJ / mol H) [9] is much greater than the activation energy for the α- to β-phase transition (~-16 kJ / mol H),[7] it is reasonable to assume that reaction [III.E.2] is faster than reaction [III.E.3]. The diffusion coefficient of hydrogen in the bulk alloy is important for some MH electrodes.[10] In $LaNi_5$, however, it is on the order of 10^{-12} cm^2/s,[11] and its effects will not dominate in the range of the time constants of the other electrode processes. The mechanisms of nucleation and growth of the hydride (β-) phase are not formally understood, but it is believed that they are of the same order as the hydrogen diffusion coefficient in the hydride. Other elements that are present in the electrochemical circuit are the electrolyte resistance between the electrodes, the contact resistance and capacitance between the current collector and the sample (alloy + diluent + binder), and the contact resistance and capacitance between alloy particles.

The kinetic models developed at least include steps 1-4 outlined above. The current density due to the charge-transfer reaction is usually assumed to be given by the Butler-Volmer equation:

$$\frac{i}{i_0} = \frac{C_O(0,t)}{C_O^*} e^{\alpha\, nF\eta\ /RT} - \frac{C_R(0,t)}{C_R^*} e^{-(1-\alpha)nF\eta\ /RT}. \qquad [III.E.8][12]$$

$C_{O,R}(0,t)$ = oxidant and reductant surface concentrations.

$C^*_{O,R}$ = oxidant and reductant bulk concentrations.

i_0 = exchange current density. F = Faraday constant.

n = number of electrons. R = gas constant.

η = electrode over-potential. T = temperature [K].

α = transfer coefficient (reaction reversibility).

If the solution is well stirred or currents are kept so low that the surface concentrations do not differ appreciably from the bulk values, then [III.E.8] reduces to:

$$\frac{i}{i_0} = e^{\alpha\, nF\eta\ /RT} - e^{-(1-\alpha)nF\eta\ /RT}. \qquad \text{[III.E.9]}^{12}$$

Other phenomena accounted for include surface hydrogen coverage, modeled by a Langmuir isotherm;[13,14] particle size;[15] spherical diffusion;[4,16] electrode porosity;[13] and alloy electrocatalytic activity.[17] For our purposes, however, we will merely use the unmodified Butler-Volmer equation to obtain the kinetic parameters, as outlined below. Three different techniques were used to characterize the electrochemical kinetics of the alloys: DC micro-polarization, Tafel polarization, and AC impedance spectroscopy.

i. Micro-Polarization

If the electrode over-potential is small, $\eta << RT/\alpha nF$, the current in eq. [III.E.9] can be approximated through a Taylor's expansion of the exponential to

$$i / i_0 = nF\eta / RT. \qquad \text{[III.E.10]}$$

The ratio $-\eta/i$ has units of resistance and is often called the charge transfer resistance,

$$R_{ct} = RT / nF\, i_0. \qquad \text{[III.E.11]}$$

This parameter characterizes the electrode's resistance to charge transfer in the absence of chemical reactions. By the same token the exchange current, i_0, characterizes the electrode's ability to pass current under near equilibrium conditions.

DC micropolarization measurements were performed on the alloys under potentiodynamic conditions at scan rates of 0.02 mV/s. The scan rate was so chosen to provide near-steady state conditions with minimal changes in the state of charge of the electrode or its surface conditions. Although these tests were done in open cells, the results should be valid for sealed cells as well, because additional experiments on the x_{Sn} = 0.2 alloy have demonstrated that the kinetics as measured by micro- and Tafel polarization are fairly independent of the state of charge of the material.

ii. AC Impedance Spectroscopy

Electrochemical (or AC) Impedance Spectroscopy (EIS) is another powerful technique that may be used to characterize electrochemical systems.[18] One way to implement this method is to control the magnitude of an applied AC potential and measure the phase and magnitude of the resulting current for a range of frequencies. If measurements are made over a wide-enough frequency range, then different time constants, resistances, and capacitances corresponding to different physical processes can be extracted. An equivalent circuit is assigned to this preliminary data. Individual circuit elements can be assigned to particular physical phenomena by varying the electrode construction or its conditions during testing.

The problem of determining the AC response of a simple electrochemical system with either charge transfer or diffusion-limited kinetics has been considered by several authors. The equivalent circuit for this situation was first proposed by Randles [19] and is shown in **Figure III-15**. In this figure, R_1 represents the electrolyte resistance, C_{DL} is the double layer capacitance, and Z_w* is the Warburg impedance, resulting from diffusion of the electroactive species. EIS was first used on an ingot $LaNi_5$ electrode by Agarwal and Orazem, who used a transport based mathematical model to analyze the results of the EIS data.[20]

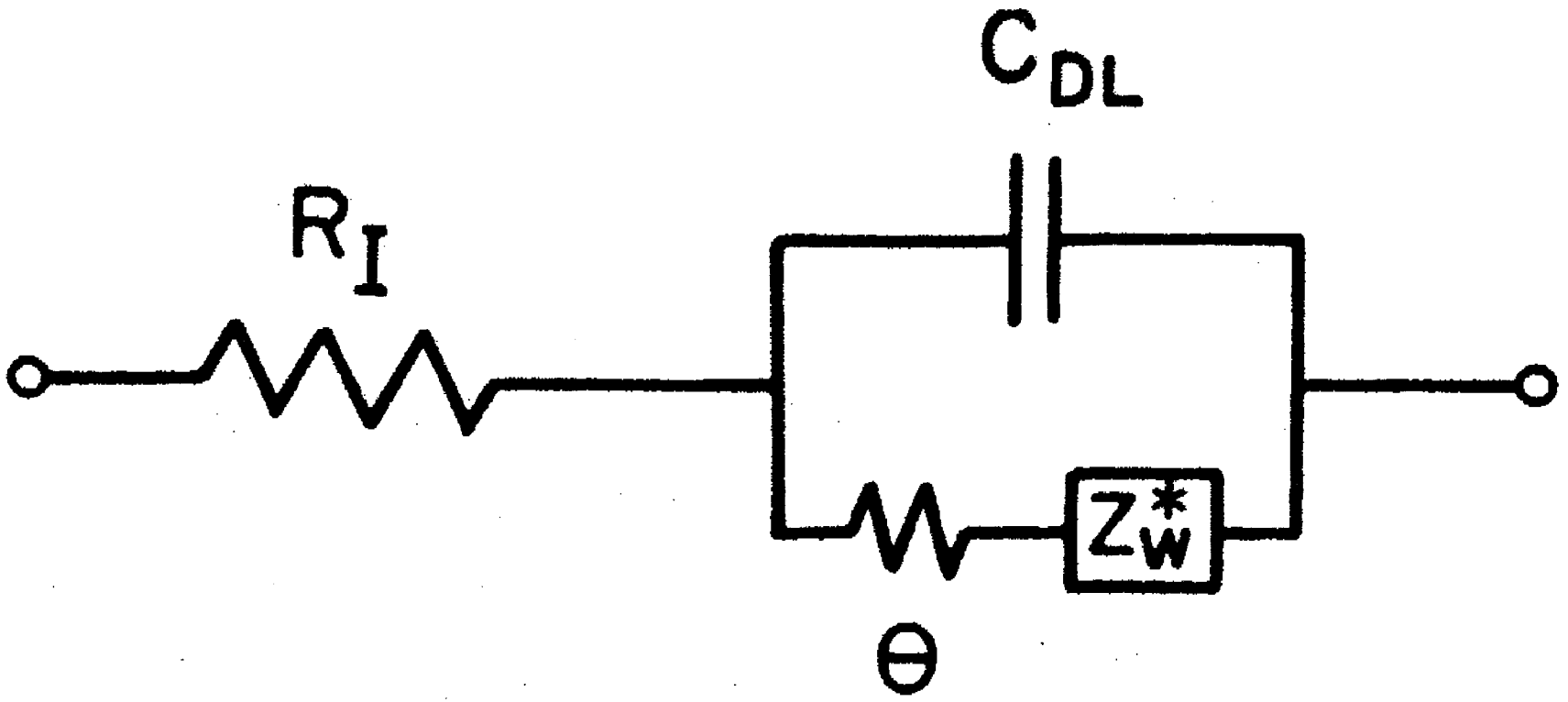

Figure III-15 Equivalent circuit for charge-transfer reaction at an electrode. (reprinted from C. Ho, I.D. Raistrick, and R.A. Huggins, *J. Electrochem. Soc.*, **127** (1980): 343.)

The procedure described above was followed by Kuriyama, *et al.*, who used the AC impedance technique to investigate deterioration of MH electrodes during charge-discharge cycling.[21,22] A schematic Cole-Cole plot of the impedance spectrum from the electrodes is shown in **Figure III-16**, reprinted from ref. 22, and the equivalent circuit for this data is shown in **Figure III-17**. The capacitive components labeled by Q are modeled as constant-phase elements (CPE) to describe the depressed nature of the semi-circles.[18] The circuit elements were assigned to their various physical effects by analyzing impedance spectra of several series of electrodes: series 1 electrodes with constant alloy weight and binder fraction were tested at varying depths of discharge (DOD) and temperatures; series 2 electrodes contained different alloy weights with a constant fraction of binder; and series 3 electrodes contained a constant alloy weight and varying binder content.

From the results of these tests, Kuriyama, *et al.* determined that R_1 corresponded to the resistance of the electrolyte between the working and the reference electrode, R_2 was a result of the contact resistance between the current collector and the alloy, and R_3 and C_3 were related to the alloy particle-to-particle contact. These were all effects of the battery construction. The reaction resistance for the hydrogen transfer and double layer capacitance were responsible for elements R_4 and Y_{04}.[22] Zhang, *et al.* concluded later that the linear region at low frequencies was an effect of the porous structure of the electrode rather that being a Warburg impedance.[3]

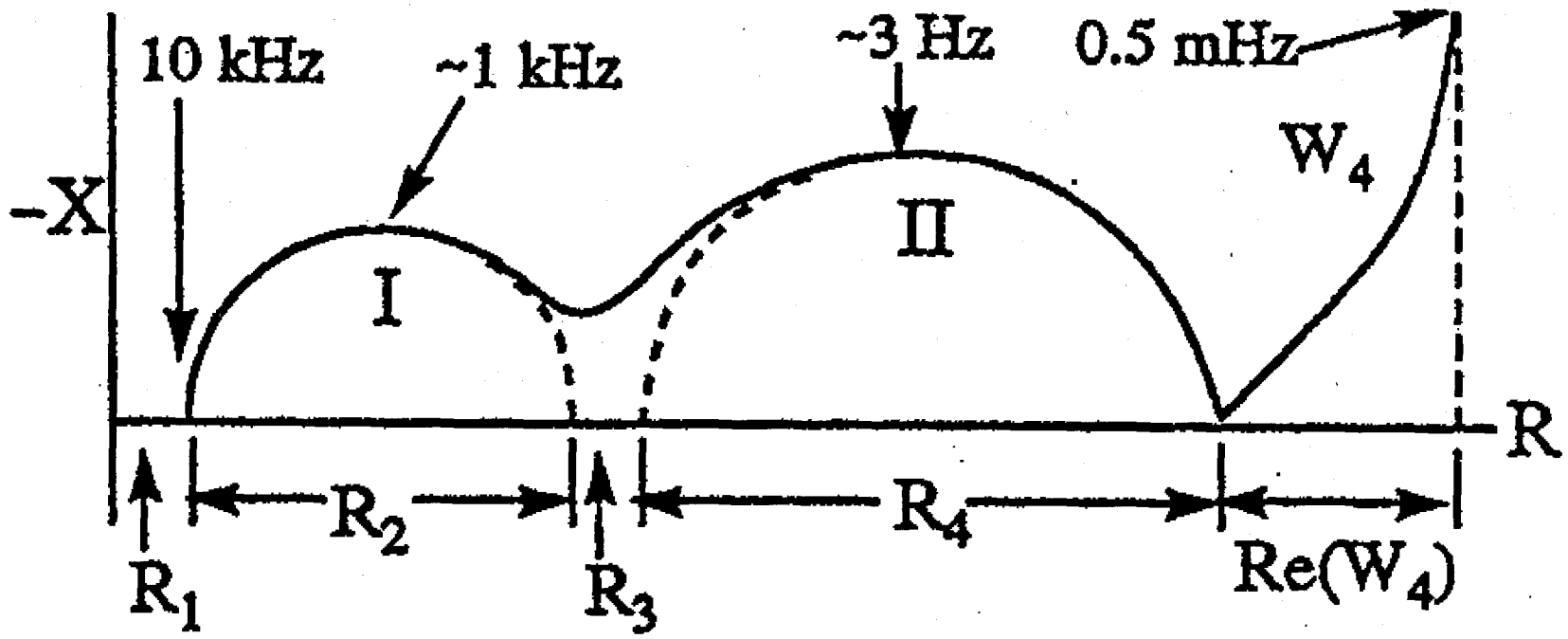

Figure III-16 Schematic of Cole-Cole plot of MH impedance spectrum. (reprinted from N. Kuriyama, et al., *J. Alloys Comp.*, **202** (1993): 183.)

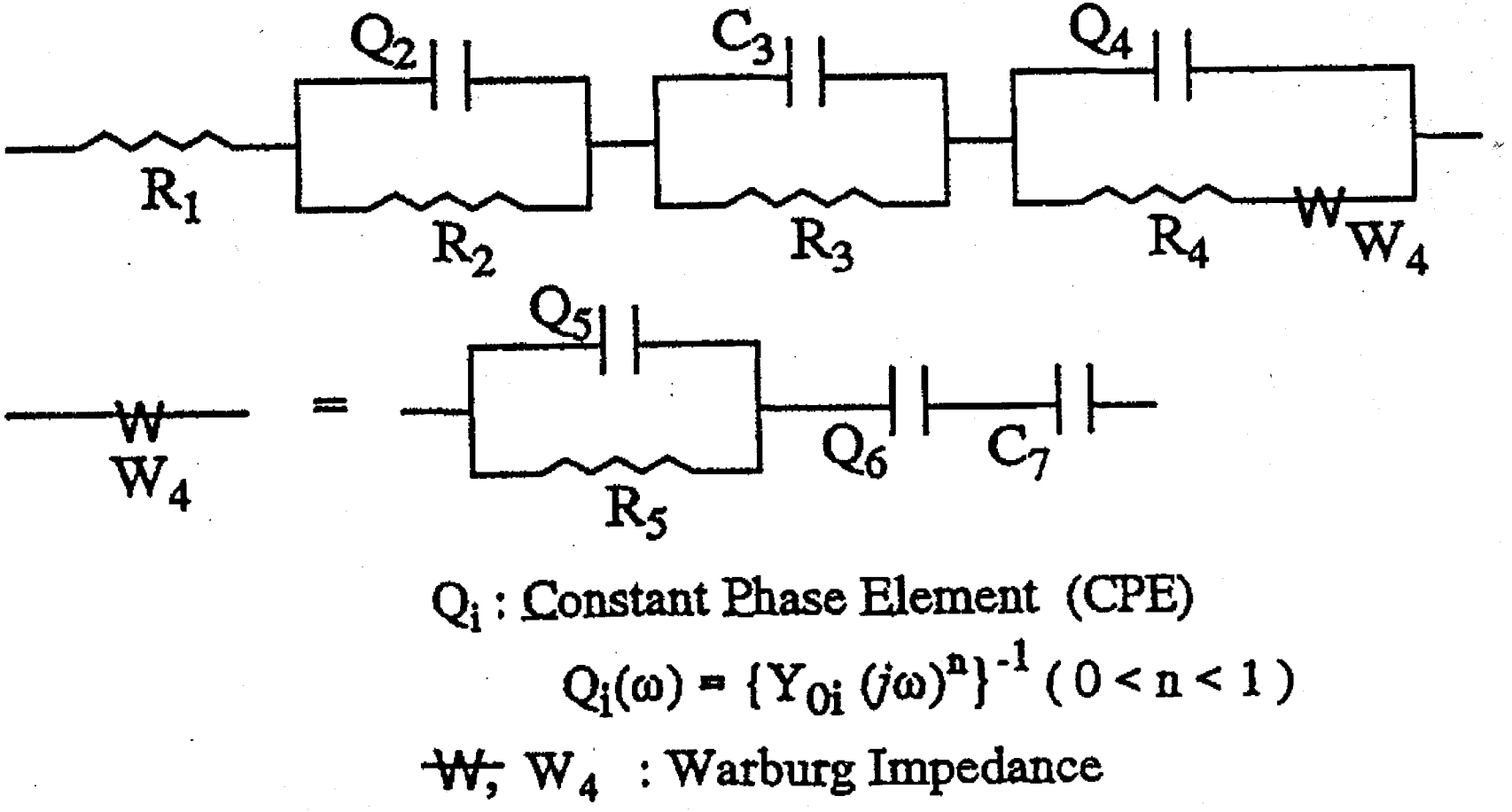

Figure III-17 Equivalent circuit for MH electrode. (reprinted from N. Kuriyama, et al., *J. Alloys Comp.*, **202** (1993): 183.)

iii. Tafel Polarization

When the electrode over-potential is large, the second term of eq. [III.E.9] becomes very small, and

$$\frac{i}{i_0} = e^{\alpha nF\eta / RT}. \qquad \text{[III.E.12]}$$

Under this condition, the electrode potential has the exponential relationship to current *first given by Tafel in 1905*

$$\eta = a + b \log i. \qquad \text{[III.E.13]}$$

We can rewrite eq. [III.E.12] as

$$\ln\frac{i}{i_0} = 2.303\log\frac{i}{i_0} = \alpha nF\eta / RT \qquad \text{[III.E.14]}$$

In this case, the effective charge transfer resistance is the semi-log slope, 2.303RT/αnF of the asymptote of the Tafel curve at infinite current. The effective exchange current is the intercept of the asymptote with the current axis. The Tafel exchange current can be considered the maximum exchange current for all electrochemical processes at high over-potentials. The transfer coefficient is the inverse semi-log slope.

The following description of Tafel polarization from Bard & Faulkner is helpful in understanding the type of kinetic phenomena that it measures:

> When electrode kinetics are sluggish and significant activation overpotentials are required, good Tafel relationships can be seen. This point underscores the fact that Tafel behavior is an indicator of *totally irreversible* kinetics. Systems in that category allow no significant current flow except at high overpotentials, where the faradaic process is effectively unidirectional and, therefore, chemically irreversible.[12]

Tafel polarization measurements can be used to independently determine the kinetics of charge and discharge, or absorption and desorption in the case of MH electrodes. However, the presence of mass transfer effects in the electrolyte should dominate

cathodic Tafel polarization measurements. For the Tafel polarization experiments performed here, the potential was scanned from extreme anodic (positive) values to the cathodic (negative) values, to avoid the uncertainties arising from hydrogen bubbles adhering to the surface of the MH electrode. The data deviate from linear behavior as η approaches zero, because the back reactions can no longer be regarded as negligible. The data indicate strong mass transfer effects at high currents. The cathodic Tafel plot of $LaNi_5$ appears to show a different slope at high overpotentials, possibly corresponding to hydrogen evolution.

In the analysis of the Tafel polarization data, the limiting current is used to correct for mass transport effects. The limiting currents (i_{lim}) are measured in a separate potentiodynamic experiment at a potential 400 mV more positive than the equilibrium potential. The Tafel plots can be corrected for the mass transfer effects by plotting the logarithm of $i_{exp}/(1-i_{exp}/i_{lim})$ against the electrode potential. The exchange current density and transfer coefficients for hydrogen absorption are then calculated from the intercept and inverse slope of the corrected cathodic Tafel plots, respectively. The corresponding coefficients for hydrogen desorption are calculated from the corrected anodic Tafel plots. The exchange current density is the current at which the electrode begins to exhibit Tafel, or irreversible, behavior. "The transfer coefficient, α, is a measure of the symmetry of the energy barrier." [12] It quantifies the change in the activation energy of the charge transfer reaction for a given electrode potential.

2. Cyclic Lifetime Tests

a. Prismatic cell construction

A picture of the prismatic cell used for lifetime measurements is given in **Figure III-18.** The anode was constructed by spreading an amount of the anode mixture containing approximately 1g MH alloy onto 1 sq. inch Ni ExMet and hot pressing at 150° C and 69

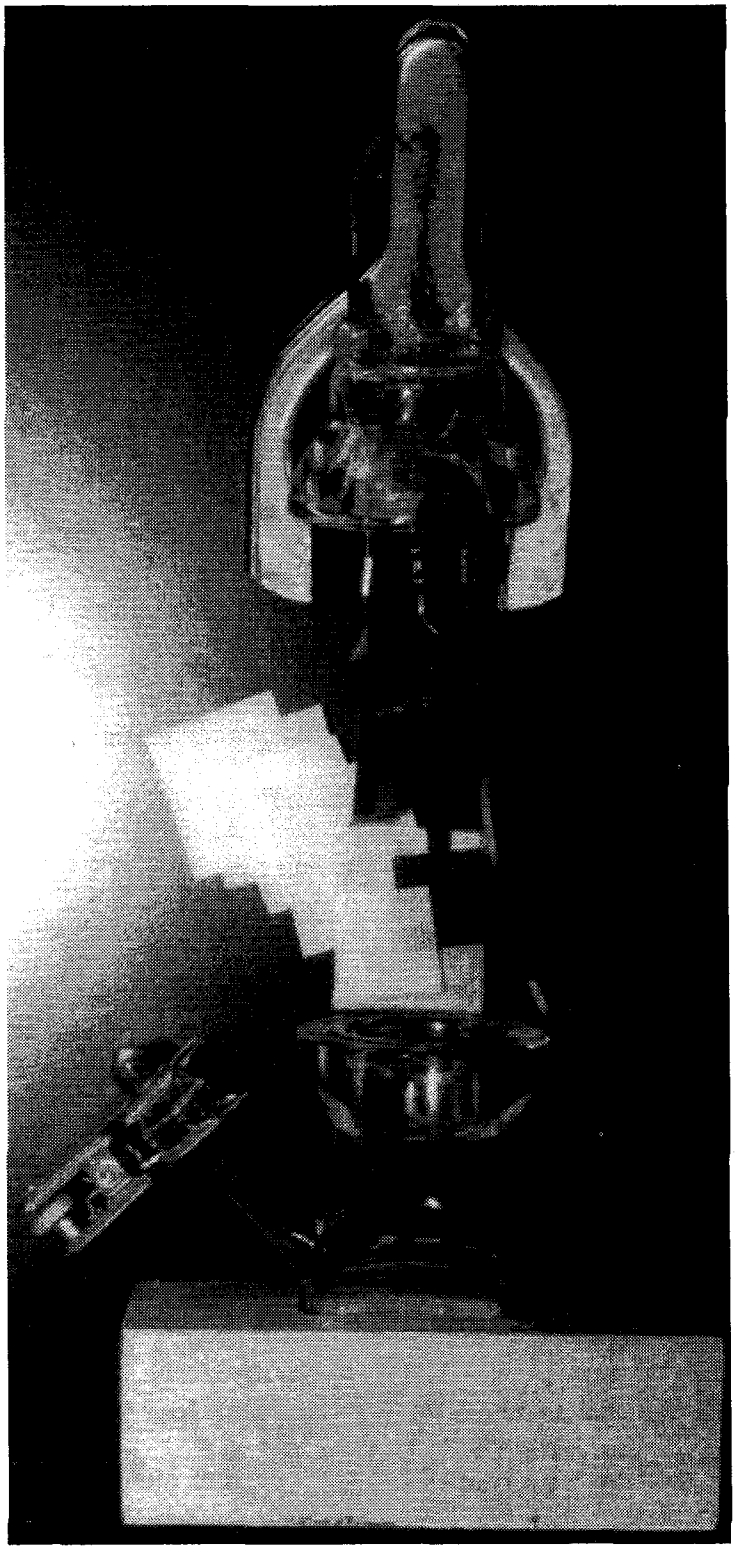

Figure III-18 Picture of prismatic cell.

MPa for 30 minutes. The cathodes consisted of two ~4 sq. inch flight quality NiOOH cathodes from Eagle-Picher wrapped in Ni ExMet, each bagged with woven nylon paper. The anode was then bagged with woven nylon paper and inserted between the cathodes. Teflon shims were used for compaction. A Hg/HgO reference electrode was inserted in the cell next to the electrodes.

b. Cycling conditions

Cells were initially charged at 60 mA/g for 7 hours, ~150% of their theoretical capacity. After charging, the cells were left at open circuit for 15 minutes to allow their potentials to equilibrate. Then the cells were discharged at C/2 rate, or 150 mA/g, to -0.5V, a particularly low cut-off potential for AB_5 alloys that insures 100% DOD. After another 15 minutes at open circuit, the cells were charged at C/5 rate, or 60 mA/g, to 115% of their previous discharge capacity. These conditions were designed to accelerate the capacity loss of the anodes. The -0.5V cutoff potential insured some MH alloy oxidation at each cycle, and the high discharge current created a large over-potential that would induce hydrogen evolution and MH alloy oxidation.

[1] M. Viitanen, *J. Electrochem. Soc.*, **143** (1993): 936.

[2] W. Zhang, M.P.S. Kumar, K. Petrov, and S. Srinivasan, Abstract No. 593, May 22-27, 1994 ECS meeting.

[3] W. Zhang, M.P.S. Kumar, S. Srinivasan, and H.J. Ploehn, *J. Electrochem. Soc.*, **142** (1995): 2935.

[4] L.O. Valøen, S. Sunde, and R. Tunold, *J. Alloys Comp.*, **253-254** (1997): 656.

[5] G. Zheng, B.N. Popov, and R.E. White, *J. Electrochem. Soc.*, **143 (3)**, 834 (1996).

[6] B.S. Haran, B.N. Popov, and R.E. White, *J. Electrochem. Soc.*, **145 (12)** (1998): 4082.

T. Sakai, M. Matsuoka, and C. Iwakura, in *Handbook on the Physics and Chemistry of Rare Earths*, K. A. Gschneidner, Jr. and L. Eyring, eds., Vol. **21**, Elsevier Science B. V., Amsterdam (1995), p. 133.

[8] B.V. Ratnakumar, A. Hightower, C. Witham, R.C. Bowman, Jr., and B. Fultz, in *Aqueous Batteries*, P.D. Bennett and S. Gross, Eds., **PV 96-16**, abs. # 0053, The Electrochem. Soc. Proceedings Series, Pennington, NJ (1997).

[9] F.D. Manchester and D. Khatamian, *Mat. Sci. Forum*, **31** (1988): 261

[10] S. Wakao and Y. Yonemura, *J. Less-Common Met.*, **89** (1983) 481.

[11] D. Richter, R. Hempelmann, and R.C. Bowman, Jr., in *Topics in Applied Physics: Hydrogen in Intermetallic Compounds II*, Chapter 3, L. Schlapbach, ed., Springer Verlag (Berlin: 1988), p. 97.

[12] *Electrochemical Methods,* A.J. Bard and L.R. Faulkner, Eds., John Wiley & Sons, Inc., New York (1980).

[13] G. Zheng, B.N. Popov, and R.E. White, *J. Electrochem. Soc.*, **143** (1996): 435.

[14] Y. Leng, J. Zhang, S. Cheng, C. Cao, and Z. Ye, *Electrochim. Acta*, **43** (1998): 1

[15] J.M. Heikonen, H.J. Ploehn, and R.E. White, *J. Electrochem. Soc.*, **145** (1998): 1840.

[16] P. De Vidts, J. Delgado, and R.E. White, *J. Electrochem. Soc.*, **142** (1995): 4006.

[17] W. Zhang, S. Srinivasan, and H. Ploehn, *J. Electrochem. Soc.*, **143** (1996): 4039

[18] J.R. Macdonald, *Impedance Spectroscopy*, John Wiley & Sons, New York, 1987.

[19] J.E.B. Randles, *Discuss. Faraday Soc.*, **1** (1947): 11.

[20] P. Agarwal, M.E. Orazem and A. Hiser, in *Hydrogen Storage Materials, Batteries, and Electrochemistry*, D.A. Corrigan and S. Srinivasan, eds., PV 92-5, p. 120, The ECS Proc. Series, Pennington, NJ (1992).

[21] N. Kuriyama, T. Sakai, H. Miyamura, I. Uehara, H. Ishikawa, and T. Iwasaki, *J. Electrochem. Soc.*, **139** (1992): L72; N. Kuriyama, T. Sakai, H. Miyamura, I. Uehara, and H. Ishikawa, *J. Alloys Comp.*, **192** (1993): 161.

[22] N. Kuriyama, T. Sakai, H. Miyamura, I. Uehara, H. Ishikawa, and T. Iwasaki, *J. Alloys Comp.*, **202** (1993): 183.

IV. X-ray Diffraction

A. Phase Composition

One of the first things learned in materials science is that chemical composition alone does not decide what a material's properties will be. Hence, the first test to be performed before alloy properties were measured was to confirm that we had Haucke phase material with no secondary phases present. This was determined by performing X-ray diffraction (XRD) and examining the patterns for diffraction peaks that did not correspond to a Haucke phase crystalline lattice. Diffraction patterns for $LaNi_{5-x}Sn_x$, $LaNi_{5-x}Ge_x$, $LaNi_{4.8}M_{0.2}$, and $LaNi_{5-x}M_x$, can be seen, respectively, in **Figures IV-1**, **IV-2a**, **IV-3a** and **b**, and **IV-4**. In some cases, the alloy compositions were verified by Scanning Electron Microscopy (SEM) and Energy Dispersive X-ray spectroscopic microprobe analysis (EDAX).

Most of the alloys melted at Caltech were found to be single-phase. This observation was confirmed by microprobe analysis, which found a minute precipitation of LaO particles in all samples. Diffraction peaks from secondary phases are denoted by an asterisk (*).

All Ge_x alloys but $Ge_{0.5}$ were found to be single phase. An example of the microstructure of the $Ge_{0.5}$ alloy after annealing can be seen in the SEM micrograph shown in **Figure IV-2b**. The second phase, identified as having approximately LaNiGe composition, is present as small equi-axed inclusions in the $LaNi_{4.5}Ge_{0.5}$ matrix. The EDAX results for Ge_x alloys are displayed in **Table IV-1**.

The $Bi_{0.2}$ and Sb_x alloys were decidedly multiphase, as can be seen in **Figure IV-3b**. Microprobe analysis revealed the $Bi_{0.2}$ alloy to have two phases, one equivalent to $LaNi_{5-x}Bi_x$ and one of approximate composition LaNiBi. The $Sb_{0.2}$ alloy (not included in **Figure**

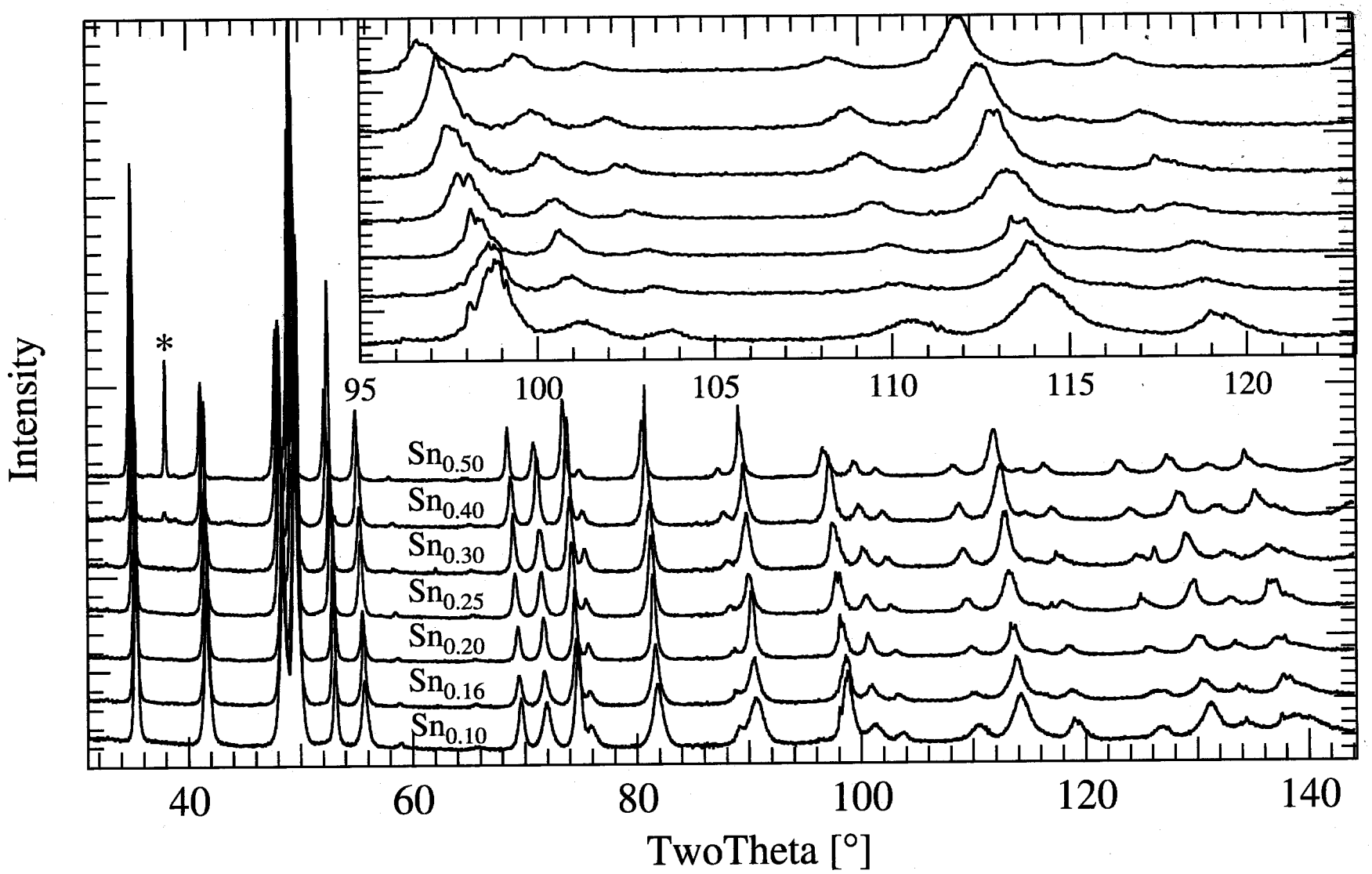

Figure IV-1 XRD patterns of hydrogen activated $LaNi_{5-x}Sn_x$ alloys.

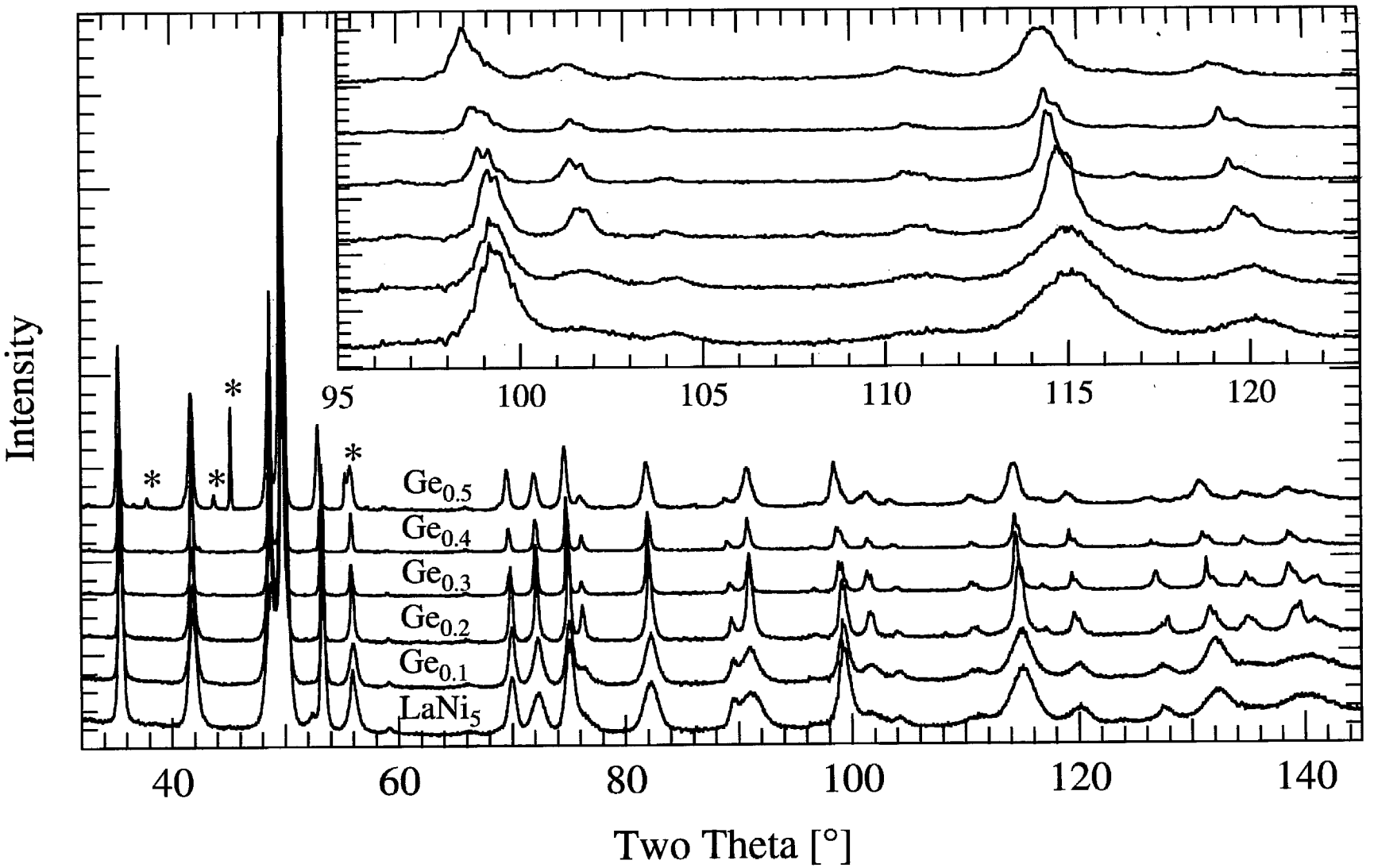

Figure IV-2a XRD patterns of hydrogen activated $LaNi_{5-x}Ge_x$ alloys.

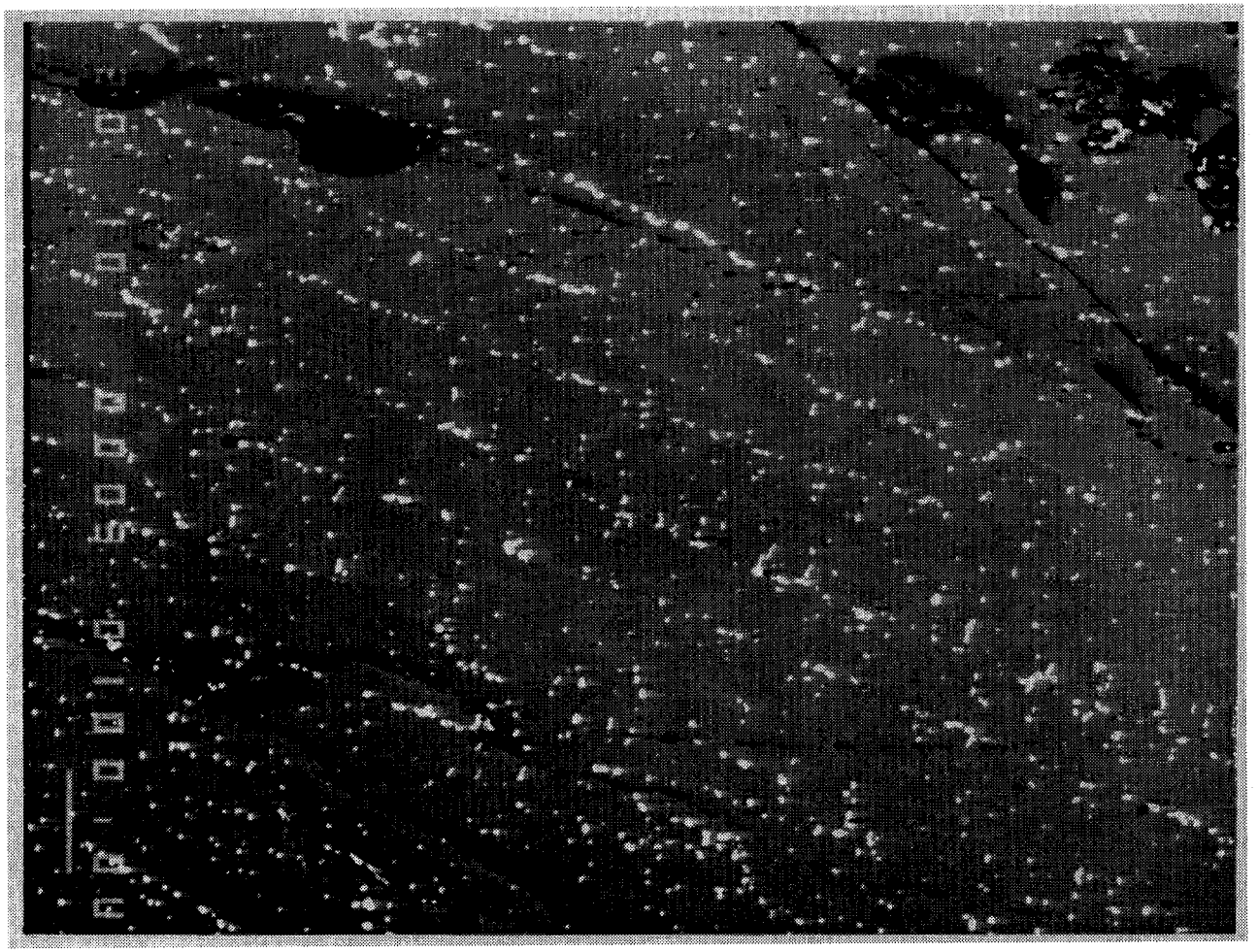

Figure IV-2b SEM micrograph of annealed $LaNi_{4.5}Ge_{0.5}$ ingot.

Alloy	# meas.	$\langle x_{Ge} \rangle$	$\langle x_{Ge} \rangle / x_{Ge}^{nom}$	$B = \lvert x_{Ge} \rvert + \lvert x_{Ni} \rvert$	$\langle x_{Ge} \rangle * 5 / B$	$\langle x_{Ge} \rangle * 5 / B / x_{Ge}^{nom}$
$Ge_{0.1}$	6	0.101	1.010	4.90	0.103	1.030
$Ge_{0.2}$	7	0.196	0.980	5.05	0.194	0.972
$Ge_{0.3}$	7	0.286	0.953	4.96	0.288	0.960
$Ge_{0.4}$	17	0.385	0.963	4.95	0.389	0.973
$Ge_{0.5}$	7	0.461	0.922	4.84	0.476	0.952

Table IV-1 EDAX composition analysis of $LaNi_{5-x}Ge_x$ alloys.

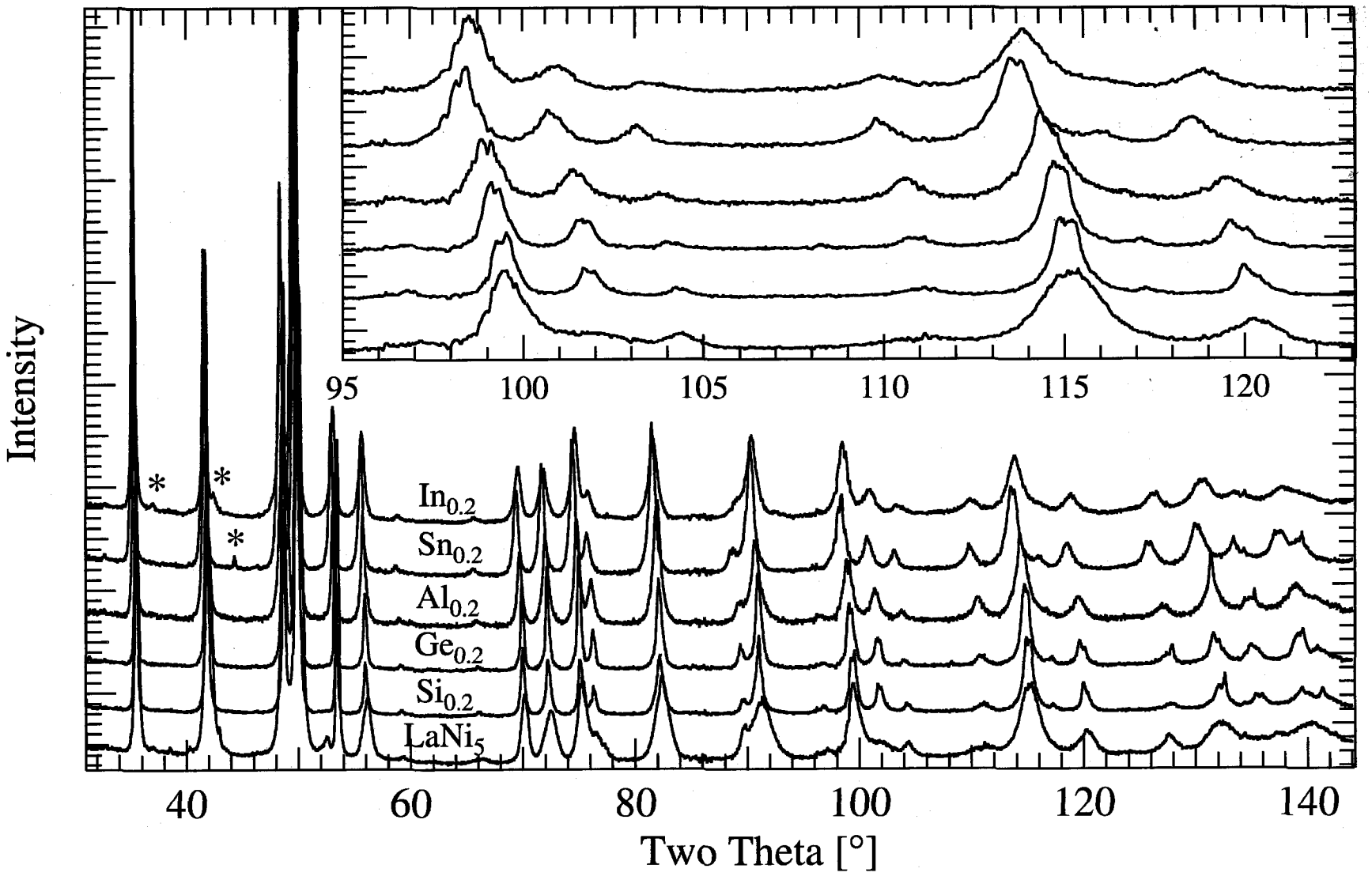

Figure IV-3a XRD patterns of hydrogen activated single-phase $LaNi_{4.8}M_{0.2}$ alloys.

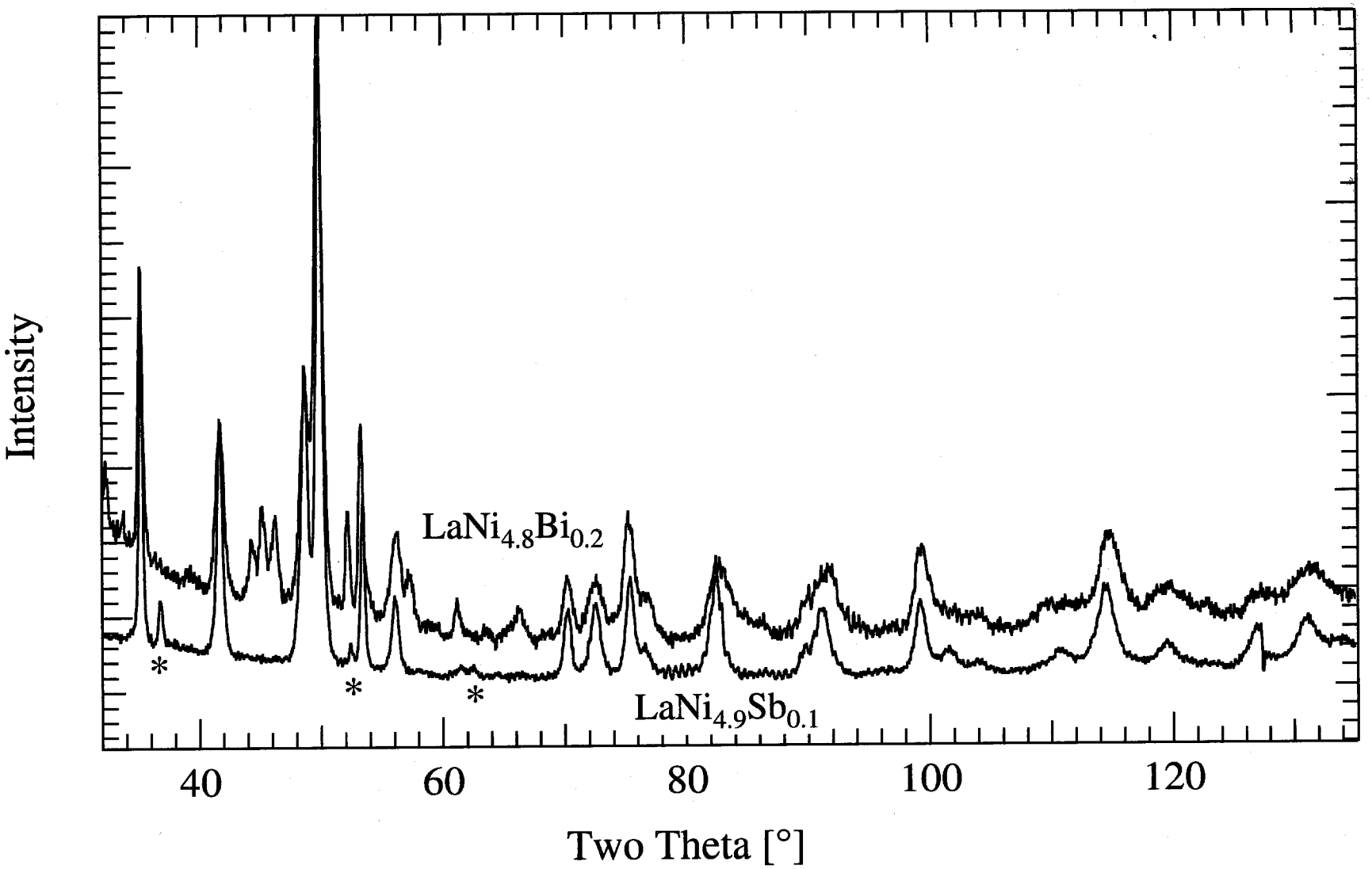

Figure IV-3b XRD patterns of hydrogen activated multi-phase $LaNi_{4.8}M_{0.2}$ alloys.

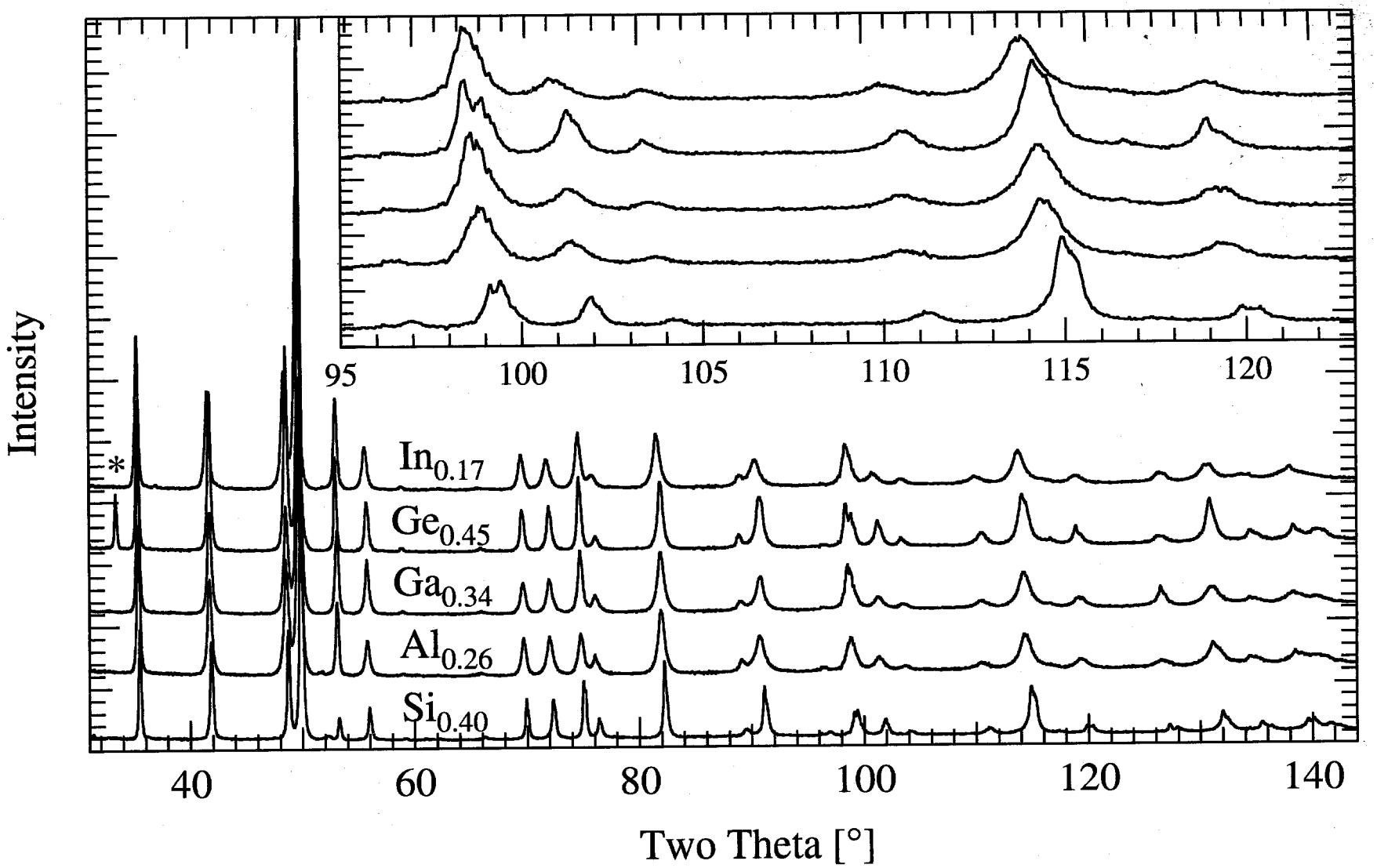

Figure IV-4 XRD patterns of hydrogen activated $LaNi_{5-x}M_x$ alloys.

IV-3b) had three phases present, which were identified as $LaNi_{5-x}Sb_x$, $LaNi_5$, and ~LaNiSb. Multi-phase alloys were not included in the subsequent testing.

XRD can also be used to identify the presence of corrosion products and the extent of decomposition. This technique will be discussed further in section VII.B for the case of $LaNi_{4.8}Sn_{0.2}$.

3. Discussion

Included in **Table IV-1** are the ratios of the measured Ge composition ($<x_{Ge}>$) and the Ge composition scaled by the alloy stoichiometry ($<x_{Ge}> * 5 / B$) to the nominal composition (x_{Ge}^{nom}). The composition of the $Ge_{0.5}$ matrix measured by SEM microprobe was lower in all cases than the composition trend set by the other Ge_x alloys. Because the $Ge_{0.5}$ alloy was not single phase, we believe the solubility limit of Ge for Ni, under the annealing conditions used here, is in the range $0.45 < x_{Ge} < 0.5$. The inclusions present in **Figure IV-2b** are in rows, implying that they were ejected from the melt as the alloy solidified, resulting in a eutectic structure. During annealing, these lamellar grains would break up and become spherical to reduce surface energy effects. Because this phase is present is such a small quantity, we assumed that it would have a small effect on the alloy's properties, and $Ge_{0.5}$ was used in further measurements.

There is an interesting trend that can be seen in the equilibrium solubilities of the p-shell metals for Ni in $LaNi_5$. Of the group IIIA metals, Al has a solubility limit of $x \approx 1.5$,[1] Ga has a solubility limit somewhere within $1^{2} < x < 2$,[3] and In has a solubility limit of at least $x = 0.4$.[4] In group IVA, Si,[5] Ge,[6] and Sn [7] all have solubility limits of $x \approx 0.5$. In group VA, Sb has a solubility less than $x = 0.1$ and Bi has a solubility less than $x = 0.2$. It seems then, that as the number of valence electrons (electron-to-atom ratio) and "electronegativity" of the solute atom increases, its solubility for Ni in $LaNi_5$ decreases. This should be strongly dependant on the heat of formation of the solute with La (ΔH_{LaM}), which would drive the precipitation of LaM_x binary alloys for those solutes with large

ΔH_{LaM}. It is also intriguing that ΔH_{LaM} is negatively correlated with the metallic radius of the solute. Within each of the groups mentioned above, increasing the atomic number of the solute results in an increase in ΔH_{LaM}, making the solute less stable in $LaNi_5$ (decrease in solutility limit). However, the simultaneous decrease in the solute excess metallic radius, $(r_M - r_{Ni})$, decreases the misfit energy and lattice strain in the alloy, making the solute more stable. It is likely that the solubility limits of elements within each group of the periodic table stays approximately constant because of these competing effects.

B. Lattice Parameters of Dehydrided Alloys

1. Literature Survey

A review of the literature was made to find previous measurements of the lattice parameters of $LaNi_{5-x}M_x$ metal alloys. The unit cell volumes of transition metal substituted $LaNi_5$ has been covered in the introduction, §II.D.1. Of the non-transition metals, Al was extensively studied as a solute as early as 1977 by the groups Mendelsohn, *et al.*[8] and Diaz, *et al.*[9] It is quite effective in expanding the lattice, and the unit cell volume expands linearly with composition to $x_{Al} \approx 1.0$. Mendelsohn, *et al.* made alloys with other non-transition metals, including Sn,[4] In,[4] Ga,[10] Ge,[10] and Si.[4] Unit cell volumes were given for all alloys at compositions of x=0.4 and for $In_{0.07}$, $In_{0.15}$, although graphs of unit cell volume *vs* x showed that all solutes expanded the lattice linearly with composition. The crystal structure of $LaNi_4Ga$ has recently been studied.[2] Alloys $Si_{0.3}$ and $Si_{0.5}$ were studied by Meli, *et al.*,[11] and Achard, *et al.*[5] More recently, Sn has been extensively studied by Luo, *et al.*[12] and Percheron, *et al.*[13]

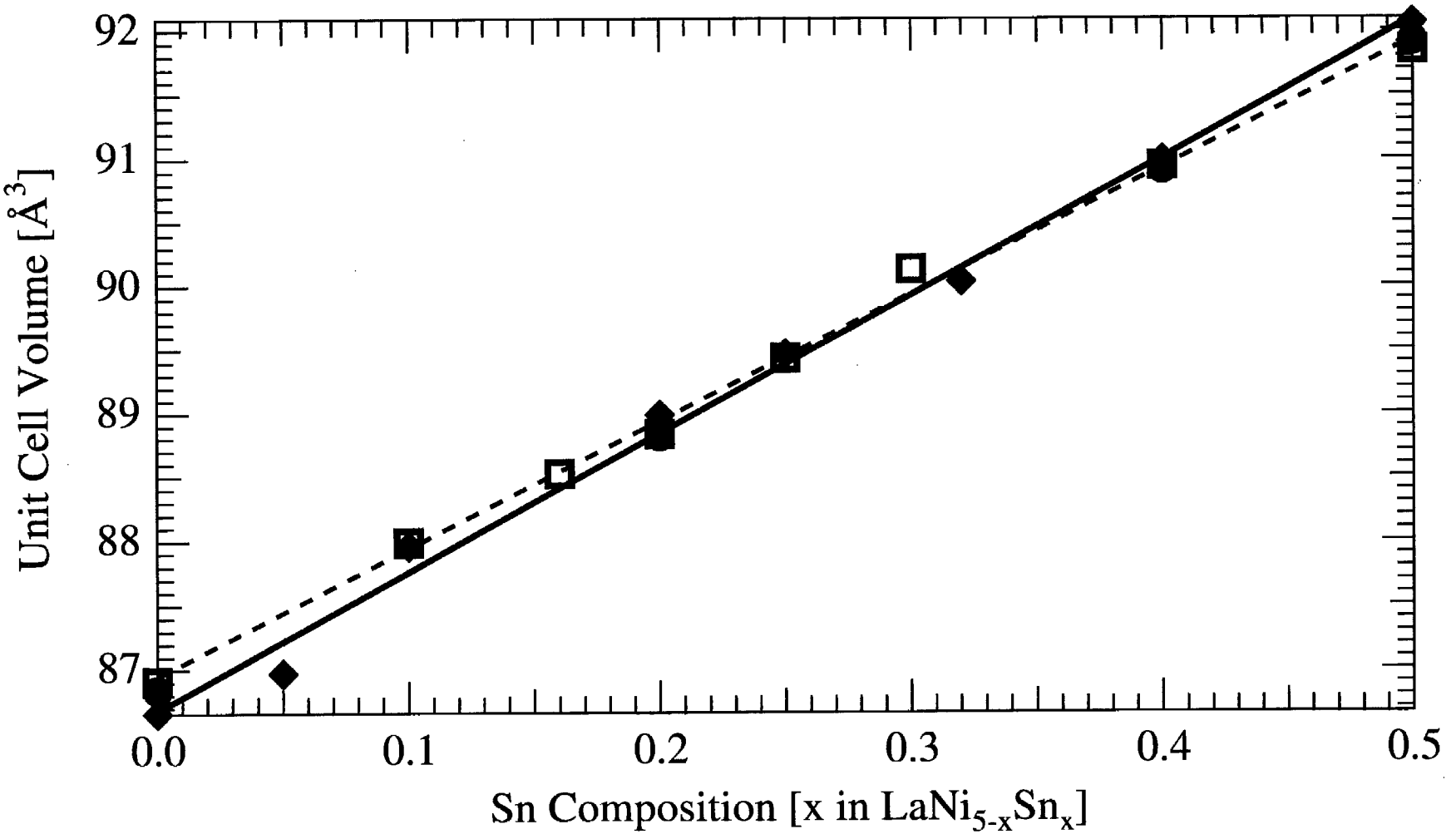

Figure IV-5 Unit Cell Volumes of $LaNi_{5-x}Sn_x$ alloys *vs* Sn composition, x.
{ ◆ , ● - literature measurements, ◘ - Caltech measurements}

2. Caltech Results

Lattice parameters of dehydrided alloys were calculated from XRD patterns taken on the Inel CPS-120 diffractometer with Co Kα radiation. **Figure IV-5** shows the unit cell volumes measured at Caltech of Sn_x alloys *vs* x (open squares). Sn-substitution in $LaNi_5$ has been extensively studied, and included in this figure for comparison are unit cell volume measurements from XRD (Luo, *et al.*,[12] diamonds) and NPD data (Joubert, *et al.*,[13] circles) data. *The Caltech measurements agree more closely with the NPD results.* Judging from the linear fits to the data from the literature, **equation IV.1** and the Caltech data, **equation IV.2**, the lattice parameter measurements made at Caltech are accurate.

3. Discussion

Figures IV-6 - 10 show the unit cell volume data extracted from the literature (diamonds) *with measurements made at Caltech (open squares) for Ge, Si, In, Ga, and Al,* respectively. The only measurements which seem inconsistent with the rest of the data are the Si_x alloys tested by Meli, *et al.*[11] (**Figure IV-7**, circles). While the scatter in all of the unit cell volume measurements is 0.1 - 0.15%, the volumes for these alloys deviate by ~1% from the other measurements. These data points were not included in further analysis. For all other alloys, the Caltech measurements are consistent with those found in the literature, and all measurements are approximately linear with solute composition, x. The dependencies of unit cell volumes on solute atom and composition are shown in **equations IV.1 - IV.12.**

Group IVA	$V_{Sn}^{Lit.} = 86.73 + 10.18 * x_{Sn}$	[IV.1] [13]
	$V_{Sn}^{CIT} = 86.95 + 9.97 * x_{Sn}$	[IV.2]
	$V_{Ge} = 86.85 + 2.27 * x_{Ge}$	[IV.3] [10]
	$V_{Si} = 86.91 - 0.28 * x_{Si}$	[IV.4] [5,10]
Group IIIA	$V_{In} = 86.85 + 10.35 * x_{In}$	[IV.5] [4]

	$V_{Ga} = 86.76 + 3.84 * x_{Ga}$	[IV.6]	[2]
	$V_{Al} = 86.72 + 3.77 * x_{Al}$	[IV.7]	[8,9]
Transition	$V_{Cr} = 87.01 + 1.50 * x_{Cr}$	[IV.8]	[14]
Metals	$V_{Mn} = 86.92 + 4.87 * x_{Mn}$	[IV.9]	[15,16]
	$V_{Fe} = 86.83 + 2.02 * x_{Fe}$	[IV.10]	[17]
	$V_{Co} = 86.71 + 0.59 * x_{Co}$	[IV.11]	[18,19]
	$V_{Cu} = 86.55 + 1.70 * x_{Cu}$	[IV.12]	[20]

The lattice parameters of Ni-substituted $LaNi_5$ are frequently found to follow Vegard's law, but this has not been related to the solute metallic radius. Although the alloy lattice parameters may depend on several effects (magnetic, bond strength, site occupation), the predominant controlling factor is the solute metallic radius. The effect of bond strength should be small in transition metal-substituted alloys, because they do not have large heats of formation with La. Fe and Co are magnetic, and order on the Ni sublattice. As all of the p-shell metals used in this work are non-magnetic and are expected to occupy the crystallographic 3g site, their effects on the alloy lattice parameters should be comparable. When the lattice parameters and unit cell volumes are plotted *vs* solute composition, the slopes of the lines characterize the effectiveness of the solute in expanding the lattice. These values should be proportional to the metallic radius of the solute, or more accurately, the difference R_{Ni}-R_M (included in the table of solute properties found in **Appendix A**). **Figure IV-11** displays the slopes found in **equations IV.1 - IV.12** *vs* the difference between the solute metallic radius and that of nickel.

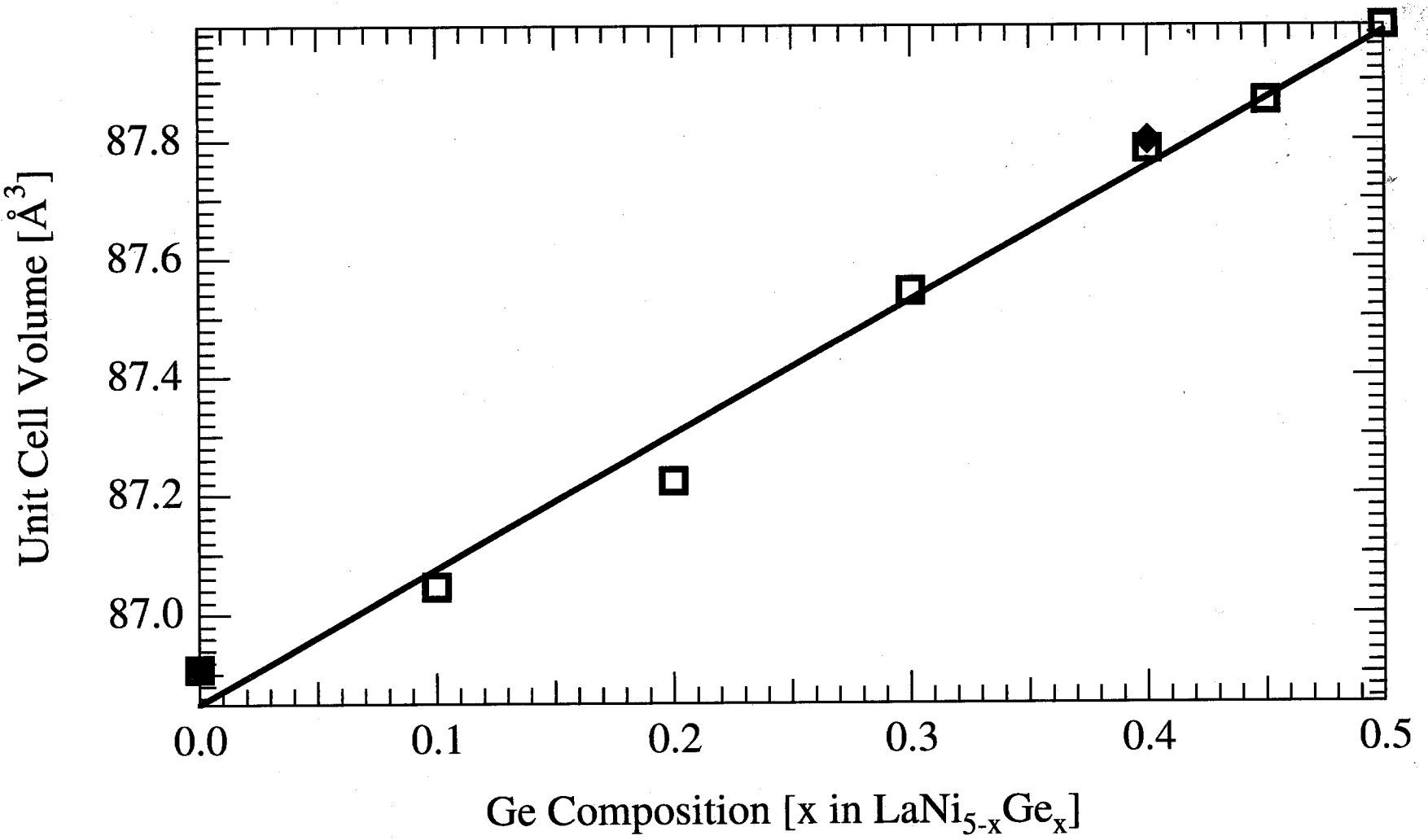

Figure IV-6 Unit cell volumes of $LaNi_{5-x}Ge_x$ alloys *vs* Ge composition, x.
{ ◆ - literature measurements, ◘ - Caltech measurements}

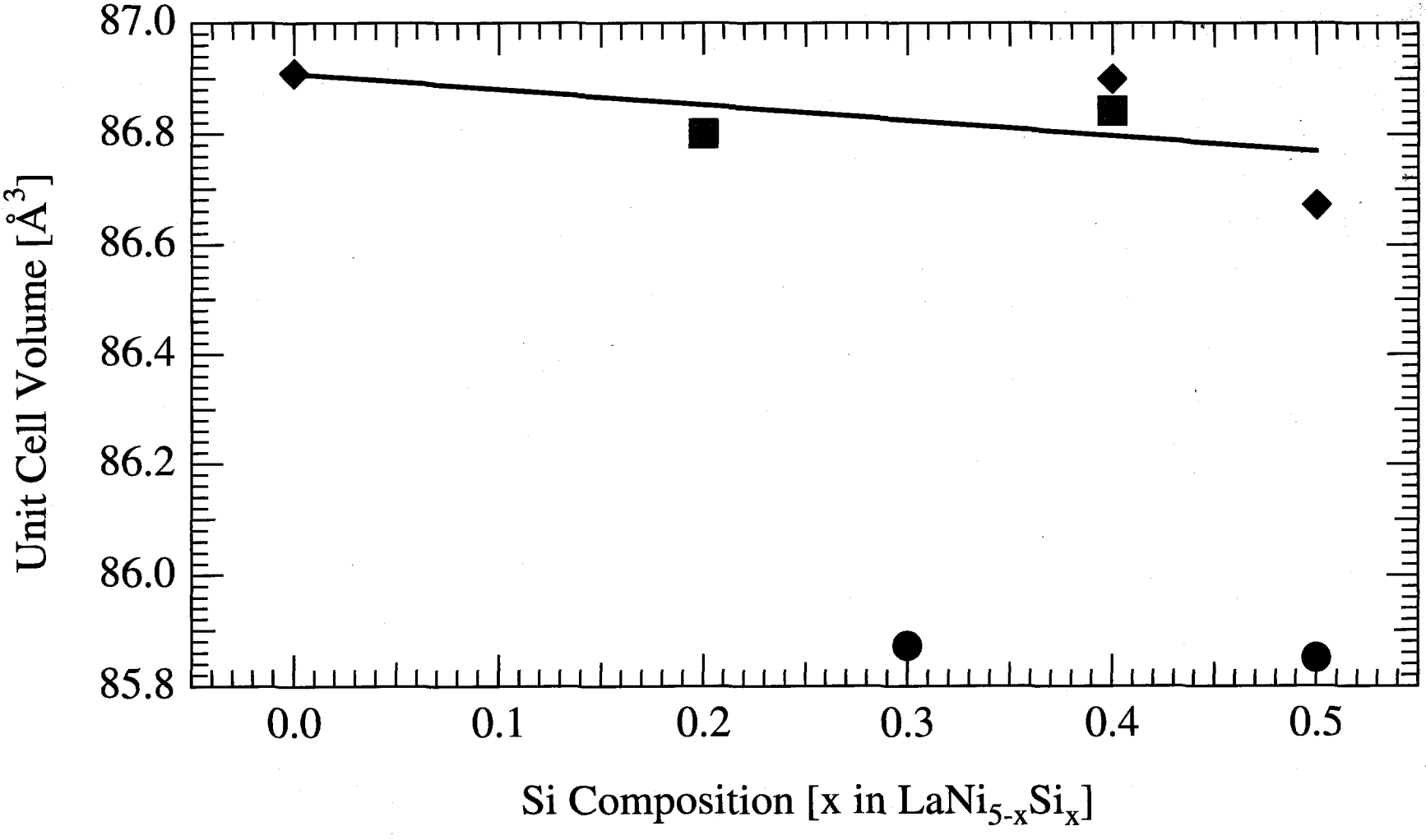

Figure IV-7 Unit cell volumes of $LaNi_{5-x}Si_x$ alloys *vs* Si composition, x.
{ ◆ , ● - literature measurements, ◘ - Caltech measurements}

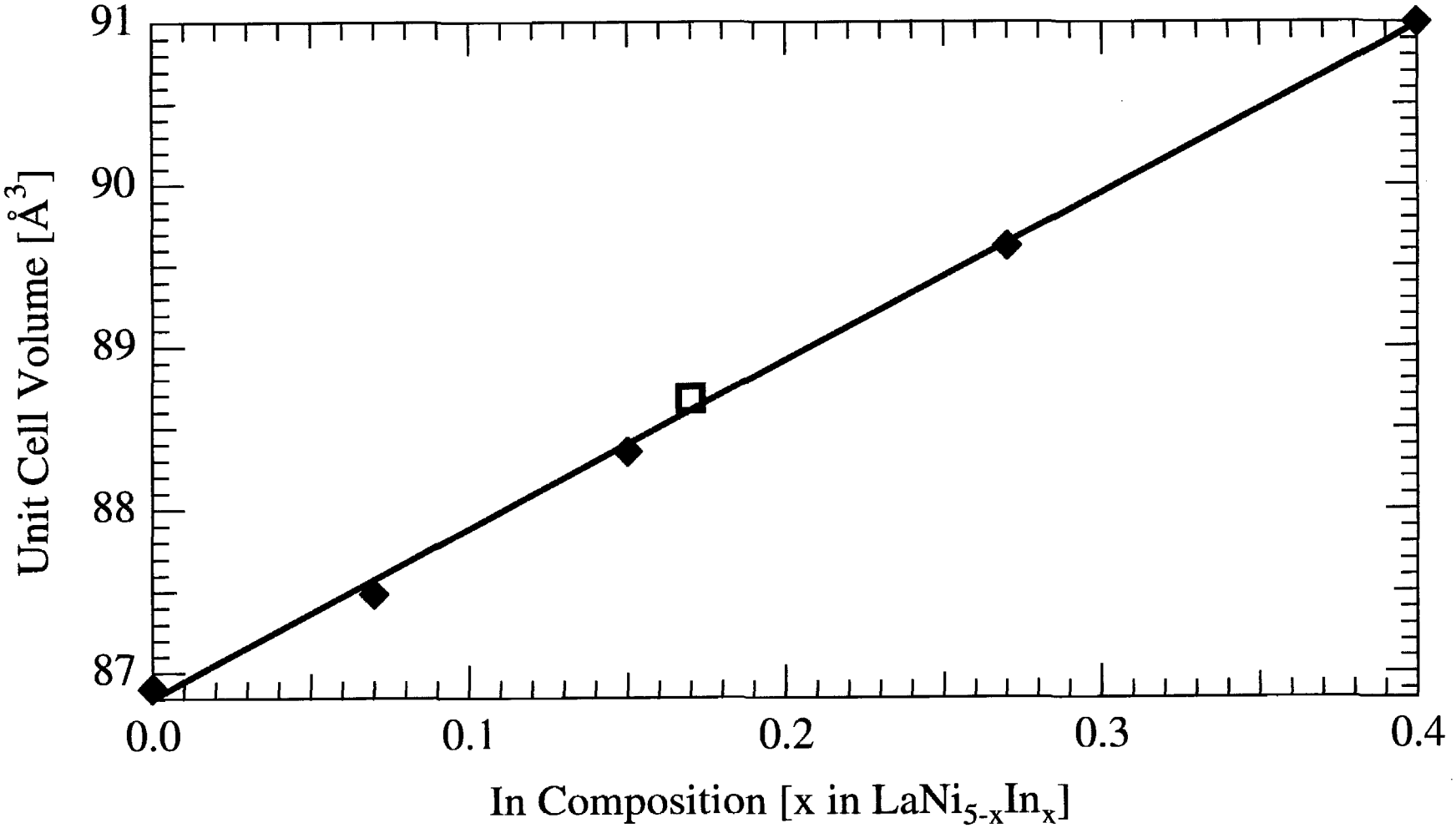

Figure IV-8 Unit cell volumes of $LaNi_{5-x}In_x$ alloys *vs* In composition, x.
{ ◆ - literature measurements, ◘ - Caltech measurements}

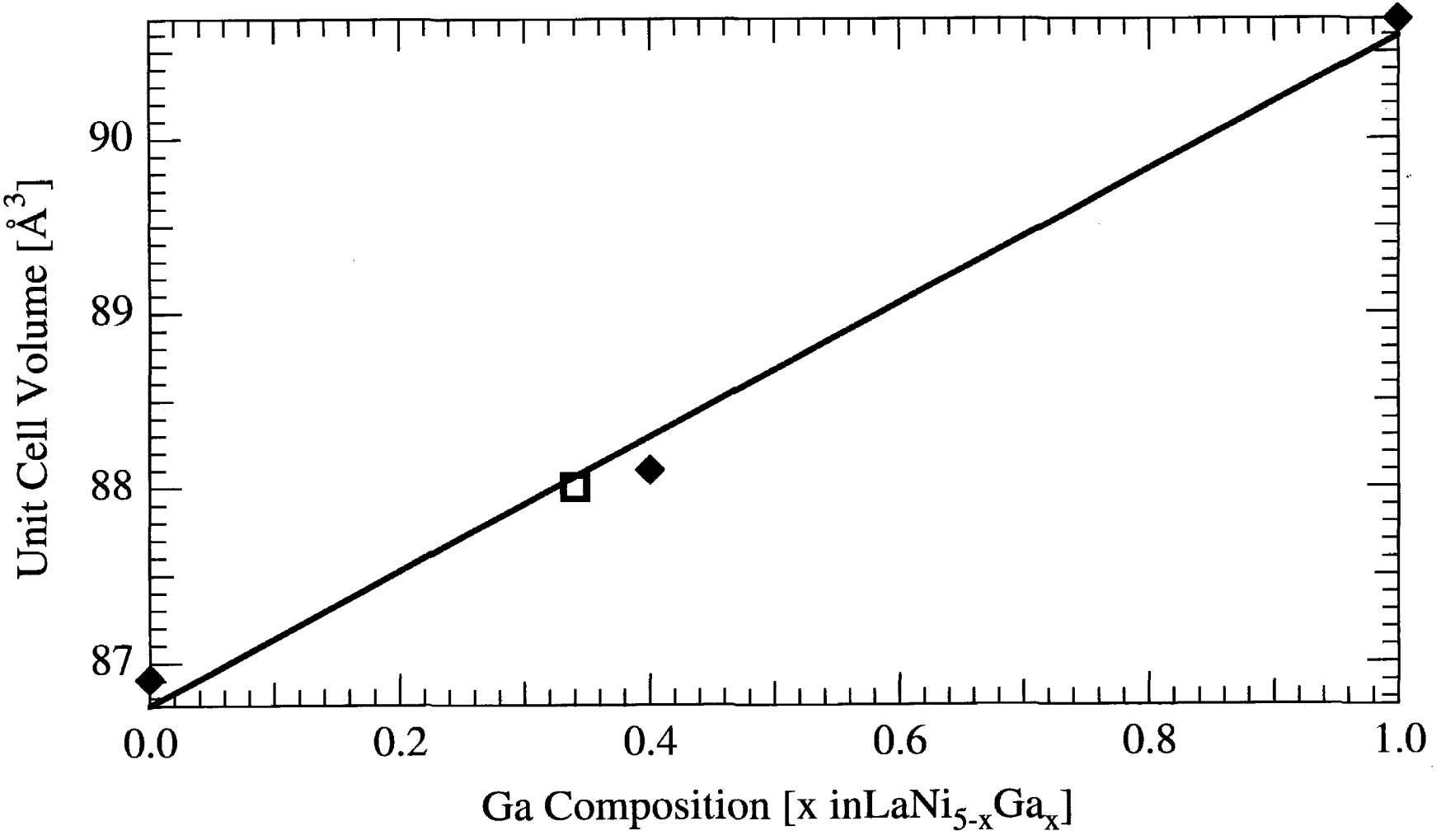

Figure IV-9 Unit cell volumes of $LaNi_{5-x}Ga_x$ alloys *vs* Ga composition, x.
{ ◆ - literature measurements, ◘ - Caltech measurements}

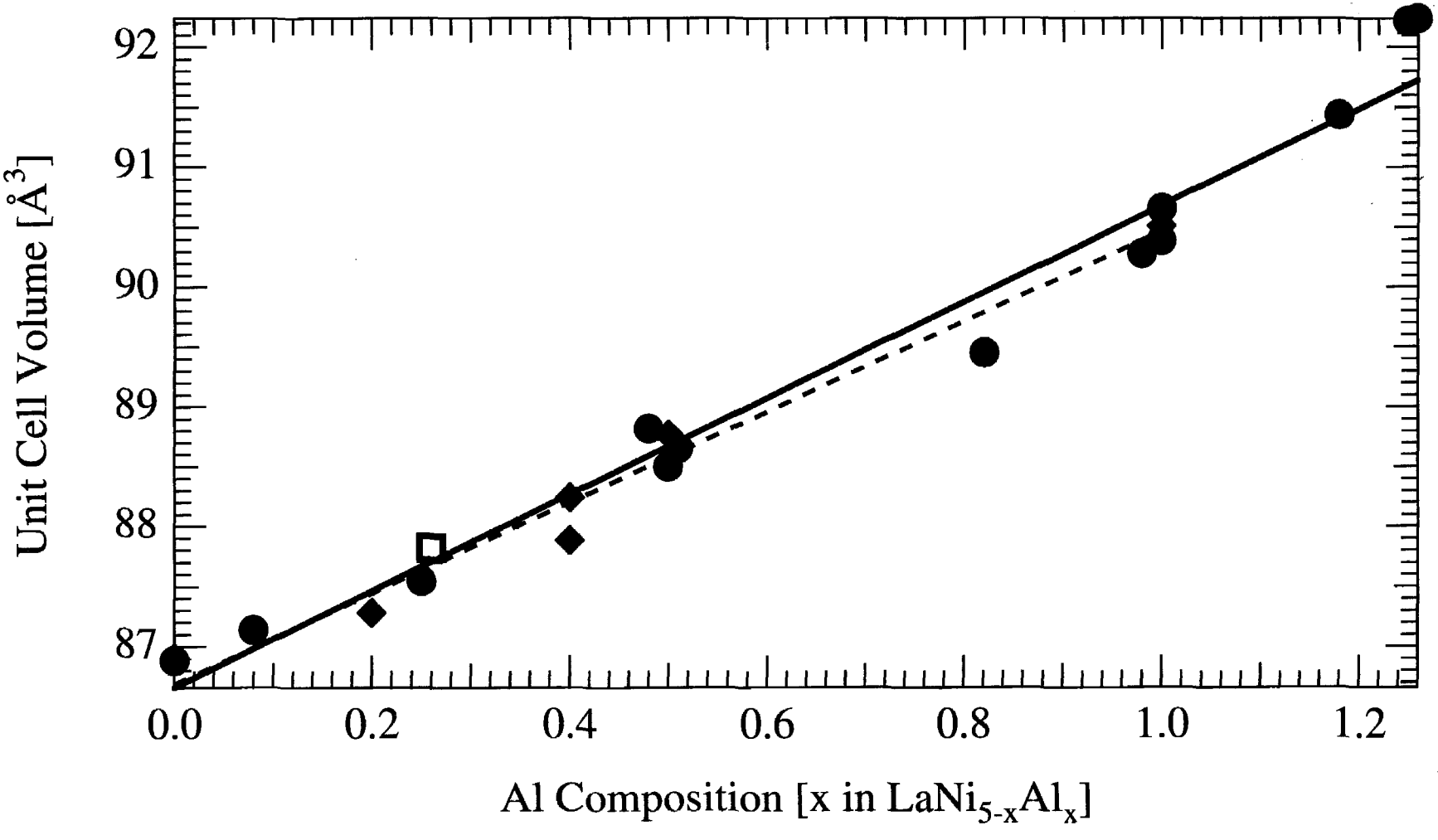

Figure IV-10 Unit cell volumes of $LaNi_{5-x}Al_x$ alloys *vs* Al composition, x.
{ ● , ◆ - literature measurements, ◘ - Caltech measurements}

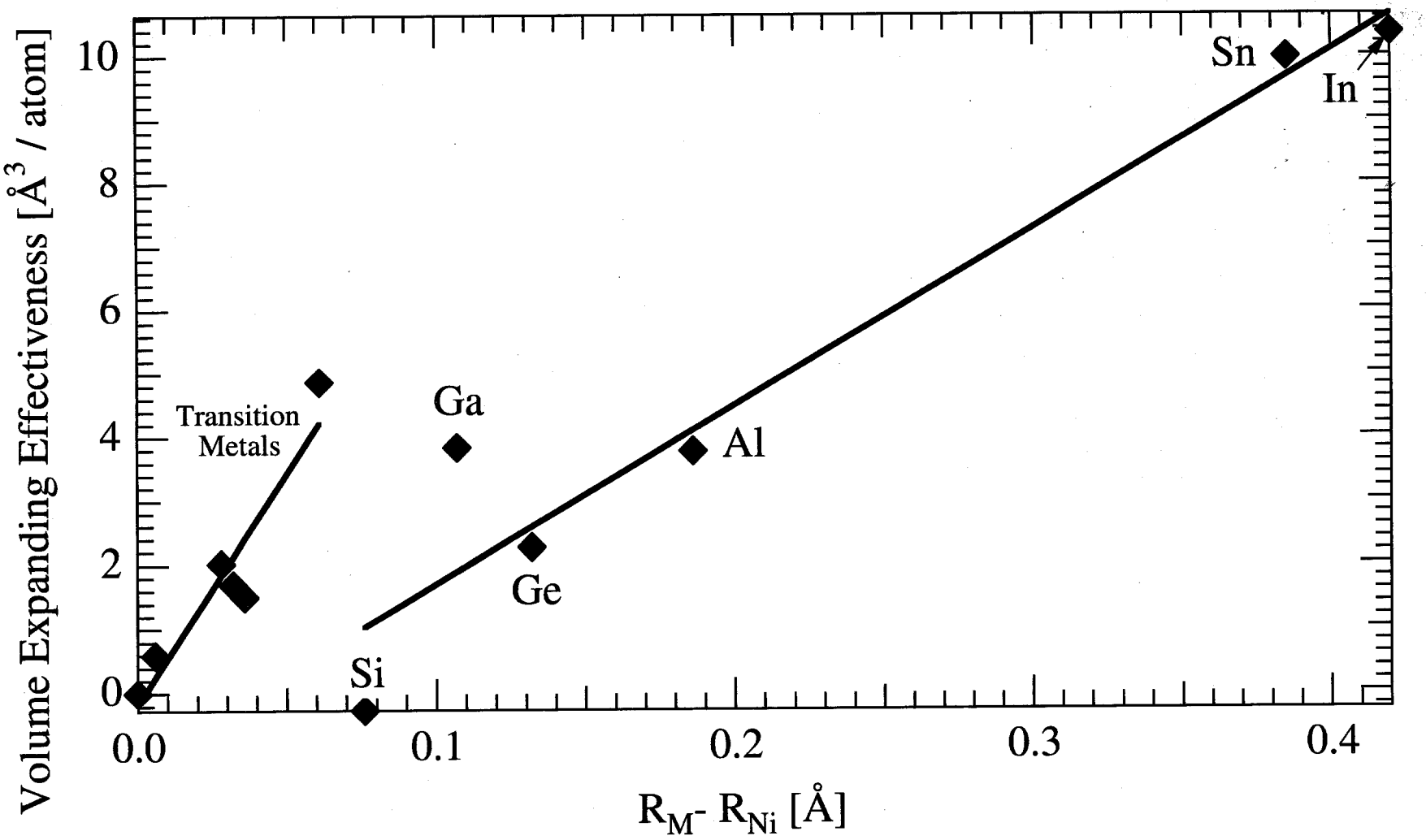

Figure IV-11 Correlation of solute effectiveness in expanding $V_{unit\ cell}$ with solute metallic radius.

C. Hydride Volume Expansion

1. Literature Survey

The lattice expanding behavior of $LaNi_5$ and its Ni-substituted alloys has been discussed in the introduction, sections §II.C.3 and §II.D.3, respectively. There are numerous measurements of *total* lattice expansions between dehydrided and fully hydrided alloys to be found in the literature. **Figures IV-12 - IV-14** show total a-axis, c-axis, and volume expansions of ternary $LaNi_5$ alloys substituted with transition metals *vs* solute composition x. **Equations IV.13 - IV.16** are linear fits to the lattice expansion data available in the literature. Lattice expansions for sp-shell metal-substituted $LaNi_5$ are included with the results in the next section.

$\Delta a/a^{Cr} = 7.73 - 0.09\ x$; $\Delta c/c^{Cr} = 7.47 - 1.00\ x$; $\Delta V/V^{Cr} = 24.71 - 1.01\ x$ [IV.13][14]

$\Delta a/a^{Mn} = 7.59 - 1.28\ x$; $\Delta c/c^{Mn} = 7.64 - 1.57\ x$; $\Delta V/V^{Mn} = 24.58 - 4.66\ x$ [IV.14][14,15,24]

$\Delta a/a^{Cu} = 7.57 - 0.55\ x$; $\Delta c/c^{Cu} = 7.08 - 3.25\ x$; $\Delta V/V^{Cu} = 23.88 - 5.04\ x$ [IV.15][5,14]

$\Delta a/a^{Fe} = 7.39 - 1.05\ x$; $\Delta c/c^{Fe} = 7.01 - 2.38\ x$; $\Delta V/V^{Fe} = 24.08 - 5.61\ x$ [IV.16][25,27]

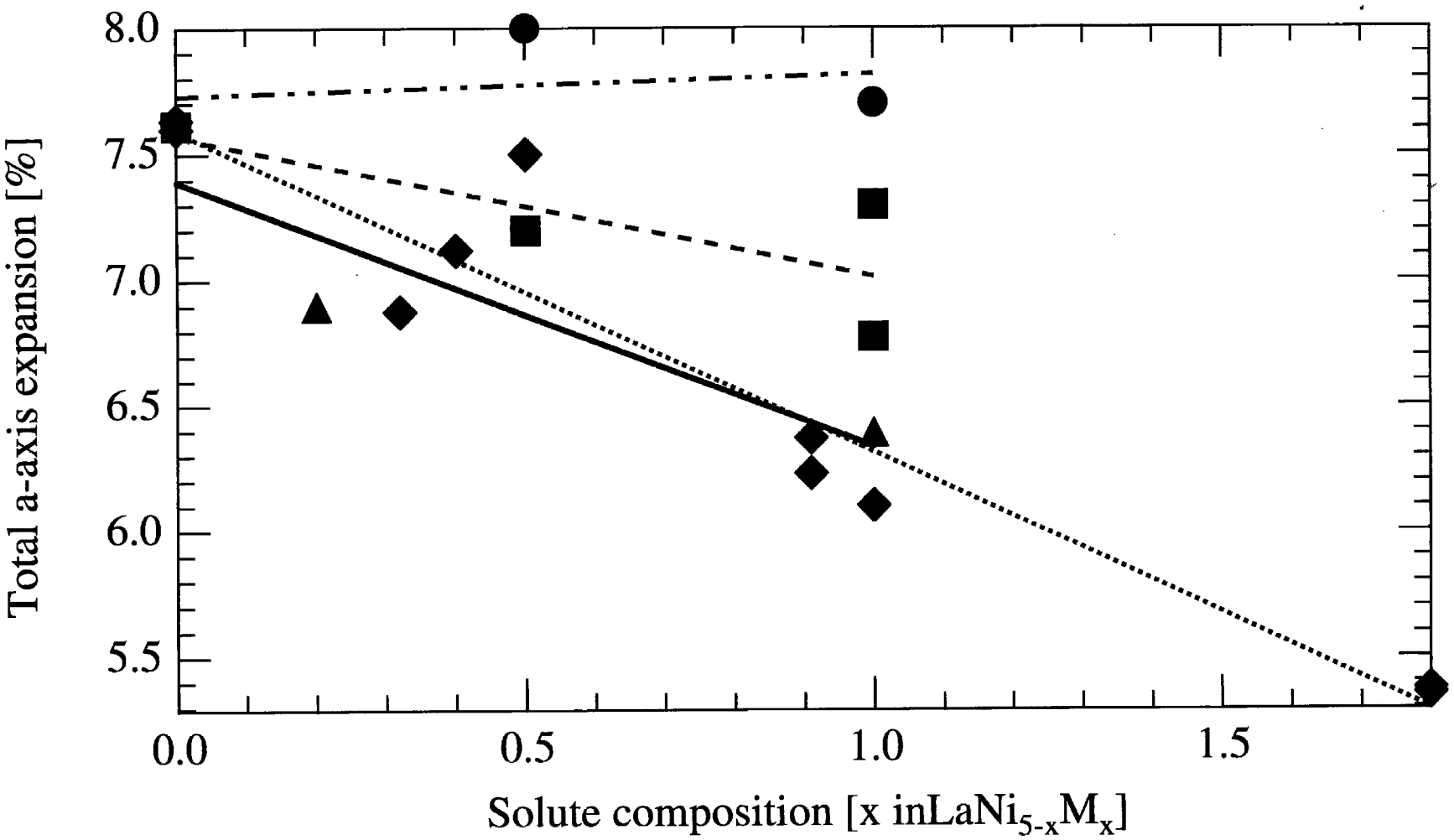

Figure IV-12 Δa/a [%] for transition-metal substituted $LaNi_{5-x}M_x$.
{– · –, ● - Cr; ····· , ◆ - Mn; – – –, ■ - Cu; ——, ▲ - Fe}

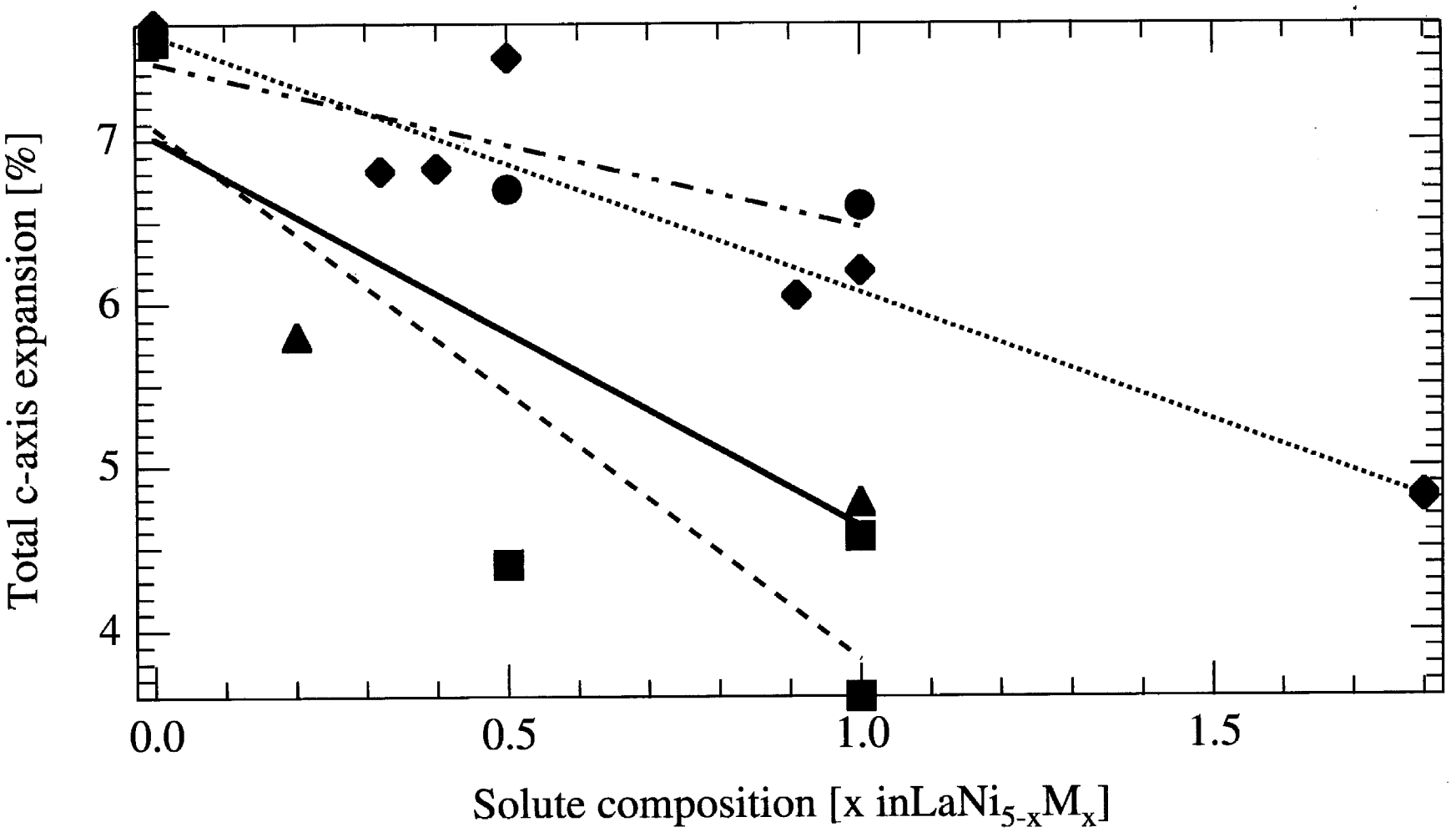

Figure IV-13 $\Delta c/c$ [%] for transition-metal substituted $LaNi_{5-x}M_x$.
{– · ·, ● - Cr; ·····, ◆ - Mn; - - -, ■ - Cu; ——, ▲ - Fe}

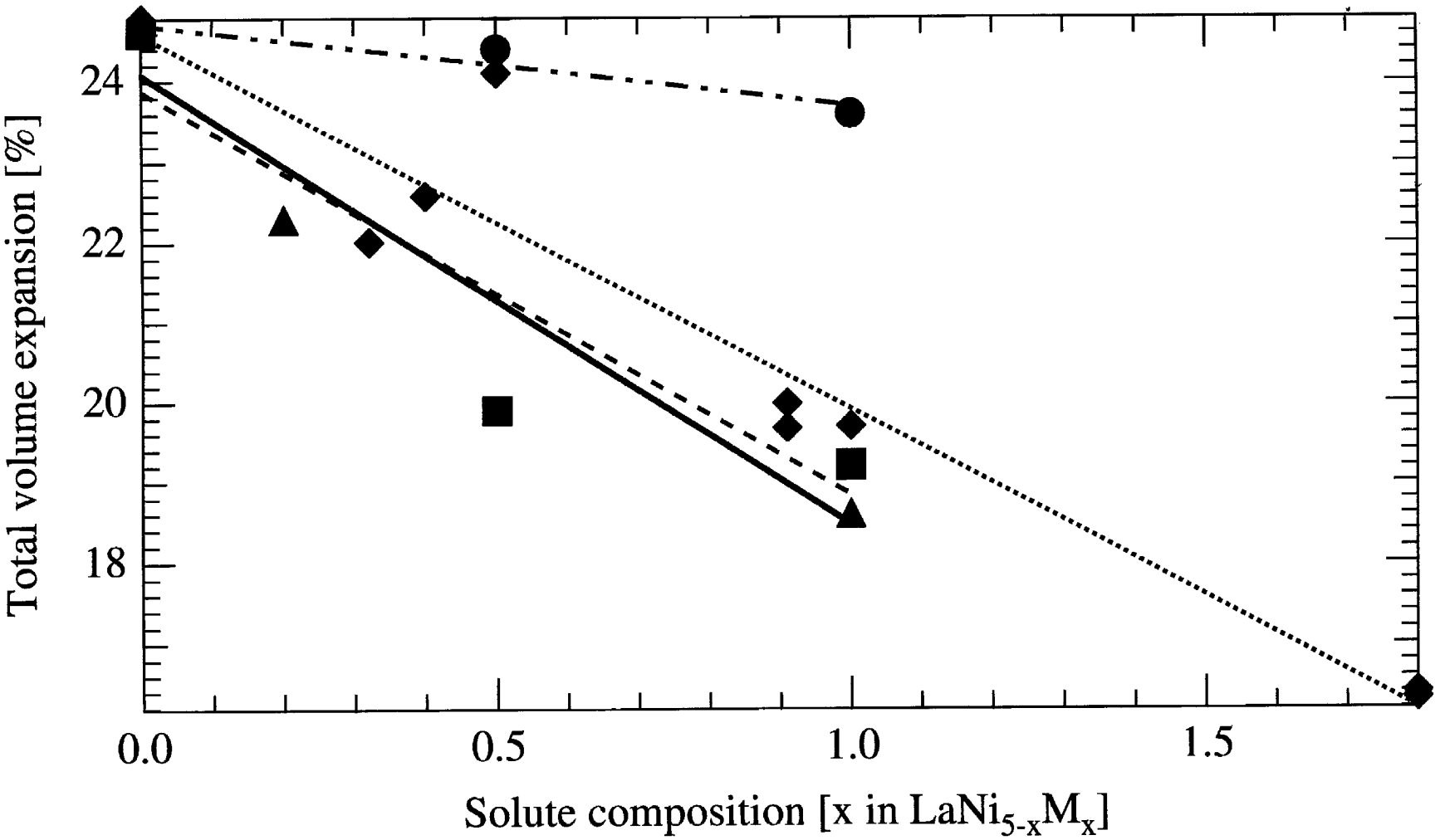

Figure IV-14 $\Delta V/V$ [%] for transition-metal substituted $LaNi_{5-x}M_x$.
{– · · –, ● - Cr; ····· , ◆ - Mn; – – –, ■ - Cu; ——, ▲ - Fe}

2. Caltech Results

As discussed in *Methods* (III.C.5), the lattice parameters of hydrided alloys were measured by 'poisoning' the surface of the alloys with CO after they had been fully charged with hydrogen. Evolution of the diffraction patterns of several metal hydrides as they desorbed hydrogen are exhibited in **Figures IV-15 - IV-23**. Total lattice expansion was determined between lattice parameters obtained from patterns taken immediately after hydriding and those of dehydrided (10^{-4} torr @ 300° C) alloys. Discontinuous lattice expansion was determined from patterns containing diffraction peaks from both the α- and β-phase hydrides.

Figures IV-24 - IV-26 show the a-axis, c-axis, and volume expansions of sp-shell metal substituted $LaNi_5$. Data from the literature are denoted by closed symbols and Caltech measurements (both total and discontinuous) by open symbols. Total lattice expansion values measured at Caltech are consistent with those taken from the literature. The total and discontinuous lattice expansion values measured at Caltech in **Figures IV-24 - IV-27** are connected by vertical lines, and total expansion is in all cases greater than discontinuous.

The lattice expansions of Ge_x alloys measured at Caltech are shown in **Figure IV-27**. There is some experimental scatter in the total lattice expansion values of the Ge_x alloys (closed symbols). This can be attributed to a variation in the alloy hydrogen composition after poisoning resulting from inconsistencies in the poisoning procedure. This is confirmed by examining the diffraction patterns during hydrogen desorption, **Figures IV-19 - IV-23**. There is no diffraction pattern of the $Ge_{0.4}$ alloy exclusively in the β-phase (**Figure IV-22**). The β-phase lattice parameters of the first $Ge_{0.4}H_y$ diffraction pattern after hydriding were used to calculate total lattice expansion, as they are greater than those obtained from subsequent patterns. The presence of diffraction peaks from the α-phase while the β-phase is in the continuous regime of volume expansion implies that

some of the alloy was passivated, and did not absorb hydrogen. The total volume expansion measured for this alloy is smaller than that measured for $Ge_{0.5}$, implying that the $Ge_{0.4}$ alloy was not at its maximum hydrogen composition when the diffraction pattern was measured. Similarly, the total volume expansion measured for the $Ge_{0.2}$ alloy is less than that of the $Ge_{0.3}$ alloy. The XRD patterns in **Figure IV-20** show that this alloy desorbed hydrogen very quickly. The diffraction pattern taken 1 day after hydriding shows only a few small peaks from the β-phase (<5%). It is probable that this alloy lost hydrogen before diffraction patterns were measured. Because the total lattice expansion values measured at Caltech for M_x alloys are consistent with those values found in the literature, the results for Ge_x alloys will be considered accurate except when obvious inconsistencies are present, as in $Ge_{0.2}$ and $Ge_{0.4}$.

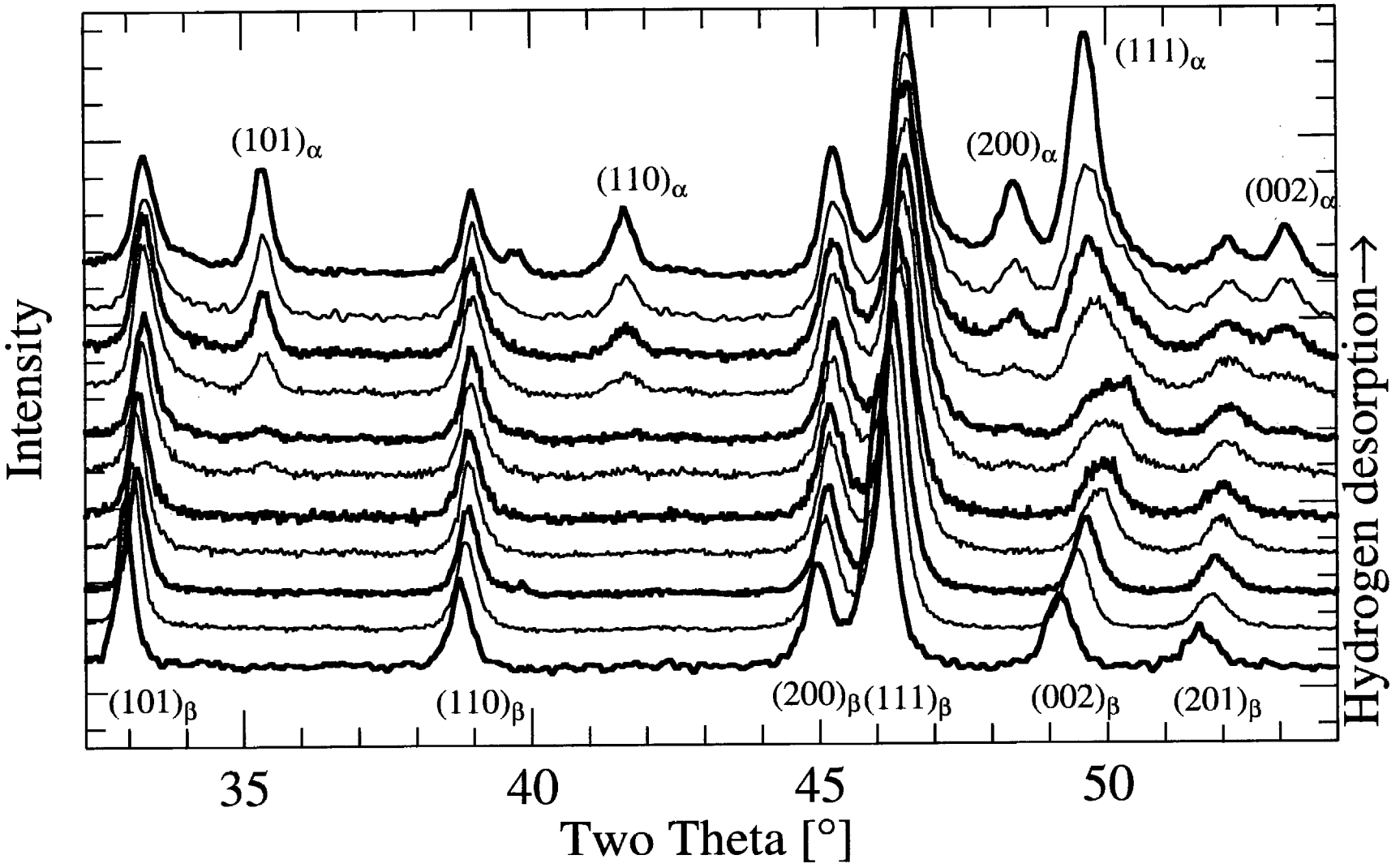

Figure IV-15 Evolution of XRD pattern of $LaNi_{4.83}In_{0.17}H_y$ as alloy evolves hydrogen.

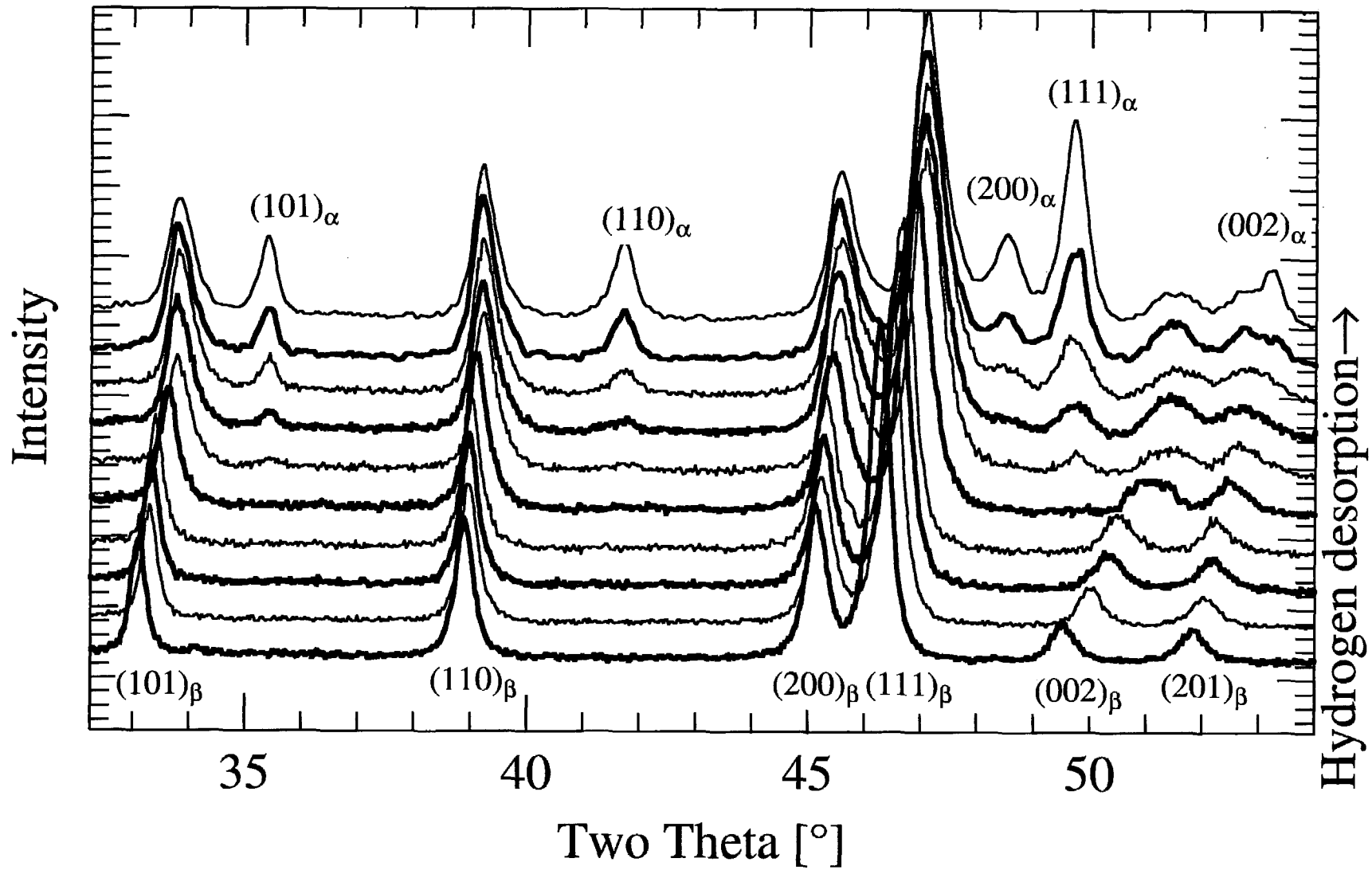

Figure IV-16 Evolution of XRD pattern of $LaNi_{4.74}Al_{0.26}H_y$ as alloy evolves hydrogen.

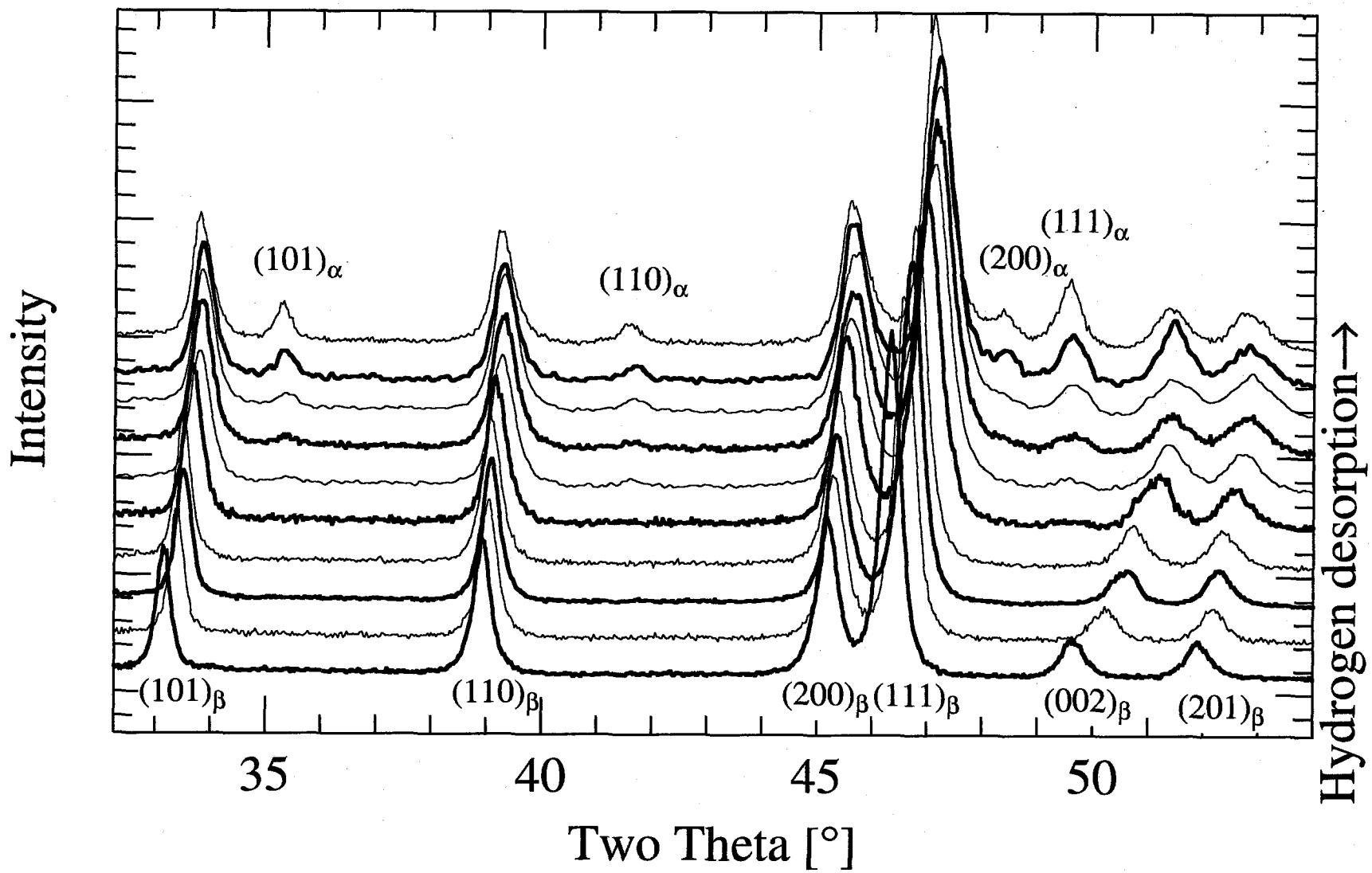

Figure IV-17 Evolution of XRD pattern of $LaNi_{4.66}Ga_{0.34}H_y$ as alloy evolves hydrogen.

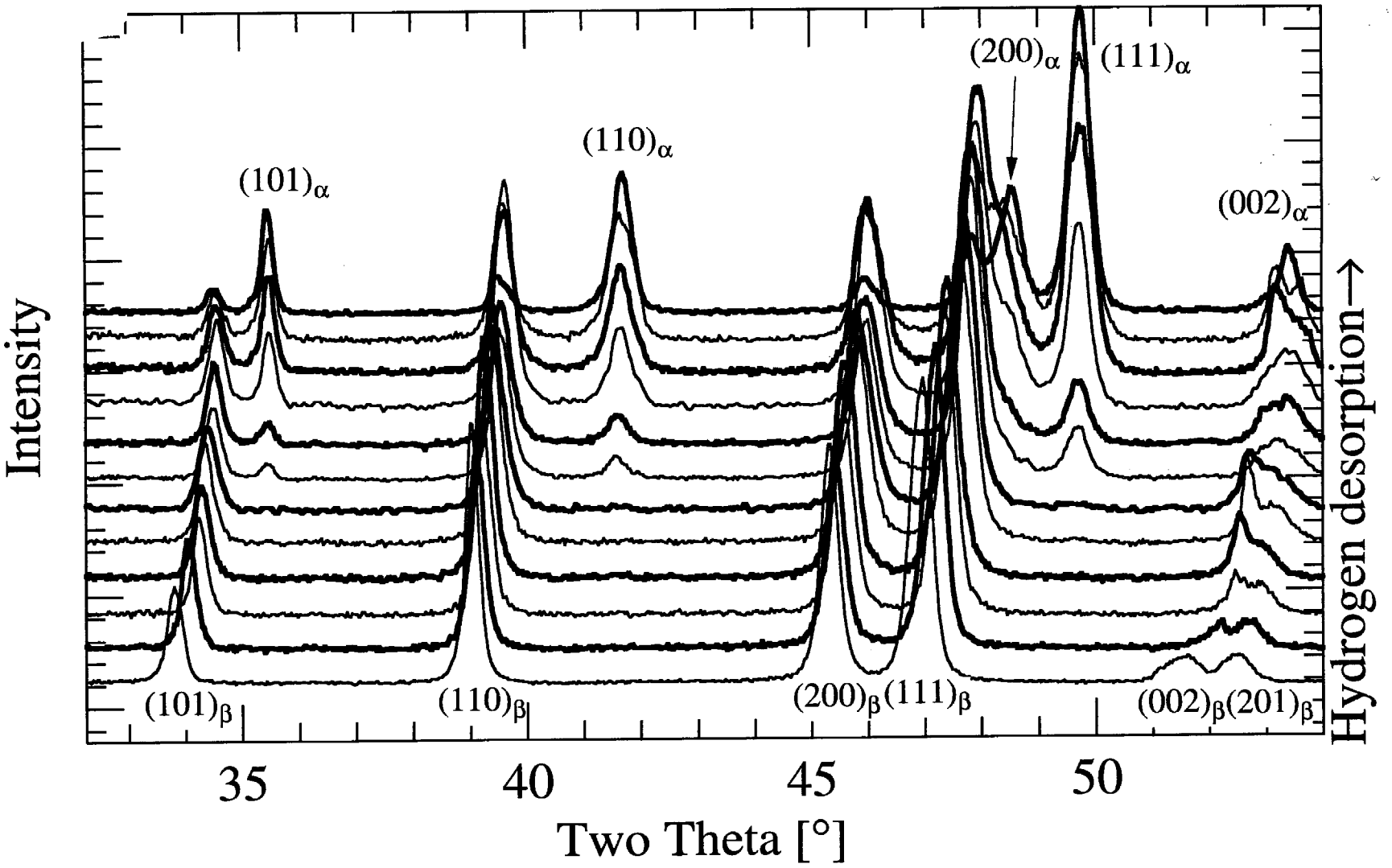

Figure IV-18 Evolution of XRD pattern of $LaNi_{4.6}Si_{0.4}H_y$ as alloy evolves hydrogen.

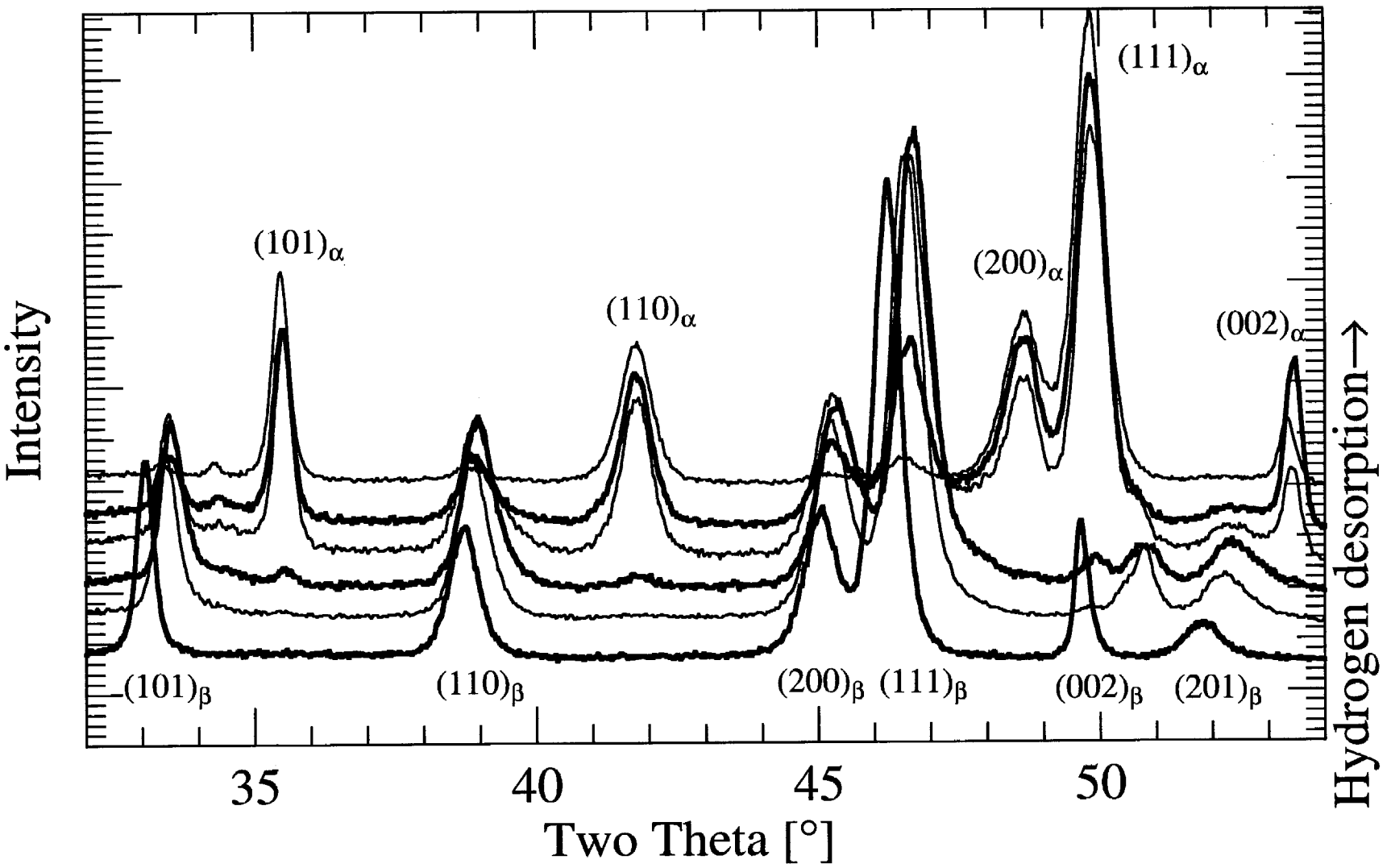

Figure IV-19 Evolution of XRD pattern of $LaNi_{4.9}Ge_{0.1}H_y$ as alloy evolves hydrogen.

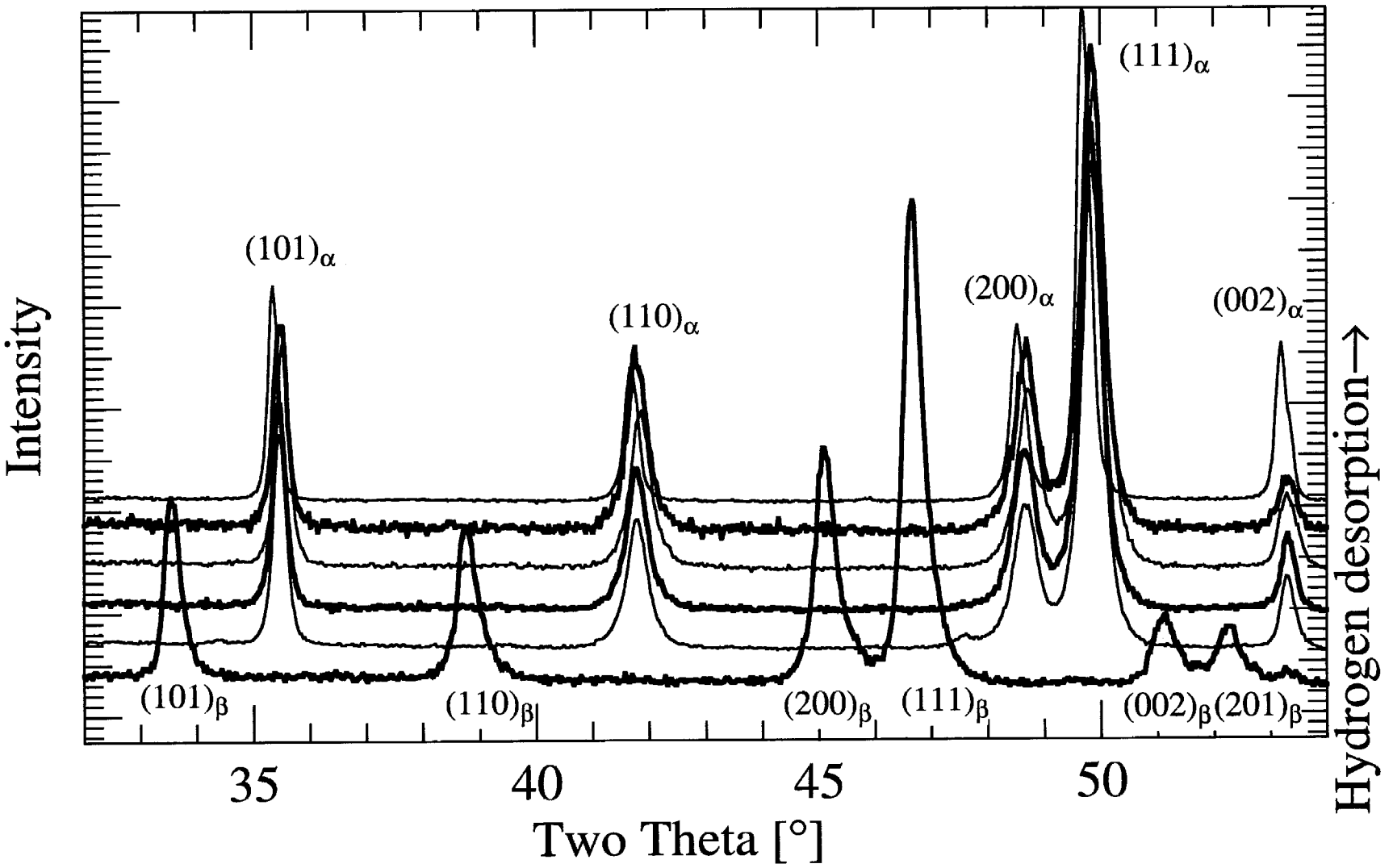

Figure IV-20 Evolution of XRD pattern of $LaNi_{4.8}Ge_{0.2}H_y$ as alloy evolves hydrogen.

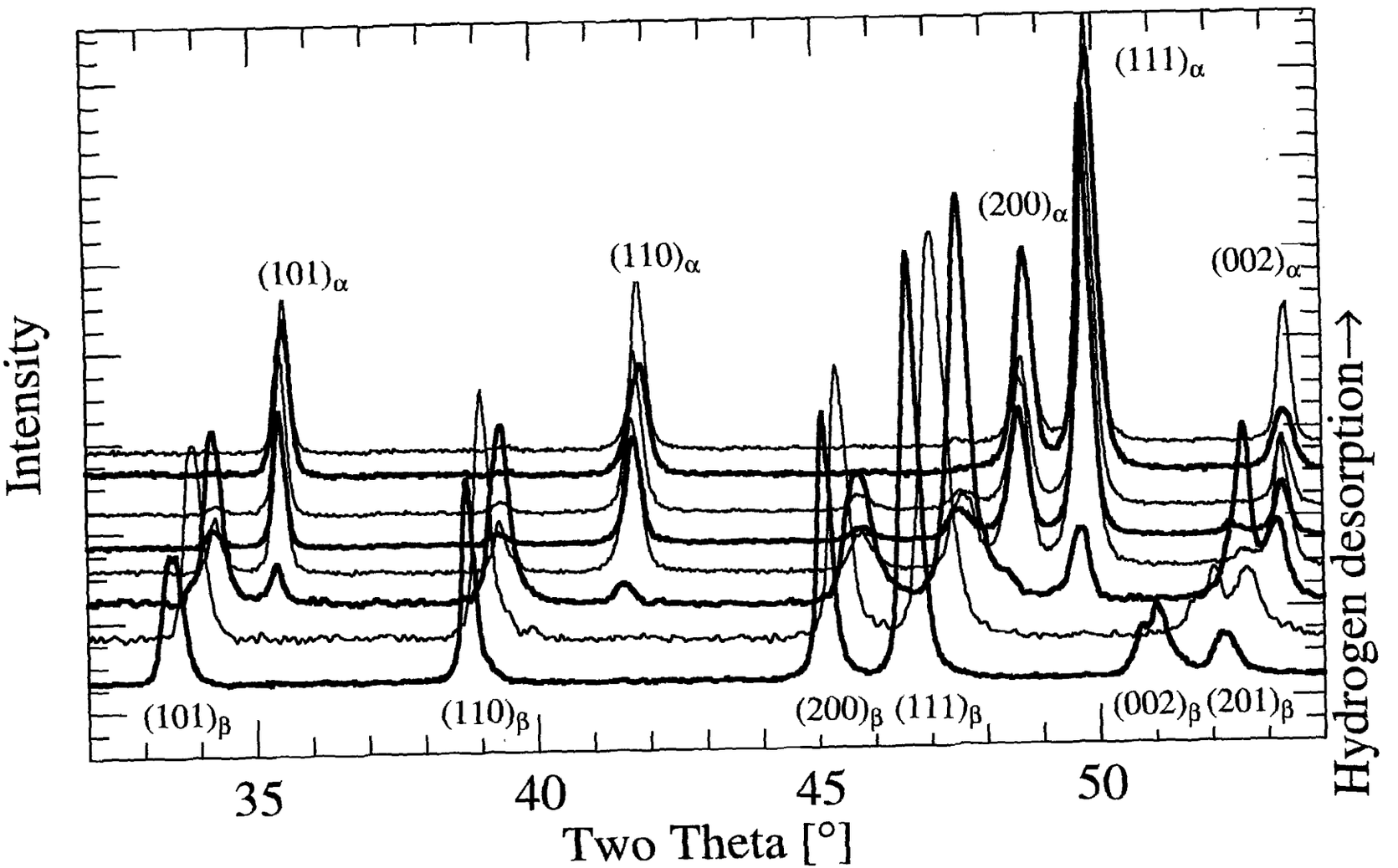

Figure IV-21 Evolution of XRD pattern of $LaNi_{4.7}Ge_{0.3}H_y$ as alloy evolves hydrogen.

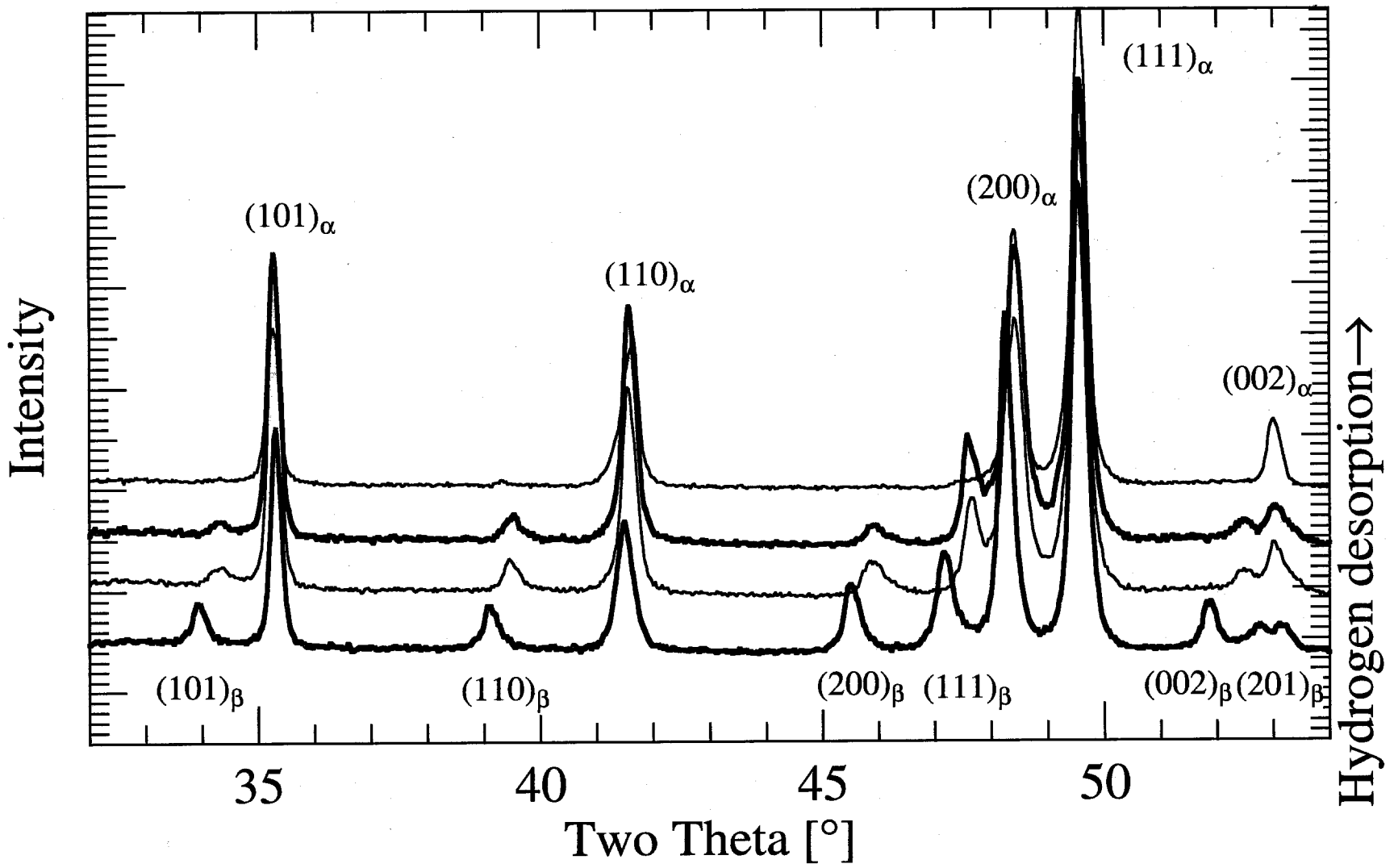

Figure IV-22 Evolution of XRD pattern of $LaNi_{4.6}Ge_{0.4}H_y$ as alloy evolves hydrogen.

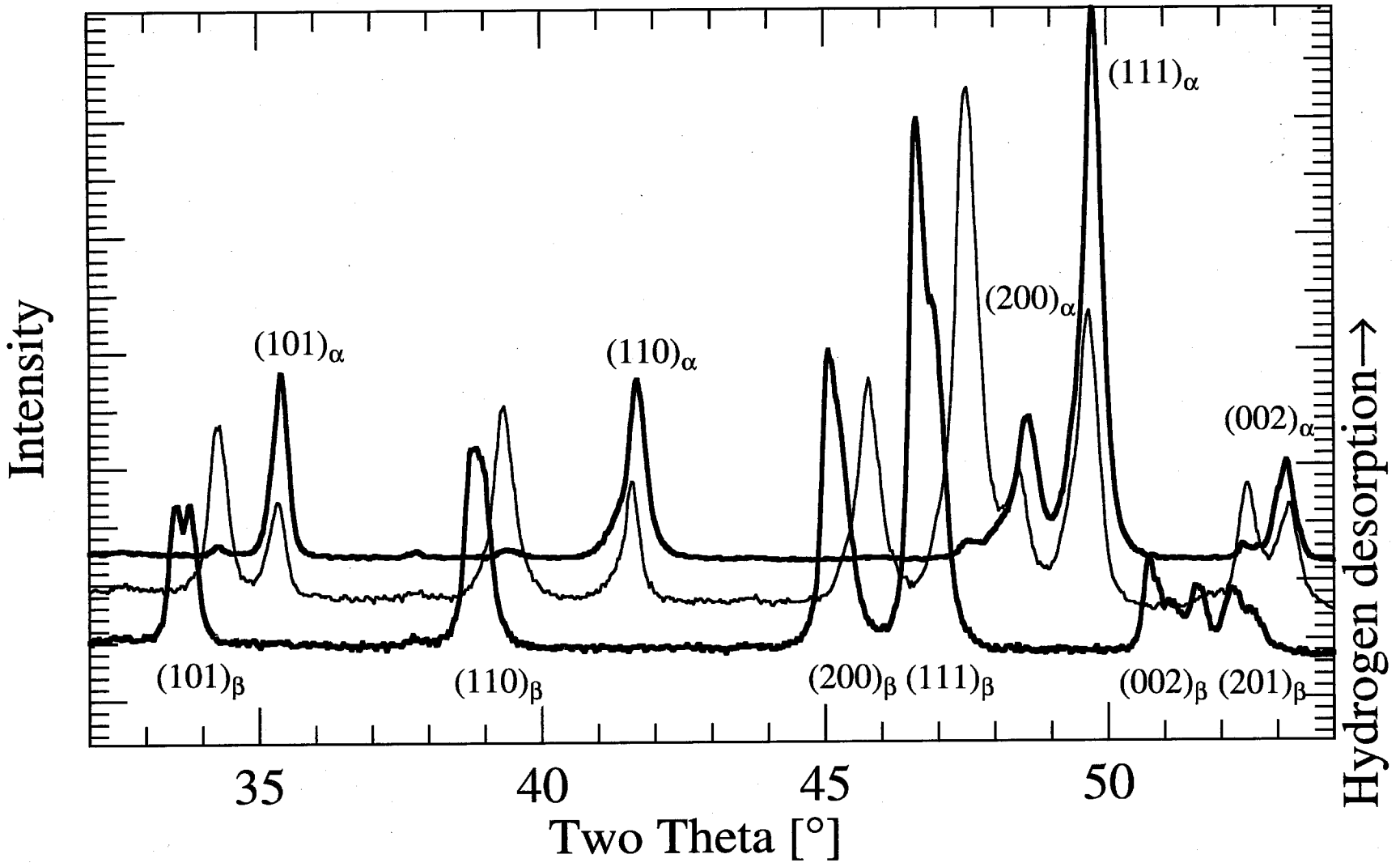

Figure IV-23 Evolution of XRD pattern of $LaNi_{4.5}Ge_{0.5}H_y$ as alloy evolves hydrogen.

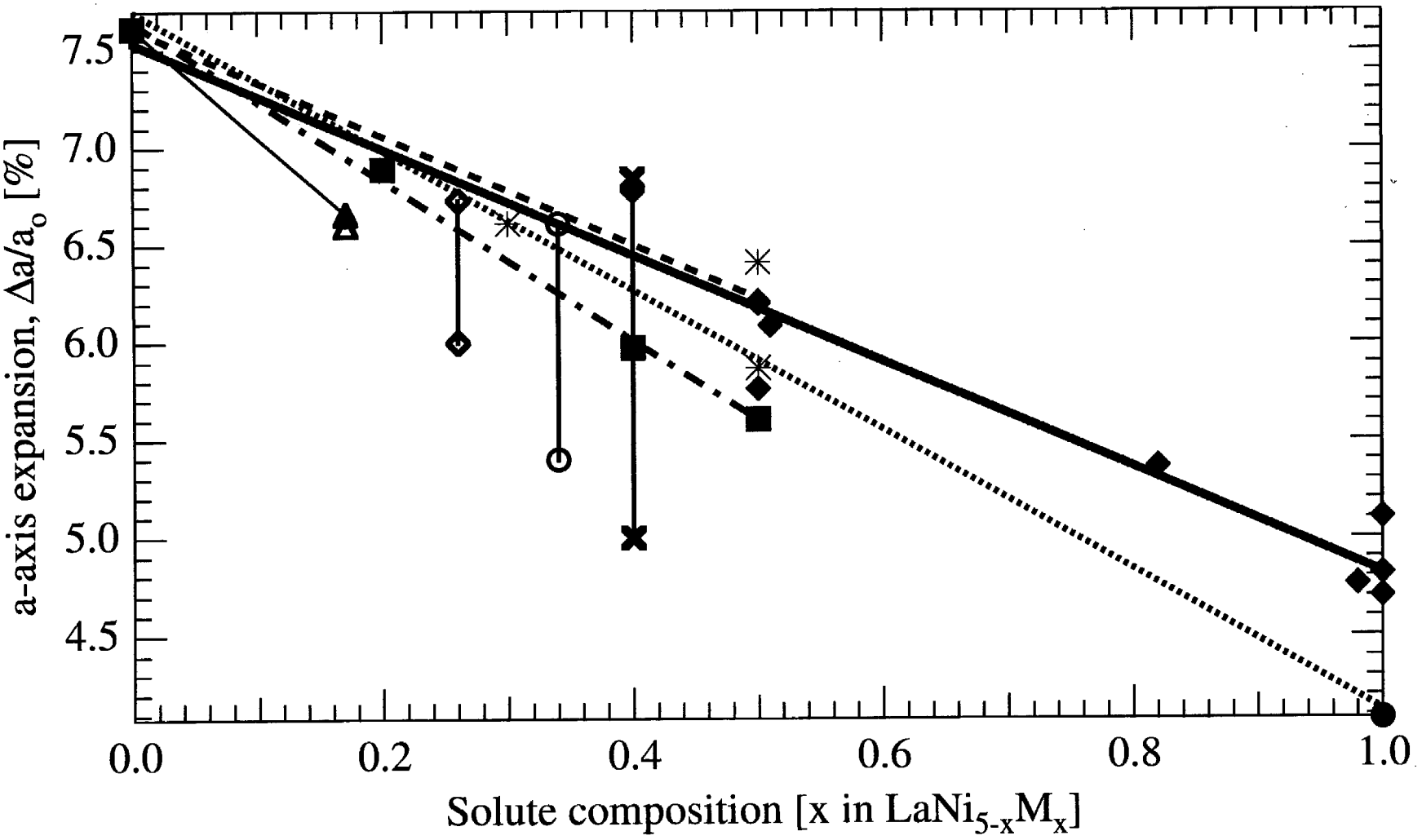

Figure IV-24 Δa/a [%] for p-shell metal-substituted $LaNi_{5-x}M_x$.
{—○—, ● - Ga; ■ - Sn;—◆—, ◆ - Al;—✖—, ✳ - Si;—△—, ▲ - In}

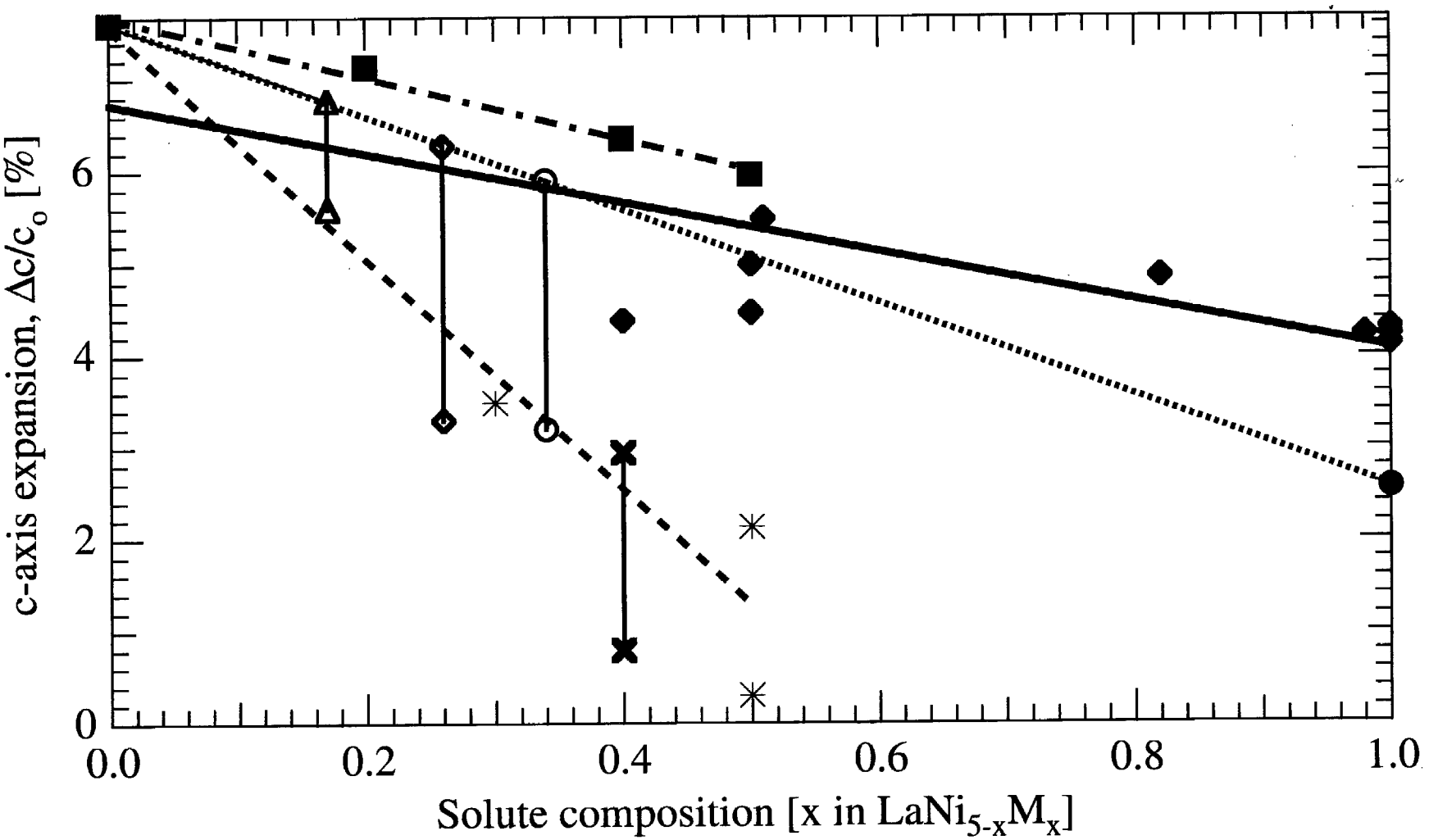

Figure IV-25 Δc/c [%] for p-shell metal-substituted $LaNi_{5-x}M_x$.
{—o—, ● - Ga; ■ - Sn;—◆—, ◆ - Al;—✖—, ✳ - Si;—△—, ▲ - In}

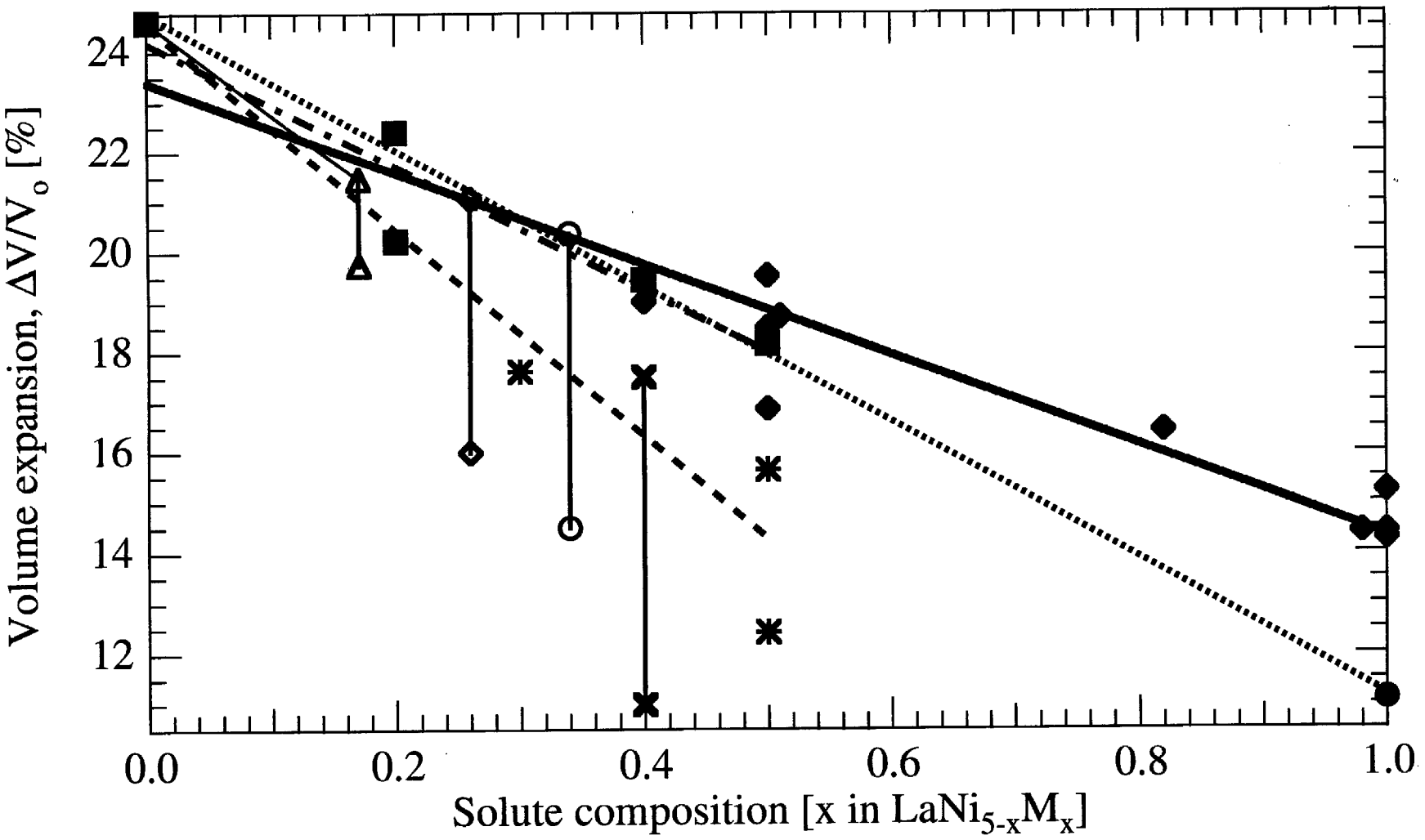

Figure IV-26 ΔV/V [%] for p-shell metal-substituted $LaNi_{5-x}M_x$.
{—o—, ● - Ga; ■ - Sn;—◆—, ◆ - Al;—✱—, ✱ - Si;—△—, ▲ - In}

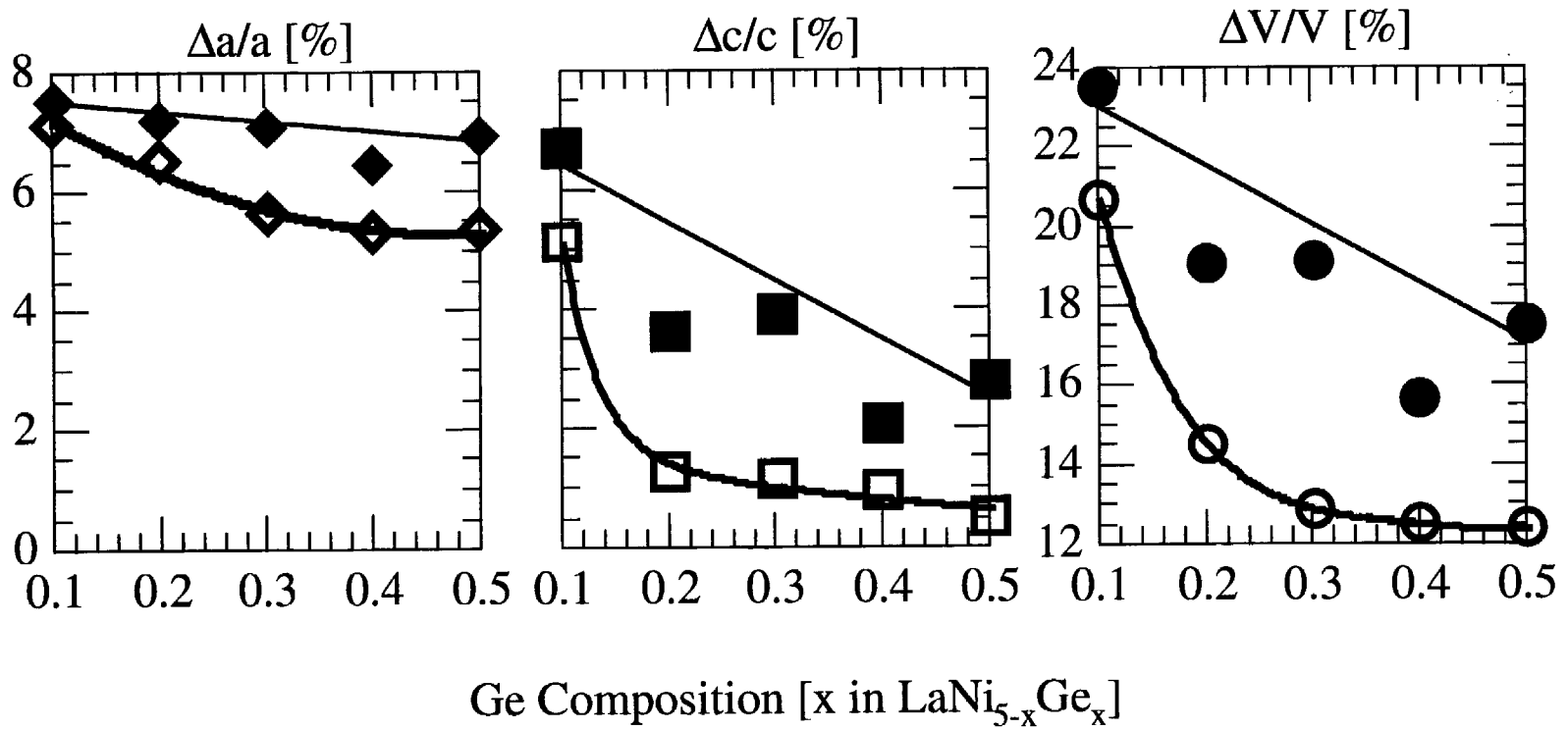

Figure IV-27 Discontinuous (open symbols) and total (closed symbols) lattice expansions for $LaNi_{5-x}Ge_x$.

3. Discussion

In general, the reduction in total lattice expansions of hydriding are approximately linear with substituted composition. **Equations IV.17 - IV.21** are linear fits of the total lattice expansion data to substituted composition. The somewhat non-linear behavior of $\Delta c/c$ and $\Delta V/V$ in Al_x alloys results from the inclusion of measurements by Gruen, *et al.* (x_{Al} = 0.4 & 0.5). Only data from $Ge_{0.1}$, $Ge_{0.3}$, and $Ge_{0.5}$ were used in the Ge_x fits of total expansion data. Because the intercepts of the Ge_x fits are consistent with the total lattice expansion of unsubstituted $LaNi_5$, we have confidence in these fits.

$\Delta V/V^{Si} = 24.54 - 20.53x$; $\Delta a/a^{Si} = 7.61 - 2.78x$; $\Delta c/c^{Si} = 7.56 - 12.55x$. [IV.17] [5,11]

$\Delta V/V^{In} = 24.61 - 18.46x$; $\Delta a/a^{In} = 7.61 - 5.61x$; $\Delta c/c^{In} = 7.60 - 4.85x$. [IV.18]

$\Delta V/V^{Ge} = 24.52 - 14.90x$; $\Delta a/a^{Ge} = 7.68 - 1.67x$; $\Delta c/c^{Ge} = 7.42 - 9.81x$. [IV.19]

$\Delta V/V^{Ga} = 24.76 - 13.59x$; $\Delta a/a^{Ga} = 7.70 - 3.58x$; $\Delta c/c^{Ga} = 7.61 - 5.05x$. [IV.20] [2]

$\Delta V/V^{Sn} = 24.18 - 12.32x$; $\Delta a/a^{Sn} = 7.64 - 4.09x$; $\Delta c/c^{Sn} = 7.68 - 3.31x$. [IV.21] [12,14,26]

$\Delta V/V^{Al} = 23.40 - 9.08x$; $\Delta a/a^{Al} = 7.54 - 2.72x$; $\Delta c/c^{Al} = 6.74 - 2.66x$. [IV.22] [9]

$\Delta V/V^{Ge} = 26.85 - 61.52x$; $\Delta a/a^{Ge} = 7.73 - 6.31x$; $\Delta c/c^{Ge} = 9.00 - 38.50x$. [IV.23]

$\Delta V/V^{Ge} = 13.61 - 2.44x$; $\Delta a/a^{Ge} = 6.02 - 1.44x$; $\Delta c/c^{Ge} = 1.90 - 2.61x$. [IV.24]

The discontinuous lattice expansion values of Ge_x alloys, however, are not at all linear with x_{Ge}. The c-axis and volume expansions are substantially reduced for x = 0.2, but subsequent substitution has a much smaller effect on the lattice expansion. The reduction in a-axis expansion is more linear, but it also tapers off for higher compositions. **Equations IV.23** are fit to lattice expansions for x = 0.4 ($\Delta a/a$) and x = 0.2 ($\Delta c/c$ and $\Delta V/V$). The slopes of these lines are much greater than those of **equations IV.24**, fit to x = 0.3 ($\Delta a/a$) and x = 0.2 ($\Delta c/c$ and $\Delta V/V$). After some "critical" substituted composition,

x_c, the lattice expansion levels off and shows only a slight reduction with increasing Ge composition. In addition Ge-substitution reduces the lattice expansion anisotropically.

In all measurements of discontinuous lattice expansion (above and §II.D.3), the discontinuous lattice expansion is more anisotropic than the total lattice expansion. That is, the c-axis continues to expand much more that does the a-axis as more hydrogen is absorbed. The intercepts of $\Delta c/c^{Al}$ (**Figure IV-25**) and $\Delta V/V^{Al}$ (**Figure IV-26**) are less than the expansion values of $LaNi_5$, while the intercept of $\Delta a/a^{Al}$ is approximately equal to that of $\Delta a/a^{LaNi_5}$ (**Figure IV-24**). This implies that the measurements by Gruen, *et al.* were not taken on alloys at their maximum hydrogen compositions.

A solute's effectiveness in suppressing lattice expansion of hydriding is quantified by the slopes of **equations IV-17 - IV.22. Figure IV-28** plots the slopes of $\Delta V/V$ from total lattice expansion measurements *vs* the ΔH^f_{LaM}. The two parameters are certainly correlated, but the scarcity of data limits further analysis.

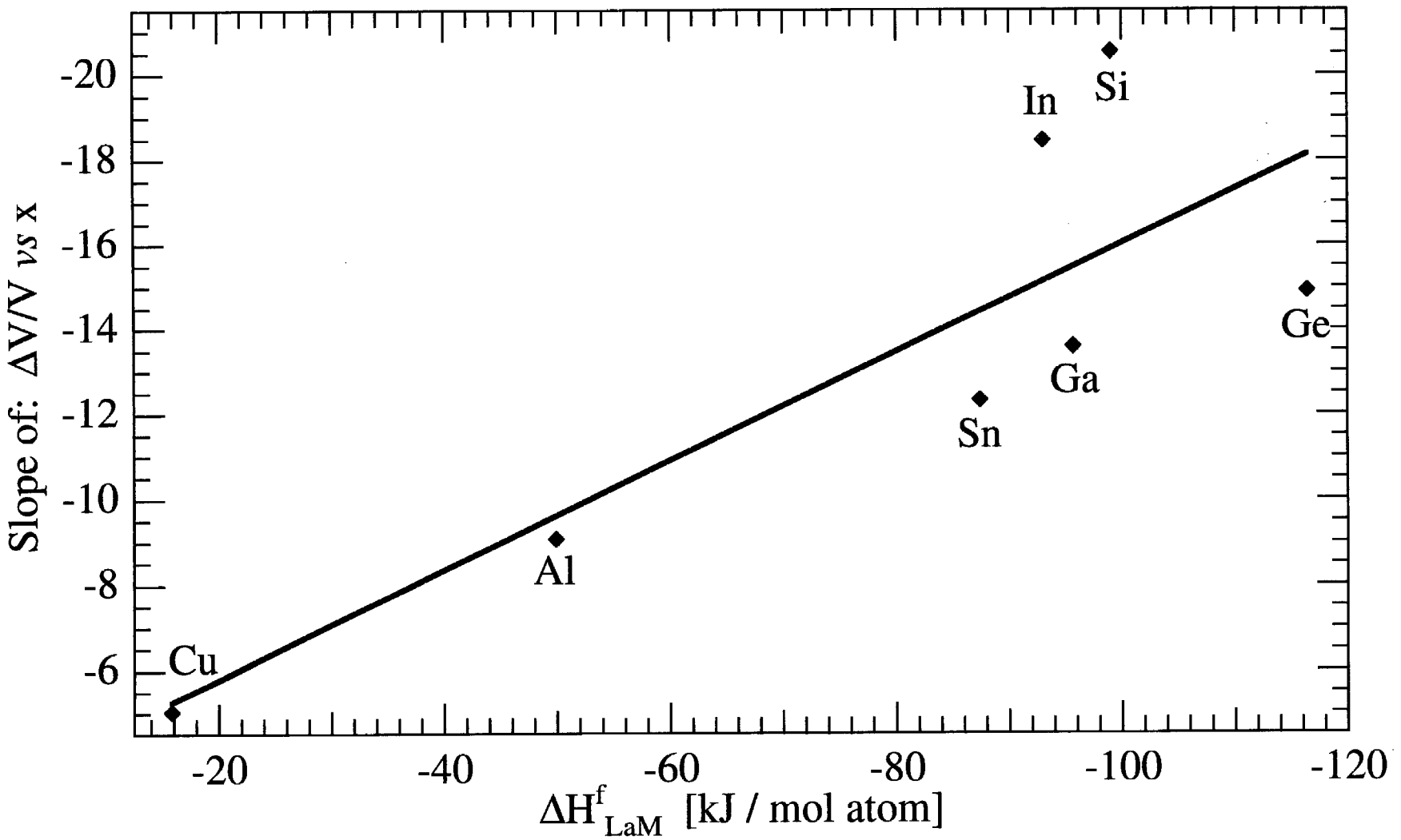

Figure IV-28 Solute effectiveness in suppressing total volume expansion *vs* solute heat of formation with La.

D. Microstrain of Dehydrided Alloys

1. Literature Survey

The pronounced anisotropic peak broadening present in XRD and neutron diffraction patterns of hydrogen activated $LaNi_5$ and its substituted alloys was first noted by Achard, *et al.*,[29] and by Fischer, *et al.*[30] Percheron, *et al.* later performed strain analyses of $LaNi_{5-x}M_x$ alloys using the Williamson-Hall method, as explained in §III.C.1.b.ii.[27] They found prominent anisotropic strain broadening in XRD patterns of $LaNi_{5-x}Mn_x$ and $LaNi_{5-x}Al_x$ alloys, as seen in **Figures IV-29** and **IV-30**, reprinted from reference 29. Large microstrains were found in the (*hh*0) and (0*k*0) directions and almost none in the (00*l*) direction. The microstrains and their anisotropy were found to diminish with alloy substitutions. Mn substituted $LaNi_5$ was found to have an isotropic microstrain distribution for compositions $x_{Mn} \geq 1$, and Al relieved the anisotropy for $x_{Al} > 0.2$.[27] In later work, this microstrain anisotropy was refined from XRD patterns with modified Rietveld refinement codes.[31,32] MH microstrain refinement is now routine, and code for this has been implemented in the publicly available program FullProf.[33]

2. Caltech Results

Our original work on lattice microstrain analysis studied the microstrain developed in $LaNi_{4.8}M_{0.2}$ alloys after a single gas-phase hydrogen absorption/desorption cycle.[34] We found a pronounced variation in lattice microstrain with solute chemistry. The XRD patterns taken from these alloys are displayed in **Figure IV-3a**. These measurements were performed with the Inel CPS-120 in a low-resolution configuration and the $K\alpha_1/K\alpha_2$ radiation splitting was not accounted for in the analysis. The $d\Delta k$ *vs* Δk relationship is shown in **Figure IV-31** for each $M_{0.2}$ alloy. Only reflections perpendicular to the basal plane {(110), (200), and (220)} were used in the Williamson-Hall plot. This is consistent

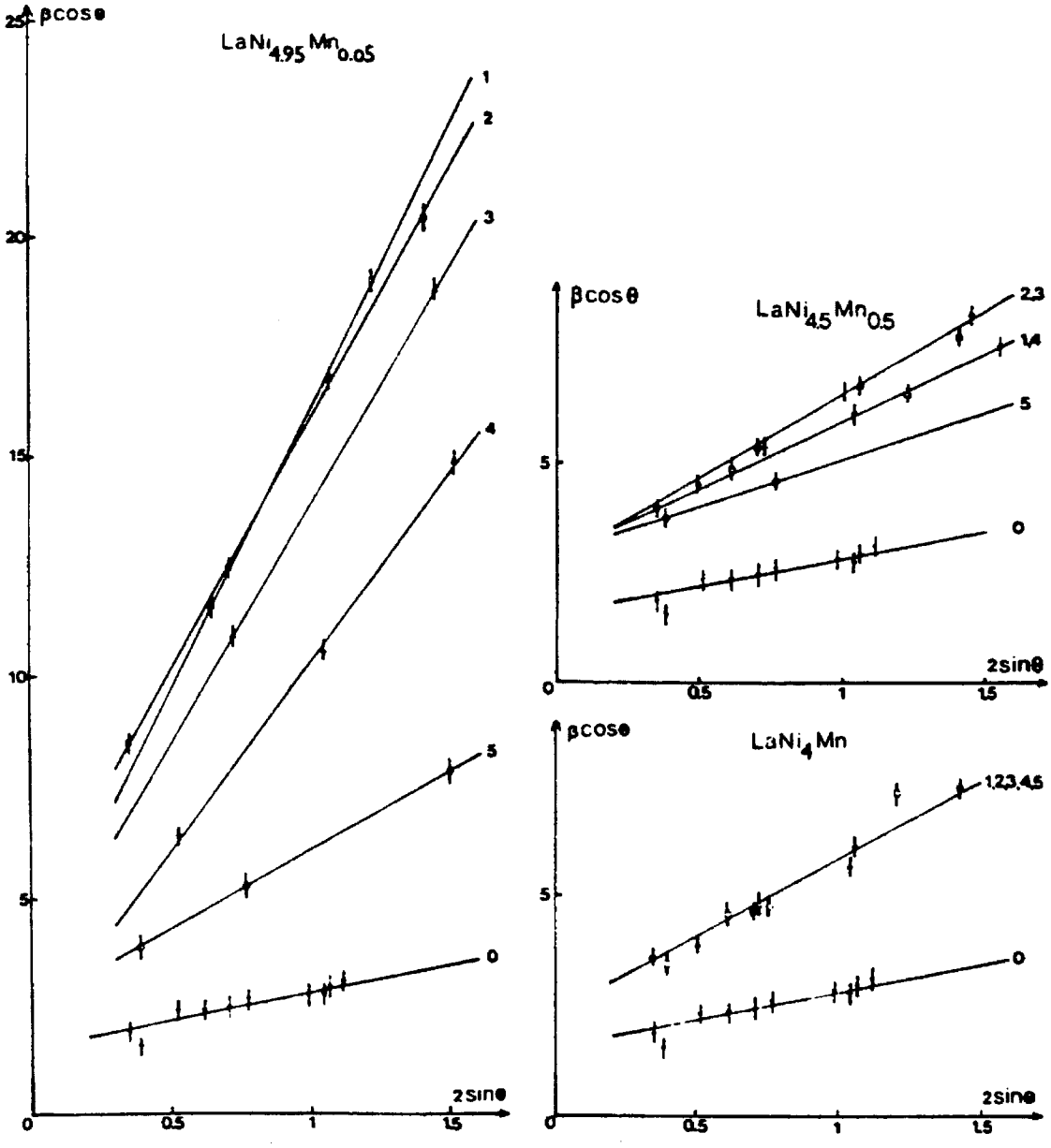

Figure IV-29 Williamson-Hall plots of anisotropic XRD line broadening in $LaNi_{5-x}Mn_x$. Data points "i" represent hki families of diffraction peaks (reprinted from ref. 29).

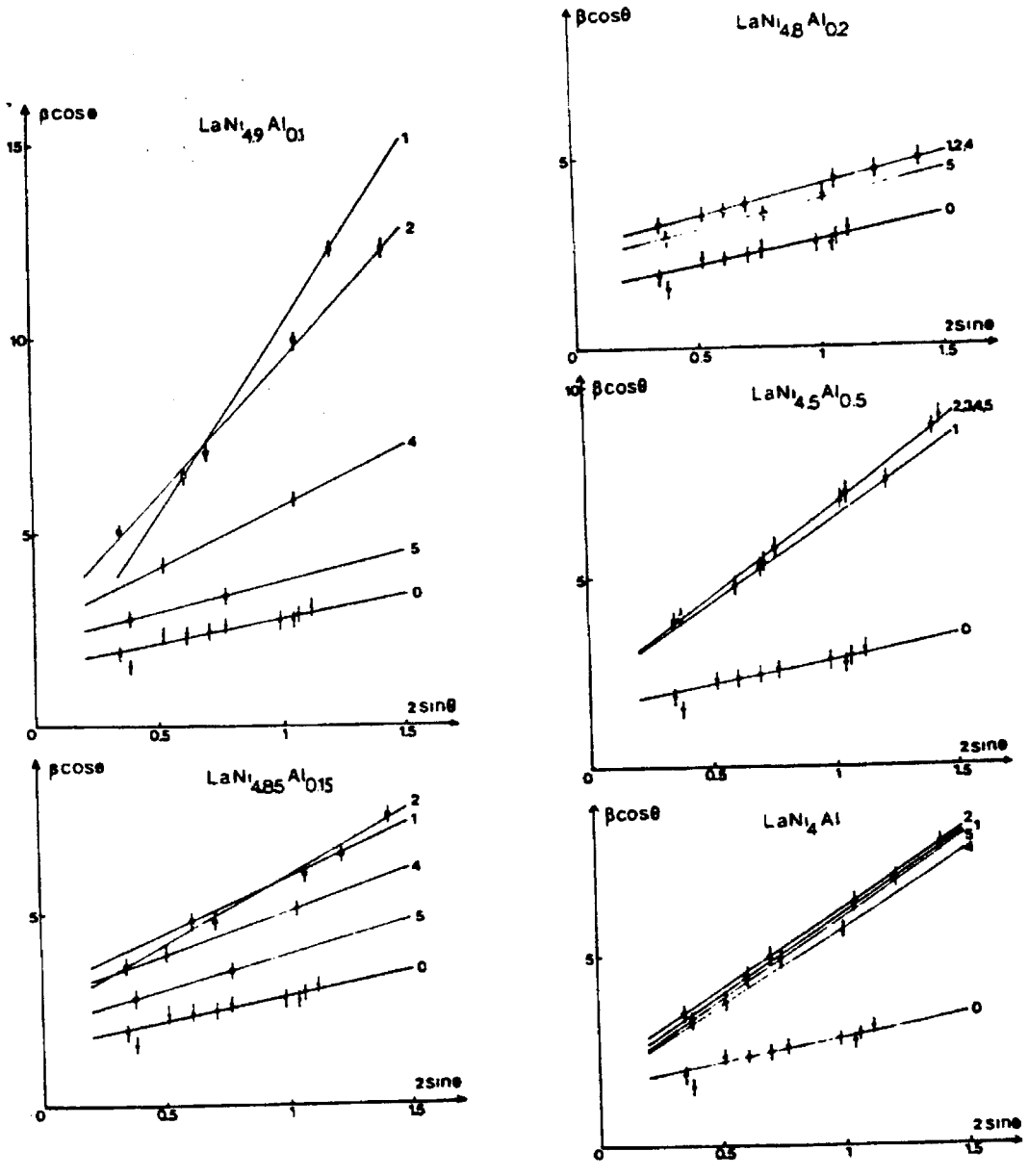

Figure IV-30 Williamson-Hall plots of anisotropic XRD line broadening in $LaNi_{5-x}Al_x$. Data points "i" represent hki families of diffraction peaks. (reprinted from A. Percheron-Guégan...)

with the findings by Percheron-Guégan, *et al.* that microstrain occurs predominantly in that direction upon hydrogen absorption.[27,29] When a linear fit is applied to these points, the microstrain distribution in each sample can be correlated with the slope of the line, and the grain size with the y-intercept.

3. Discussion

The diffraction patterns in **Figure IV-3a** are displayed in order of increasing heat or formation of binary La-M compounds, ΔH_{LaM}. We can see in the insert that the widths of the diffraction peaks seem to decrease in the same sequence. Figure IV-32 displays the microstrains extracted from the diffraction patterns by the Williamson-Hall method. The correlation observed in the peak breadths is confirmed by **Figure IV-32**, which displays the microstrains obtained from **Figure IV-31** *vs* ΔH_{LaM}. This figure shows that the microstrain decreases with increasing heat of formation of a compound of the solute with La.

The significance of this measurement of the microstrain in the alloy is that it can be used to rank the resistance of the lattice to defect generation. Alloys with low values of microstrain resulting from hydrogen activation would either have a small driving force for defect generation (small lattice dilatation), or would be more resistant to this type of defect generation. In either case, such alloys are candidates for long-lived anodes in Ni-MH cells. The hypothesis that such a stabilization of the lattice can be produced by alloying $LaNi_5$ with large ΔH_{LaM} elements is supported by the X-ray line broadening results. As seen in **Figure IV-32**, the abundance of lattice defects found in the crystalline structures of hydrogen activated $LaNi_{5-x}M_x$ alloys is negatively correlated with $|\Delta H_{LaM}|$. If the Haucke phase lattice is made more stable with respect to crystalline defect generation, it is reasonable to assume that it will be more stable during hydrogen absorption-desorption cycling. This will also be true because, as mentioned in the introduction, lattice defects promote metal atom diffusion.

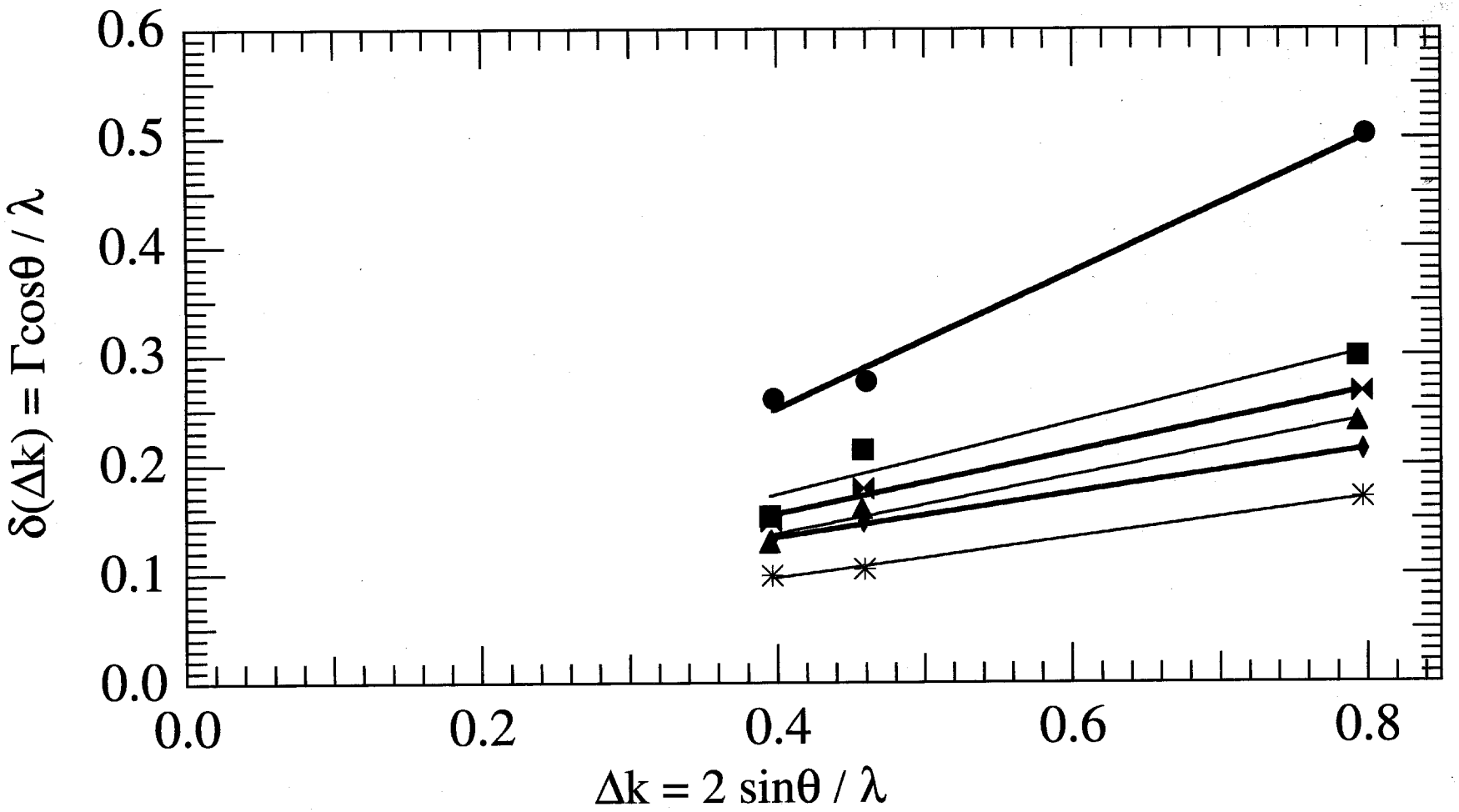

Figure IV-31 Microstrain of singly activated $LaNi_{4.8}M_{0.2}$ alloys, obtained from (hk0) X-ray diffraction peak broadening.
{ ● - $LaNi_5$; ■ - $In_{0.2}$; ⋈ - $Al_{0.2}$; ▲ - $Sn_{0.2}$; ♦ - $Si_{0.2}$; ✳ - $Ge_{0.2}$}

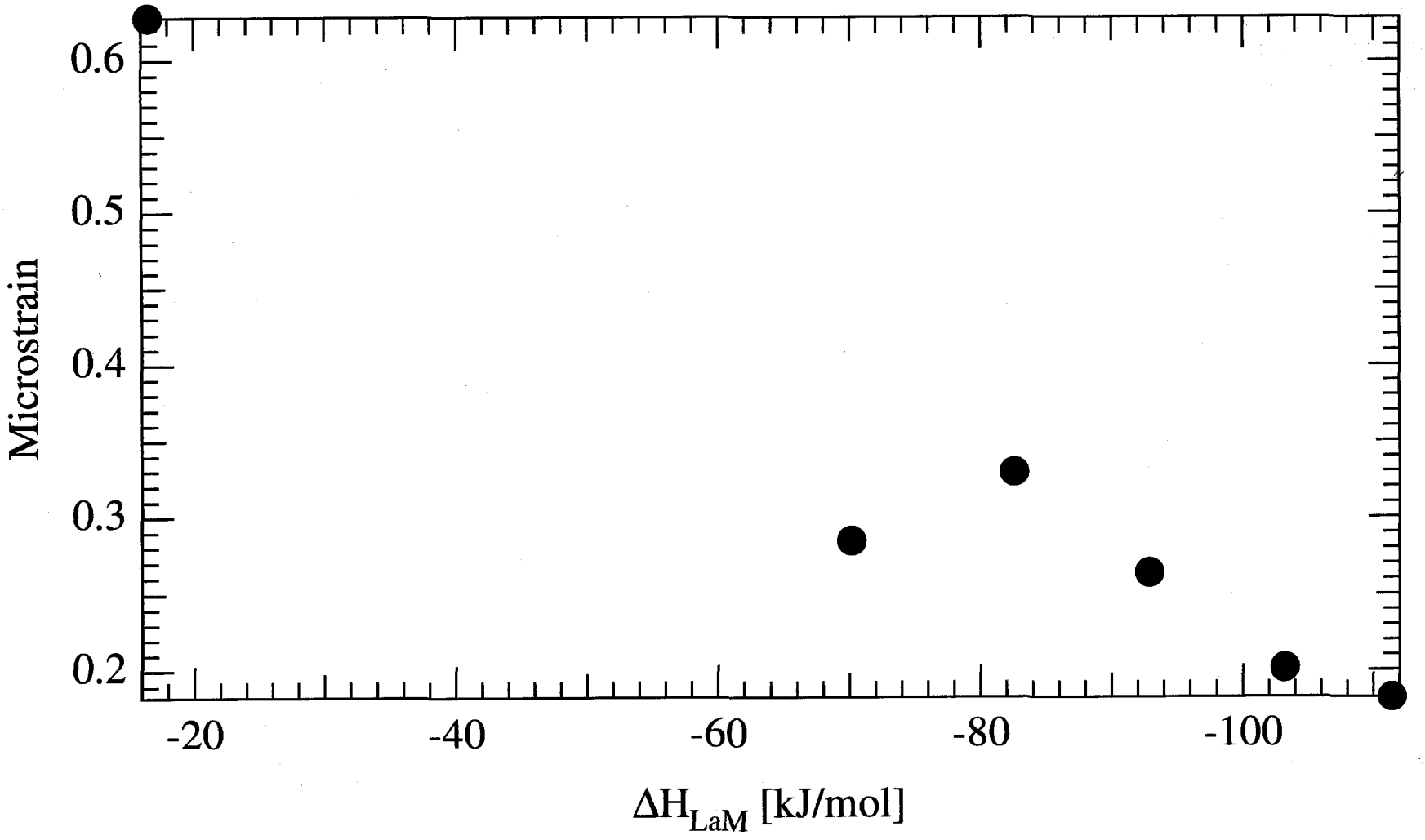

Figure IV-32 Microstrain of singly activated $LaNi_{4.8}M_{0.2}$ alloys *vs* solute heat of formation with La.

[1] M.H. Mendelsohn, D.M. Gruen, and A.E. Dwight, *Nature*, **269** (1977): 45.

[2] Z. Blazina and A. Drasner, *J. Phys.: Condens. Matter*, **10** (1998): 4777.

[3] M.A. Fremy, D. Gignoux, J.M. Moreau, D. Paccard, and L. Paccard, *J. Less-Common Met.*, **206** (1985): 251.

[4] M.H. Mendelsohn, D.M. Gruen, and A.E. Dwight, *Mat. Res. Bull.*, **13** (1978): 1221.

[5] J.C. Achard, A.J. Dianoux, C. Lartigue, A. Percheron-Guégan, and F. Tasset, in *The Rare Earths in Modern Science and Technology*, vol. 3, eds. G.J. McCarthy and J.J. Rhyne (Plenum Press, New York, 1982), p. 481.

[6] C. Witham, R.C. Bowman, Jr., and B. Fultz, *J. Alloys Comp.*, **253-254** (1997): 574.

[7] S. Luo, W. Luo, J.D. Clewley, Ted B. Flanagan, and L.A. Wade, *J. Alloys Comp.*, **231** (1995): 467.

[8] D.M. Gruen, M.H. Mendelsohn, and A.E. Dwight, *Advances in Chemistry Series 167 Transition Metal Hydrides*, R. Bau, ed., American Chemical Society, Wash. DC, (1978): 327.

[9] H. Diaz, A. Percheron-Guégan, and J. C. Achard, *Int. J. Hydrogen Energy*, **4** (1979): 445.

[10] M.H. Mendelsohn, D.M. Gruen, and A.E. Dwight, *Inorg. Chem.*, **18**(12) (1979): 3443.

[11] F. Meli, A. Zuettel, and L. Schlapbach, *J. Alloys Comp.*, **190** (1992): 17.

[12] S. Luo, J.D. Clewley, T.B. Flanagan, R.C. Bowman, and L.A. Wade, *J. Alloys Comp.*, **267** (1998): 171.

[13] J.-M. Joubert, M. Latroche, R. Cerby, R.C. Bowman, Jr., A. Percheron-Guégan, and K. Yvon, *J. Alloys Comp.*, in press.

[14] T. Sakai, K. Oguro, H. Miyamura, N. Kuriyama, A. Kato, and H. Ishikawa, *J. Less-Common Met.*, **161**, 193 (1990).

[15] C. Lartigue, A. Percheron-Guégan, J.C. Achard, and F. Tasset, *J. Less-Common Met.*, **75** (1980): 23.

[16] R. C. Bowman, Jr., J. S. Cantrell, T. W. Ellis, T. B. Flanagan, J. D. Clewley, and S. Luo, in *Proc. 10th World Hydrogen Energy Conf.*, Cocoa Beach, FL, June, 1994, pp. 1199-1207.

[17] J. Lamloumi, A. Percheron-Guégan, J.C. Achard, G. Jehanno, and D. Givord, *J. Physique*, **45** (1984): 1643.

[18] H.H. van Mal, K.H.J. Buschow, and F.A. Kuijpers, *J. Less-Common Met.*, **32** (1973): 289.

[19] C. Colinet, A. Pasturel, A. Percheron-Guégan, and J.C. Achard, *J. Less-Common Met.*, **134** (1987): 109.

[20] A. Pasturel, F. Liautaud, C. Colinet, C. Allibert, A. Percheron-Guégan, and J.C. Achard, *J. Less-Common Met.*, **96** (1984): 93.

[21] M. Latroche, J. Rodríguez-Carvajal, A. Percheron-Guégan, and F. Bourée-Vigneron, *J. Alloys Comp.*, **218** (1995): 64; M. Latroche, A. Percheron-Guégan, and F. Bourée-Vigneron, *J. Alloys Comp.*, **265** (1998): 209.

[22] S. Ono, K. Nomura, E. Akiba, and H. Uruno, *J. Less-Common Met.*, **113** (1985): 113.

[23] E.MacA. Gray, E.H. Kisi, and R.I. Smith, *J. Alloys Comp.*, in press.

[24] S. Bagchi, D. Chandra, W.N. Cathey, R.C. Bowman, Jr., and F.E. Lynch, subm. 1997 TMS Meeting.

[25] J. Lamloumi, A. Percheron-Guégan, C. Lartigue, J.C. Achard, and G. Jehanno, *J. Less-Common Met.*, **130** (1987): 111.

[26] W.L. Zhang, M.P.S. Kumar, A. Visintin, S. Srinivasan, and H.J. Ploehn, *J. Alloys Comp.*, **242** (1996): 143.

[27] A. Percheron-Guégan, C. Lartigue, J.C. Achard, P. Germi, and F. Tasset, *J. Less-Common Met.*, **74** (1980): 1.

[28] M.H. Mendelsohn, D.M. Gruen, and A.E. Dwight, *J. Less-Common Met.*, **63** (1979): 193.

[29] J.C. Achard, F. Givord, A. Percheron-Guégan, J.L. Soubeyroux, and F. Tasset, *J. Phys. (Paris), Colloq.* **5, 40** (1979): 218.

[30] P. Fischer, A. Furrer, G. Busch, and L. Schlapbach, *Helv. Phys. Acta*, **50** (1977): 421.

[31] C. Lartigue, A. Le Bail, and A. Percheron-Guégan, *J. Less-Common Met.*, **129** (1987): 65.

[32] P. Thompson, J.J. Reilly, and J. M. Hastings, *J. Less-Common Met.*, **129** (1987): 105.

[33] J. Rodríguez-Carvajal, "FULLPROF: A Program for Rietveld Refinement and Pattern Matching Analysis," Abstracts of the Satellite Meeting on Powder Diffraction of the XV Congress of the IUCr, p. 127, Toulouse, France (1990).

[34] C.K. Witham, R.C. Bowman, Jr., B.V. Ratnakumar, B. Fultz, and S. Surampudi, in *Proc. 11th Annual Battery Conf. on Apps. and Adv.*, January 9-12, 1996, Long Beach, CA, p. 129.

V. Isotherms

A. Gas-phase

1. Literature Survey

There are a variety of hydrogen pressure-composition isotherms of Ni-substituted $LaNi_5$ that have been reported in the literature. Isotherm measurements have been reported for ternary alloys of transition metals Cr,[1] Mn,[2-5] Fe,[1,2,6] Co,[7] and Cu [1,2,8]; and p-shell metals Al,[2,9-14] Si,[2,13,15-18] Ga,[10,15,19] Ge,[15,16] In,[15,20] and Sn.[20-23] Almost all elemental substitutions for Ni have the effects of decreasing the plateau pressure, maximum hydrogen capacity, and pressure hysteresis of the isotherms. Notable exceptions to this are Mn, which has almost no effect on hydrogen capacity for $x < 1.0$; and Co, which exhibits ordering on the $LaNi_5$ lattice as discussed in the introduction, changing the stability of the hydrogen sites.

Extensive work has been done on alloys substituted with Sn [22,23] and with Al,[10,11,24] and isotherm characteristics for these alloys are included in **Tables V-1 and 2.** The isotherms measured by Meli, *et al.* of Si-substituted alloys were measured dynamically,[17] and these results can only be compared to the current work sparingly. Isotherm characteristics for the alloys $Ga_{0.4}$, $Si_{0.4}$, $Ge_{0.4}$, and In_x will be quoted here (**Table V-3**) but the thermodynamic parameters were obtained from isotherms at only two temperatures, and are therefore less certain.[15,16]

Alloy	Δn_{plat} [H/LaNi$_5$]	P_{abs} [bar]	P_{des} [bar]	Hysteresis [J/mol H]	$\lvert\Delta H_{abs}\rvert$ kJ/mol H	$\lvert\Delta S_{abs}\rvert$ J/K/mol H	$\lvert\Delta H_{des}\rvert$ kJ/mol H	$\lvert\Delta S_{des}\rvert$ J/K/mol H
$LaNi_5$	5.5	25.40	20.80	310	15.7	54.8	15.1	53.9
$Sn_{0.05}$					15.2	53.1	16.0	54.2
$Sn_{0.1}$	5.4	17.40	13.20	430	16.2	55.1	16.4	54.0
$Sn_{0.2}$	5.3	8.48	7.17	260	16.5	52.5	16.5	52.5
$Sn_{0.25}$	5.3	6.74	5.79	235	17.2	52.9	17.4	53.3
$Sn_{0.32}$	5.1	4.23	3.95	106	18.3	54.9	18.5	54.6
$Sn_{0.4}$	4.9	2.34	2.22	82	19.0	54.3	19.1	54.4
$Sn_{0.5}$	4.5	1.32	1.26	72	20.2	55.2	20.3	55.2

Table V-1 Hydriding parameters for $LaNi_{5-x}Sn_x$ alloys. Isotherms measured at 100° C. (from S. Luo, et al., *J. Alloys Comp.*, **231** (1995): 467.)

Alloy	Δn_{max} [H/LaNi$_5$]	P_{abs} [atm]	P_{des} [atm]	Hysteresis [J/mol H]	$\lvert\Delta H_{des}\rvert$ kJ/mol H	$\lvert\Delta S_{des}\rvert$ J/K/mol H
$LaNi_5$	6	2.3	1.7	400	-15.9	-54.3
$Al_{0.08}$	6.15	1.3	1.1	265	-16.3	-54.5
$Al_{0.25}$	5.56	0.78	0.47	665	-17.4	-54.5
$Al_{0.51}$	5.48	0.21	0.13	635	-19.2	-54.9
$Al_{0.82}$	4.53	0.032	0.025	305	-22.2	-58.2
$Al_{0.98}$	4.23	0.010	0.0069	510	-24.0	-58.6

Table V-2 Hydriding parameters for $LaNi_{5-x}Al_x$ alloys. Isotherms measured at 40° C. (from H. Diaz, et al., *Int'l J. Hydrogen Energy*, **4** (1979): 445.)

Alloy	Δn_{max} [H/LaNi$_5$]	P_{abs} [atm]	P_{des} [atm]	Hysteresis [J/mol H]	$\lvert\Delta H_{des}\rvert$ kJ/mol H	$\lvert\Delta S_{des}\rvert$ J/K/mol H
$In_{0.07}$			1.37		17.3	58.4
$In_{0.15}$			0.78		15.7	50.6
$In_{0.4}$	5.6	0.097	0.095	26	19.5	54.7
$Ga_{0.4}$	6		0.49		17.3	54.1
$Si_{0.4}$	4.3	0.73	0.67	108	17.5	56.3
$Ge_{0.4}$	5	0.85	0.78	108	17.2	55.4

Table V-3 Hydriding parameters for sp-shell metal substituted $LaNi_5$ alloys. Isotherms measured at 30° C. (from M.H. Mendelsohn, et al., in *Rare Earths in Modern Sci. and Technol.*, G.J. McCarthy and J.J. Rhyne, eds. (Plenum press, New York: 1980), p. 593.)

2. Caltech Results

a. $LaNi_{5-x}Ge_x$

Room temperature isotherms of all Ge substituted alloys are shown in **Figure V-1**. The reversible hydrogen capacity is reduced with Ge substitution, and the capacities at 2 atm. are shown in **Table V-4**. Both the absorption and desorption plateau pressures and the hydrogen absorption capacities decrease with Ge substitution. **Figure V-1** also shows that the hysteresis between the absorption and desorption isotherms is decreased with increasing Ge composition. The hysteresis ratios of the hydride formation and decomposition plateau pressures at mid-plateau have been calculated using **equation III.2** and are shown for room temperature isotherms in **Table V-4**.

Elevated temperature isotherms were measured for all Ge substituted alloys, and are presented in **Figures V-2** through **V-6** for alloys $Ge_{0.1}$, $Ge_{0.2}$, $Ge_{0.3}$, $Ge_{0.4}$, and $Ge_{0.5}$, respectively. The pressures at mid-plateau are used in van't Hoff plots (**Figure V-7**) to calculate the enthalpies and entropies of hydride formation and decomposition for each alloy, which are presented in **Table V-4**. The isotherm and thermodynamic data for x = 0.4 agree with the values reported by Mendelsohn, *et al* (**Table V-3**).[16] We see that in all cases the enthalpy of hydride decomposition is higher in magnitude than that of formation. The absolute enthalpy also decreases with increasing Ge composition. Both of these points are consistent with the decrease in isotherm plateau pressure. The entropy calculations show a somewhat less consistent trend of an increase in absolute entropy with increasing Ge composition. The enthalpies of hydride formation and decomposition are approximately linear with substituted composition, and can be expressed by:

$$\Delta H^{Ge}_{abs}(x) = -14.54 \; - \; 6.8\, x_{Ge} \;\; kJ, \;\; \text{and} \qquad [V.1]$$

$$\Delta H^{Ge}_{des}(x) = \; 15.26 \; + \; 5.5\, x_{Ge} \;\; kJ. \qquad [V.2]$$

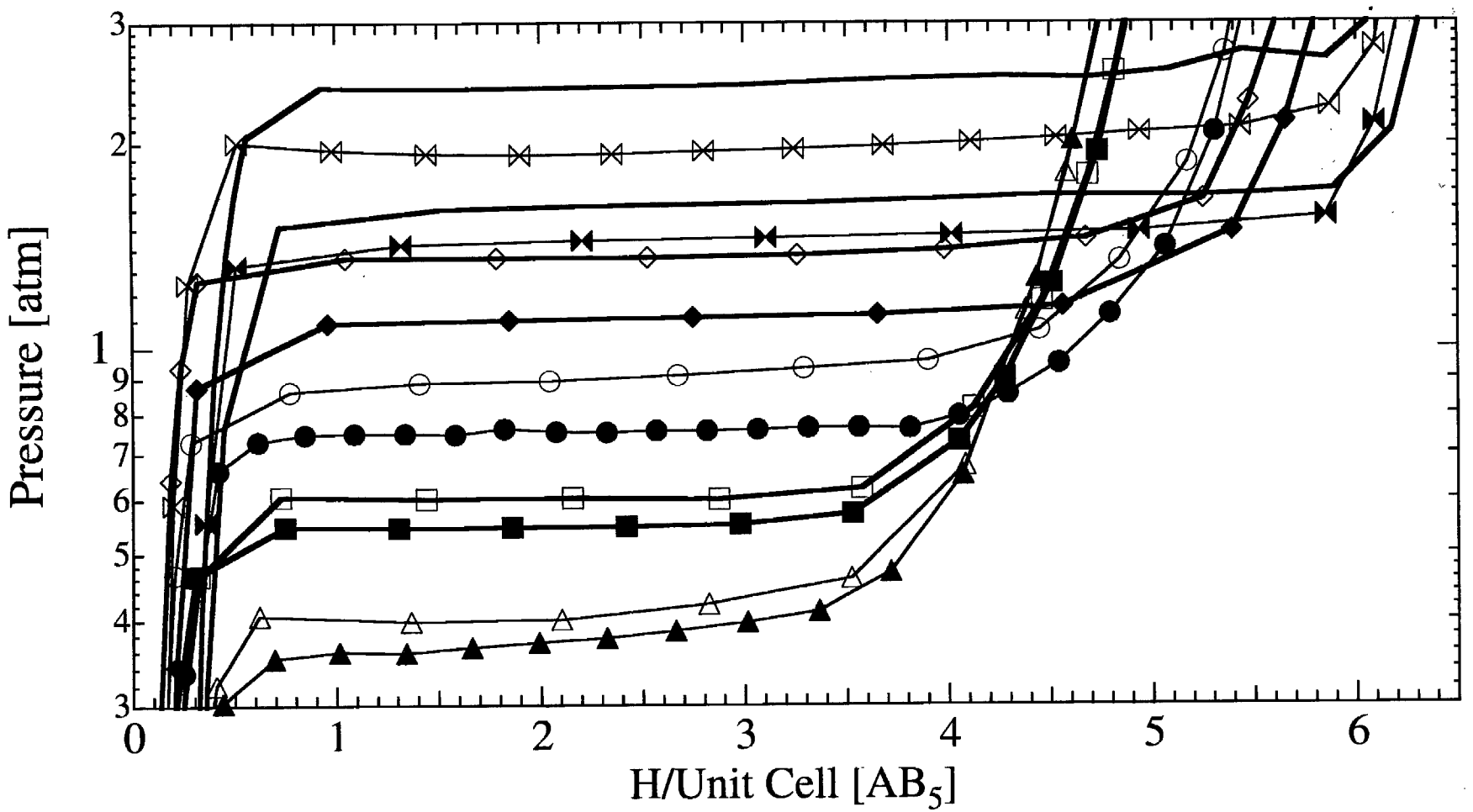

Figure V-1 Room temperature gas-phase isotherms of $LaNi_{5-x}Ge_x$ alloys.
{x_{Ge} = —— - 0.0, —⋈— - 0.1, —◆— - 0.2, —●— - 0.3, —■— - 0.4, —▲— - 0.5}
Open symbols - absorption, closed symbols - desorption.

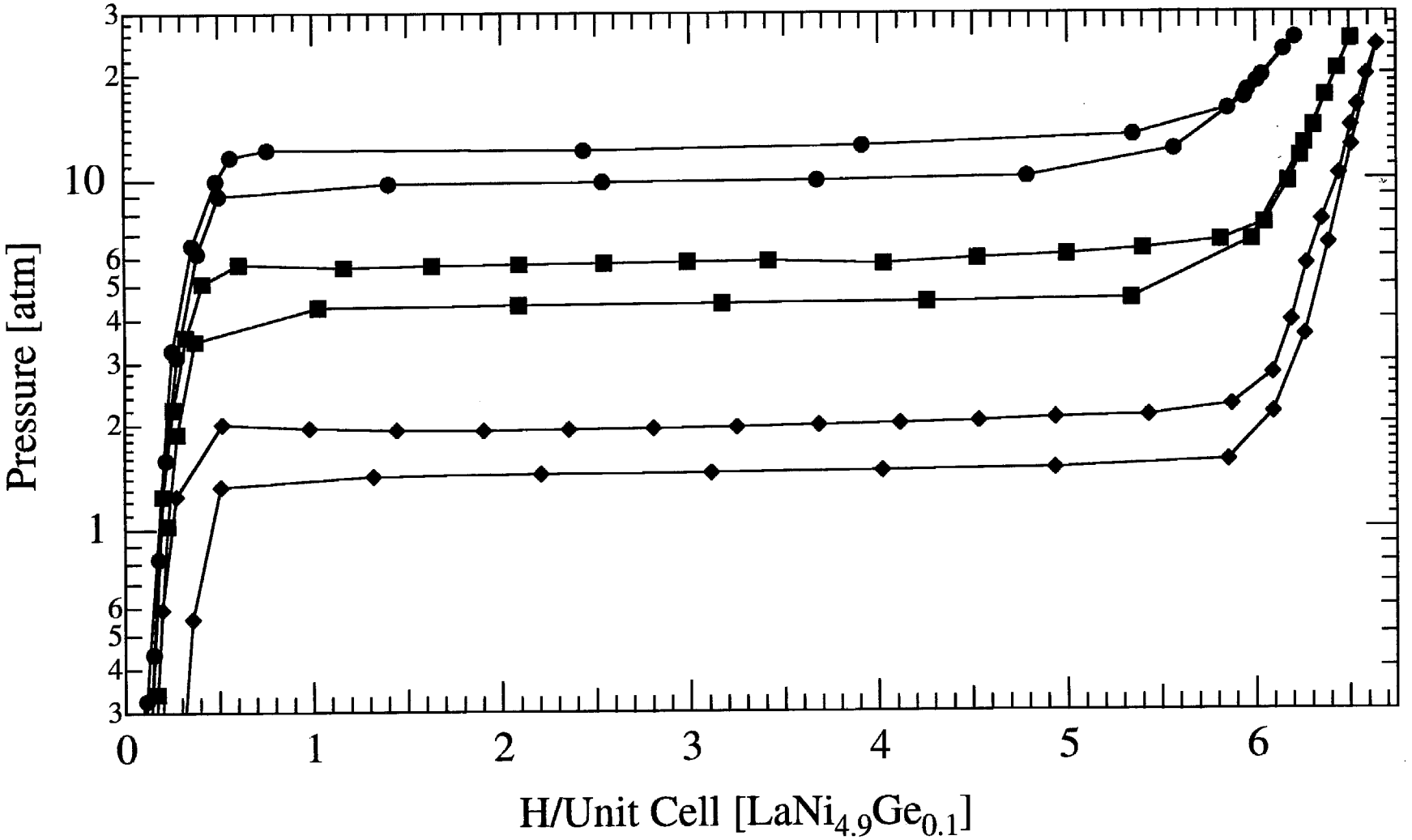

Figure V-2 Elevated temperature isotherms of $LaNi_{4.9}Ge_{0.1}$.
{—●— - 348 K, —■— - 323 K, —◆— - 296 K}

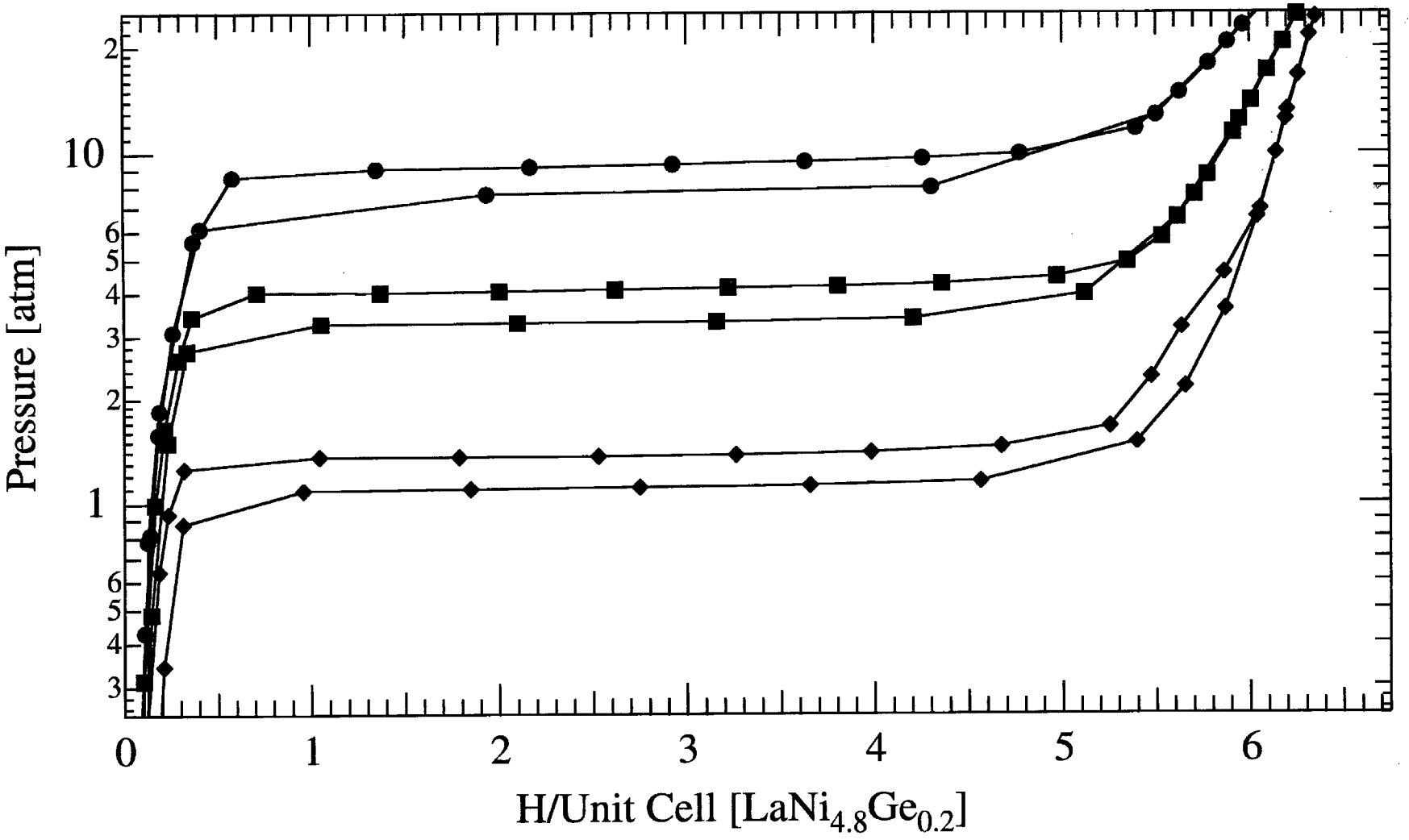

Figure V-3 Elevated temperature isotherms of $LaNi_{4.8}Ge_{0.2}$.
{—●— - 348 K, —■— - 323 K, —◆— - 296 K}

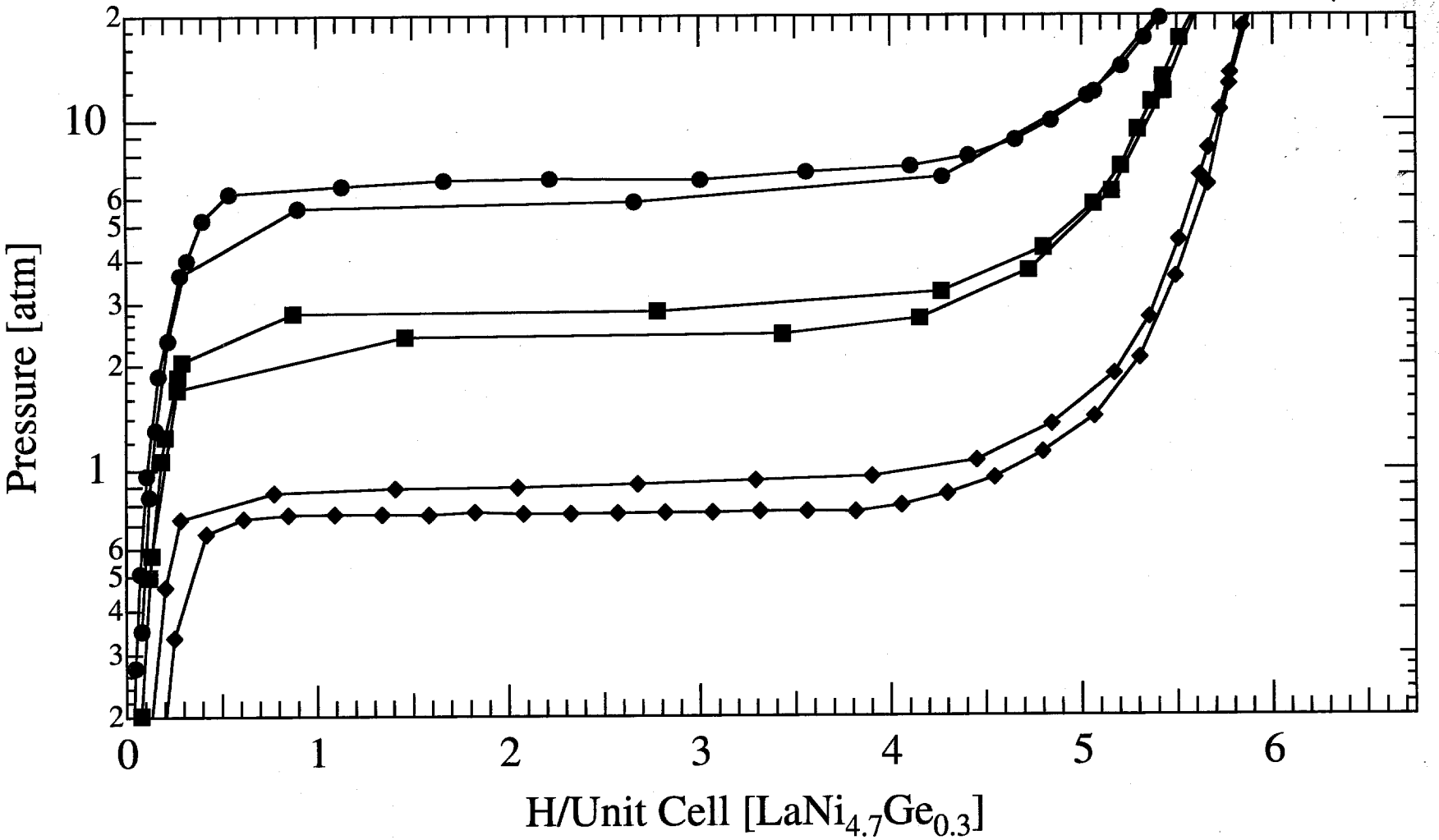

Figure V-4 Elevated temperature isotherms of $LaNi_{4.7}Ge_{0.3}$.
{—●— - 348 K, —■— - 323 K, —◆— - 296 K}

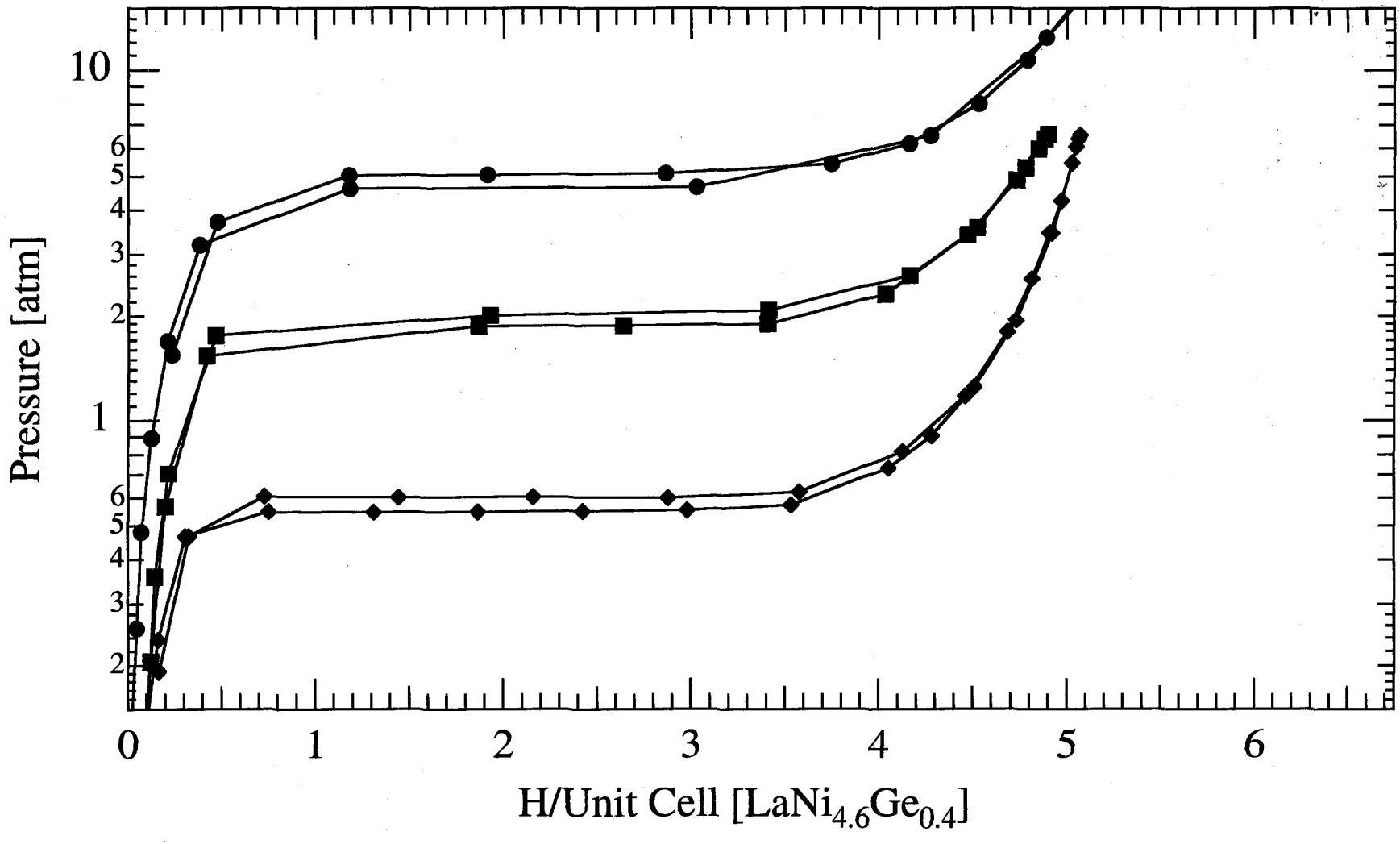

Figure V-5 Elevated temperature isotherms of $LaNi_{4.6}Ge_{0.4}$.
{—●— - 348 K, —■— - 323 K, —◆— - 296 K}

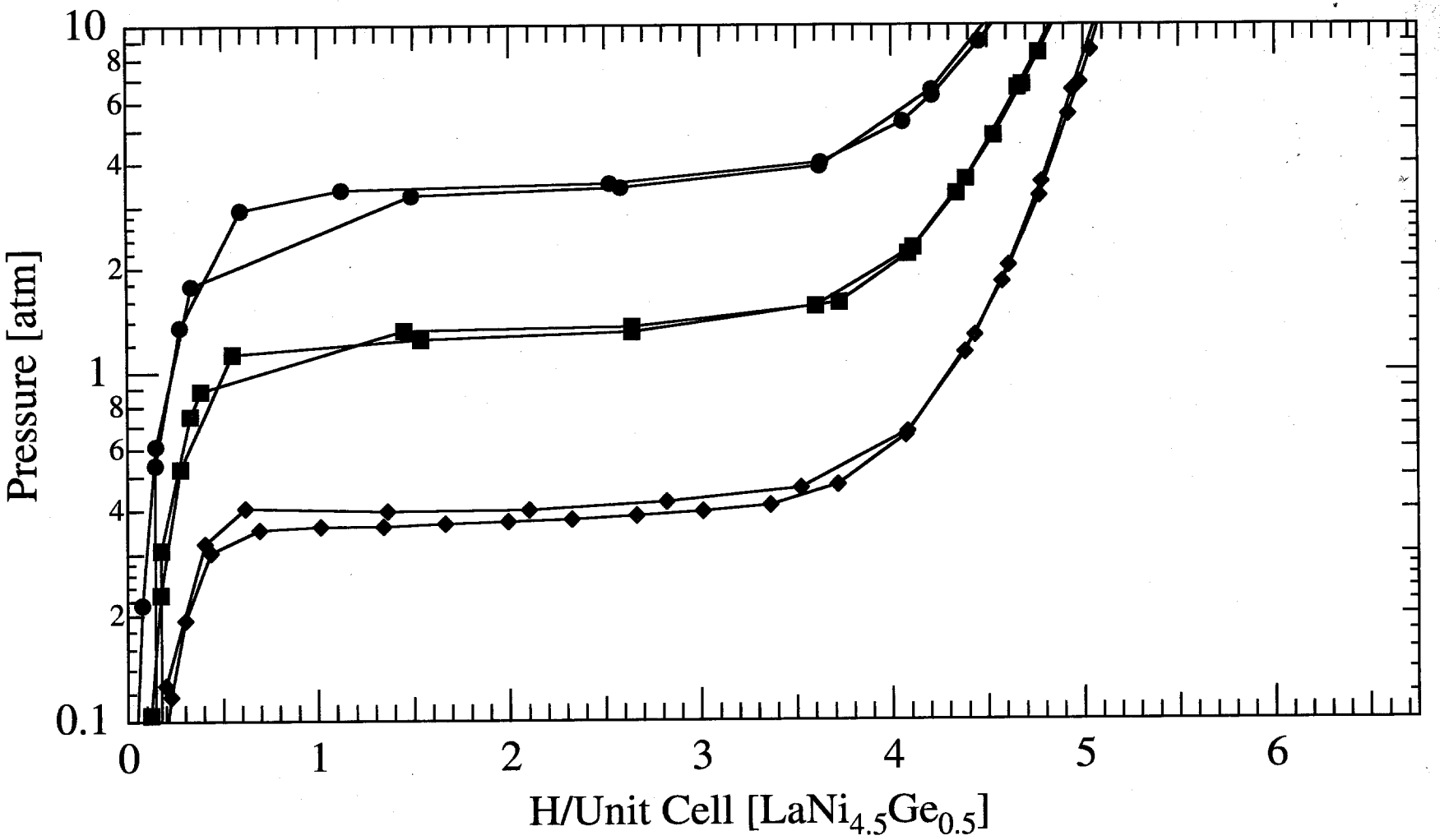

Figure V-6 Elevated temperature isotherms of $LaNi_{4.5}Ge_{0.5}$.
{—●— - 348 K, —■— - 323 K, —◆— - 296 K}

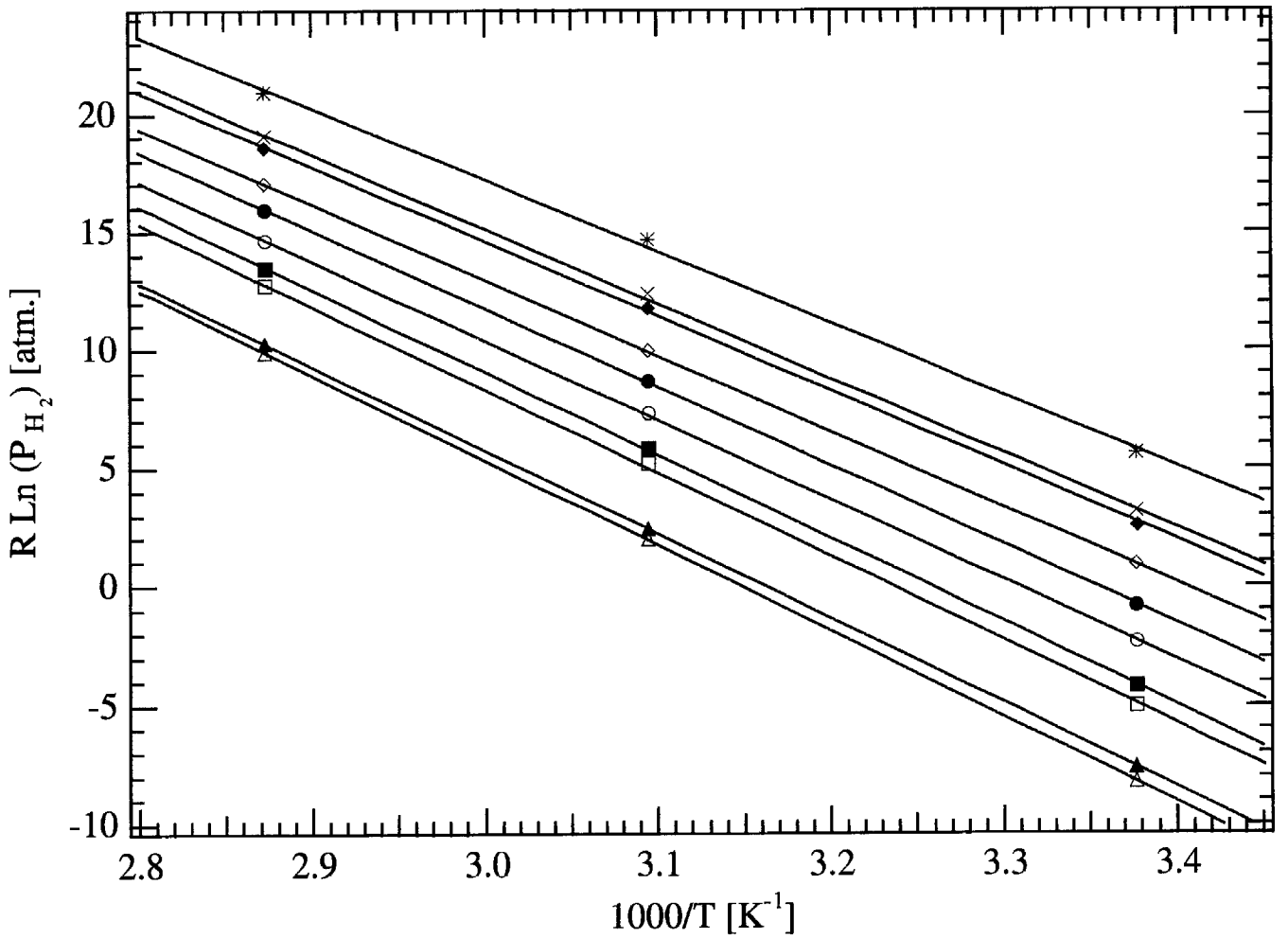

Figure V-7 Van't Hoff plots of R $\ln(P_{H_2})$ *vs* 1/T for $LaNi_{5-x}Ge_x$ alloys.
{x_{Ge} = ✸ - 0.1, ◆ - 0.2, ● - 0.3, ■ - 0.4, ▼ - 0.5}.

Alloy	Δn_{plat} [H/LaNi$_5$]	P_{abs} [atm]	P_{des} [atm]	Hysteresis [J/mol H]	$\lvert\Delta H_{abs}\rvert$ kJ/mol H	$\lvert\Delta S_{abs}\rvert$ J/K/mol H	$\lvert\Delta H_{des}\rvert$ kJ/mol H	$\lvert\Delta S_{des}\rvert$ J/K/mol H
$LaNi_5$	6.10	2.48	1.65	507			15.4	53.9
$Ge_{0.1}$	6.05	1.96	1.46	368	15.2	54.2	15.8	55.1
$Ge_{0.2}$	5.50	1.37	1.11	254	15.8	54.8	16.1	54.6
$Ge_{0.3}$	5.25	0.906	0.755	226	16.6	55.8	16.9	55.8
$Ge_{0.4}$	4.75	0.603	0.548	118	17.6	57.2	17.6	57.0
$Ge_{0.5}$	4.60	0.400	0.372	92.4	17.7	56.1	18.0	56.7

Table V-4 Hydriding parameters for $LaNi_{5-x}Ge_x$ alloys. Isotherms measured at 23° C.

By examining **Figures V-2** through **V-6**, we can determine the boundaries of the dilute (α) and ordered (β) hydride phases. The room temperature plateau of $LaNi_{4.9}Ge_{0.1}H_y$ is particularly flat, and extends to ~6 H/f.u. Elevated temperature isotherms exhibit a decrease in capacity. The isotherm resolution is not high enough to distinguish a splitting at $y > 4$, but we can see the 75° C plateau beginning to slope upwards. Alloys with higher Ge-composition have progressively lower capacities. The anomalous decrease in entropy for the alloy with $x_{Ge} = 0.5$ may be caused by the presence of the second phase that was found in this material. The compositional trend for the entropy of hydrogen absorption correlates with the widths of the plateau shown in **Figure V-1**. The increase in plateau slopes of the isotherms as x_{Ge} increases is indicative of a reduction in the critical temperature for hydride formation.

b. $LaNi_{5-x}M_x$

The compositions of the alloys in this set were chosen to give the alloys plateau pressures of ~0.4 atm. This would insure that the results from electrochemical cycling tests in our slightly pressurized cells would not be confused by hydrogen evolution, self-discharge, etc. The compositions were chosen by reviewing the isotherm plateau pressure data reported in the literature.

Room temperature isotherms of all alloys M_x are shown in **Figures V-8a** and **b**. The alloy $Sn_{0.2}$ was not prepared at Caltech, it was obtained from Hydrogen Consultants, Inc., and its isotherm was measured at the University of Vermont.[22] The absorption plateau pressures of most of these alloys are ~0.5 atm. as planned. $Si_{0.4}$ has an absorption plateau pressure of 0.7 atm., implying either that the solute composition of this alloy is somewhat less than 0.4 or the values quoted in the literature are in error. The widths of the isotherm plateaus are shown in **Table V-5**. Absorption and desorption pressures are taken at mid-plateau and the hysteresis ratios calculated from these values using **equation III.2** are

also shown in **Table V-5**. Hysteresis values are a maximum for $Al_{0.26}$ and minimum for $Si_{0.4}$.

3. Discussion

To note the differences between these sets of alloys, we must examine their properties more closely. The maximum capacities of the alloys in these sets follow approximately the same linear relationship with solute composition. These values are shown in **Figure V-9**. Also included in this figure are the capacities of the M_x alloys. For the most part, the Ge_x alloys have capacities that are slightly lower than the Sn_x and M_x alloys. With the exception of $In_{0.17}$ and $Si_{0.4}$, the M_x alloys have capacities that are approximately equal to the Sn_x alloys.

In the introduction, an overview was given of the deuterium site occupation of a variety of deuterided alloys of $LaNi_5$ and $LaNi_{5-x}M_x$. Recall that a loss in overall capacity was predominantly accompanied by the blocking of the 4h (1 site/cell) and 12o (2 sites/cell) sites in the 6d cluster. This corresponds with Ni-substitution at the 3g site preventing hydrogen (deuterium) occupation in these sites. Assuming all Ni-substitution occurs at the 3g site, an alloy M_x will have an average of x 3g Ni sites per unit cell substituted by M. The approximately linear relationship between maximum hydride capacity and substituted composition seen in **Figure V-9** implies that there is a simple blocking of hydrogen occupation sites by the substituting metal atom. The above considerations imply that a substituted composition of x will block 3x sites from being occupied by hydrogen (deuterium). This is consistent with the reduction in capacity from $y = 6.0$ at $x = 0$ to $y = 4.5$ at $x = 0.5$ that is seen in **Figure V-9**.

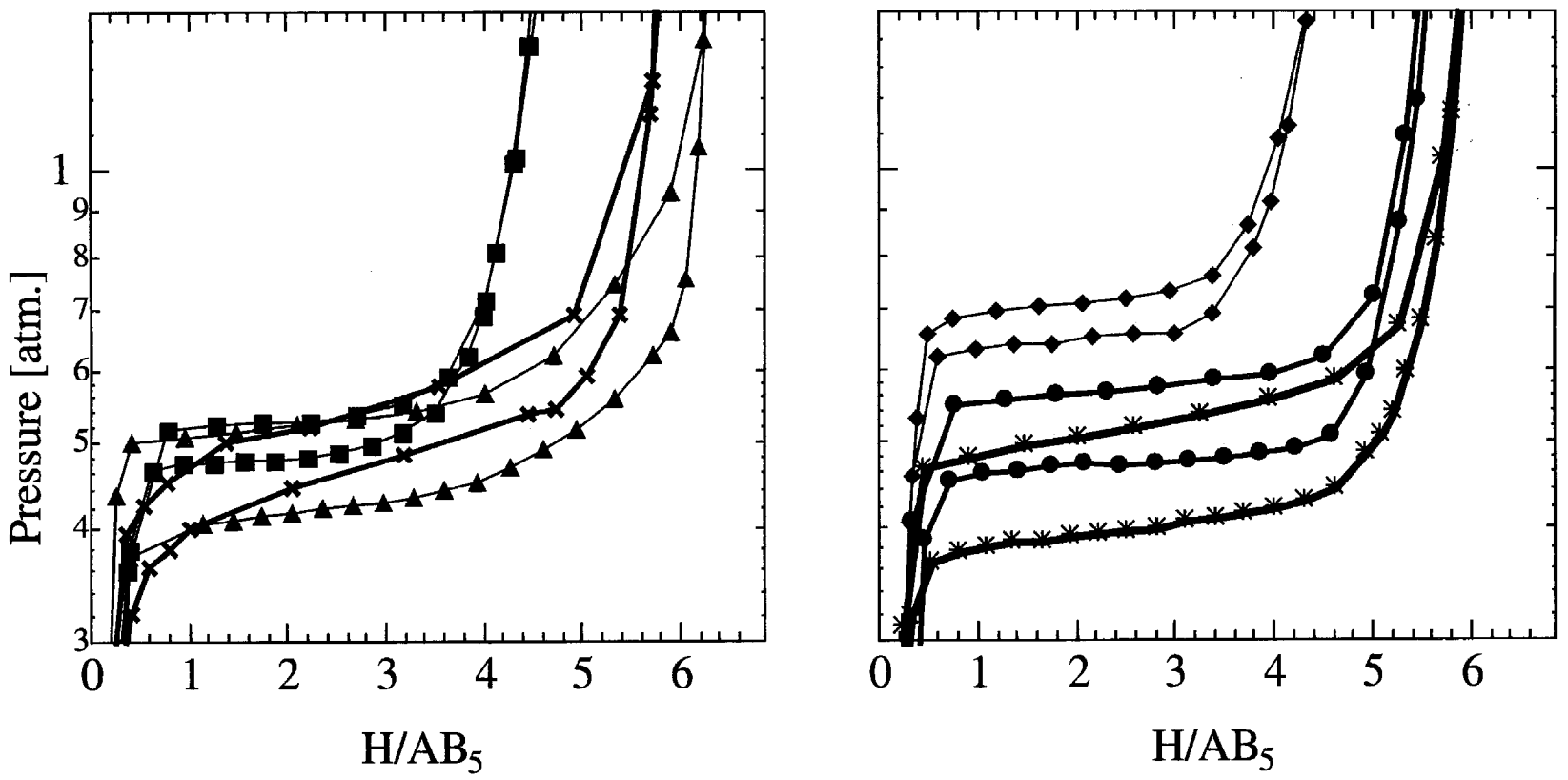

Figure V-8 Room temperature isotherms of $LaNi_{5-x}M_x$ alloys.
{▼ - $In_{0.17}$, x - $Sn_{0.2}$, ✸ - $Al_{0.26}$, ● - $Ga_{0.34}$, ◆ - $Si_{0.4}$, ■ - $Ge_{0.45.}$}

Alloy	Δn_{plat} [H/LaNi$_5$]	P_{abs} [atm]	P_{des} [atm]	Hysteresis [J/mol H]
$In_{0.17}$	4.2	0.53	0.42	273
$Al_{0.26}$	4.6	0.52	0.40	330
$Ga_{0.34}$	4.0	0.57	0.47	236
$Si_{0.4}$	2.9	0.71	0.65	114
$Ge_{0.45}$	2.9	0.53	0.48	122

Table V-5 Hydriding parameters for $LaNi_{5-x}M_x$ alloys. Isotherms measured at 23° C.

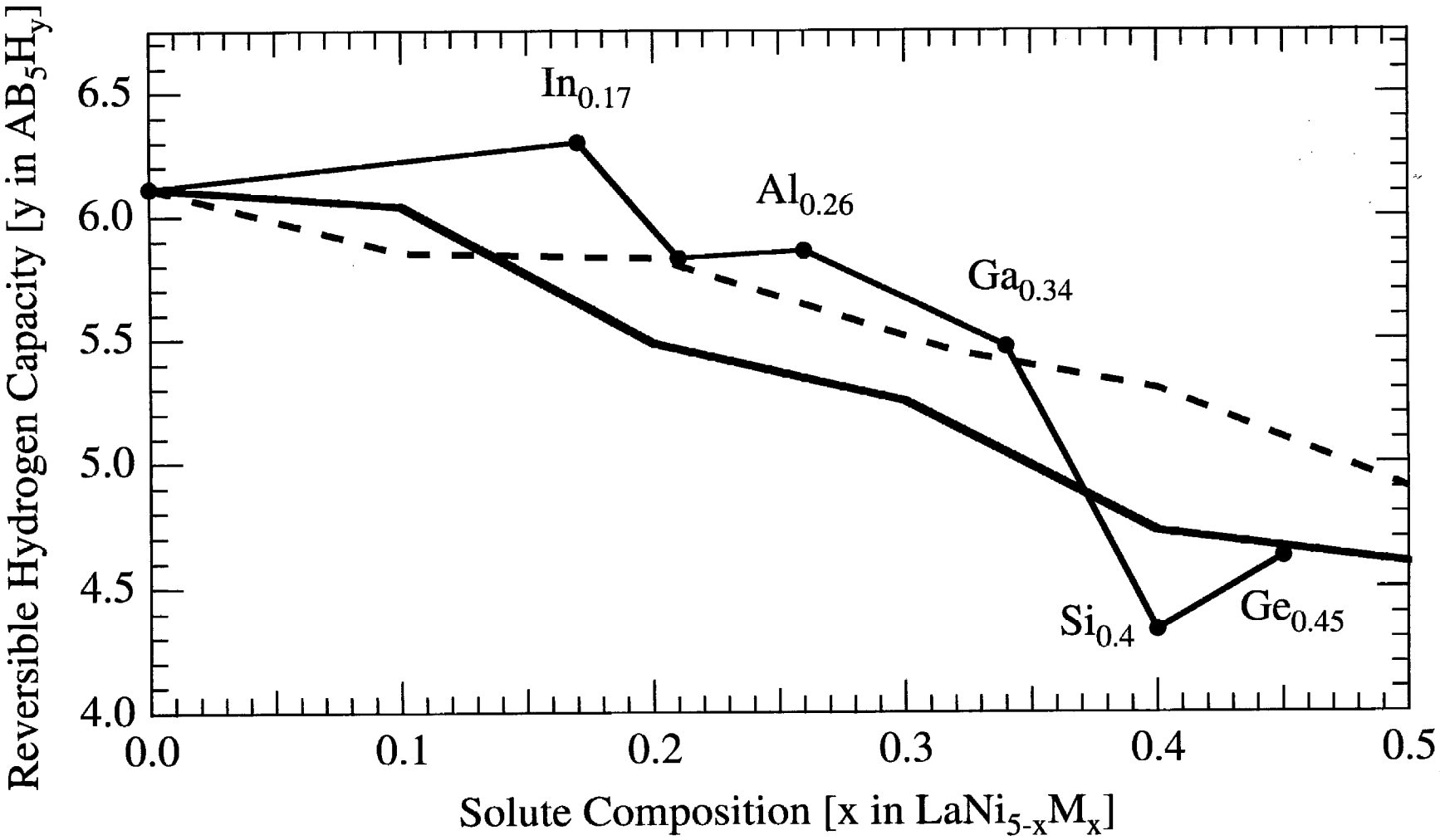

Figure V-9 Gas-phase hydrogen capacities of Ni-substituted $LaNi_5$ alloys.
{– – - Sn_x; —— - Ge_x; —●— - M_x}

It is instructive to compare the isotherms of $LaNi_{5-x}Ge_x$ alloys to those of $LaNi_{5-x}Sn_x$ alloys, taken from ref. 22. **Figure V-10** presents these 2 sets of data side by side. It should be noted that the ordinate of the Ge graph covers 1 order of magnitude in pressure, while that of the Sn graph covers 2 orders of magnitude. The alloys $Sn_{0.2}$ and $Sn_{0.32}$ have sloping plateaus, indicating some inhomogeneity in Sn distribution. The diffraction peaks from these alloys are quite sharp, implying that this inhomogeneity does not exist on a macroscopic scale, and likely results from non-equilibrium site occupation on the crystalline lattice. The hysteresis between absorption and desorption curves seems quite different, but this is an artefact of the different scaling. Otherwise, these 2 graphs are almost identical. Each isotherm is spaced evenly throughout the pressure range, the hydrogen capacities of correspondingly substituted alloys are almost equal, and the sloping character at the beginnings and ends of the isotherms are markedly similar. This leads us to believe that Sn and Ge act almost identically as alloying solutes, with the main distinction between them being the expansion of the $LaNi_5$ lattice, dependant upon the solute metallic radius.

When the metal hydride plateau pressures are plotted *vs* the alloy unit cell volumes on a semi-log graph (**Figure V-11a**), we see the linear relationship noted by a number of researchers.[11] However, we also notice that Ge seems more effective than Sn in suppressing the plateau pressures of the alloys. Although it takes more Ge than Sn to expand the $LaNi_5$ unit cell a given amount, a hypothetical Ge-substituted alloy will have a lower plateau pressure than a Sn-substituted alloy with the same unit cell volume. This discrepancy becomes more pronounced when we realize that the logarithm of the plateau pressure is proportional to the Gibbs' free energy of hydride formation, and subtract the effect of entropy. Because our hypothetical Ge alloy has a larger solute composition than the Sn alloy, it has a lower hydrogen composition. Hydrogen absorbed into the Ge-substituted lattice has a more restricted configuration, leading to a greater loss of entropy

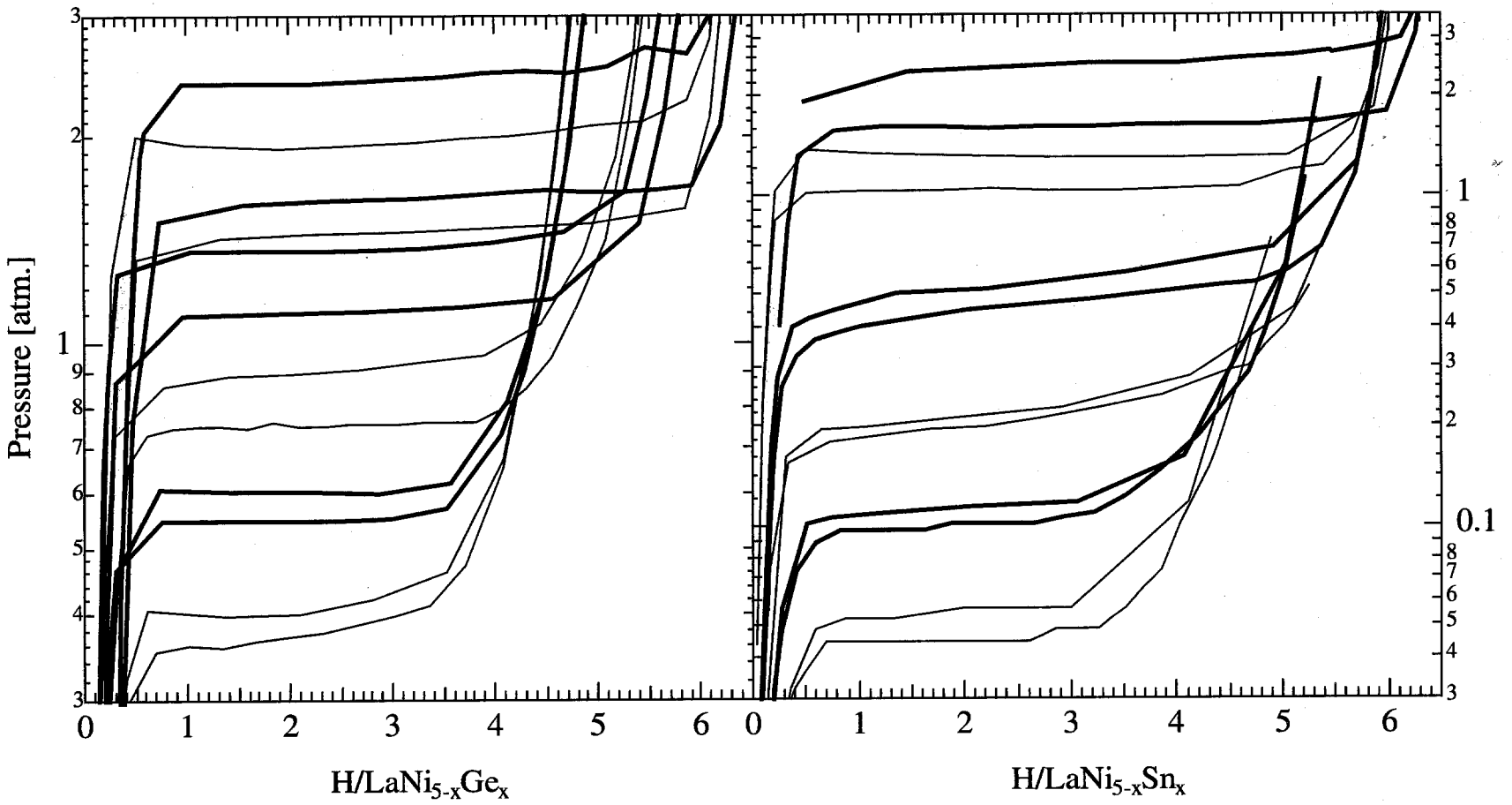

Figure V-10 Juxtaposed isotherms of $LaNi_{5-x}Ge_x$ (left) and $LaNi_{5-x}Sn_x$ (right) alloys, $0 \leq x \leq 0.5$.

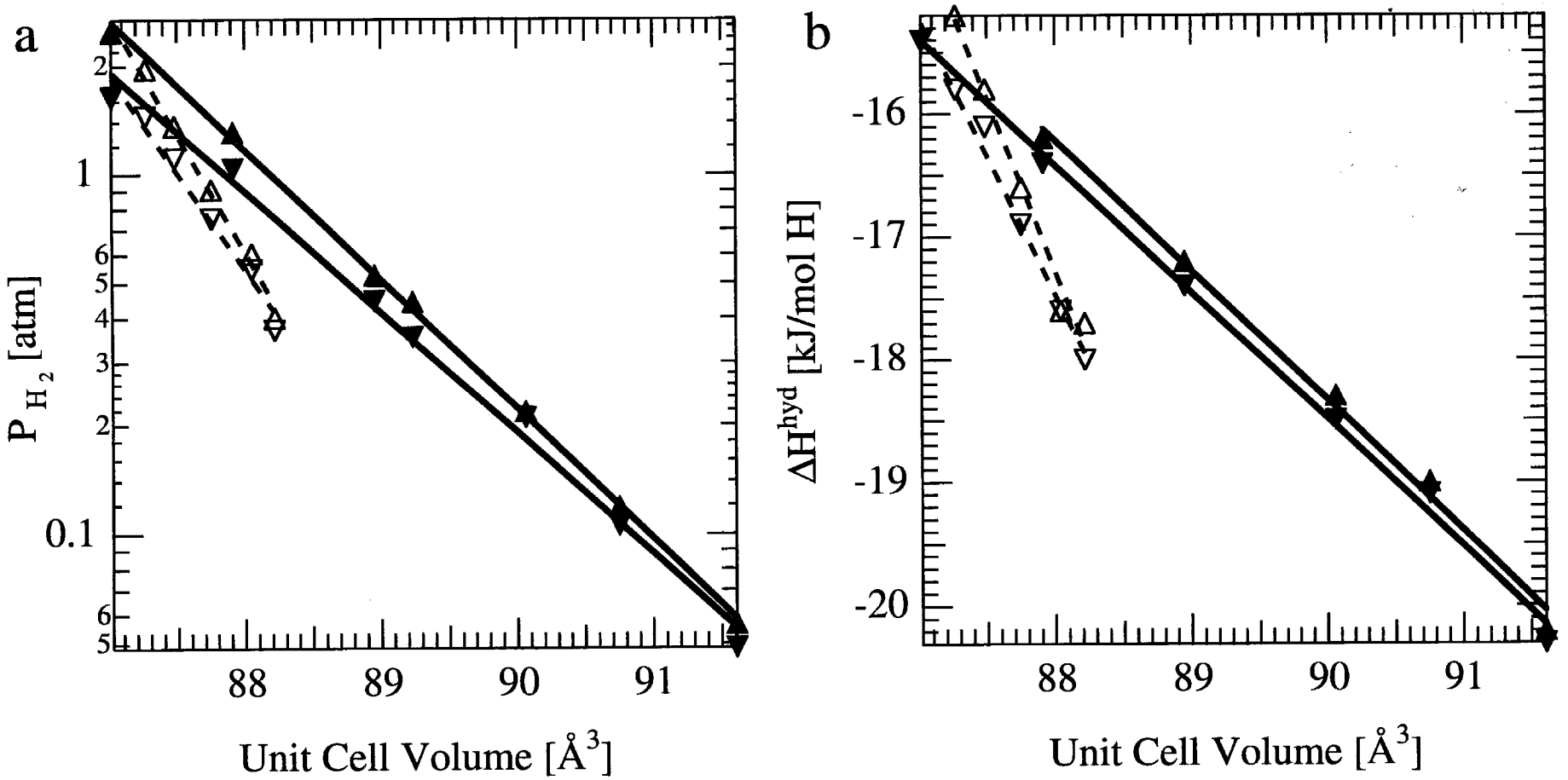

Figure V-11 a) Semi-log plot of plateau pressure *vs* $V_{unit\ cell}$ (▲ - abs., ▼ - des.).
b) Enthalpies of hydride formation (▲) and decomp. (▼) *vs* $V_{unit\ cell}$.
{ ▲ , ▼ - Sn_x; Δ , ∇ - Ge_x}

than hydrogen absorbed into the Sn-substituted lattice. To eliminate the effect of differences in entropy, the enthalpies of hydride formation and decomposition should be plotted *vs* alloy unit cell volume, as in **Figure V-11b**. We can examine the composition weighted chemical effect of the solute as the difference between the two curves.

In the literature of ternary alloys of $LaNi_5$, we found the following relationships between solute composition and enthalpy of hydride decomposition:

$$\Delta H^{Mn}_{des}(x) = 15.48 + 9.08\, x_{Mn} \pm 0.2 \text{ kJ/(mol H)} \quad [V.3]^{3}$$

$$\Delta H^{Fe}_{des}(x) = 14.88 + 1.14\, x_{Fe} \text{ kJ/(mol H)} \quad [V.4]^{6}$$

Fitting the Sn_x and Al_x data to linear relationships, we obtain:

$$\Delta H^{Sn}_{abs}(x) = -15.21 - 9.79\, x_{Sn} \text{ kJ/(mol H),} \quad [V.5]^{22,23}$$

$$\Delta H^{Sn}_{des}(x) = 15.42 + 9.58\, x_{Sn} \text{ kJ/(mol H), and} \quad [V.6]^{22,23}$$

$$\Delta H^{Al}_{des}(x) = 15.438 + 8.31\, x_{Al} \text{ kJ/(mol H).} \quad [V.7]^{11,24}$$

This relationship was not available for all solutes owing to scatter in the data or a non-linear relationship (Co).

From these equations and the unit cell volume relationships determined in §IV.B.3, we obtain the following linear relationships between ΔH^{hyd} and unit cell volume:

Absorption:

$$\Delta H^{Ge}_{abs}(V) = -229 + 2.80\, V_{Ge} \text{ kJ/(mol H),} \quad [V.8]$$

$$\Delta H^{Sn}_{abs}(V) = -77.1 + 1.06\, V_{Sn} \text{ kJ/(mol H),} \quad [V.9]^{22,23}$$

Desorption:

$$\Delta H^{Al}_{des}(V) = 193 - 2.41\, V_{Al} \text{ kJ/(mol H).} \quad [V.10]^{11,24}$$

$$\Delta H^{Ge}_{des}(V) = 180 - 2.25\, V_{Ge} \text{ kJ/(mol H),} \quad [V.11]$$

$$\Delta H^{Mn}_{des}(V) = 130 - 1.67\ V_{Mn} \quad \text{kJ/(mol H)}, \quad [V.11]^{3}$$

$$\Delta H^{Sn}_{des}(V) = 74.5 - 1.03\ V_{Sn} \quad \text{kJ/(mol H)}, \quad [V.12]^{22,23}$$

$$\Delta H^{Fe}_{des}(V) = 34.0 - 0.56\ V_{Fe} \quad \text{kJ/(mol H)}. \quad [V.13]^{6,25}$$

The intercepts of these lines are not equal to the enthalpies of hydriding because the volumes used are not differential volumes, $(V_M - V_{LaNi_5})$. The slope of the corresponding equation V.8 – V.13, characterizes the change in hydriding enthalpy per $Å^3$ of unit cell volume for each solute. This enthalpy *vs* unit cell volume parameter has been plotted *vs* solute atom metallic radius and the heat of formation with La in **Figures V-12a** and **b**, respectively. If the unit cell volume were the only factor affecting the enthalpy of hydride formation, this parameter would not vary with solute element. From the spread in these values (0.56 – 2.8) is clear than there are second order effects controlling the alloy plateau pressure, but the available data are too sparse to discern any trends.

The sloping nature at the ends of the plateaus is more pronounced for solutes with larger metallic radii, even though these alloys have smaller substituted compositions. This is indicative of larger solutes being more effective in reducing the miscibility gap between the α- and β-phases. It is possible that the disorder retained after the annealing treatment used to homogenize the alloys is greater for large solutes. The interaction energy between solute atoms would drive them to form inhomogeneous concentration distributions, leading to a sloping plateau. It is also true that the larger strain field resulting from larger solutes could create a distribution of H sites with a broader range of energies.

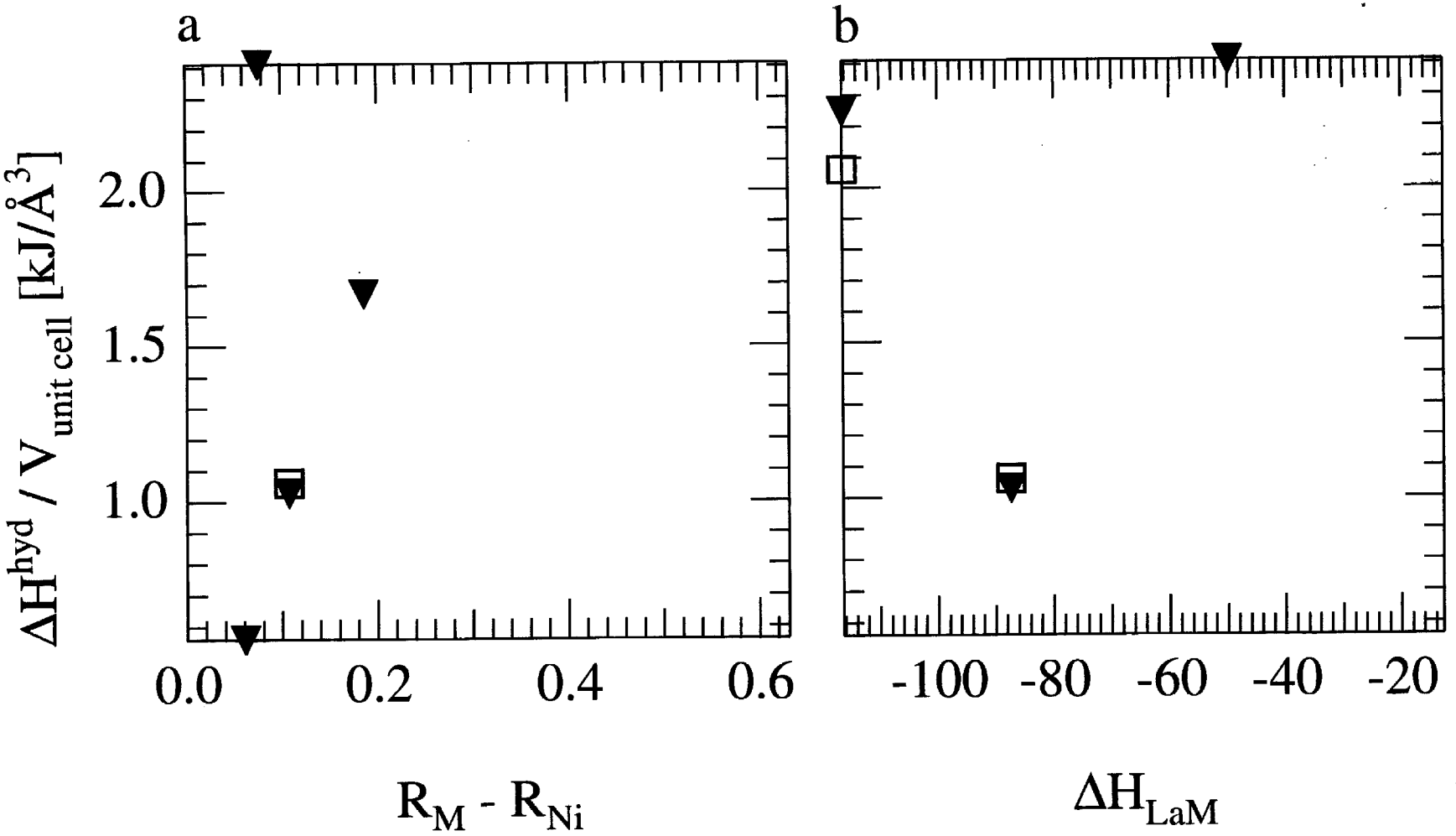

Figure V-12 Hydride enthalpy *vs* volume parameter plotted with:
a) solute metallic radius; b) heat of formation of the solute with La.

[1] H.H. van Mal, K.H.J. Buschow, and A.R. Miedema, *J. Less-Common Met.*, **35** (1974): 65.

[2] A. Percheron-Guégan, C. Lartigue, and J.C. Achard, *J. Less-Common Met.*, **109** (1985): 287.

[3] C. Lartigue, A. Percheron-Guégan, J.C. Achard, and F. Tasset, *J. Less-Common Met.*, **75** (1980): 23.

[4] W. Luo, S. Luo, J.D. Clewley, T.B. Flanagan, R.C. Bowman, Jr., and J.S. Cantrell, *J. Alloys Comp.*, **75** (1993): 147.

[5] S. Bagchi, D. Chandra, W.N. Cathey, R.C. Bowman, Jr., and F.E. Lynch, subm 1997 TMS Meeting.

[6] J. Lamloumi, A. Percheron-Guégan, C. Lartigue, J.C. Achard, and G. Jehanno, *J. Less-Common Met.*, **130** (1987): 111.

[7] H.H. van Mal, K.H.J. Buschow, and F.A. Kuijpers, *J. Less-Common Met.*, **32** (1973): 289.

[8] J. Shinar, D. Shaltiel, D. Davidov, and A. Grayevsky, *J. Less-Common Met.*, **60** (1978): 209.

[9] M.H. Mendelsohn, D.M. Gruen, and A.E. Dwight, *Nature*, **269** (1977): 45.

[10] M.H. Mendelsohn, D.M. Gruen, and A.E. Dwight, *RE In Mod Sci & Tech*, **1** (1977): 25.

[11] M.H. Mendelsohn, D.M. Gruen, and A.E. Dwight, *J. Less-Common Met.*, **63** (1979) 193; D.M. Gruen, M.H. Mendelsohn, and A.E. Dwight, *Advances in Chemistry Series 167 Transition Metal Hydrides*, R. Bau, ed., American Chemical Society, Wash. DC, (1978): 327.

[12] J.-M. Park and J.-Y. Lee, *Mat. Res. Bull.*, **22** (1987): 455.

[13] T. Sakai, H. Miyamura, N. Kuriyama, A. Kato, K. Oguro, H. Ishikawa, and C. Iwakura, *J Less-Com Met.*, **159** (1990): 127.

[14] M. Latroche, A. Percheron-Guégan, Y. Chabre, C. Poinsignon, and J. Pannetier, *J. Alloys Comp.*, **189** (1992): 59.

[15] M.H. Mendelsohn and D.M. Gruen, *Rare Earths In Mod Sci & Tech*, **2** (1980): 593.

[16] M.H. Mendelsohn, D.M. Gruen, and A.E. Dwight, *Inorg. Chem.*, **18**(12) (1979): 3443.

[17] F. Meli, A. Züttel, and L. Schlapbach, *J. Alloys Comp.*, **190** (1992): 17.

[18] S. Srivastava and O.N. Srivastava, *J. Alloys Comp.*, **267** (1998): 240.

[19] Z. Blazina and A. Drasner, *J. Phys.: Condens. Matter*, **10** (1998): 4777.

[20] M.H. Mendelsohn, D.M. Gruen, and A.E. Dwight, *Mat. Res. Bull.*, **13** (1978): 1221.

[21] J.S. Cantrell, T.A. Beiter, and R.C. Bowman, Jr., *J. Alloys Comp.*, **207/8** (1994): 372.

[22] S. Luo, W. Luo, J.D. Clewley, T.B. Flanagan, and R.C. Bowman, Jr., *J. Alloys Comp.*, **231** (1995): 467.

[23] S. Luo, J.D. Clewley, Ted B. Flanagan, R.C. Bowman, Jr., and L.A. Wade, *J. Alloys Comp.*, **267** (1998): 171

[24] H. Diaz, A. Percheron-Guégan, and J. C. Achard, *Int. J. Hydrogen Energy*, **4** (1979): 445.

[25] J. Lamloumi, A. Percheron-Guégan, J.C. Achard, G. Jehanno, and D. Givord, *J. Physique*, **45** (1984): 1643.

VI. Electrochemical Kinetics

As explained in *Methods* (§III.E), the electrochemical cell is a unique, though intricate, environment to investigate chemical reactions. It provides a direct method to measure chemical potentials, but it is difficult to isolate individual species and reactions from the testing apparatus and environment. Therefore, a single electrochemical measurement should not be used exclusively to characterize a material. We are more likely to obtain accurate information about a material by interpreting the results of a series of electrochemical tests in conjunction with other techniques that characterize the microstructure of a sample. In light of this recommendation, I will present results from three different electrochemical tests and will make use of information gained from diffraction experiments to interpret these results. It should be noted, however, that the point of testing the alloys' electrochemical kinetics was to insure their viability for use in consumer Ni-MH rechargeable batteries. Gaining a deeper understanding about the electrochemical processes taking place at the MH anode is beyond the scope of this thesis.

A. DC Micropolarization

1. $LaNi_{5-x}Sn_x$

Figure VI-1 shows the micropolarization curves of the $LaNi_{5-x}Sn_x$ alloys. The values of the exchange currents estimated from the slopes of micropolarization curves of different MH alloys show an interesting trend (**Figure VI-11** and **Table VI-1**). The exchange current (i_0) increases initially upon Sn substitution from 0.77 mA for the binary alloy to 1.35 mA for the alloy with x = 0.1. Further addition of Sn decreases the exchange current. Nevertheless, the kinetics of Sn substituted alloys are superior to those of the binary alloy for Sn compositions of $x \leq 0.3$ in unsealed cells. With Sn

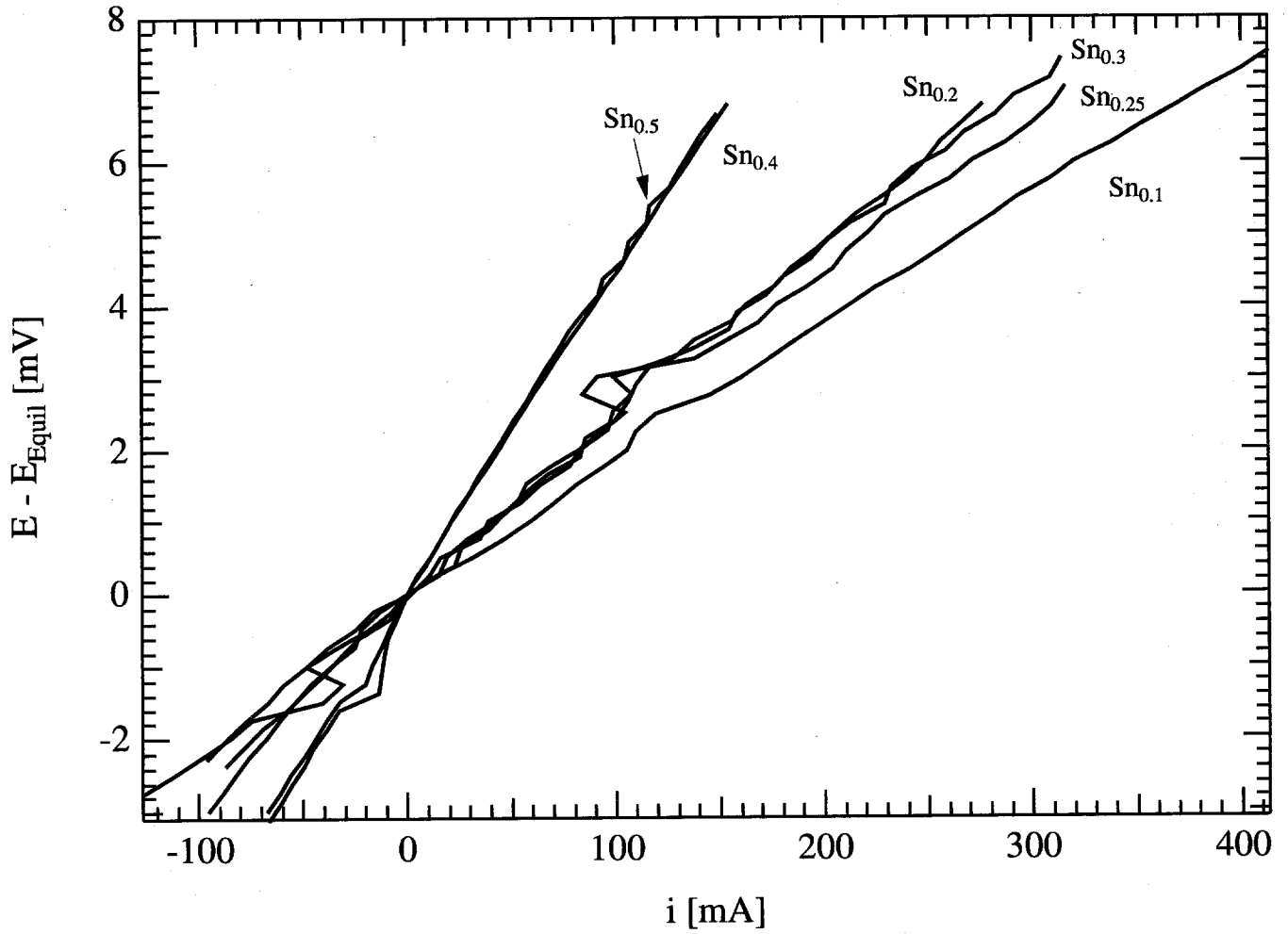

Figure VI-1 Linear polarization of $LaNi_{5-x}Sn_x$ alloys.

compositions of $x \geq 0.4$, the kinetics of hydrogen absorption and desorption are slowed considerably, and are even slower than in the binary alloy.

2. $LaNi_{5-x}Ge_x$

Figure VI-2 shows the approximately linear micropolarization curves of $LaNi_{5-x}Ge_x$ alloys. The exchange currents estimated from the slopes of micropolarization curves show an improvement in the kinetics of hydrogen absorption and desorption upon Ge substitution (**Figure VI-11** and **Table VI-2**). There is a small decrease at low Ge concentrations compared to the binary alloy, i.e., from 0.77 mA for the binary alloy to 0.63 and 0.71 for Ge compositions of 0.1 and 0.2, respectively. At higher Ge compositions, i.e., $x \geq 0.3$, the exchange current is higher than that of the binary alloy and continues to increase with Ge composition. Unlike the case for Sn solutes, which cause marginal slowing of kinetics at $x \geq 0.4$, high Ge concentrations have no adverse effects on the kinetics of the alloy.

3. $LaNi_{5-x}M_x$

Micropolarization measurements of the $LaNi_{5-x}M_x$ alloys can be seen in **Figure VI-3**. The exchange current densities calculated from these measurements, shown in **Figure VI-11** and **Table VI-3**, show a trend with composition different than that seen with the Sn_x and Ge_x alloys. The exchange currents increase slightly for substituted compounds with $x \leq 0.2$. $Al_{0.26}$ has the maximum charge transfer exchange current measured for any alloy. The exchange currents of alloys with higher nickel substitution decrease monotonically with substituted composition.

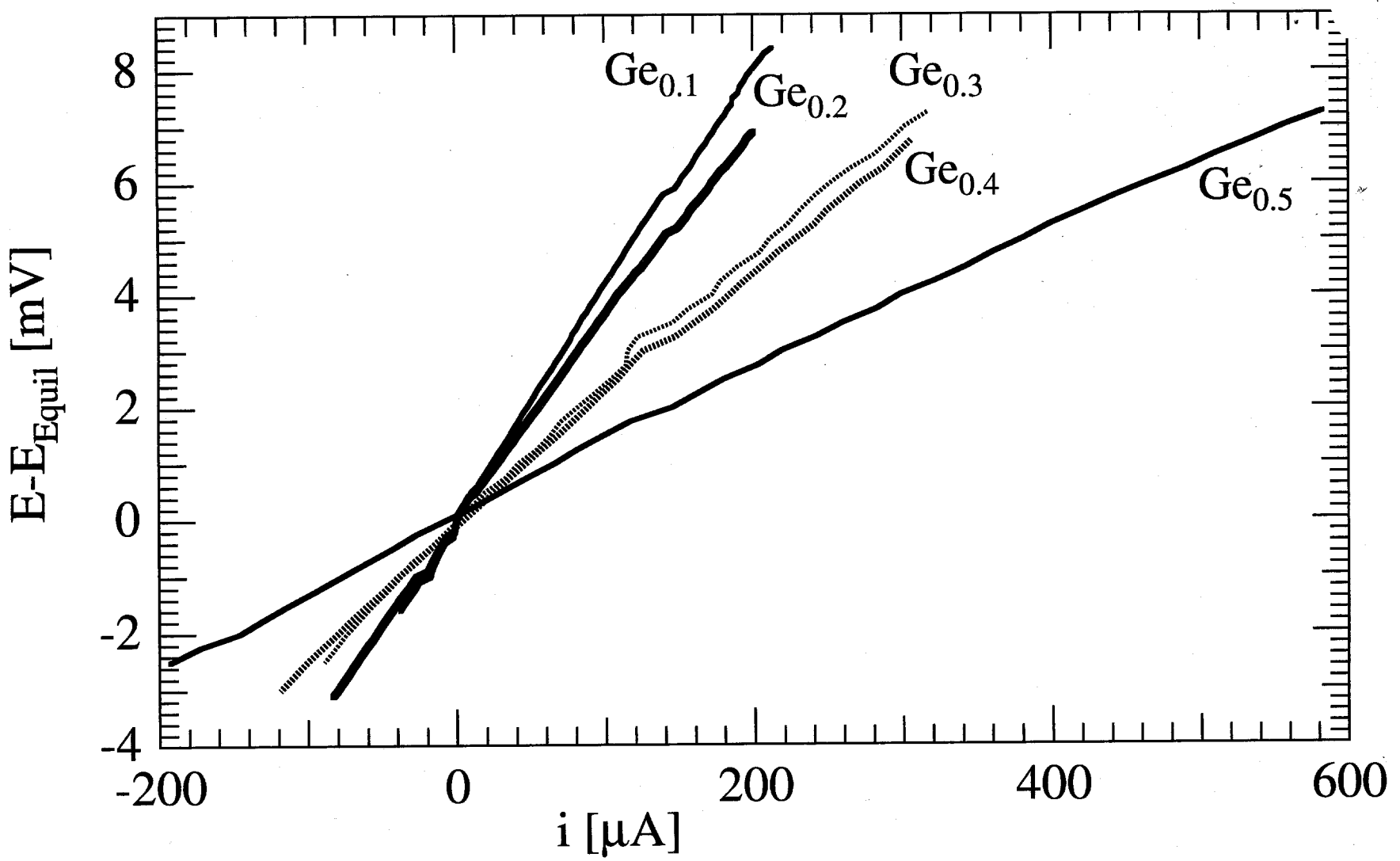

Figure VI-2 Linear polarization of $LaNi_{5-x}Ge_x$ alloys.

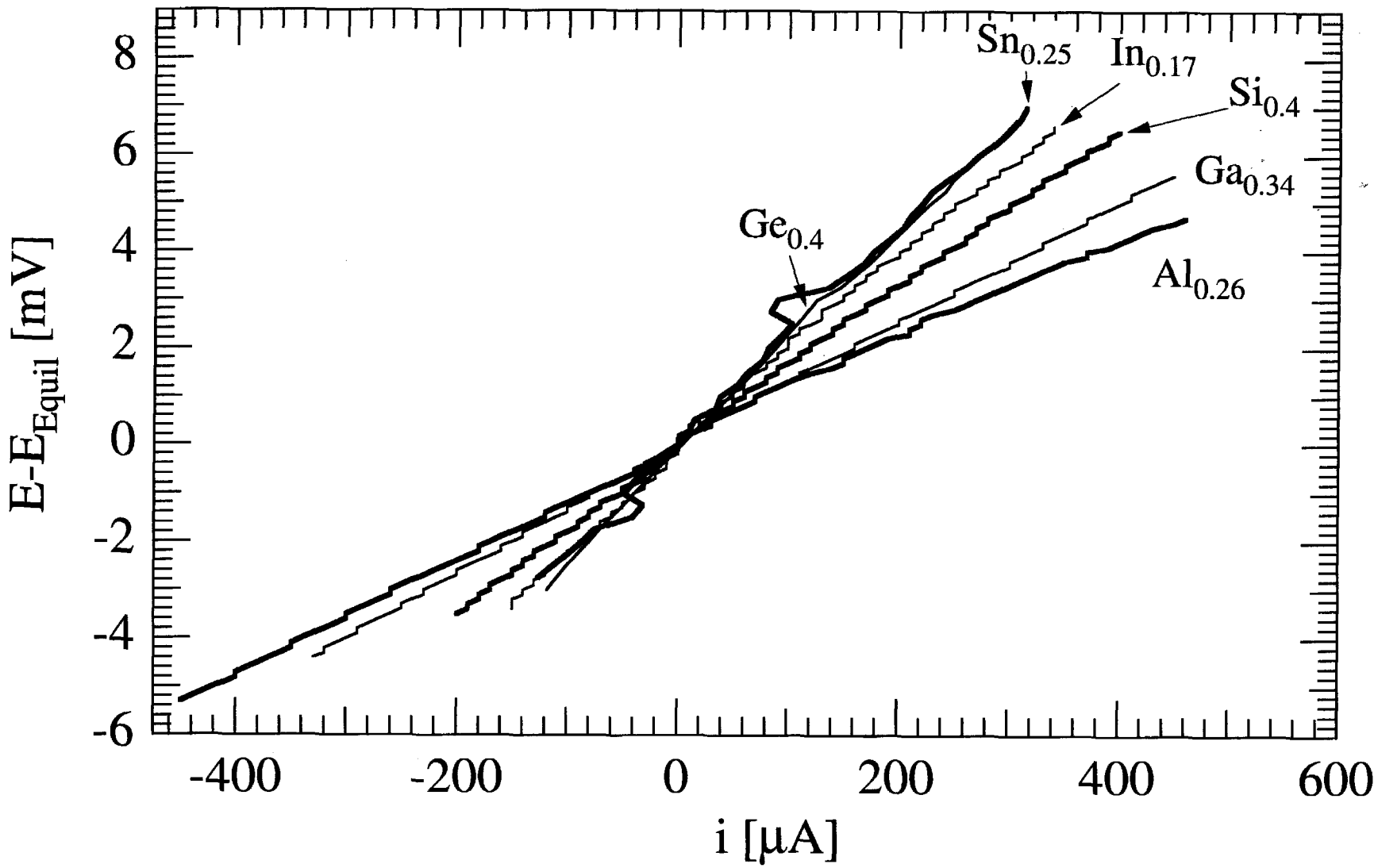

Figure VI-3 Linear polarization of $LaNi_{5-x}M_x$ alloys.

B. AC Impedance

Electrochemical impedance spectroscopic measurements were made on mixed anode powders in the charged state. The powders were activated by gas-phase absorption but were not electrochemically cycled. The AC impedance data were obtained in the frequency range of 100 kHz to 5 mHz at a low AC amplitude of 2 mV. The charge transfer resistance of the electrode can be obtained by fitting the Cole-Cole representation of the impedance spectra to the equivalent circuit shown in **Figure III-17**.[1] The observed impedance patterns of the MH electrodes are simplified by the absence of a diffusional component, and this element was excluded from the equivalent circuit. The parameters in the equivalent circuit were calculated by a non-linear least squares fit using the Boukamp method.[2] To be consistent with the other electrochemical tests shown here, the charge transfer resistance, R_{CT}, is converted to an exchange current using **equation IV.E.11**. All charge transfer exchange currents are shown in **Figure VI-12** *vs* substituted composition.

1. $LaNi_{5-x}Sn_x$

The impedance plots of $LaNi_{5-x}Sn_x$ alloy electrodes are shown in the Nyquist or Cole-Cole form in **Figure VI-4**. The observed impedance patterns of the MH electrodes are simplified by the absence of a diffusional component. As may be seen in this figure, the impedance decreases noticeably upon initial substitution of Sn, then increases with x. The trend is similar to that observed in the DC polarization experiments. It is thus clear that the kinetics of hydriding improves markedly upon Sn substitution in $LaNi_{5-x}Sn_x$, at least for $x \leq 0.3$. Higher amounts of Sn seem to cause sluggish kinetics for hydrogen absorption and desorption.

2. $LaNi_{5-x}Ge_x$

The impedance plots of $LaNi_{5-x}Ge_x$ alloy electrodes are shown in the Nyquist form in **Figure VI-5**. The figure shows that the impedance increases slightly upon initial substitution of Ge, but decreases for x = 0.3. This trend is similar to that observed in the dc polarization experiments.

3. $LaNi_{5-x}M_x$

The impedance plots of $LaNi_{5-x}M_x$ alloy electrodes are shown in the Nyquist form in **Figure VI-6**. The figure shows that the impedance of all substituted are less than that of $LaNi_5$. The impedance follows a trend similar to that observed in the dc polarization experiments. All substituted alloys have lower impedance than $LaNi_5$. There is a minimum *vs* substituted composition for $Al_{0.26}$.

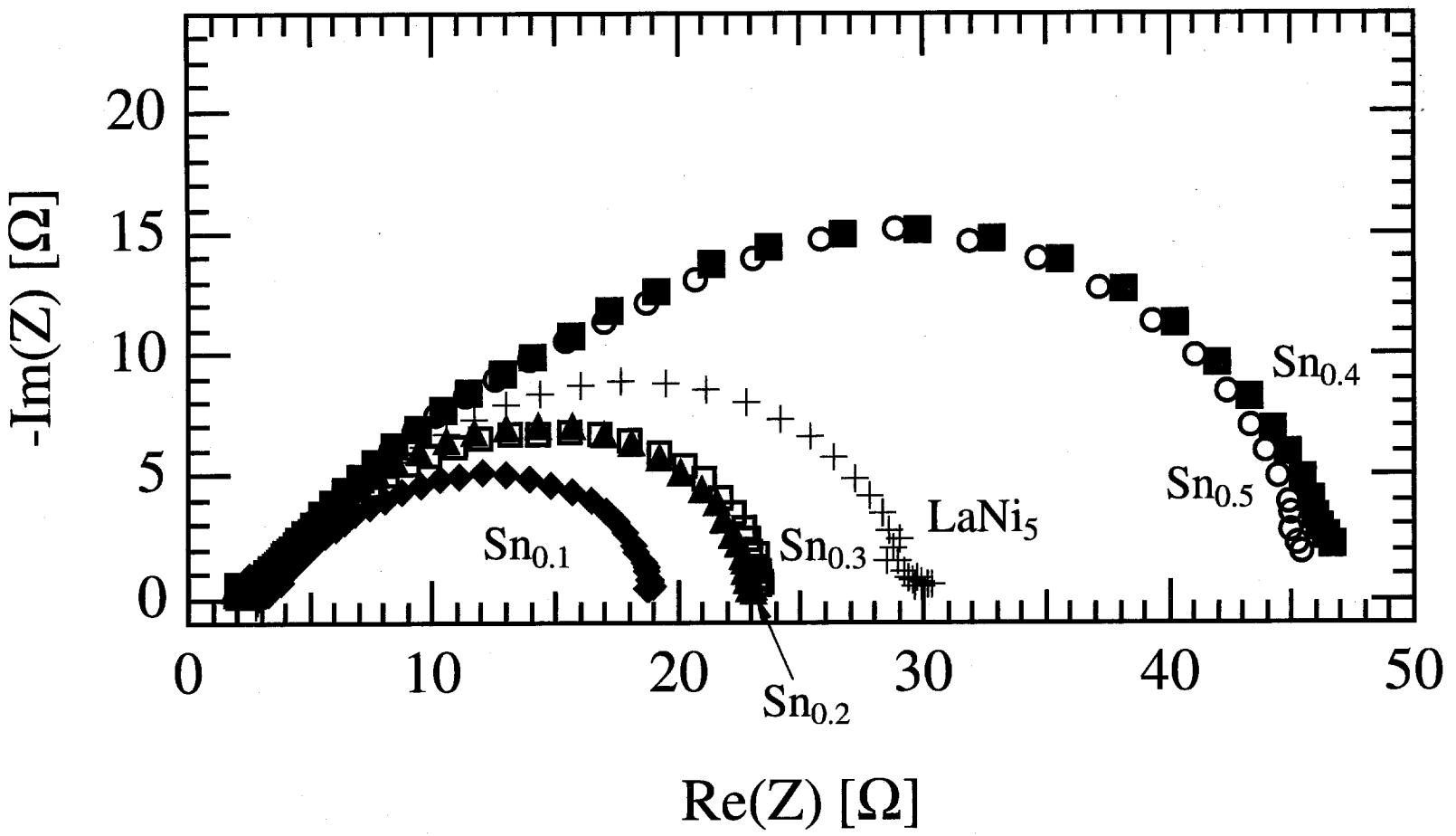

Figure VI-4 AC Impedance spectra of $LaNi_{5-x}Sn_x$ alloys.
{✚ - $LaNi_5$; ◆ - $Sn_{0.1}$; ▲ - $Sn_{0.2}$; □ - $Sn_{0.3}$; ■ - $Sn_{0.4}$; ○ - $Sn_{0.5}$}

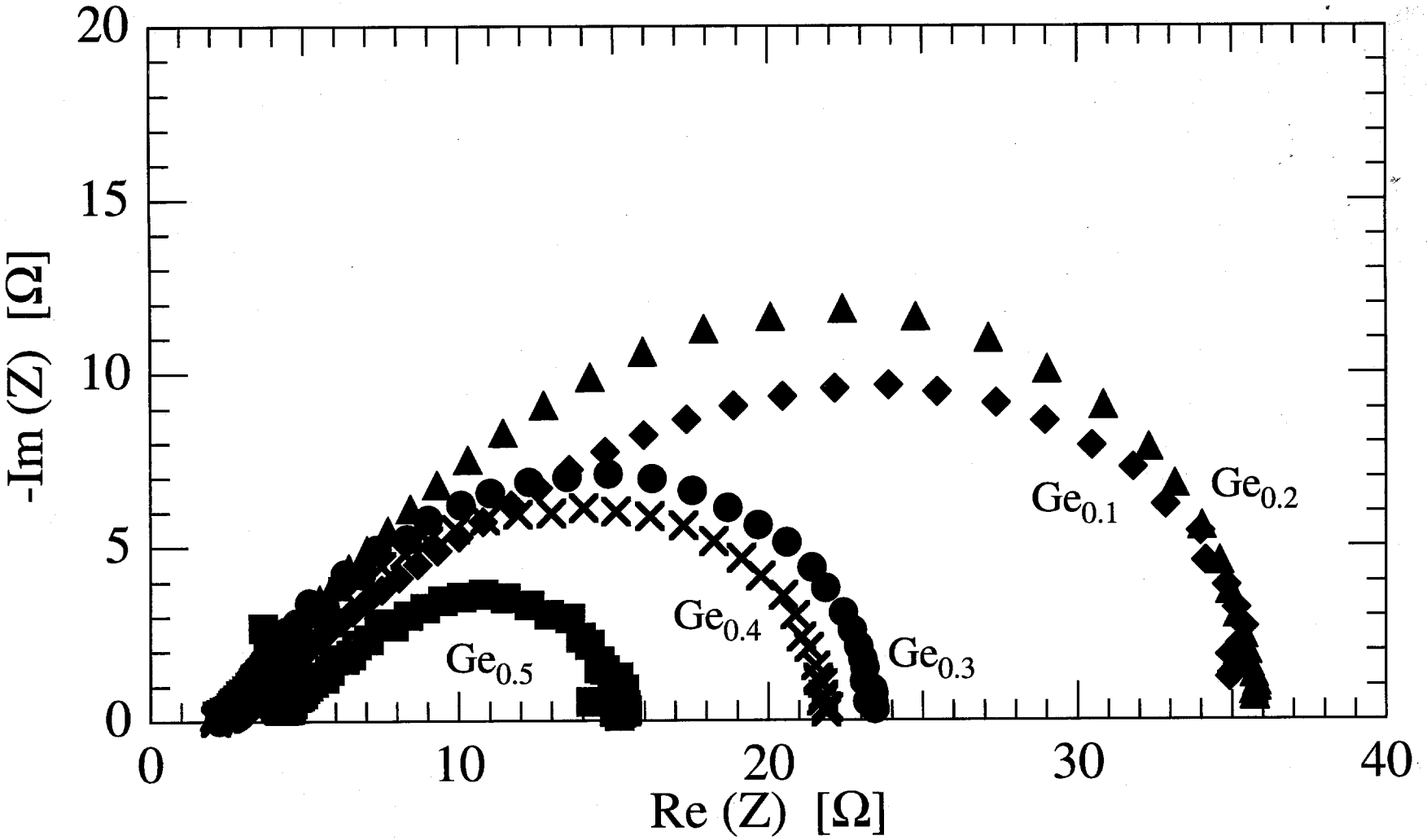

Figure VI-5 AC Impedance spectra of $LaNi_{5-x}Ge_x$ alloys.
{ ◆ - $Ge_{0.1}$; ▲ - $Ge_{0.2}$; ● - $Ge_{0.3}$; ✕ - $Ge_{0.4}$; ■ - $Ge_{0.5}$}

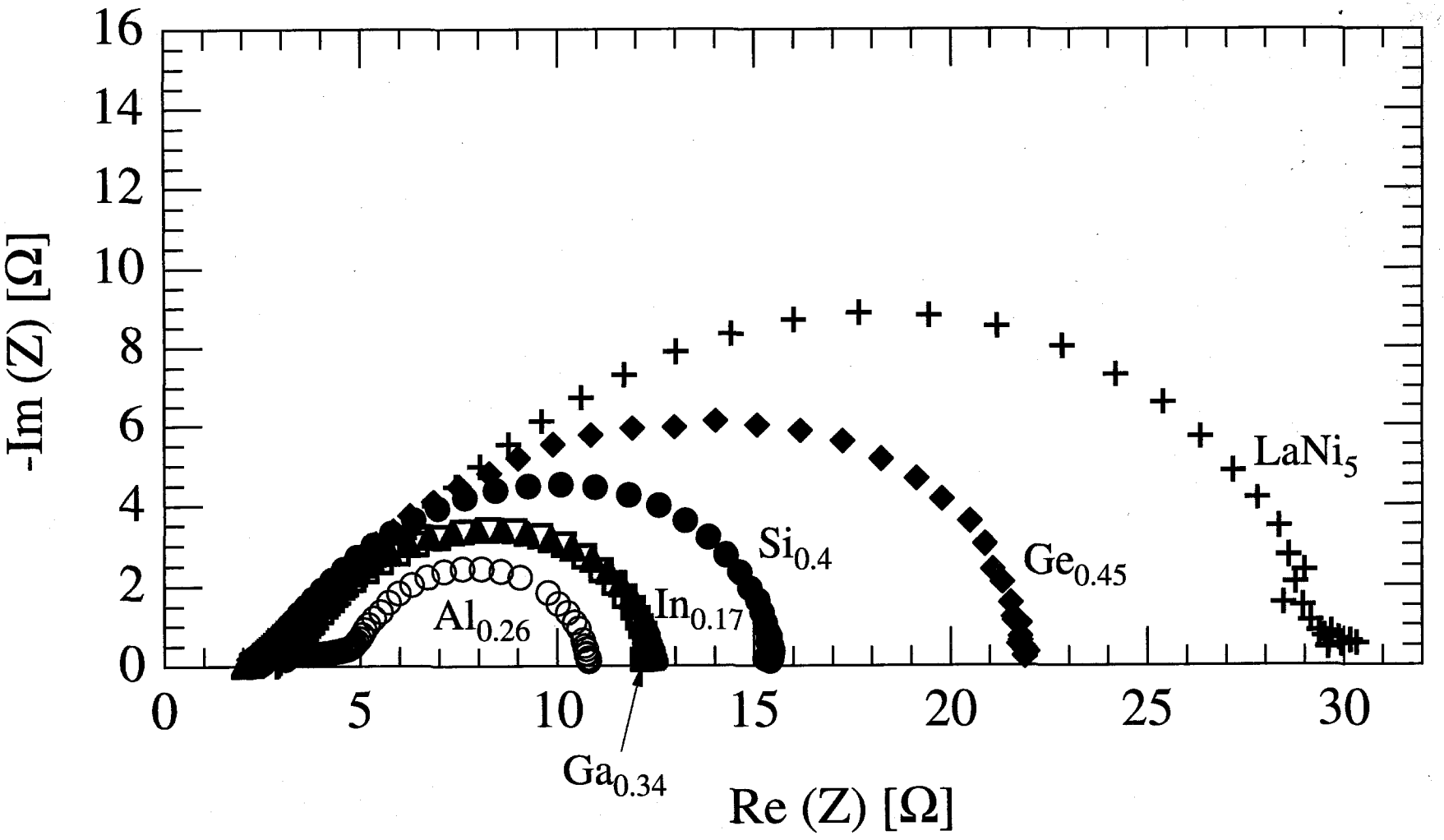

Figure VI-6 AC Impedance spectra of $LaNi_{5-x}M_x$ alloys.
{ + - $LaNi_5$; ▲ - $In_{0.17}$; ○ - $Al_{0.26}$; □ - $Ga_{0.34}$; ● - $Si_{0.4}$; ◆ - $Ge_{0.45}$}

C. Tafel Polarization

As mentioned in *Methods* (§III.E.1.b.iii), the Tafel polarization measurements of MH electrodes show interference from mass transfer effects. Desorption limiting currents are used here to correct both anodic (desorption) and cathodic (absorption) Tafel plots for the mass transfer interference. This is in contrast to the approach of Zheng, *et al.*[4] who used different limiting currents for charge and discharge. The latter approach might introduce uncertainties in the cathodic limiting currents, due to simultaneous hydrogen evolution at high negative potentials.[3] Anodic Tafel exchange currents for all alloys are shown in **Figure VI-13** *vs* substituted composition, and cathodic Tafel exchange currents appear in **Figure VI-14**. Transfer coefficients calculated from the inverse slopes of anodic and cathodic Tafel polarization are plotted *vs* substituted composition in **Figures VI-15** and **VI-16**, respectively.

1. $LaNi_{5-x}Sn_x$

Figure VI-7 illustrates the Tafel behavior of $LaNi_{5-x}Sn_x$ alloys during charge and discharge. The overpotentials at any current density can be seen to decrease upon the initial substitution of Sn, but increase for the highest Sn concentration. The limiting currents were measured in separate potentiodynamic measurements at a potential 400 mV more positive than the equilibrium potential, and are listed in **Table VI-1**. The corrected Tafel plots (**Figure VI-8**) are more linear.

The absorption exchange current (**Table VI-1**) increases upon Sn substitution and shows a maximum at a Sn composition of $x = 0.2$. The desorption exchange current improves more significantly upon Sn substitution, but has a maximum near $x = 0.1$. Nevertheless, the kinetics of desorption continue to be better than the binary alloy for $x < 0.4$. The Tafel slopes show an interesting trend: the slope for the absorption process decreases with increasing Sn concentration, whereas the slope for the desorption process

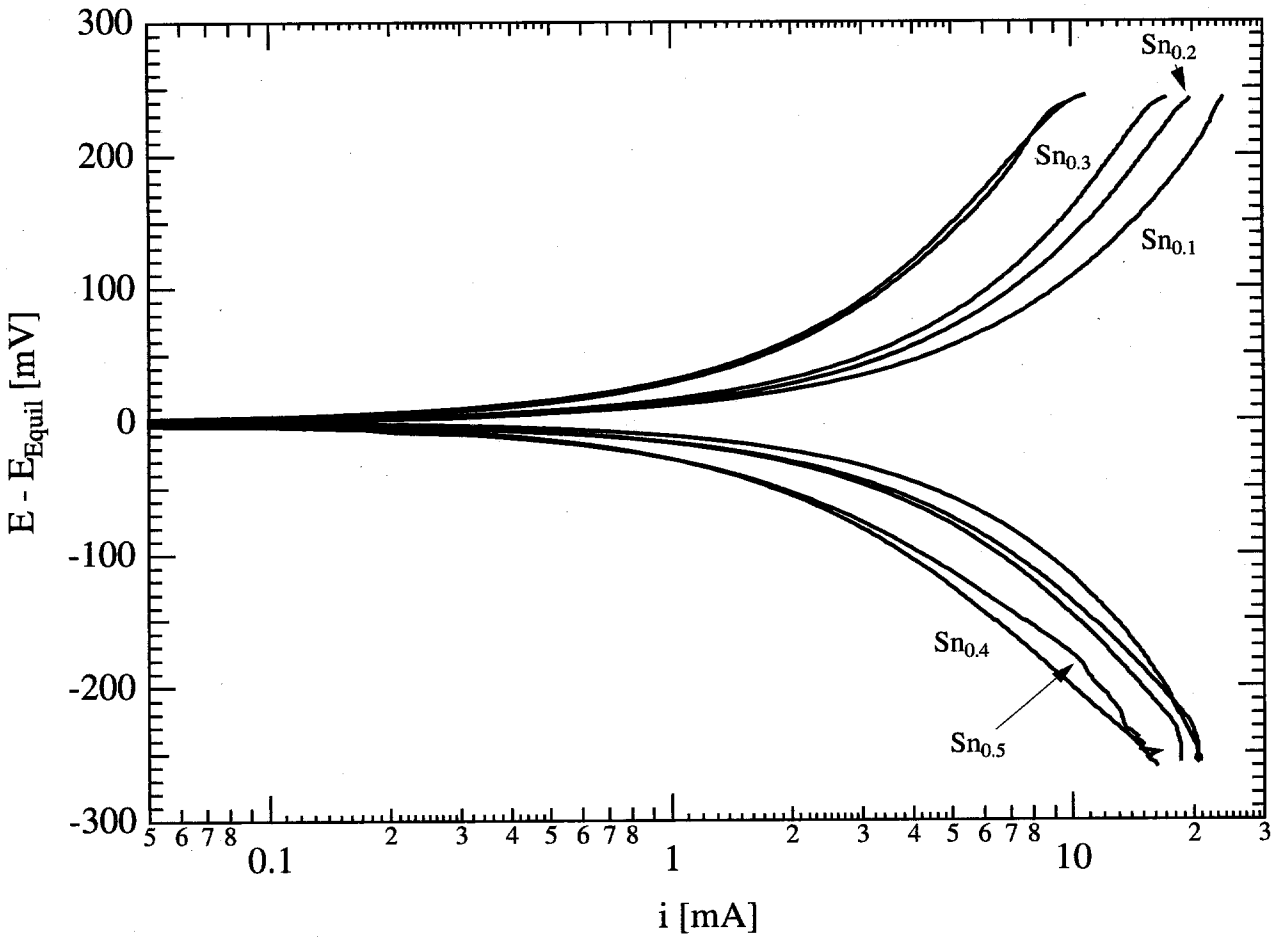

Figure VI-7 Tafel polarization of $LaNi_{5-x}Sn_x$ alloys.

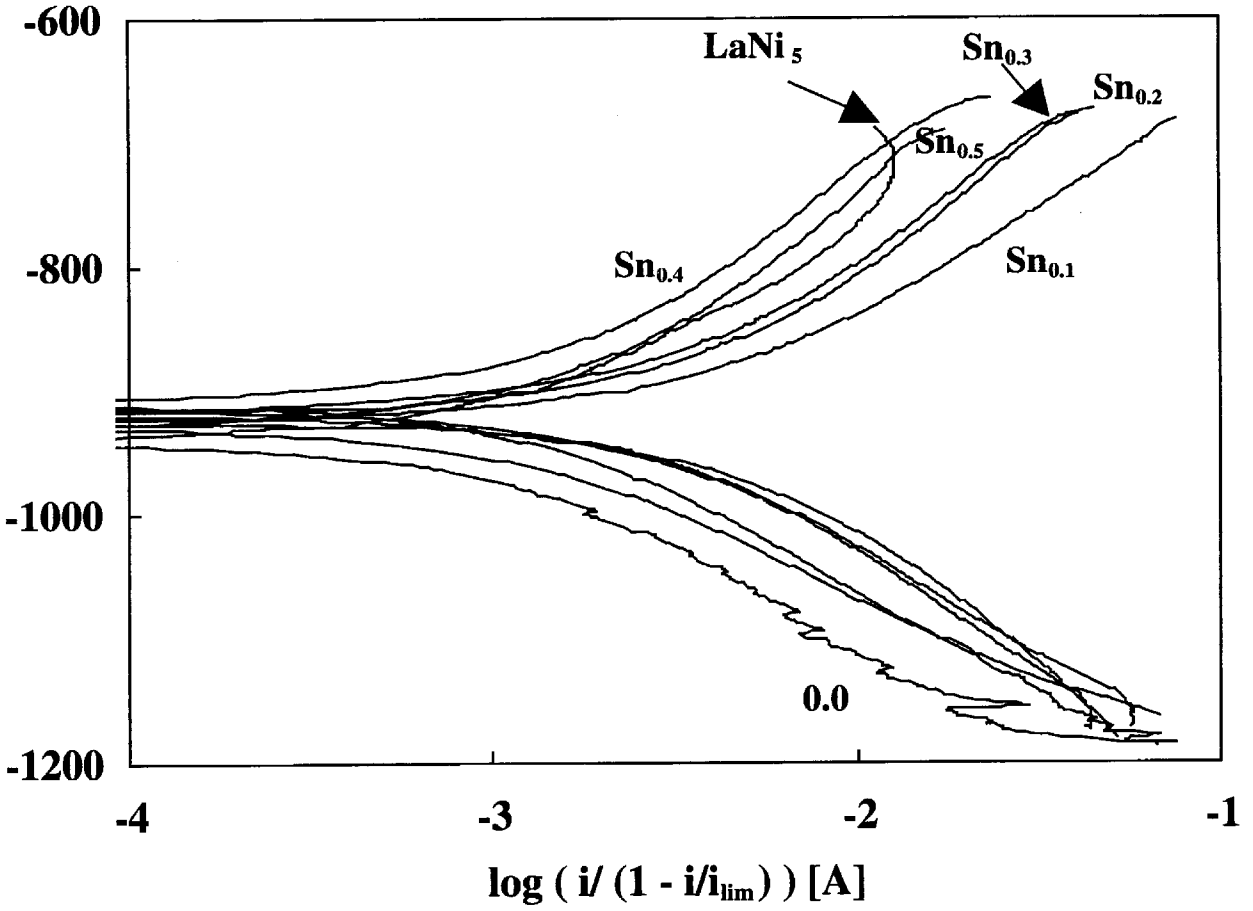

Figure VI-8 Mass corrected Tafel polarization of $LaNi_{5-x}Sn_x$ alloys.

increases (**Table VI-1**). The change in both the parameters is less marked for $x > 0.2$. The transfer coefficients during absorption (**Figures VI-15**) calculated from the Tafel slopes increase with increasing Sn composition. The corresponding transfer coefficients during desorption(**Figures VI-16**), however, decrease with increasing Sn composition.

2. $LaNi_{5-x}Ge_x$

Figure VI-9 illustrates the Tafel behavior of $LaNi_{5-x}Ge_x$ alloys during charge and discharge. The limiting currents were measured in a separate potentiodynamic experiment at higher positive potentials, i.e., 400 mV away from the reversible potential (**Table VI-2**), and used to correct for the above mass-transfer interference. The diffusion limiting current on discharge is highest for a Ge composition of $0.1 \leq x \leq 0.2$ (in the range of 500 mA/g) and is reduced at high Ge compositions.

The absorption exchange current density increases upon Ge substitution and shows a maximum at a Ge composition of $x = 0.3$ (**Figure VI-13** and **Table VI-2**). The desorption exchange current (**Figure VI-14** and **Table VI-2**) improves more significantly upon Ge substitution, and also has a maximum near $x = 0.3$. The transfer coefficient for the absorption process is not monotonic with substituted composition, although all Ge_x alloys have absorption transfer coefficients greater than that of $LaNi_5$. The transfer coefficient for the desorption process has a minimum at $x = 0.3$.

3. $LaNi_{5-x}M_x$

Measurements of the Tafel behavior of $LaNi_{5-x}M_x$ alloys are shown in **Figure VI-10**. The limiting currents were estimated from the Tafel curves using trends noted with the previous measurements. The anodic and cathodic exchange currents show the same trend. The exchange currents increase with substituted composition except for $Ga_{0.34}$, which has exchange currents slightly lower than the other alloys. The transfer coefficients are somewhat less regular. The desorption transfer coefficient of $In_{0.17}$ (0.59)

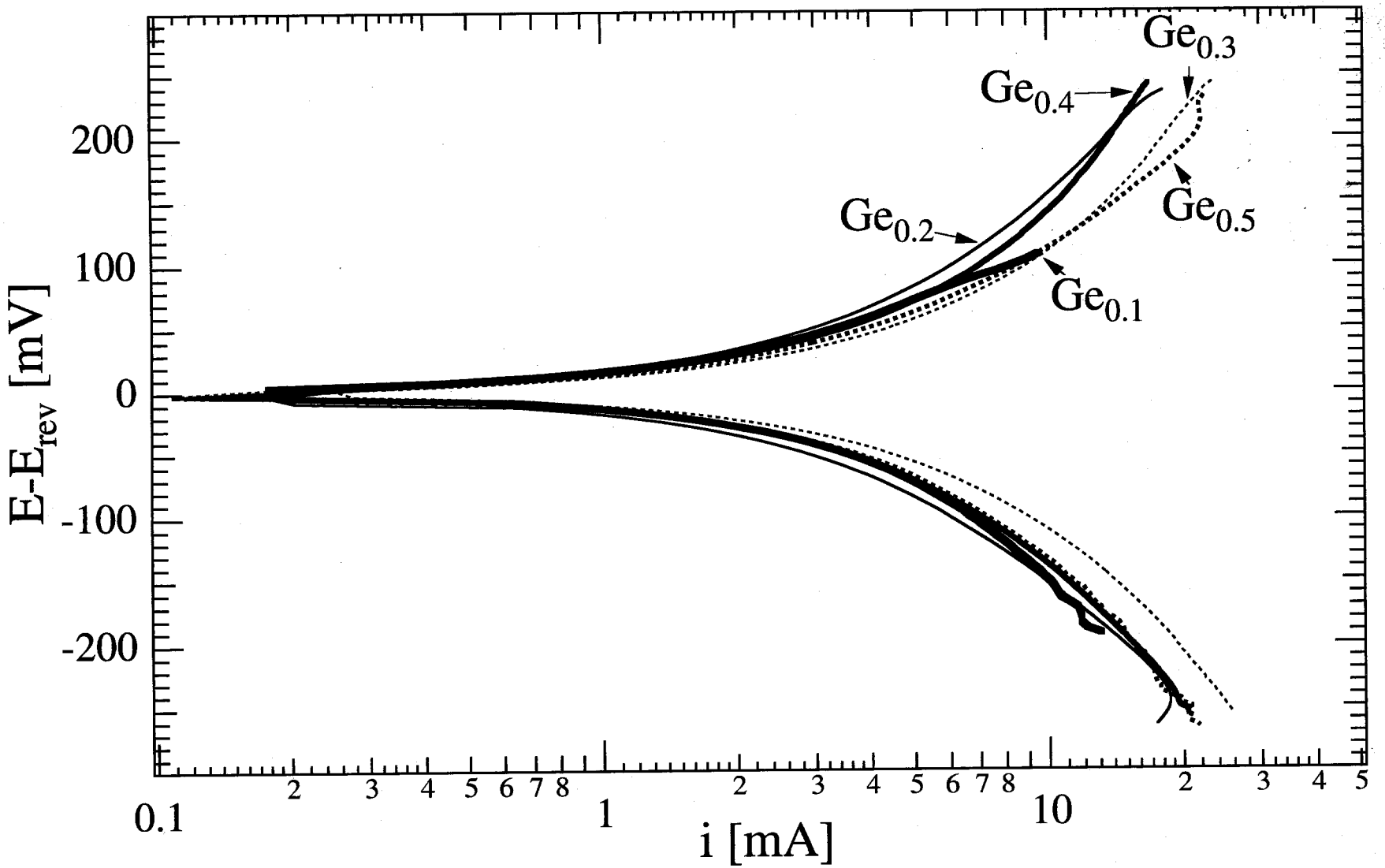

Figure VI-9 Tafel polarization of $LaNi_{5-x}Ge_x$ alloys.

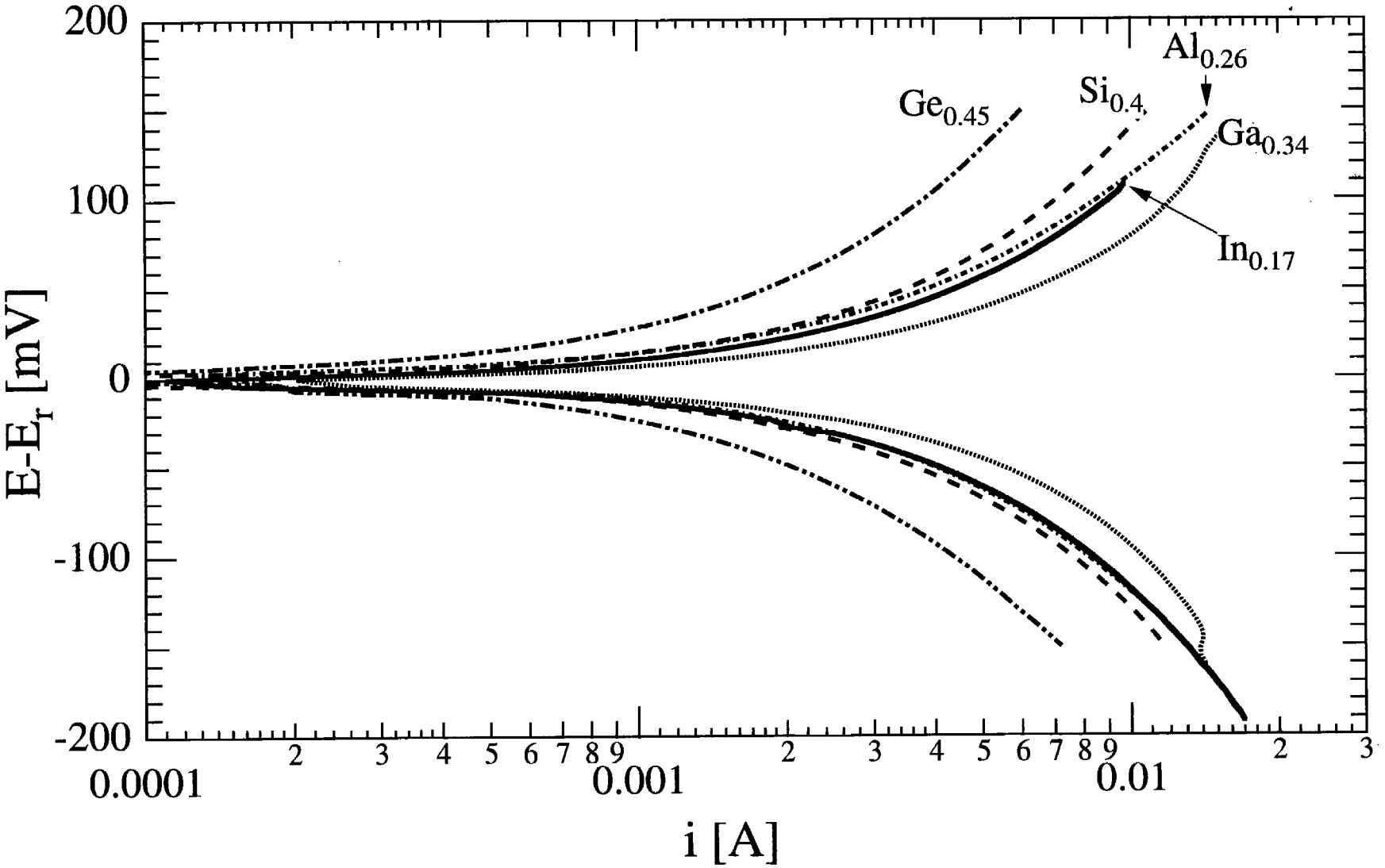

Figure VI-10 Tafel polarization of $LaNi_{5-x}M_x$ alloys.

is slightly greater than that of $LaNi_5$ (0.55) and subsequent alloys have transfer coefficients decreasing slightly with substituted composition. The absorption transfer coefficients are not monotonic with substituted composition. All transfer coefficients of the M_x alloys are approximately 0.5 except for the absorption transfer coefficient of $Ga_{0.34}$, which is ~ 0.33.

D. Discussion

Because the potentials used in DC micro-polarization and AC impedance experiments are perturbed only slightly from equilibrium (8 and 2 mV, respectively), they should reflect the kinetics of charge transfer at the interface between the electrolyte and the MH surface. The exchange currents measured by these two techniques (**Figures VI-11** and **12**) are very similar, indicating that they are accurate. For all alloys but $Sn_{0.4}$ and $Sn_{0.5}$, $i_0^{AC} > i_0^{DC}$. The only measurements that seem anomalous are from $Ge_{0.5}$. As noted in §IV.D.2, the diffraction pattern of this alloy showed substantial peak broadening and the presence of a second phase. Although there is no obvious reason for a second phase to make the reaction resistance different when measured by an AC technique, it will change the resistive and capacitive behavior of the alloy. This could easily change the effective reaction resistance measured by AC impedance.

The broad diffraction peaks of the $Ge_{0.5}$ alloy are indicative of a grain size much smaller than those of the other Ge-substituted alloys, resulting in a higher specific surface area and more available sites for charge (hydrogen) transfer. This explains why the exchange currents of the $Ge_{0.5}$ alloy is substantially higher than other Ge-substituted alloys. The XRD measurements of the M_x alloys also showed that the grain size decreases in the order Ge > Si > Ga > Al, resulting in a corresponding increase in surface area. This can be used to rationalize a corresponding increase in electrode kinetics. It is certain that other phenomena are important in charge transfer, and this trend with alloy surface area is not consistent with all of the measurements.

The exchange currents calculated from Tafel polarization measurements are different from those described above. These exchange currents should reflect the total current from all electrochemical reactions taking place during charge (absorption) and discharge (desorption) at high overpotentials, $E-E_{Equil}$. The reactions at least include: charge/discharge, hydrogen and oxygen evolution, and corrosion. For Sn_x and Ge_x alloys having low substituted-compositions, x, the Tafel exchange currents are higher than the charge transfer exchange currents. These alloys have plateau pressures greater than 1 atm, and hydrogen evolution would be favored at the high over-potentials used in Tafel measurements. The Tafel exchange currents of the M_x alloys are approximately equal, implying that the reactions occurring are equivalent. The Ge_x alloys kinetics are depressed, rather than enhanced, for $x > 0.3$.

The Tafel transfer coefficients characterize the change in activation energy for the forward and backward processes during charge and discharge. It is known[3] that lower plateau pressures facilitate absorption, whereas higher plateau pressures are desirable for desorption. This can be used to rationalize an increase in the absorption transfer coefficient, and a decrease in the desorption transfer coefficient, with increasing substituted composition. The plateau pressures of the M_x alloys are ~0.5 atm. This plateau should be favorable for both absorption and desorption. The transfer coefficients of the M_x alloys for both absorption and desorption are ~0.5, indicating activation barriers changing symmetrically with electrode overpotential.

It is thus clear that the electrochemical kinetics of hydrogen absorption and desorption improve markedly upon substitution of Ni with sp-shell metals. Because substituted alloys have smaller surface areas than the binary alloy, substitution must affect the charge transfer process more directly. One obvious explanation for this change is the increase in the lattice constants of the alloys and the corresponding decrease in plateau pressure. Alloys with lower plateau pressures and larger heats of formation for hydrogen absorption should have higher kinetics. It is possible that on an atomic scale, a solute

causing a large lattice mismatch will disrupt the atomic configuration at the surface of the alloy, facilitating hydrogen absorption.

Unlike $LaNi_{5-x}Sn_x$ alloys, the kinetics of hydrogen absorption in $LaNi_{5-x}Ge_x$ alloys do not seem to be suppressed at high solute concentrations. Instead, the kinetics appear to be more facile in alloys with high Ge concentrations. The Tafel kinetics of the M_x alloys are similar to each other, implying that the kinetics of hydrogen evolution is similar, as would be expected from their similar plateau pressures. The charge transfer kinetics of the M_x alloys, however, are almost all correlated with alloy grain size. As mentioned several times, the grain size, substituted composition, solute metallic radius, and ΔH_{LaM} are all correlated, making determination of the rate determining phenomena difficult at best.

[1] N. Kuriyama, T. Sakai, H. Miyamura, I. Uehara, and H. Ishikawa, *J. Alloys Comp.*, **192**, 161 (1993).

[2] B.A. Boukamp, *Solid State Ionics*, **20**, 31 (1986).

[3] T. Sakai, M. Matsuoka, and C. Iwakura, in *Handbook on the Physics and Chemistry of Rare Earths*, K. A. Gschneidner, Jr., and L. Eyring, eds., Vol. **21**, Elsevier Science B. V., Amsterdam (1995), p. 133.

[4] G Zheng, B.N. Popov, and R.E. White, *J. Electrochem. Soc.*, **143 (3)**, 834 (1996).

x in $LaNi_{5-x}Sn_x$	Micropoln.	AC Impedance	Tafel Polarization				Des. Lim. Curr.
			i_0 [mA]		Tafel Slope [mV/dec]		
	i_0 [mA]	i_0 [mA]	Abs.	Des.	Abs.	Des.	[mA]
0.0	0.77	1.02	0.96	1.09	242	108	14.0
0.1	1.35	1.54	2.39	4.89	233	183	480.5
0.2	1.02	1.15	3.03	2.86	185	220	501.7
0.3	1.05	1.15	2.79	2.22	173	210	354.7
0.4	0.57	0.51	1.51	1.12	167	224	251.8
0.5	0.54	0.52	1.09	1.40	147	229	265.6

Table VI-1 Kinetic parameters of $LaNi_{5-x}Sn_x$ alloys.

x in $LaNi_{5-x}Ge_x$	Micropoln.	AC Impedance	Tafel Polarization				Des. Lim. Curr.
			i_o [mA]		Tafel Slope [mV/dec]		
	i_0 [mA]	i_0 [mA]	Abs.	Des.	Abs.	Des.	[mA]
0.0	0.77	1.02	0.96	1.51	242	108	14
0.1	0.63	0.70	1.54	1.74	150	96	12
0.2	0.71	0.80	1.57	1.99	147	167	20
0.3	1.07	1.13	3.06	3.83	170	192	24
0.4	1.13	1.20	1.95	3.37	217	184	16
0.5	2.00	3.15	2.27	1.86	168	126	24

Table VI-2 Kinetic parameters of $LaNi_{5-x}Ge_x$ alloys.

M_x in $LaNi_{5-x}M_x$	Micropoln.	AC Impedance	Tafel Polarization				Des. Lim. Curr.
			i_o [mA]		Tafel Slope [mV/dec]		
	i_0 [mA]	i_0 [mA]	Abs.	Des.	Abs.	Des.	[mA]
$LaNi_5$	0.77	1.04	0.96	1.09	242	108	14.0
$In_{0.17}$	1.28	1.70	2.73	2.67	101	116	18.6
$Al_{0.26}$	2.27	2.60	2.76	2.67	107	127	21.5
$Ga_{0.34}$	2.01	2.11	2.53	2.27	104	179	22.8
$Si_{0.4}$	1.54	2.07	2.71	2.71	128	121	17.6
$Ge_{0.45}$	1.14	1.23	3.02	3.02	127	113	10.8

Table VI-3 Kinetic parameters of $LaNi_{5-x}M_x$ alloys.

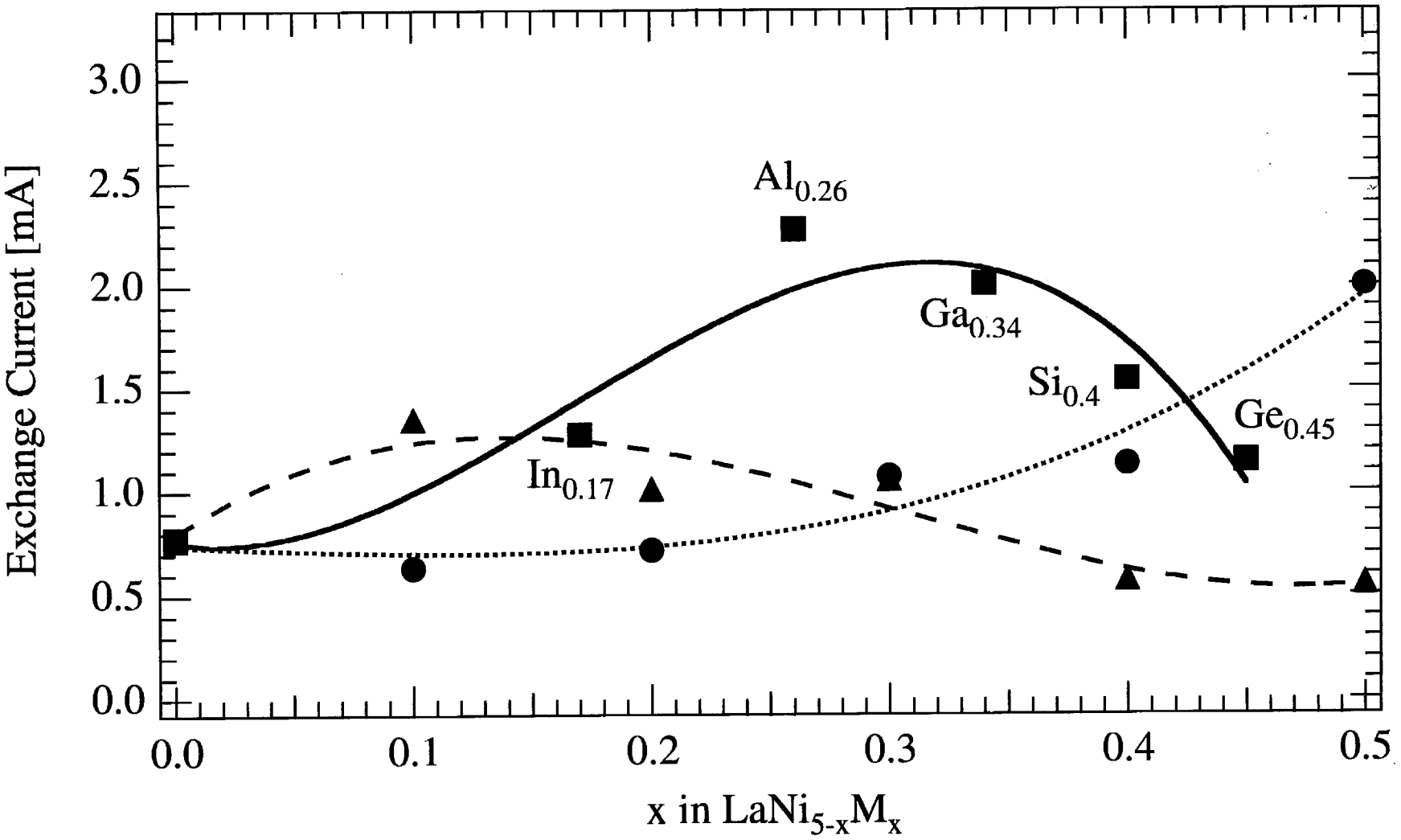

Figure VI-11 Exchange currents measured by micropolarization.
{ ▲ ,– – - Sn_x; ● ,····· - Ge_x; ■ ,—— - M_x}

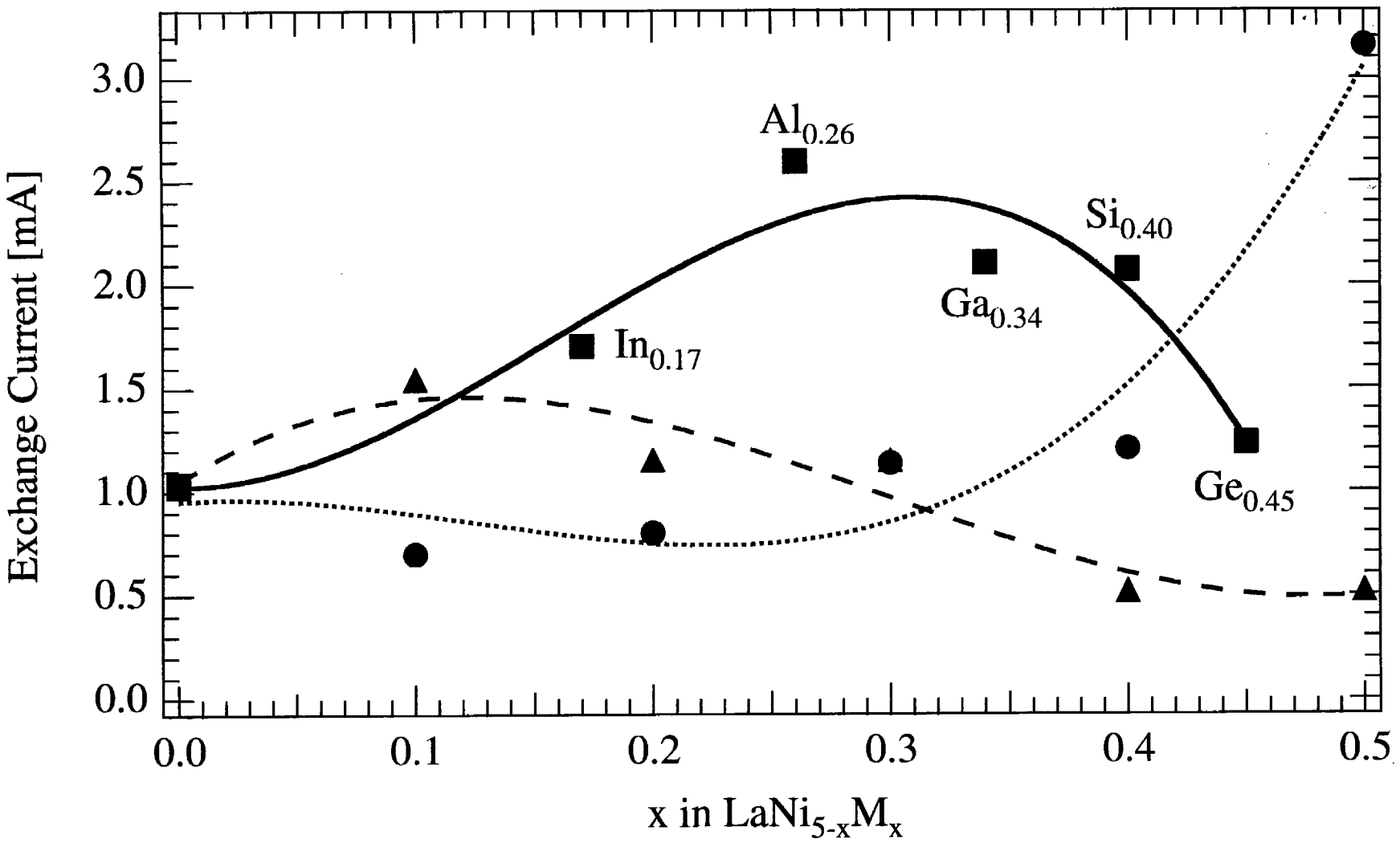

Figure VI-12 Exchange currents measured by AC Impedance.
{ ▲ ,– – - Sn_x; ● ,····· - Ge_x; ■ ,—— - M_x}

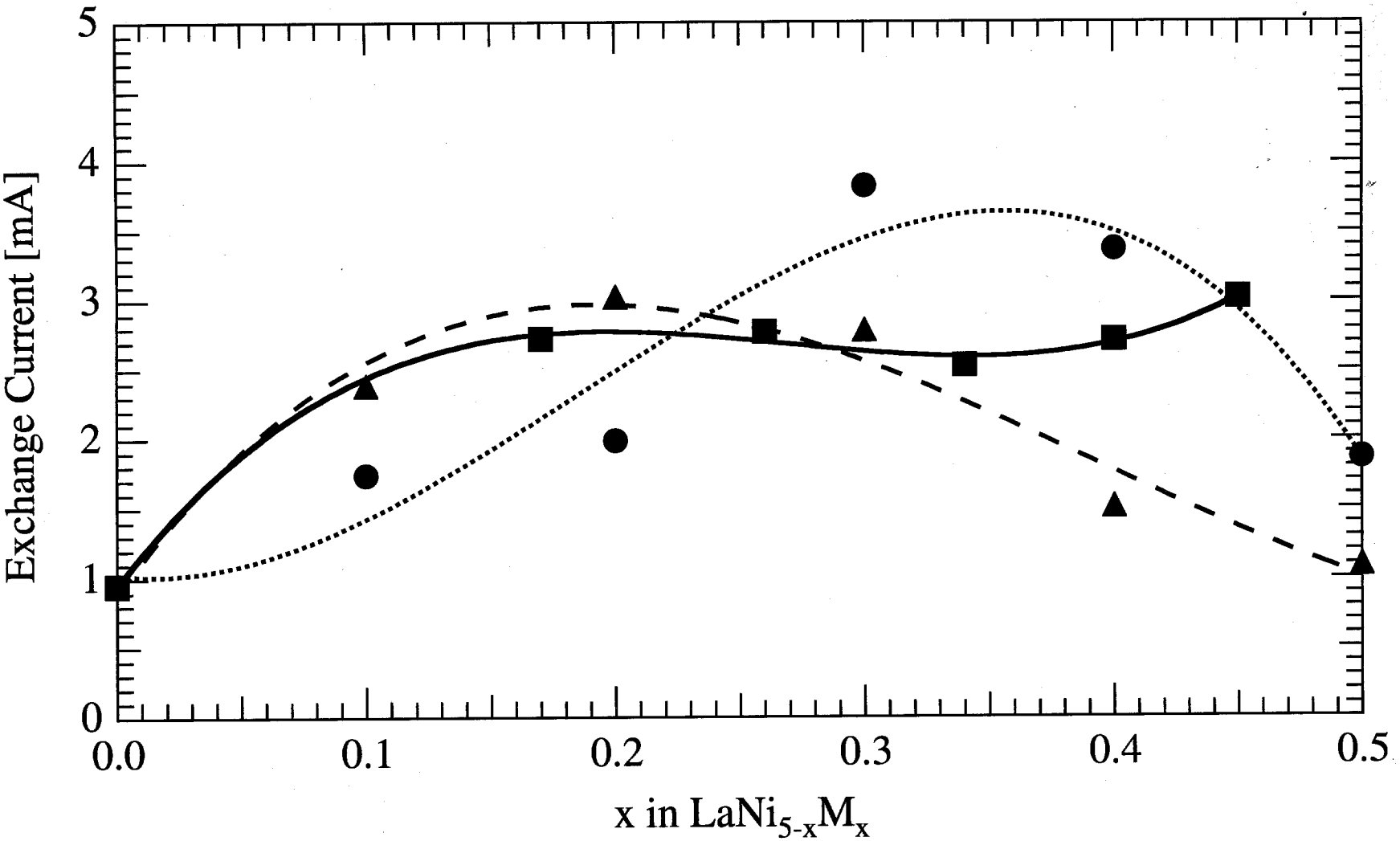

Figure VI-13 Exchange currents measured by anodic Tafel polarization.
{ ▲ ,– – - Sn_x; ● ,····· - Ge_x; ■ ,—— - M_x}

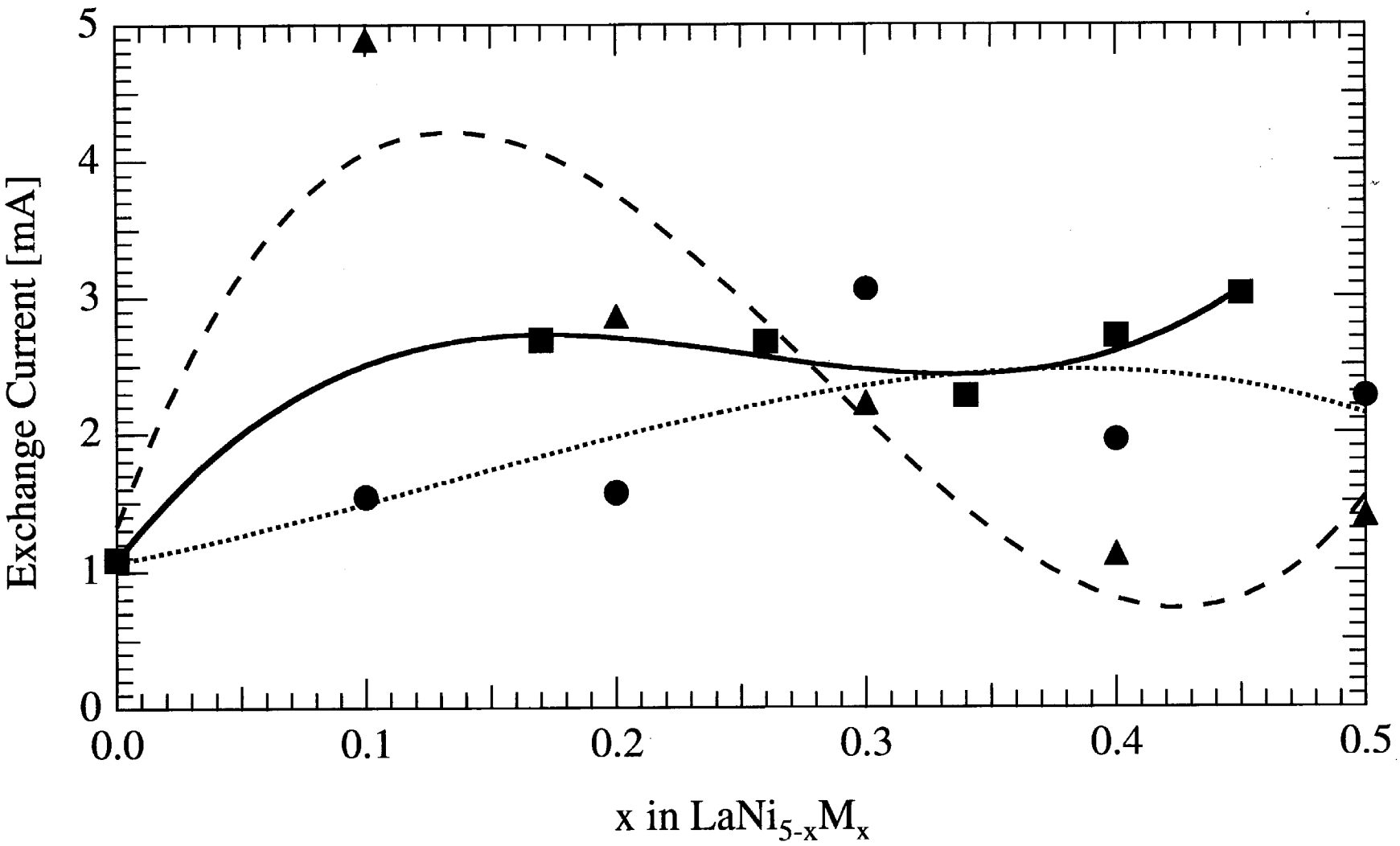

Figure VI-14 Exchange currents measured by cathodic Tafel polarization.
{ ▲ ,– – - Sn_x; ● ,····· - Ge_x; ■ ,—— - M_x}

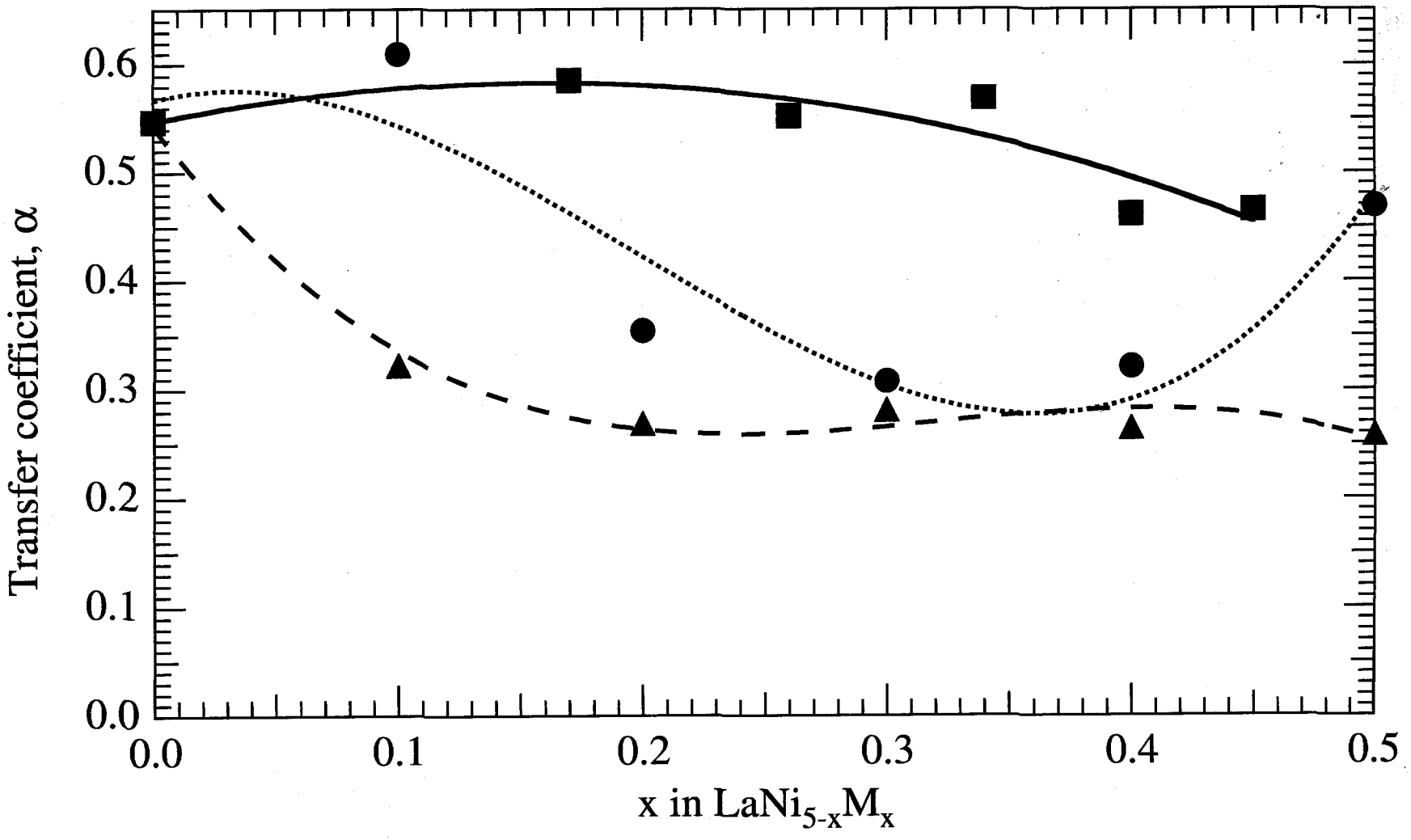

Figure VI-15 Transfer coefficients measured by anodic Tafel polarization.
{ ▲ ,– – - Sn_x; ● ,····· - Ge_x; ■ ,—— - M_x}

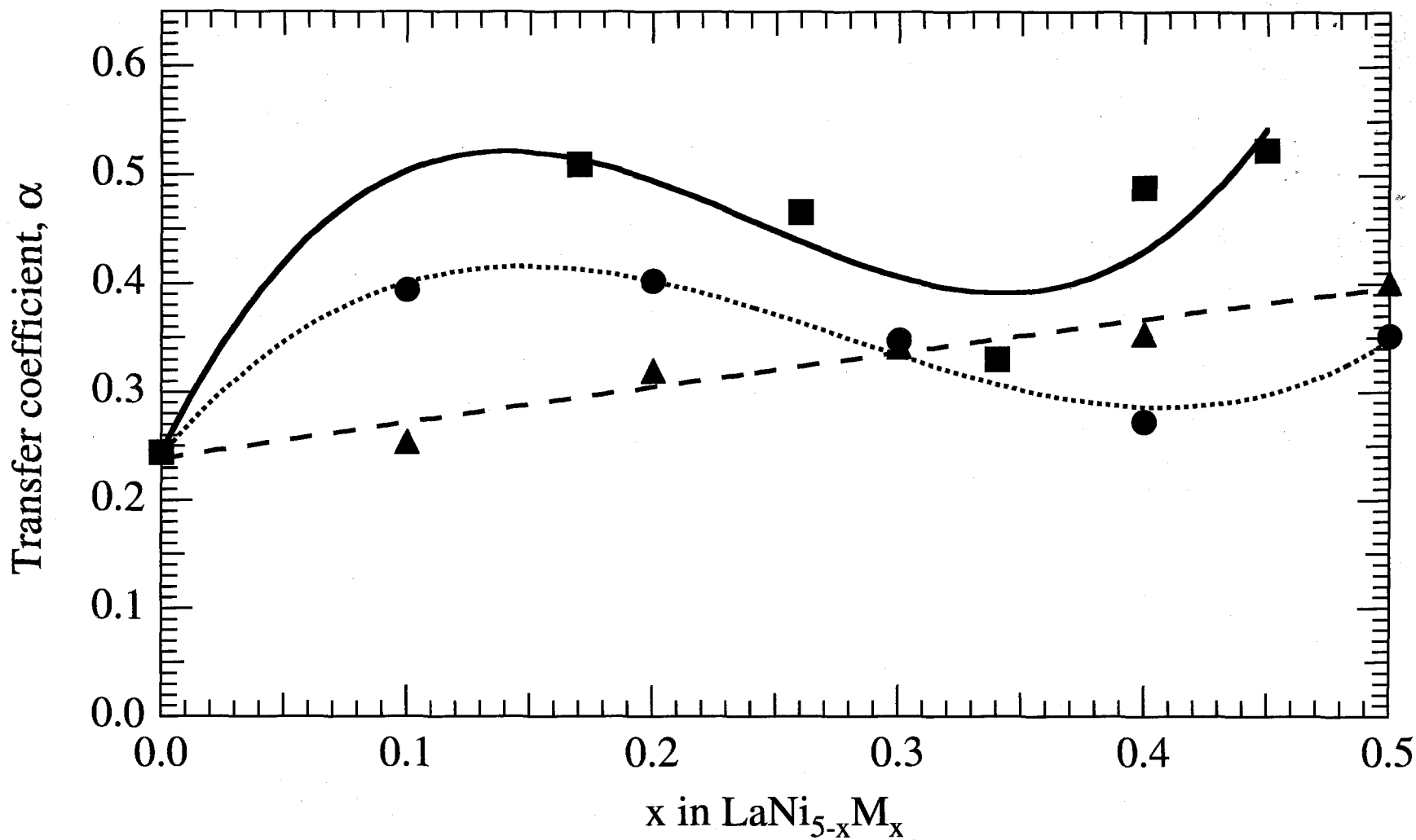

Figure VI-16 Transfer coefficients measured by cathodic Tafel polarization.
{ ▲ ,– – - Sn_x; ● ,····· - Ge_x; ■ ,—— - M_x}

VII. Electrochemical Cycling

A. Cycling conditions

Before lifetime testing of the alloys began, the cycling conditions were varied using the alloy $LaNi_{4.8}Sn_{0.2}$. These tests were performed both to find the optimal conditions for cycling, to insure that our testing methods were not appreciably different in effect than those of other researchers, and to explore the nature of the corrosion reaction and its products. The final cycling conditions used for the cells with ~1 g MH alloy were:

i) ~C/6 charge (60 mA) to 110% of the previous discharge capacity,

ii) 15 minute open-circuit stand,

iii) ~C/2 (150 mA) discharge to -0.5V *vs* Hg/HgO,

iv) 15 minute open-circuit stand.

1. Effect of Amount of Hydrogen Absorption

The cyclic lifetime of $LaNi_{4.8}Sn_{0.2}$ (# of cycles to 50% capacity) observed in our experimental test cell is on the order of 200 cycles (**Figure VII-1**), whereas the commercial Ni-MH cells are known to have a lifetime of ~1,000 cycles. The shorter cyclic lifetimes in our studies are attributed to the ratio of the electrode capacities and the test conditions. The commercial cells are fabricated in a positive-limited design, with about 1.4 - 1.5 times excess capacity in the negative electrode, to provide tolerance to overcharge reactions and to avoid hydrogen evolution at the negative electrode. Accordingly, approximately 65 - 70% of the active MH material experiences hydrogen absorption-desorption cycling during each cycle. The balance is used as reserve to replace the material that degrades during cycling. This unused alloy is presumably held at the same potentials as the utilized material with respect to the alkaline electrolyte, but

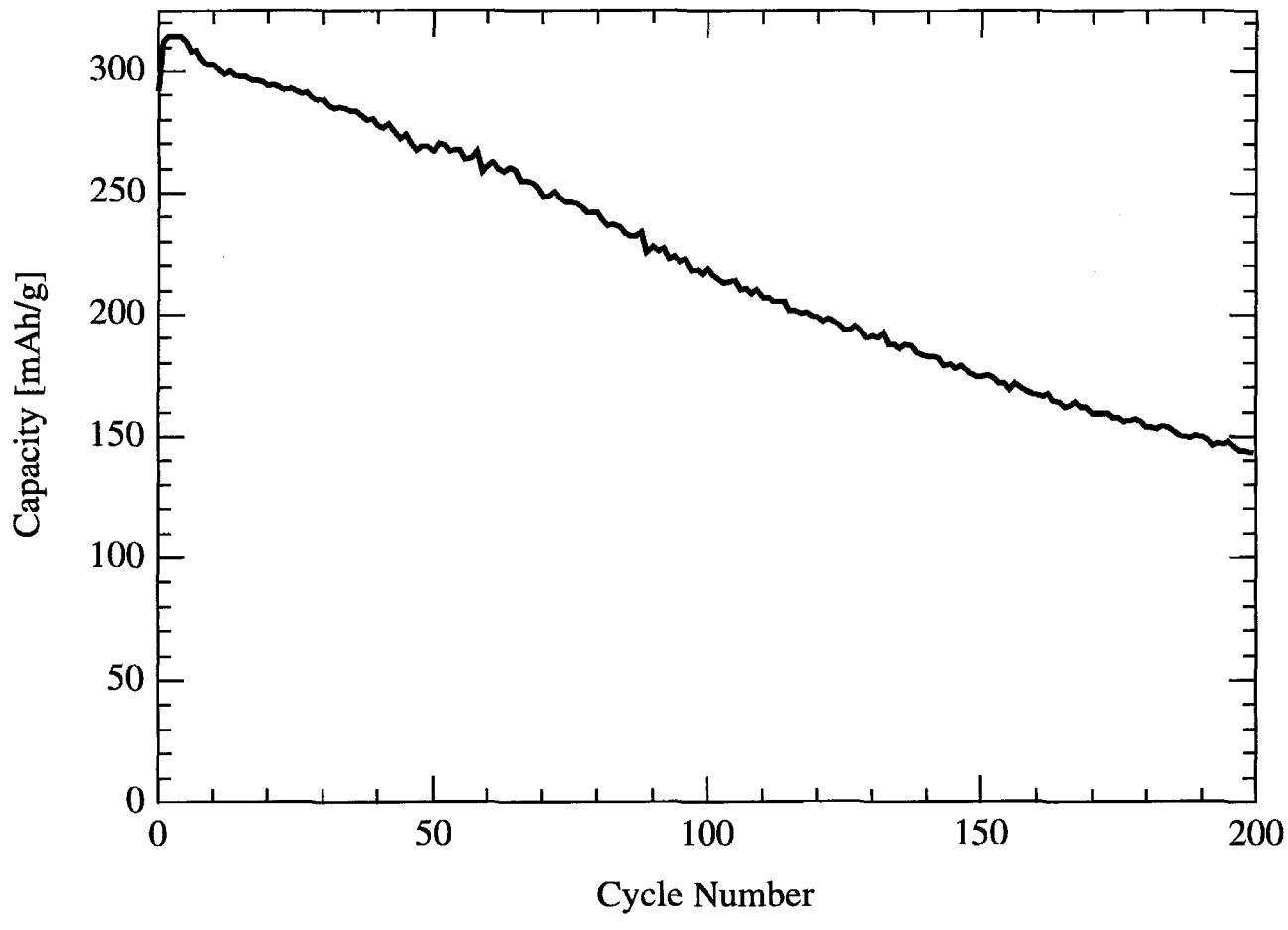

Figure VII-1 Lifetime of $LaNi_{4.8}Sn_{0.2}$ during electrochemical charge-discharge cycling.

would not experience the α- to β-phase change described in §II.C.3. The present cells, on the other hand, are negative-limited, and the MH electrode is overcharged to 110% right from the beginning to insure maximum hydrogen absorption during each cycle.

In order to simulate the conditions experienced by alloys in positive-limited cells using the present test cell, the MH electrode is charged only to about 70% of its maximum capacity (measured after activation) in each cycle and discharged to a preset cut-off voltage. This partial charge can be represented by a new variable, the state of charge (*SOC*). The limits for the SOC could be either 0 to 70% or 30 to 100%. The cells cycled from 100% capacity might experience a larger lattice volume at high hydrogen composition, possibly enhancing La diffusion. In the former case, the degradation resulting from volume dilatation could be less, but that due to corrosion would be more prominent as compared to the latter case. In this experiment, therefore, three values of the cut-off voltage were chosen for the discharge, i.e., -0.7, -0.75, and -0.8 V, while keeping the SOC the same (0 to 70%).

An additional factor to consider when interpreting the results of this experiment is the nature of the hydrogen absorption and resulting lattice expansion. Presumably, the first step during charge would be to hydride all of the available (not degraded or passivated) MH material to the limit of the α-phase,

$$M + y_\alpha H \rightarrow MH_{y\alpha}. \qquad [VII.1]$$

In the case of $LaNi_{4.8}Sn_{0.2}$, $y_\alpha = 0.3$ H/$LaNi_5$ [1] = 16.7 mAh/g = 5.1% of the initial capacity of 325 mAh/g. When all of the active material has been hydrided to the limit of the dilute phase, individual grains or particles of $MH_{y\alpha}$ will experience the transformation to $MH_{y\beta}$,

$$MH_{y\alpha} + (y_\beta - y_\alpha)H \rightarrow MH_{y\beta}. \qquad [VII.2]$$

In the case of $LaNi_{4.8}Sn_{0.2}$, $y_\alpha - y_\beta = \Delta n_{plat} = 5.3$ H/$LaNi_5$ [1] = 294 mAh/g = 90.5% of the initial capacity. This means that in a hypothetical anode containing activated MH powder that has experienced no degradation, (70-5.1)/90.5 = 71.7% of the active material will experience the discontinuous volume expansion during each cycle. In addition, the

discharge cut-off voltages of -0.7, -0.75, and -0.8 V imply that the cells have some residual hydrogen capacity at the beginning of each cycle. If the hydrogen composition of the discharged MH powders is y_α, then 70/90.5 = 77.3% of the active material will experience the discontinuous volume expansion during each cycle. However, dynamic electrochemical isotherms (**Figure VII-2**) show that at the current densities we use for cycling, only 30 mAh/g or 10% of the initial capacity to 0.5V is extracted between potentials of 0.8 V and 0.5 V, implying the alloy has reached < 10% SOC by the time it reaches 0.8V.

Figure VII-3 illustrates the cyclic lifetime of the alloy $LaNi_{4.8}Sn_{0.2}$ under the above conditions, with the discharge cut-off voltages of -0.7, -0.75, and -0.8 V, respectively. Because the initial charge state and amount of hydrogen absorption are the same in all these cases, the amount of MH material experiencing lattice dilatation is the same. As may be seen from the figure, the capacity decline is the same for all cut-off potentials tested. The flat region of the cyclic lifetime curves represents the cycles in which the MH material which has degraded is "replaced" by the reserve material. The cyclic lifetime of cells with a partial degree of hydrogen absorption is longer than those with complete hydrogen absorption in each cycle (**Figure VII-3**). Operating at low range of SOC, as in a positive-limited cell design, would contribute to a longer cycle life, as evident from **Figure VII-3**. The cyclic lifetime appears to be longer with a low end of charge SOC; the capacity of those cells with only 70% of charge exceeds that of the cell with 100% charge after ~90 cycles. The capacity fade of all the cells seem identical, and is therefore not dependent upon cut-off voltage in the range –0.7 V to –0.8 V.

2. Effect of Anodic Potentials

Although varying the cut-off voltage as described above did not have much effect on the MH alloy capacity fade, we were not convinced that anodic potentials are unimportant with respect to the alloy degradation. The presence of the corrosion product $Ni(OH)_2$ (see

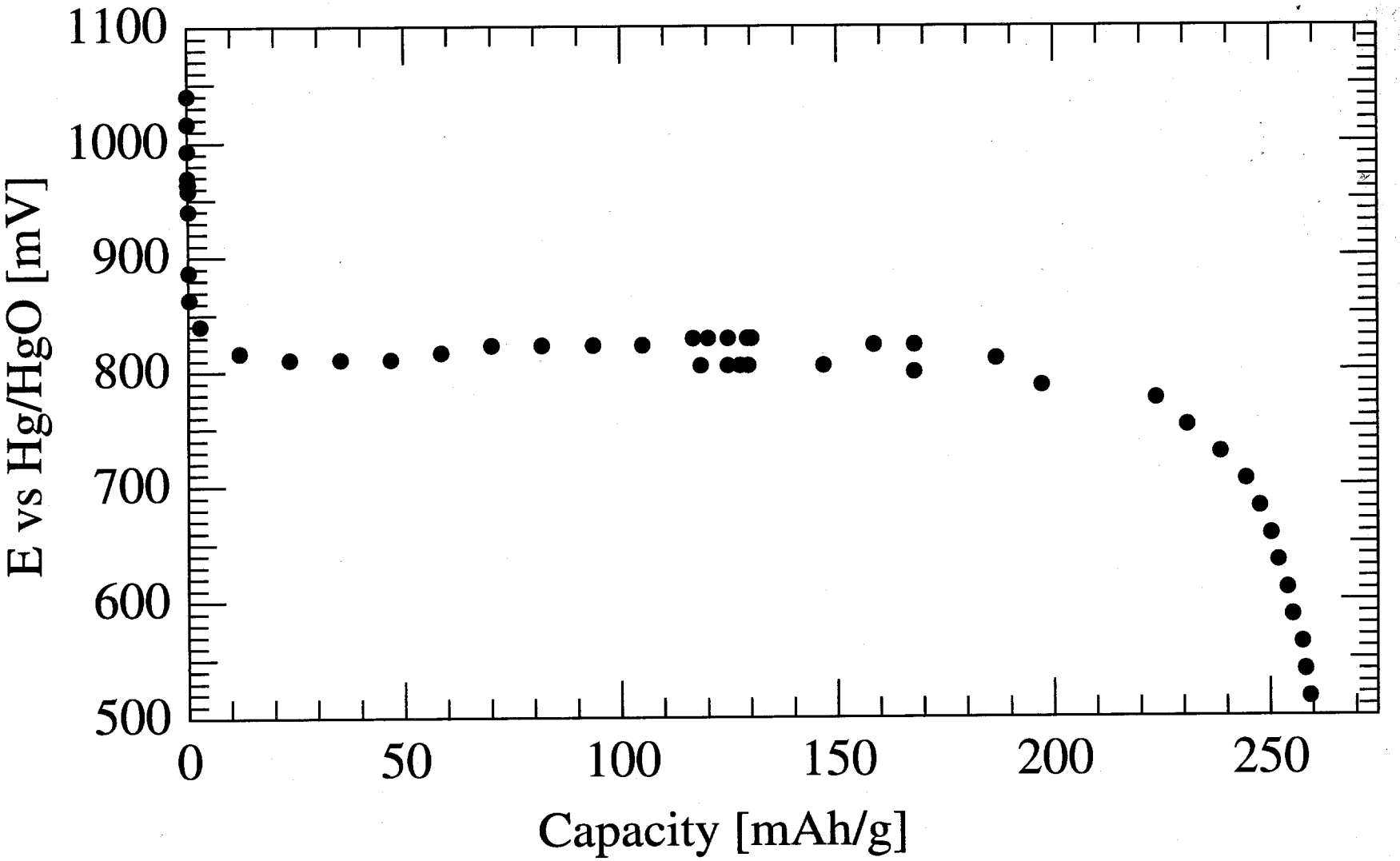

Figure VII-2 Dynamic electrochemical discharge isotherm of $LaNi_{4.8}Sn_{0.2}$, cycle # 5.

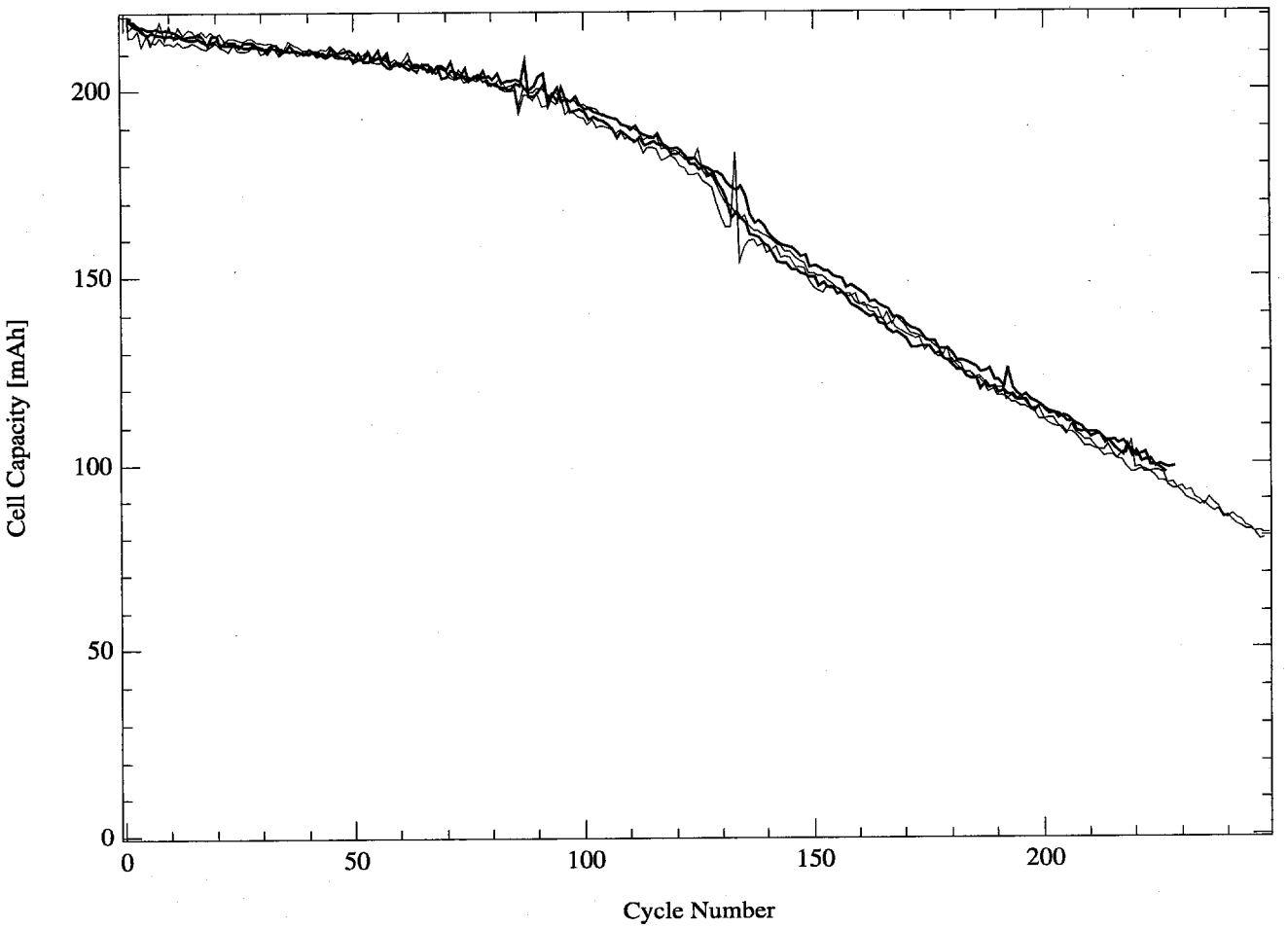

Figure VII-3 Cycle life of $LaNi_{4.8}Sn_{0.2}$ alloy with a charge return corresponding to 70% of the theoretical capacity and discharged to 1) -0.7, 2) -0.75 and 3) -0.8 V *vs* Hg/HgO, in comparison to 4) 115% charge return and discharged to -0.5 V *vs* Hg/HgO.

section VII.B below) in electrochemically cycled electrodes implies that the local potential can drop below the macroscopic measurement of the anode potential.

In order to examine the effect of the corrosion occurring in the discharged state, we varied step iii, the conditions between discharge and the subsequent charge. **Figure VII-4** shows the cyclic lifetime curves of cells with 0 and 15 minutes of open-circuit stand time, as well as a cell held for 15 minutes at the discharge cut-off voltage, -0.5 V. It is clear from the figure that the cycle life improves upon a decrease in the open-circuit stand time after discharge. The enhanced corrosion in the discharged state might be responsible for this behavior.

Figure VII-5 shows the cyclic lifetime curves of cells tested under even more severe conditions. To simulate conditions that may arise during deep discharge and over-discharge of cells, the electrode potential was held potentiostatically at -0.3 and -0.1 V for 15 min. after discharge. **Figure VII-5** shows the effect of driven oxidation on the cyclic lifetime, compared to the standard condition of a 15 min. open-circuit stand between discharge and charge. It is clear from **Figure VII-5** that the cycle life is rather strongly affected by the overdischarge. At the -0.3 V holding potential, serious degradation sets in after about 30 cycles, whereas at a potential of -0.1 V, the degradation sets in right from the beginning.

In addition to a faster degradation rate, there are large fluctuations in the capacity as shown in **Figure VII-5**. These may be attributed to the surface films formed on the MH electrode under these conditions. Due to the increased interfacial resistance, the cells quickly attain the voltage limit set for charge. Increasing the voltage limit for charge improved the capacity, but the fluctuations were still present. Returning to the standard cycling conditions, however, eliminated the fluctuations, which suggests that these fluctuations are a result of film formation and dissolution during cycling.

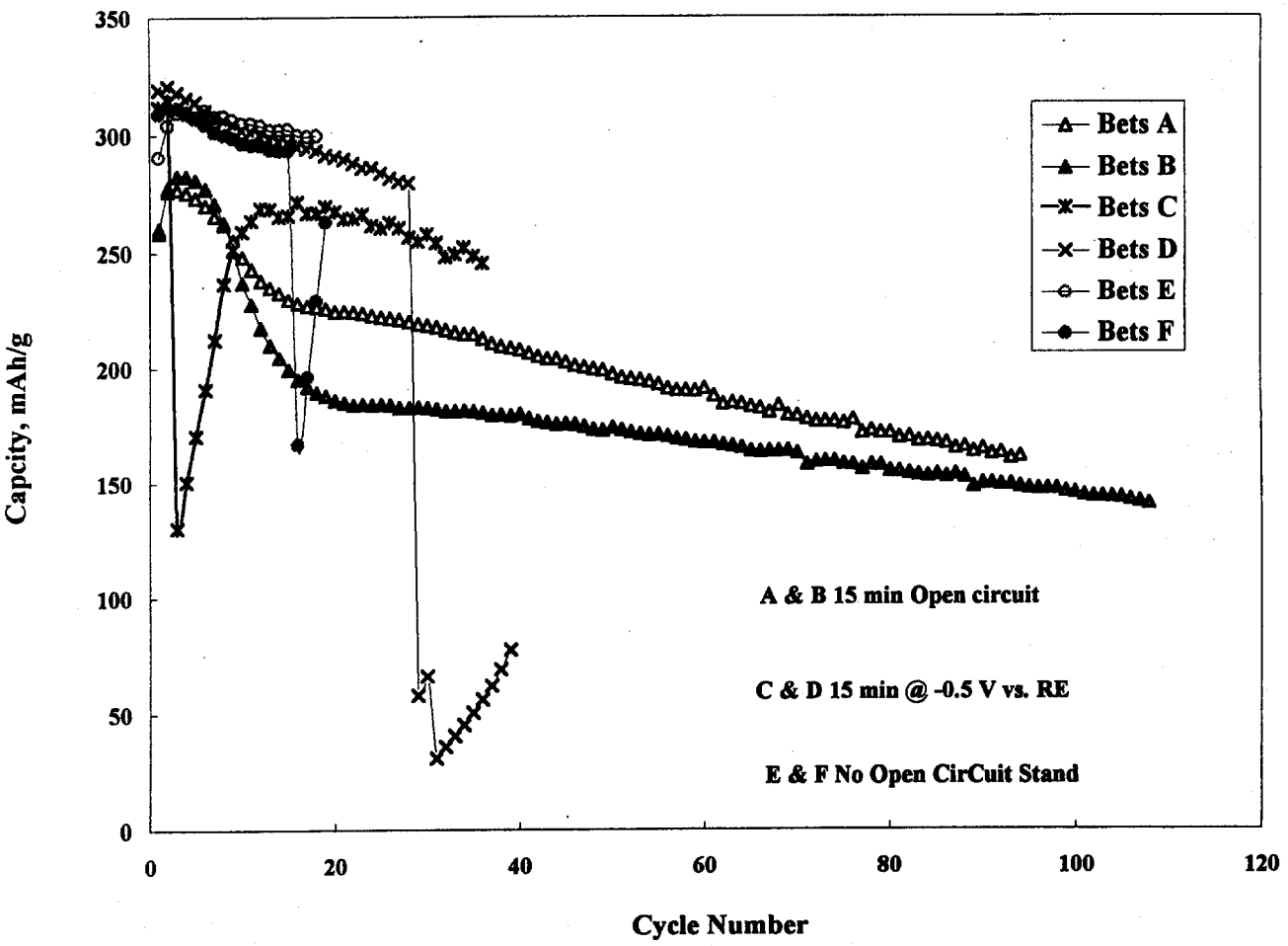

Figure VII-4 Variation of $LaNi_{4.8}Sn_{0.2}$ lifetime with length of open-circuit stand after discharge.

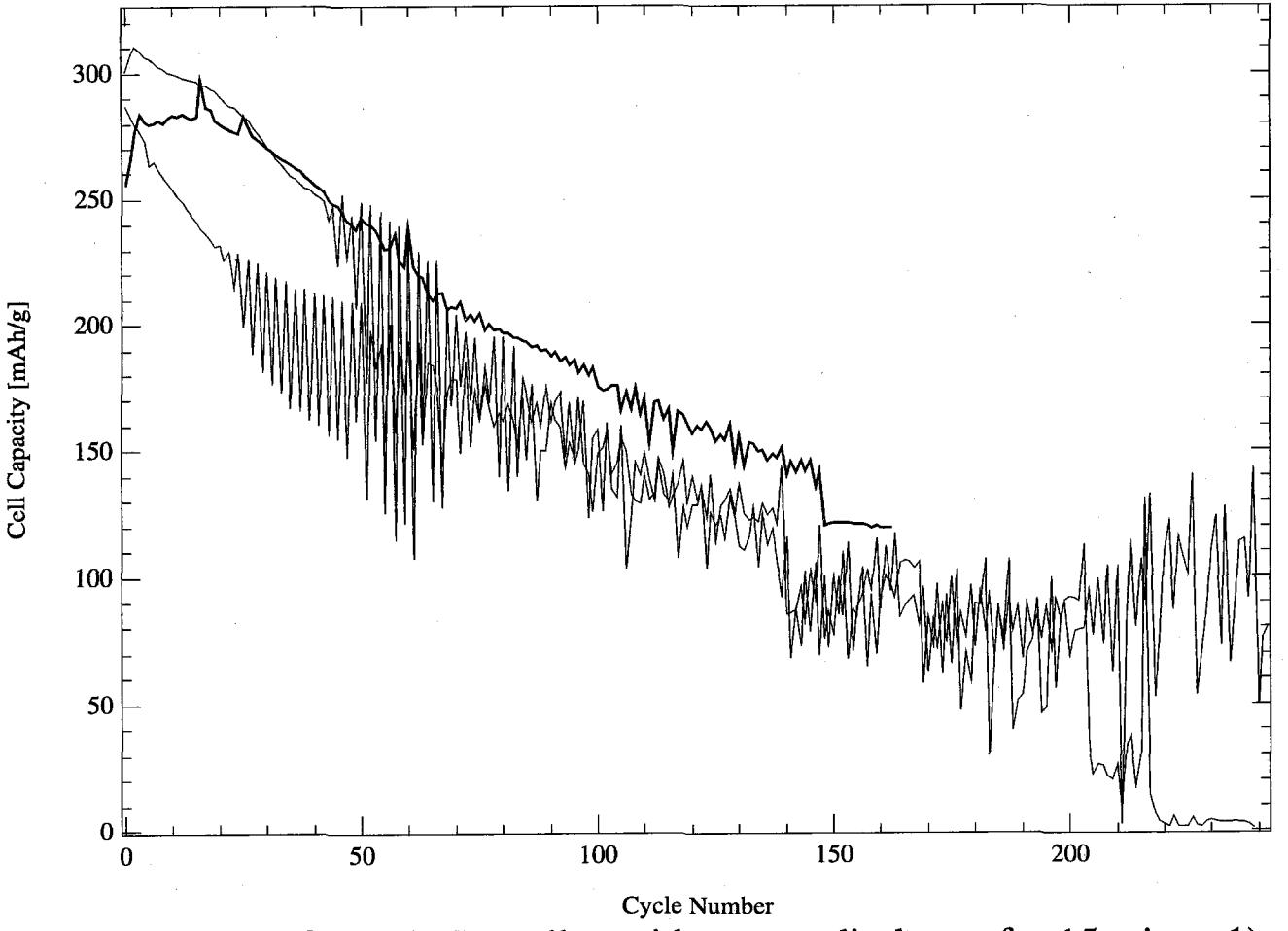

Figure VII-5 Cycle life of $LaNi_{4.8}Sn_{0.2}$ alloy with an overdischarge for 15 min at 1) at OCV, 2) -0.3 V and 3) -0.1 V *vs* Hg/HgO, before recharge in each cycle.

3. Effect of Temperature

In order to study the effect of temperature on the corrosion of the MH alloy and thus on its cycle life, cycling studies were carried out at four different temperatures. The strategy for these tests was to cycle cells with alloys Sn_x at temperatures such that the alloy plateau pressure was ~0.5 atm. This ensured that the slightly pressurized character of our test cells would not affect the results. The affect of temperature was then determined by noting the change in cyclic lifetime from that of room temperature cycled MH alloys. Differences in the cyclic life can therefore be attributed to different rates of corrosion at these temperatures. The MH alloys thus chosen include $LaNi_{4.9}Sn_{0.1}$ at 10° C, $LaNi_{4.8}Sn_{0.2}$ at 25° C, $LaNi_{4.68}Sn_{0.32}$ at 44° C, and $LaNi_{4.6}Sn_{0.4}$ at 59° C.

The cycle life of these alloys at the specified temperatures is illustrated in **Figure VII-6**. As may be seen from the figure, the cycle life does deteriorate more quickly at high temperatures, probably due to enhanced corrosion.

4. Effect of Electrode Preparation

The capacity retention that was realized in our electrodes is superior to that reported for similar formulations with electrodes made with Teflonized carbon.[2] Nevertheless, in order to verify if higher Teflon content or lower electrode density can improve the cycle life any further, cells were fabricated with 50 wt.% Teflonized (33 wt.%) Vulcan-X carbon and are being cycled under identical conditions. The results thus far (**Figure VII-7**) indicate that the cyclic lifetime of a cell with this alternative construction is not any better than our standard cells. This implies that the binder concentration in our standard electrode is enough to provide good mechanical integrity to the electrode and that the charge densities are not too high to affect the cyclic lifetime.

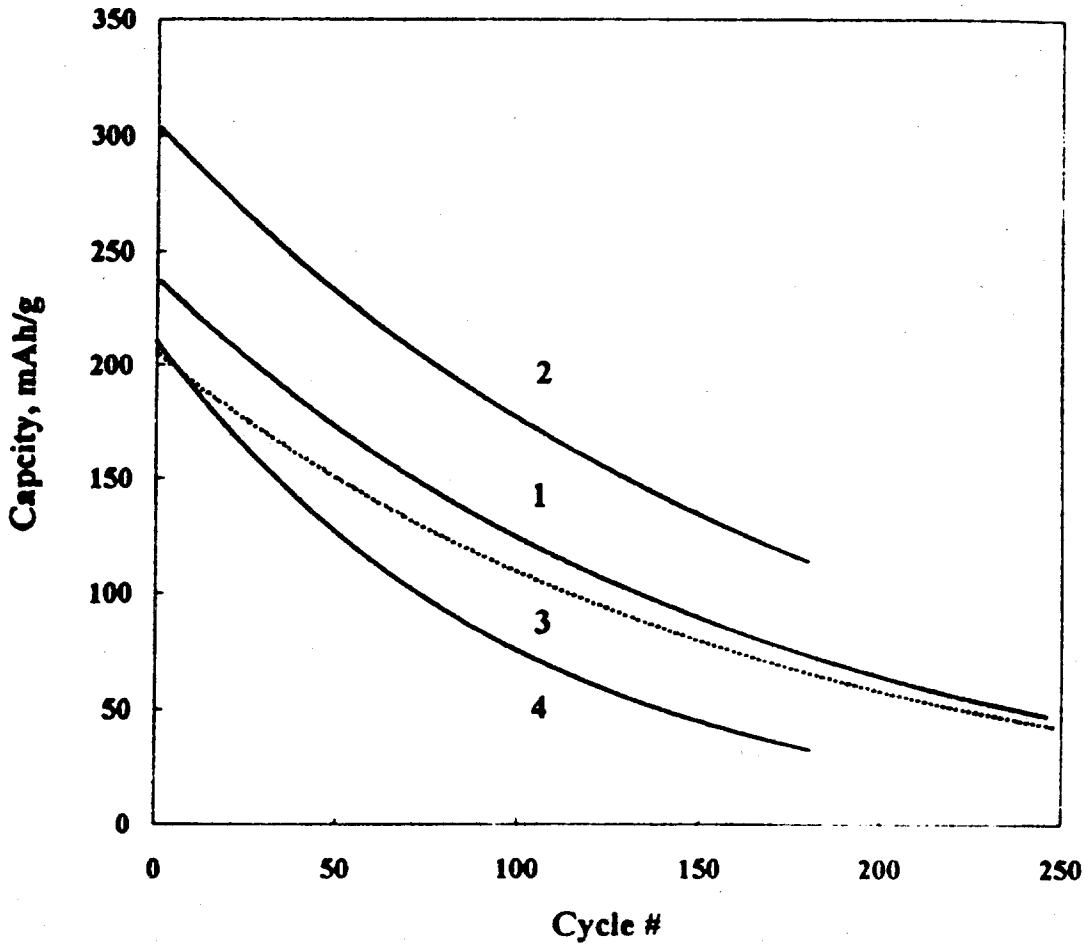

Figure VII-6 Trend lines representing the lifetimes of $LaNi_{5-x}Sn_x$ alloys at elevated temperatures. {1 - $Sn_{0.1}$ @ 10° C, 2 - $Sn_{0.2}$ @ 25° C, 3 - $Sn_{0.32}$ @ 44° C, 4 - $Sn_{0.4}$ @ 59° C}

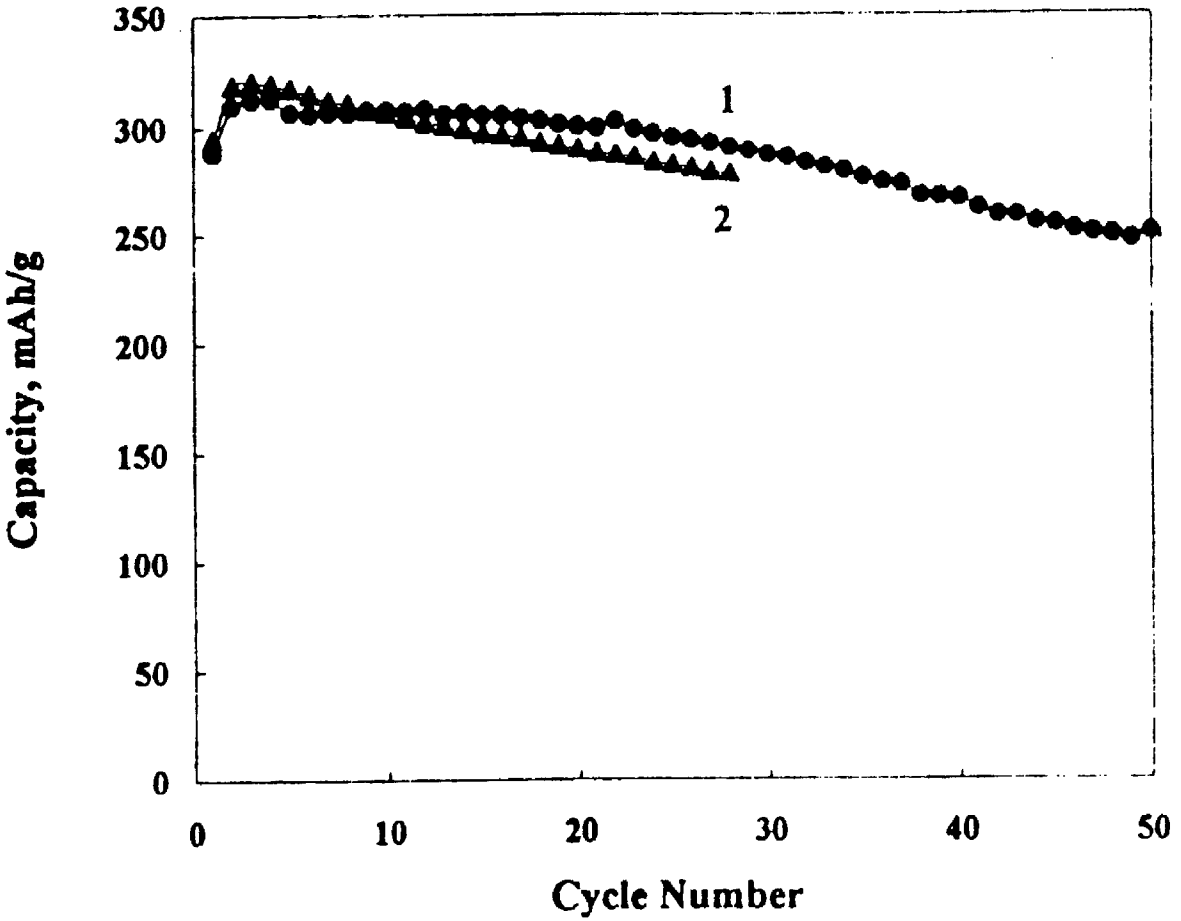

Figure VII-7 Lifetime of $LaNi_{4.8}Sn_{0.2}$ electrode with Teflonized carbon binder and diluent compared to standard $Sn_{0.2}$ electrode.

5. Conclusions

The cyclic lifetime of $LaNi_{5-x}M_x$ alloys with selected ternary solutes is governed by the nature of the ternary solute, as well as the test conditions. The corrosion of the MH alloy occurs more prominently in the discharged state and in deep and/or over-discharge. This can result in a rapid deterioration of the cell capacity during cycling. The surface films formed therein also cause large fluctuations in the measured capacity during cycling. The electrode fabrication methods used here have been found to be as good as, if not better than, other reported methods.

B. Effects of Electrochemical Cycling

The next step in our research was to learn more about the effects of electrochemical cycling on $LaNi_5$-based alloys. Comparing cycling tests with microstructural characterization of MH material in cycled electrodes would shed light on the processes involved in the alloys' capacity degradation. Therefore, cell kinetics were measured periodically during cycling, and several cells were cycled to varying levels of degradation and disassembled so that the phase composition and microstructure of the AB_5 anode material could be determined. These tests were done with $LaNi_{4.8}Sn_{0.2}$, our baseline alloy, as the anode material.[3]

1. RESULTS

The first set of cells ('d' - 'g') were cycled to give information about the effects of cycling on charge transfer kinetics. The MH powder used in these cells came from a single ingot, but the mixture used in cells 'd' and 'f' was made at an earlier time than that used in cells 'e' and 'g'. Representative linear polarizations of cell 'd' are given in **Figure VII-8.** It can be seen that there is a precipitous decrease in charge transfer resistance after the first 25 cycles and relatively minor decreases after subsequent cycling. There is also a

small increase in the equilibrium potential of the cells. Impedance spectroscopy for cell 'f' (**Figure VII-9**) shows a similar change in electrode charge transfer resistance with cycling. After the first 25 cycles, the charge transfer resistance decreases by an order of magnitude, and subsequent cycling produces a minor reduction in resistance.

Cycling of cells 'd' - 'g' is shown in **Figure VII-10**. The capacity loss the cells experienced from cycling was appreciable, ranging from 38% to 55%. Electrodes 'e' and 'g' were stored under argon in the discharged state for 1 month before XRD patterns were measured. After cycling, 'd' and 'f' electrodes were over-discharged to ~20 times their current capacities and studied by XRD. The diffraction peaks were indexed. Each X-ray peak was fit to a gaussian line shape function superimposed on a linear background to determine its integrated intensity. The XRD patterns, seen in **Figure VII-11**, of these electrodes show the presence of $LaNi_{4.8}Sn_{0.2}$, $La(OH)_3$, Ni, and $Ni(OH)_2$ in varying degrees. The initial presence of Ni powder in electrodes 'd' - 'g' makes determining the source of the Ni and $Ni(OH)_2$ phases uncertain.

To help determine the origin of the corrosion products in cycled electrodes, cells 'a' - 'c' were made without Ni powder in the mixture. These cells were then cycled under identical conditions to different levels of capacity degradation (**Figure VII-12**). When linear polarization and impedance spectroscopy were performed on new and cycled cells, it was found that the addition of Ni powder to the anode mixture did not affect the cell kinetics at these different stages of cycling. After cycling, each electrode was removed from its cell and analyzed by XRD, shown in **Figure VII-13**. The average intensity of the $La(OH)_3$ (110), (101), (200), and (201) peaks, each normalized to the $LaNi_5$ (111) peak intensity, was plotted against the capacity degradation of each cell. This analysis was also performed for the $Ni(OH)_2$ (100) and (101) peaks. These graphs, shown in **Figure VII-14**, indicate that there is a linear increase in both the $La(OH)_3$ and $Ni(OH)_2$ phases with the loss of capacity in these cells.

2. DISCUSSION

The decrease in charge transfer resistance as measured by linear polarization and by impedance spectroscopy can be explained by an increase in the surface area of the alloys. As hydrogen is electrochemically cycled in and out of each alloy, the discontinuous volume change associated with the α-/β-phase transformation causes the alloy to decrepitate. The alloy breaks into smaller powders (~1μm) and its surface fractures. The increase in surface area increases the number of reaction sites at which charge transfer can occur. This increase in surface area is supported by the increase in line width of the MH diffraction peaks. The broadening results from the small size of coherent scattering domains, caused by small grain size and microstrain in the alloys. The smaller grain size would also mean a shorter diffusion length for hydrogen that was entering and leaving the alloy, corresponding to increased electrochemical kinetics. The presence of Ni metal from the MH corrosion will also create a catalytic effect on water reduction at the alloy particle surface.

The XRD results show a strong correlation between capacity degradation and phase fractions. The fact that all the electrodes yielded similar results despite the differing cycling rates used implies that the phases identified are the products created during electrochemical cycling.

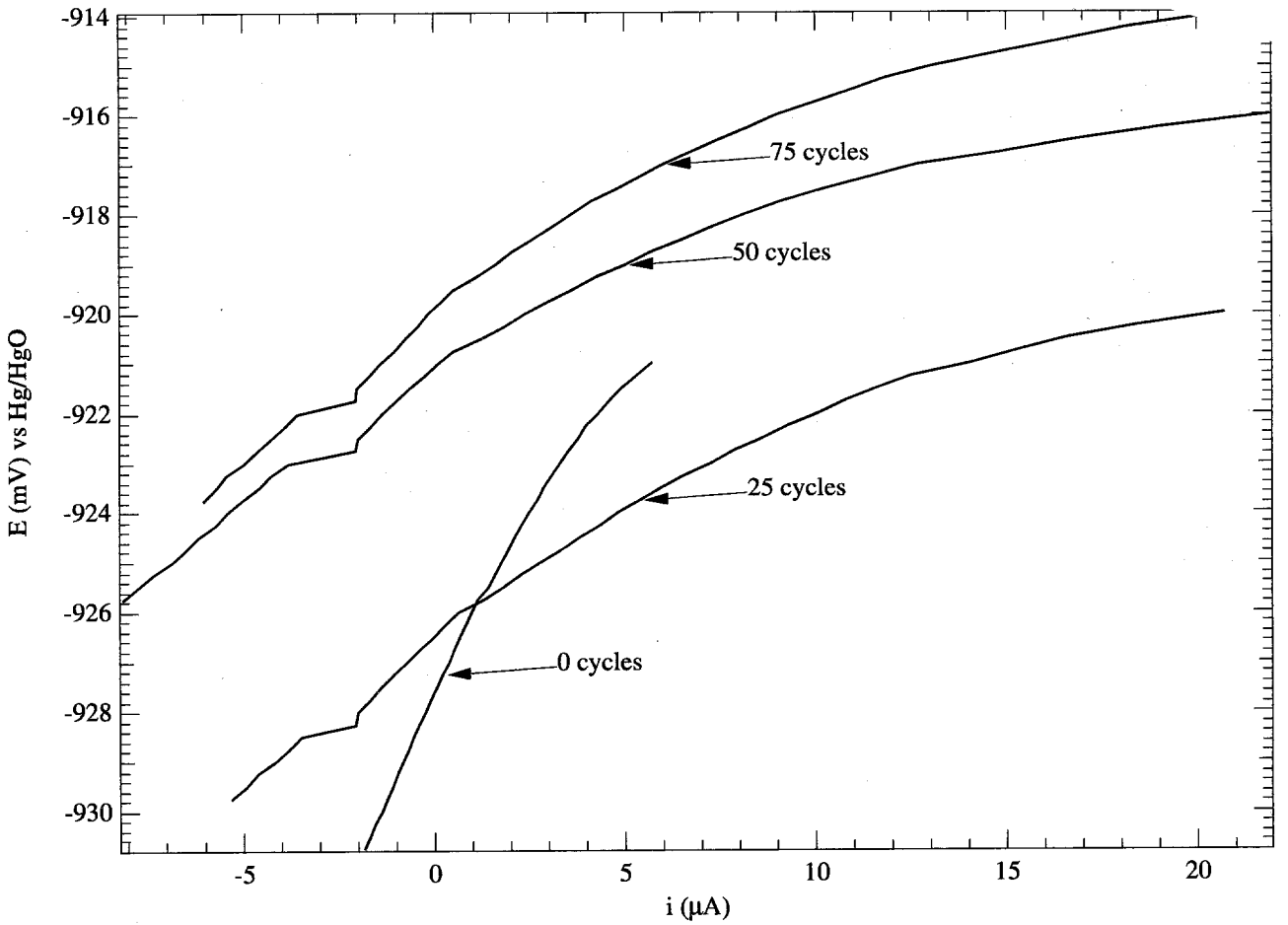

Figure VII-8 Linear polarization of $LaNi_{4.8}Sn_{0.2}$ cell at different stages of cycling

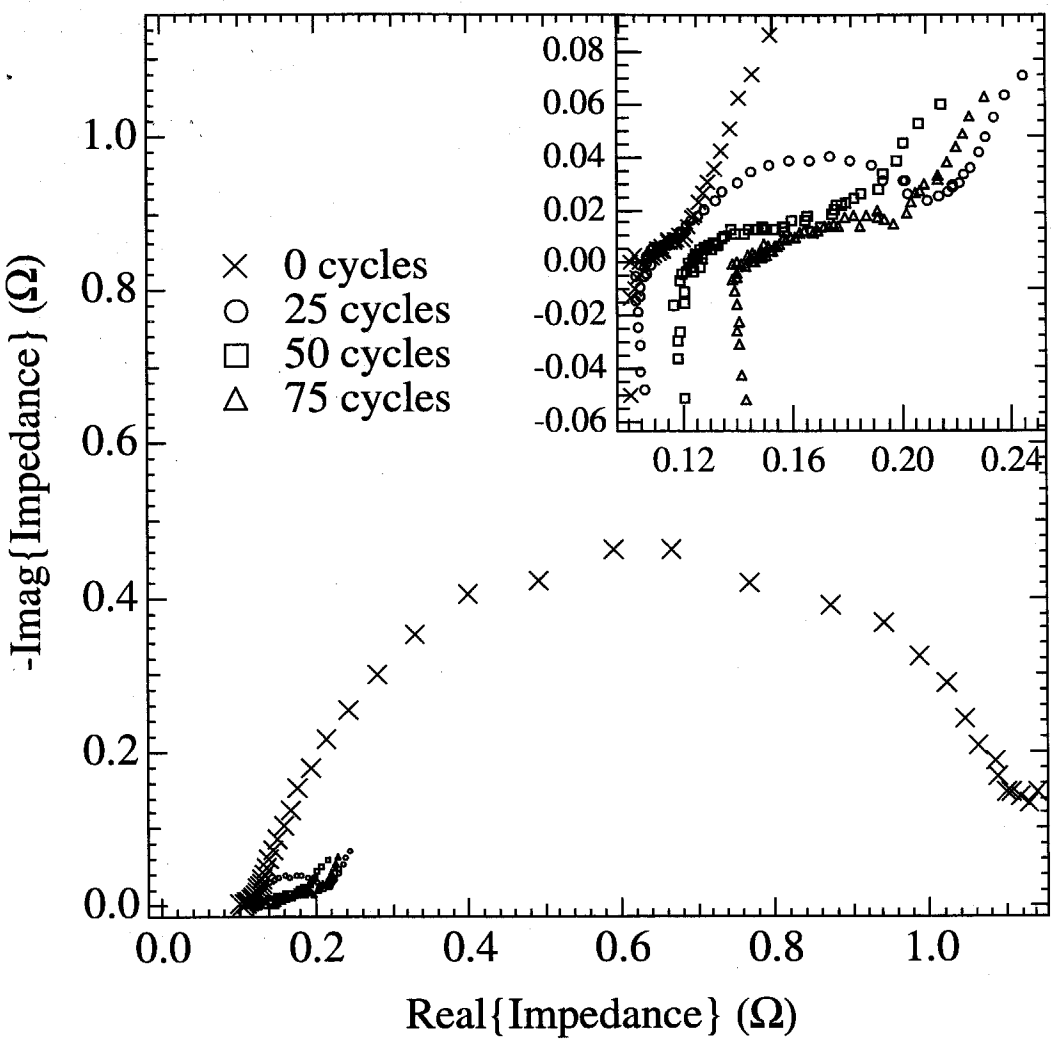

Figure VII-9 AC Impedance spectroscopy of $LaNi_{4.8}Sn_{0.2}$ cell at different stages of cycling. Insert shows expansion of region of low impedance.

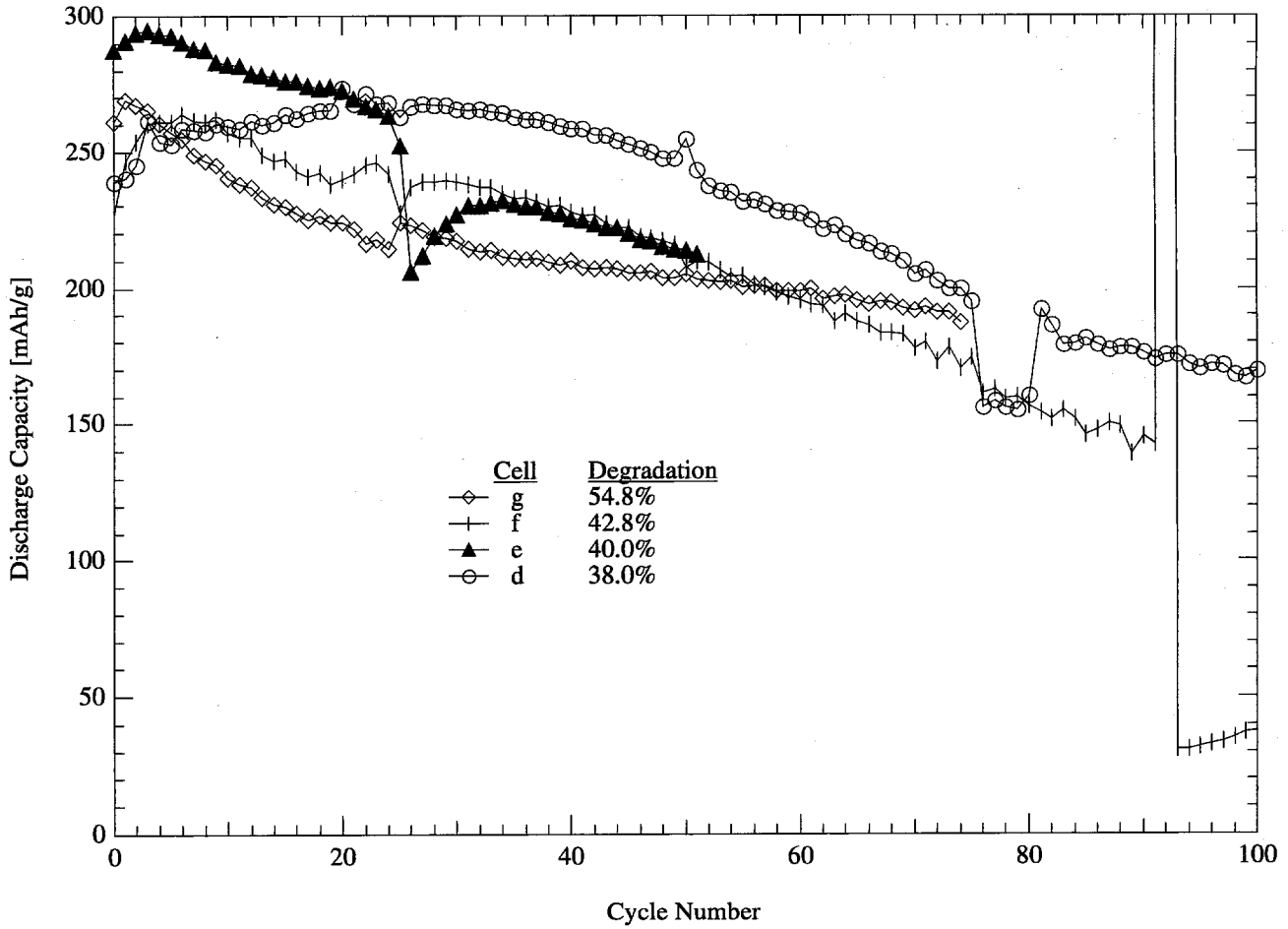

Figure VII-10 Cycling conditions and capacity cycle lifetimes of $LaNi_{4.8}Sn_{0.2}$ cells 'd' - 'g'.

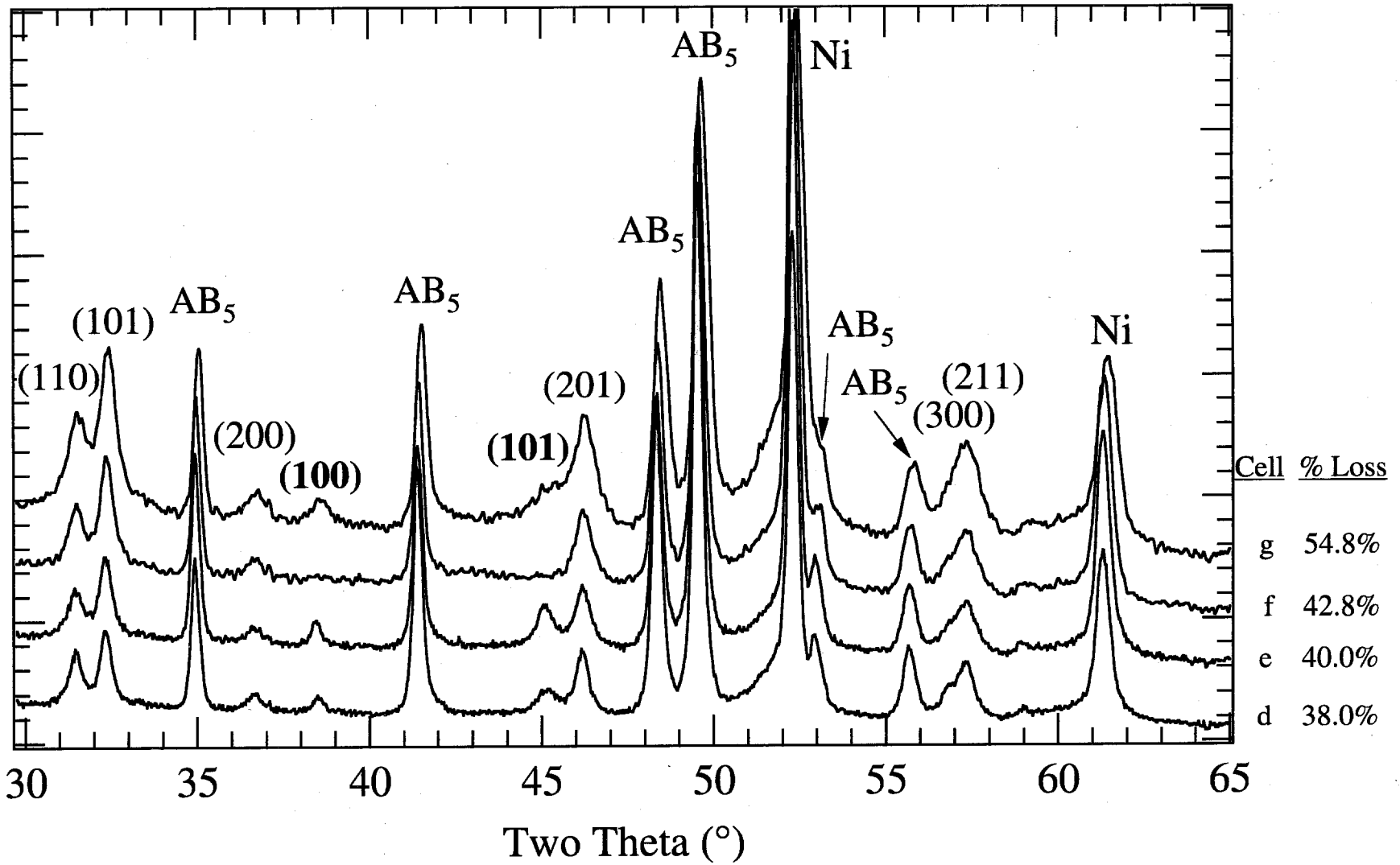

Figure VII-11 XRD patterns of cycled cells 'd' - 'e'. {(hkl) = $La(OH)_3$; **(hkl)** = $Ni(OH)_2$}

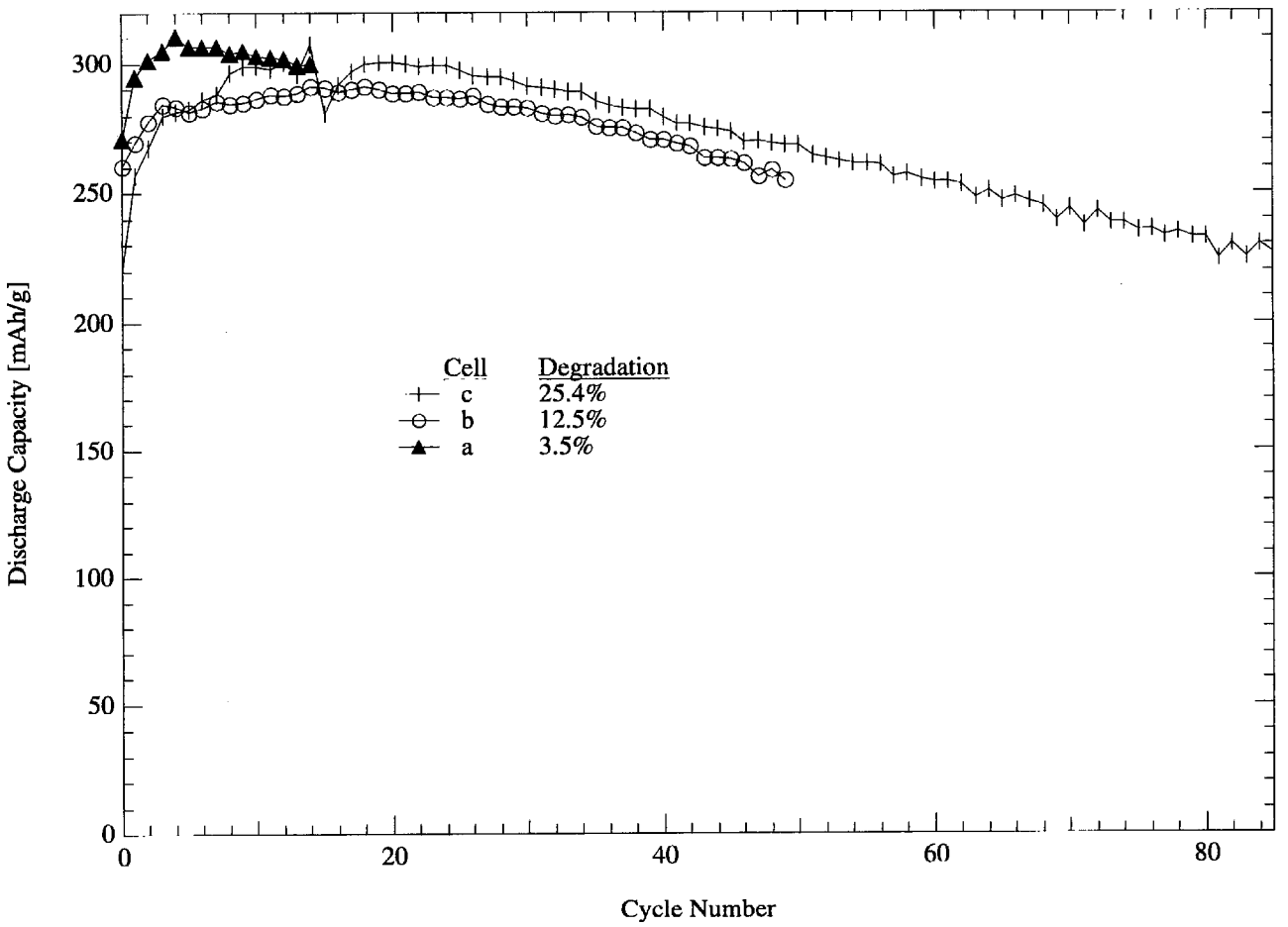

Figure VII-12 Cycling conditions and capacity cycle lifetimes of $LaNi_{4.8}Sn_{0.2}$ cells 'a' - 'c'.

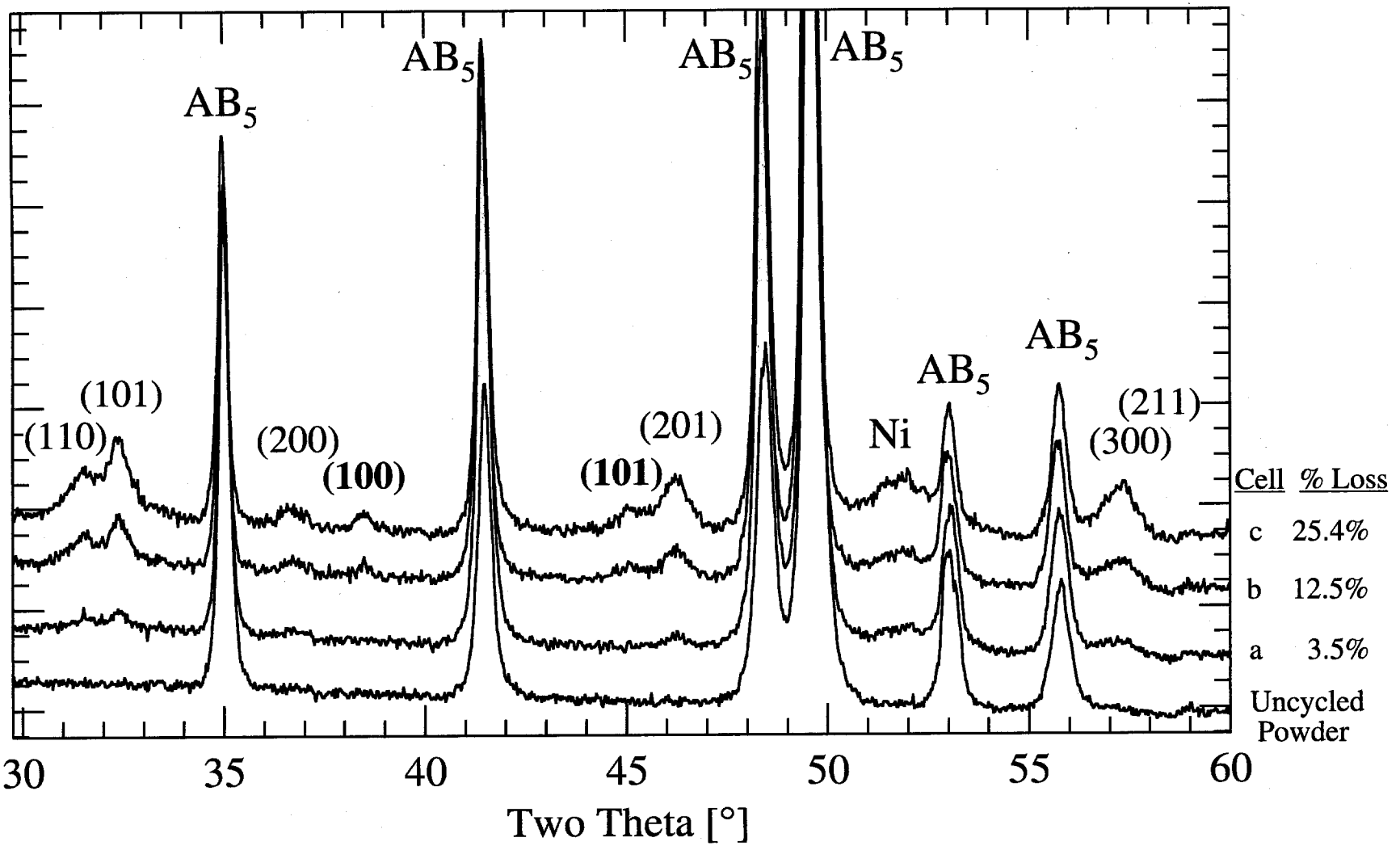

Figure VII-13 XRD patterns of virgin $LaNi_{4.8}Sn_{0.2}$ and cycled cells 'a' - 'c'.
{(hkl) = $La(OH)_3$; **(hkl)** = $Ni(OH)_2$}

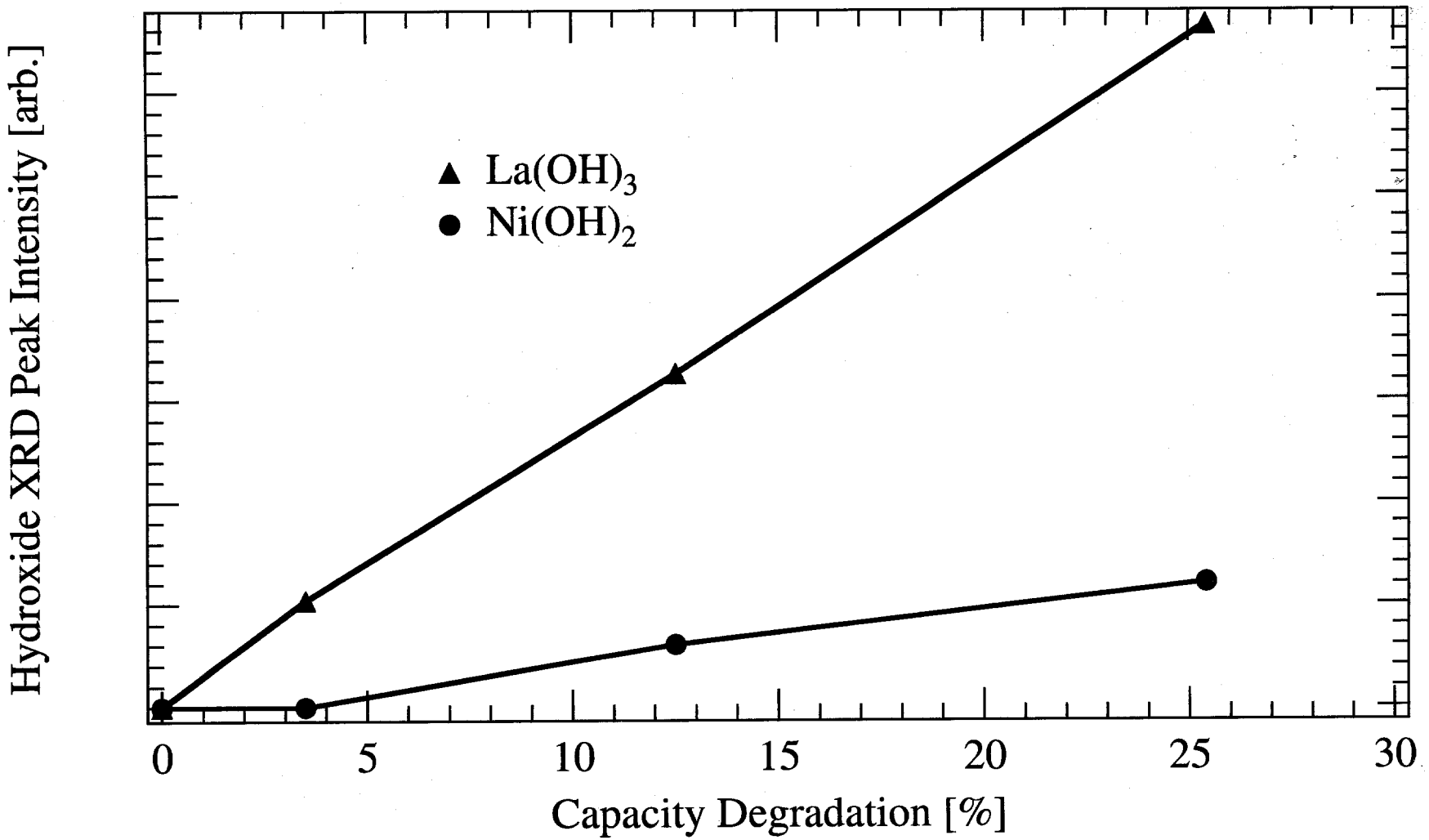

Figure VII-14 Diffraction peak intensities of corrosion products $La(OH)_3$ and $Ni(OH)_2$ in degraded $LaNi_{4.8}Sn_{0.2}$ electrodes.

C. Hydrogen Absorption Capacity

This section will revisit results from isotherm measurements of gas-phase capacities and compare them to capacities measured in electrochemical cells.

1. Literature Survey

It is well known that alloying of $LaNi_5$ reduces the hydrogen absorption capacity. It is also known that the measured electrochemical capacity of a MH electrode depends on the discharge current density used.[4,5]

It did not prove possible to use binary $LaNi_5$ in Ni-MH cells because its high plateau pressure (P_a=~2.0 atm.) meant that the alloy was not easily charged and did not retain charge well in the slightly pressurized cells we used to make electrochemical measurements. Two methods to charge binary $LaNi_5$ were found in the literature. Percheron, *et al.* were somewhat vague in explaining how they achieved capacities of 320 mAh/g.[6] They do describe activating their alloys with four hydrogen absorption-desorption cycles before electrode construction and write, "This operation is feasible at temperatures below 25·°C or with electrodes which have been treated to decrease the velocity of recombination of hydrogen at the interface."[6] Sakai, *et al.* did not hydrogen activate their crushed samples. Instead, they achieve electrochemical capacity by cycling of a $LaNi_5$ anode at -20° C, where the plateau pressure is below 1 atm. After electrochemical activation at -20° C, the metal hydride will charge at room temperature, but retains a very high rate of self-discharge.[7] "When the alloys have equilibrium pressures in the range of 10^{-2}-1 atm, the corresponding electrodes were activated easily at 20° C."[7] Tests by van Rijswick confirm that alloys used in pressurized cells need no special treatment to reach close to theoretical capacities.[8]

2. Caltech Results

Figure VII-15 compares the reversible hydrogen absorption capacities of the ternary substituted alloys of $LaNi_5$ as measured in gas-phase reactions to those measured in electrochemical cells. The electrochemical capacity of the binary alloy is particularly low. During its charging, significant hydrogen evolution is observed to occur on its surface, which seems to be favored over hydrogen absorption.

Figure VII-15 shows that the maximum capacities as measured in slightly pressurized prismatic cells are slightly lower than the corresponding gas-phase. The capacity suppression at low solute compositions is notable, and can be attributed to the high plateau (absorption) pressures of the anode materials, which prevents their complete utilization in our electrochemical test cells. The charge potential is higher for alloys with higher plateau pressures, and under these conditions the competing hydrogen evolution reaction is favored over hydrogen absorption by the metal hydride, and hydrogen gas is formed at the electrode surface. At higher solute compositions, where plateau pressure is not a problem, the charge process becomes efficient and the difference between the electrochemical capacities and gas-phase capacities is approximately constant. We believe this residual discrepancy can be attributed to several sources. Our electrodes are hot pressed at 300° C in air. During this step a surface oxidation layer will be formed from active material, thus decreasing the material's maximum capacity.[9] In addition, the stronger surface (hydroxide) films formed in the electrochemical environment may impose larger polarization losses, both in the charge transfer as well as the diffusion processes, especially at the high discharge rates and low electrode dispersion in our tests. The formation of such films is likely to be aided by the high current densities and low discharge cut-off potentials used in cycling. All the above factors can result in an incomplete utilization of the metal hydride material, making the material's measured capacities lower than would be obtained under quasi-equilibrium conditions.[6]

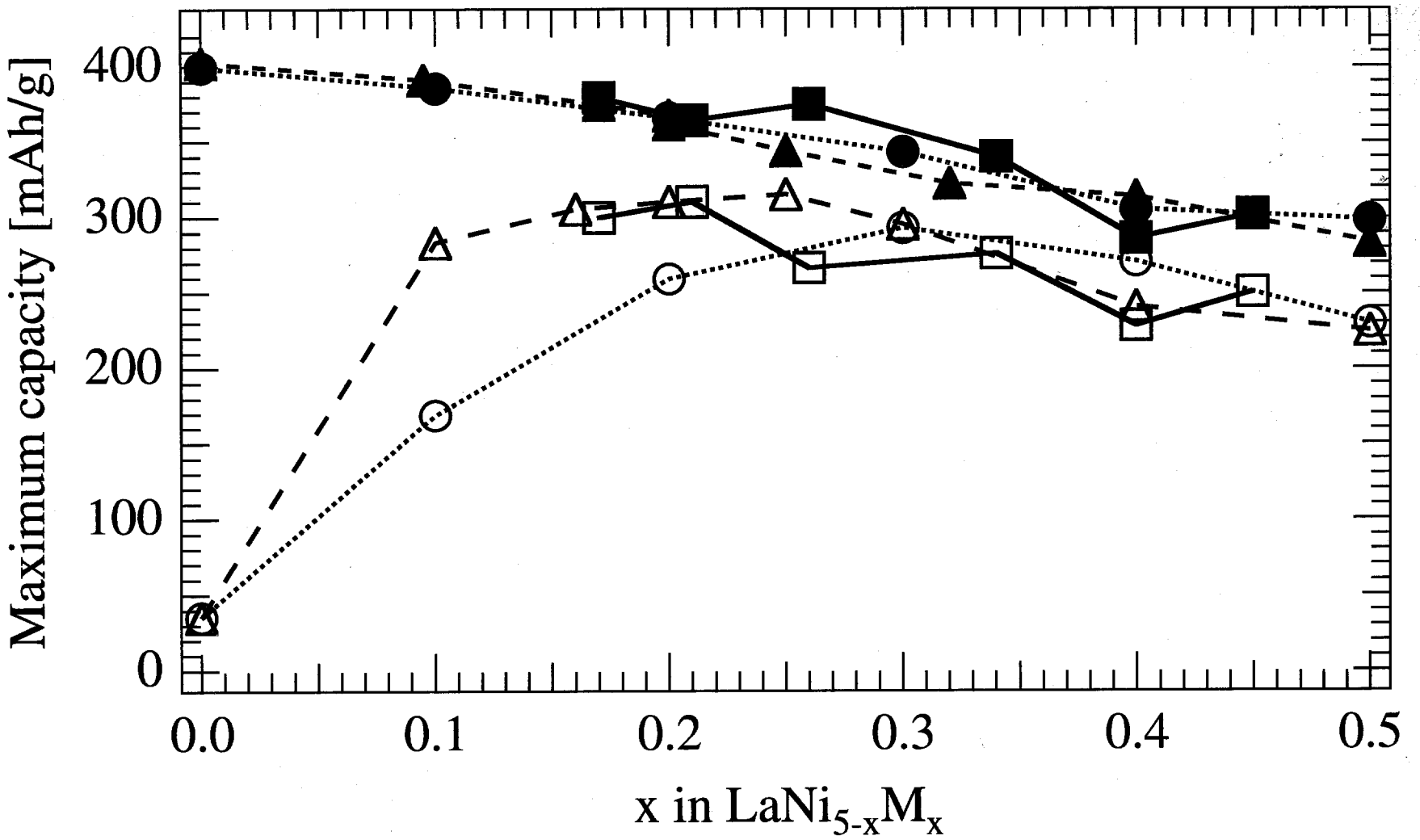

Figure VII-15 Electrochemical (open symbols) and gas-phase (closed) capacities. {-▲- - Sn_x; ···●··· - Ge_x; —■— - M_x}

Of the Ni-substituted $LaNi_5$ alloys tested here, Sn compositions of $0.2 \leq x \leq 0.3$ provide the highest maximum electrochemical capacities of approximately 325 mAh/g.

D. Cyclic Lifetime

1. Literature Survey

See § II.F.3.a.

The capacity *vs* cycle number curve of MH electrodes has been modeled by several authors.[4,10-14] As mentioned above (§VII.C), the maximum capacity of an alloy is never achieved in the first cycle. The capacity increases during the first few cycles, while the alloy undergoes an activation process usually attributed to decrepitation. The increase in surface and decrease in the path length for hydrogen diffusion that takes place during activation decreases the over-potential that causes the electrode to reach its cut-off potential before all its hydrogen is discharged. After activation is complete, the capacity begins to decay. This capacity loss is overwhelmingly dominated by the oxidation of active MH alloy, but has also been attributed to the electrical isolation of particles and an over-potential resulting from the build-up of corrosion products. The decay resulting from oxidation of active material is exponential in nature implying that degradation takes place as a first-order reaction with the amount of degraded material proportional to the amount of material involved in the charge transfer reaction. The capacity *vs* cycle number curve was first modeled by Willems, *et al.* as decaying exponentially with the number of cycles after the alloy had experienced activation.[10] Later studies confirmed the exponential decay and attempted to include alloy activation [4] and discharge current density effects [14] in their models. For some long lived alloys (e.g., $Si_{0.5}$), researchers have postulated a reduction process by which corroded material is slowly converted back to $LaNi_5$, giving the alloy a constant capacity after several hundred cycles.[4] The slow capacity decay of state-of-the-art alloys has prompted some authors to characterize their

decay by a linear function.[15] This follows from a Taylor's expansion of the exponential decay:

$$C(n) = \lim_{\delta \to 0} C_0 e^{-\delta n} = C_0 (1 - \delta n) \qquad \text{[VII.3]}$$

δ = capacity decay parameter, n = cycle number,

C_0 = hypothetical initial capacity

2. Caltech Results

It may be noted that the alloys shown here all experience a shorter cyclic lifetime than those achieved by other experimenters,[16,17] and this can be attributed to the strenuous cycling conditions used to test our cells. The deep discharge to a cut-off potential of -0.5 V *vs* Hg/HgO accelerates the loss in capacity,[9] compared to the -0.7 V often used.[16,17] The high applied current density and the low dispersion of active material used in the electrode powder mixture mean that the overpotentials experienced at a particle surface will be high, resulting in faster corrosion locally and earlier cut-off during discharge. In addition, MH alloy powder particles that do not activate during the first few cycles are more likely to become passivated by electrical isolation from the current collector. Several cells were made using each alloy, and only the cells with the best lifetimes were used in subsequent analysis. It was assumed that the vagaries of battery assembly, rather than the properties of the anode alloy, were responsible for the variability in lifetime measurements.

To characterize the lifetimes of $LaNi_{5-x}M_x$ alloys during electrochemical cycling, I will use the exponential decay parameter δ, fit to capacity-cycle curves of alloys after activation. This should be a better characterization of the alloy lifetime than a linear decay. This model is easily applicable to our alloys because the gas-phase activation and thermal cycling of all but the Sn_x alloys insured fast electrochemical activation. In addition, the fast discharge rate and low cut-off potential used insures that the capacities of even stable alloys such as MmB_5 will decay exponentially.

a. $LaNi_{5-x}Sn_x$

The cyclic lifetime of cells containing $LaNi_{5-x}Sn_x$ metal hydride alloys are presented in **Figure VII-16**. The Sn_x alloys were the first family of alloys to be melted, and our material preparation technique was unfortunately not yet perfected when they were cycled. These alloys were activated with a single gas-phase absorption. Evidence of this can be seen in the particularly slow activation of the $Sn_{0.4}$ and $Sn_{0.5}$ alloys. An additional cell was made with the $Sn_{0.4}$ alloy, denoted by "$Sn_{0.4}$a" in the figure, that had been activated by 5 thermally driven gas-phase absorption-desorption cycles, but this alloy was subsequently used in the temperature study (§VII.A.4) instead of the lifetime study.

Each cell was subjected to 200 charge-discharge cycles. The capacity retention was found to improve with increasing Sn composition. After 100 charge-discharge cycles, alloys with x = 0.25 or 0.3 exhibit capacities in excess of 200 mAh/g, an impressive number when compared to the state of art $MmNi_{3.5}Co_{0.8}Mn_{0.4}Al_{0.3}$ MH alloys evaluated at JPL[14] (Mm in **Figure VII-16**). The cyclic lifetime in cells with $x \geq 0.4$ exceeds that of cells with $0.2 \leq x \leq 0.3$, as evidenced by the capacity curves after 150 cycles.

b. $LaNi_{4.8}M_{0.2}$

The cyclic lifetimes obtained from the $LaNi_{4.8}M_{0.2}$ alloys $M \in \{Si, Ge, Al, Sn, In\}$ are shown in **Figure VII-17** with that of $LaNi_5$. These alloys were activated with one gas-phase hydrogen absorption before electrochemical cycling, and the anode mixture did not include Ni powder. The Sn alloy has the best initial capacity and cyclic lifetime of all the materials in this test. The binary, Si, Ge, and Al alloys have plateau pressures above 1 atm., and because our cells are only slightly pressurized, the electrochemical capacities of these materials could not be measured accurately. The fall in capacity experienced by the $LaNi_5$ anode after cycle #4 implies that the cell's o-ring seal failed after this cycle, limiting the cell pressure to 1 atm. During subsequent cycles, it is likely that the $LaNi_5$ alloy did not experience the discontinuous volume expansion associated with the α- to β-

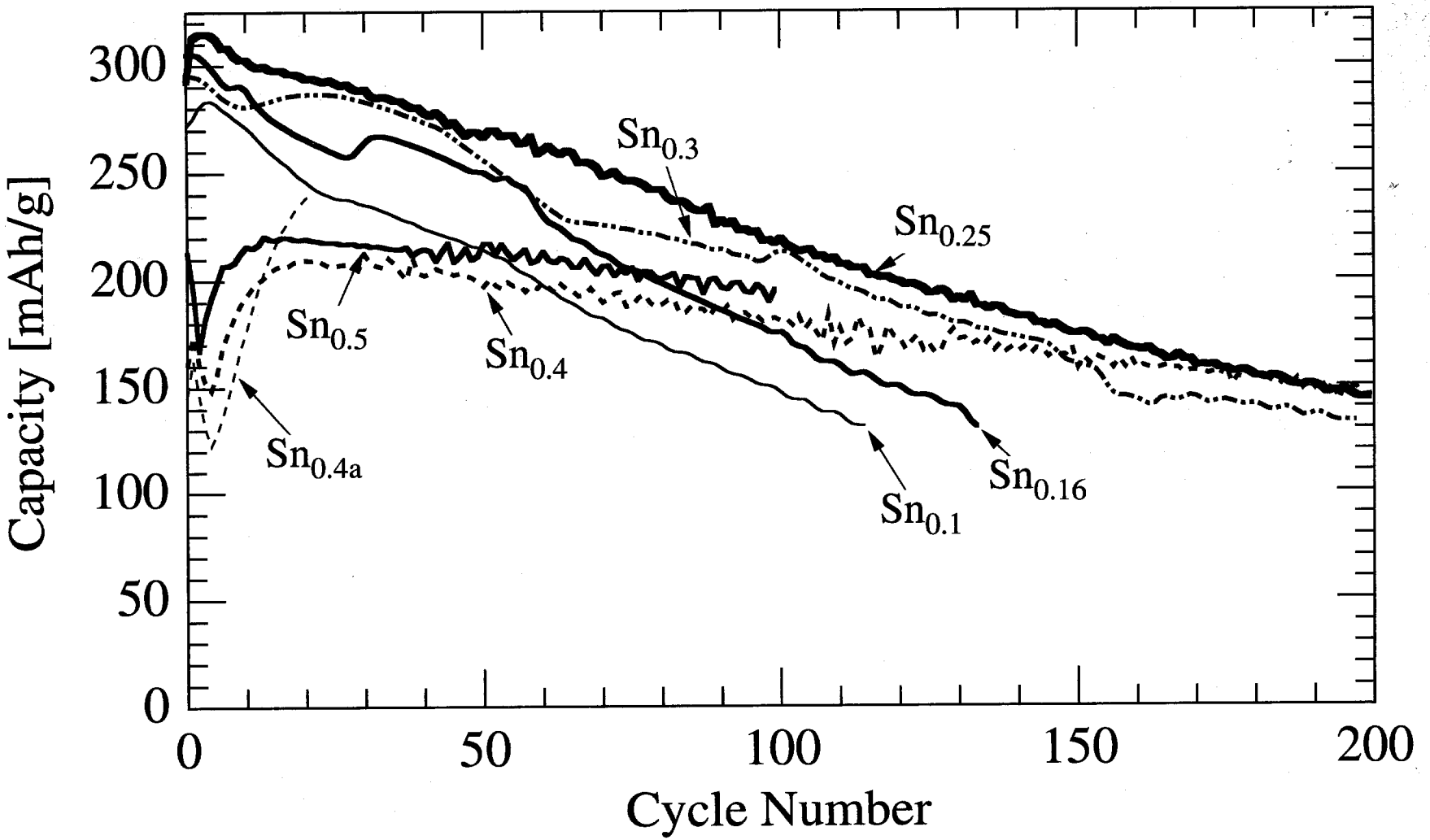

Figure VII-16 Cyclic lifetimes of $LaNi_{5-x}Sn_x$ alloys during electrochemical charge-discharge cycling.

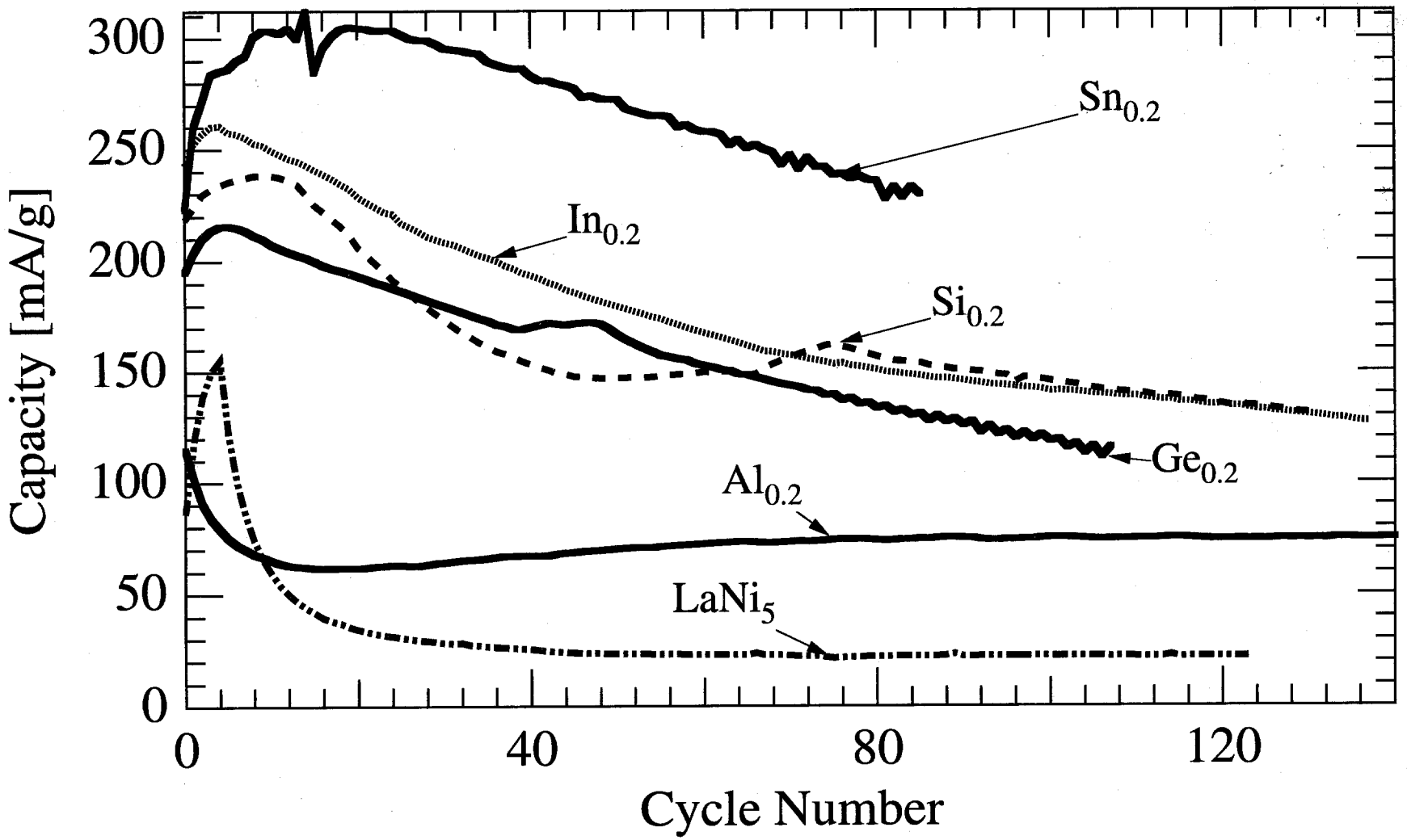

Figure VII-17 Cyclic lifetimes of $LaNi_{4.8}M_{0.2}$ alloys during electrochemical charge-discharge cycling.

phase transition. This cell maintained an extremely stable capacity corresponding to hydrogen cycled in the α-phase regime. The seal on the $Al_{0.2}$ cell failed during the first cycle, but the subsequent capacity corresponds to ~1.1 H/f.u., which is greater than the solubility limit in the α-phase (~0.3 H/f.u.). The slight increase in capacity of the $Al_{0.2}$ cell could result from continued activation.

The $Si_{0.2}$ and $Ge_{0.2}$ alloys also have plateau pressures greater than 1 atm, but the o-ring seals of these cells seem to have been sufficient to contain the increase in pressure. The Si alloy, which has been shown to perform relatively well in tests by Meli, *et al.*,[18] experienced some passivation of the electrode above cycle #15 which is removed later in the cycling. The $Ge_{0.2}$, $In_{0.2}$, and $Si_{0.2}$ alloys have similar capacities after cycle #80.

The cyclic lifetimes of these alloys were characterized with linear decay constants. The linear decay constants for these alloys are shown in **Table VII-1**. The relative stability of these alloys (In > Si > Ge > Sn) during electrochemical cycling is somewhat different than the relative stabilities determined from further testing of these solutes. The addition of Ni (or Cu) powder to the anode mixture has been shown to increase the lifetimes of MH alloys during cycling.[19-21] Although these cells did not have Ni powder present, it is possible that the production of Ni during the corrosion of $LaNi_5$ (equation III.6) in cells with faster initial corrosion stabilized the cells in subsequent cycling. Because it is not known how the lack of Ni powder or adequate activation affect cyclic lifetimes, these results are not included in the final analysis.

c. $LaNi_{5-x}Ge_x$

Figure VII-18 shows the capacities of the cells containing $LaNi_{5-x}Ge_x$ during 500 electrochemical cycles. By the time these cells were tested, our sample preparation procedures were mature, as evidenced by the nice exponential decay observed in these alloys. The capacity loss rate of the $LaNi_{5-x}Ge_x$ alloys is rather unusual. All of the Ge_x alloys experience a rapid loss of 5 to 20% of the capacities in the first ~20 cycles,

Alloy	linear δ
$LaNi_5$	N/A
$Al_{0.2}$	N/A
$Sn_{0.2}$	1.22
$Ge_{0.2}$	0.85
$Si_{0.2}$	0.51
$In_{0.2}$	0.39

Table VII-1 Linear decay constants of $LaNi_{4.8}M_{0.2}$ alloys during electrochemical cycling.

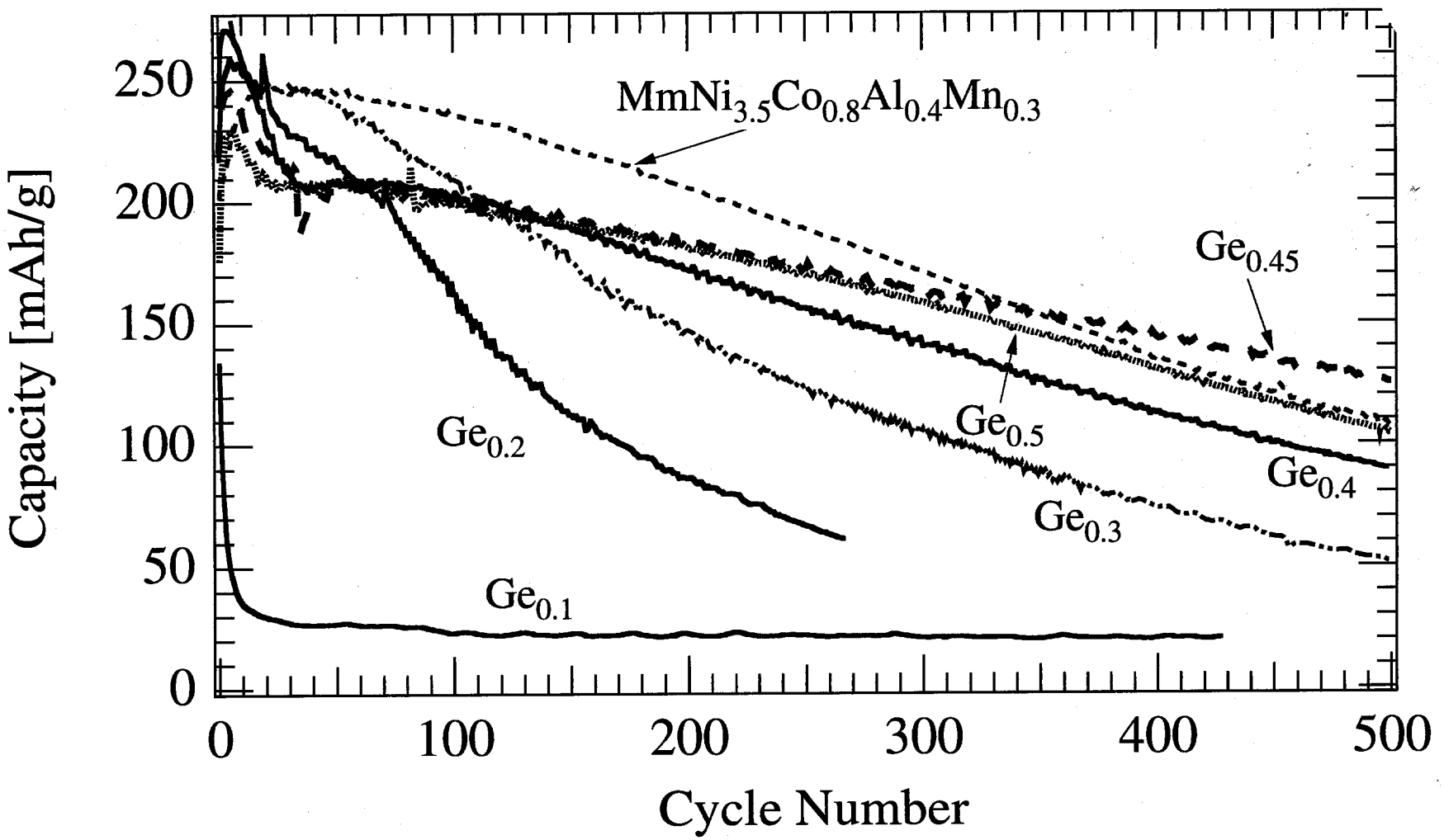

Figure VII-18 Cyclic lifetimes of $LaNi_{5-x}Ge_x$ alloys during electrochemical charge-discharge cycling.

followed by an exponential decay. The mechanism underlying this rapid initial fall is not clear. Equivalent cycle life studies completed with Sn-substituted alloys did not show this affect, so it should not result from the battery fabrication procedure. Even with this rapid initial fall, the capacity retention of the $LaNi_{5-x}Ge_x$ alloys during long term cycling is impressive compared to the binary or Sn-substituted alloys. After 400 deep (100%) discharge cycles, the capacities are still in the range of 125 and 150 mAh/g for alloys with Ge compositions of 0.4 and 0.5, respectively. The capacity decay parameters of the $Ge_{0.4}$ and $Ge_{0.5}$ alloys are almost comparable to that of the commercial $MmNi_{3.5}Co_{0.8}Mn_{0.4}Al_{0.3}$, although the capacity in the initial stages is lower. The cycling stability of the $Ge_{0.45}$ alloy is spectacular, and its capacity surpasses that of the MmB_5 alloy at cycle #350. We believe that the increased performance of this alloy over the $Ge_{0.5}$ alloy results from the second phase present in $Ge_{0.5}$.

d. $LaNi_{5-x}M_x$

Figure VII-19 shows the cyclic lifetimes of $LaNi_{5-x}M_x$ alloys during electrochemical cycling. Many of the cells experience the quick capacity loss after activation seen with the Ge_x alloys. Each cell was cycled ~400 times, until the cell capacity was approximately 50 mAh/g, or until the cell experienced catastrophic failure. Both of the cells containing the $LaNi_{4.83}In_{0.17}$ alloy cracked and burst. This could result either from a pressure build-up during cycling or from the volume expansion associated with hydride formation and the phase changes that accompany corrosion. The behavior of the $Si_{0.4}$ alloy is rather odd, and could be related to the quick capacity loss after activation.

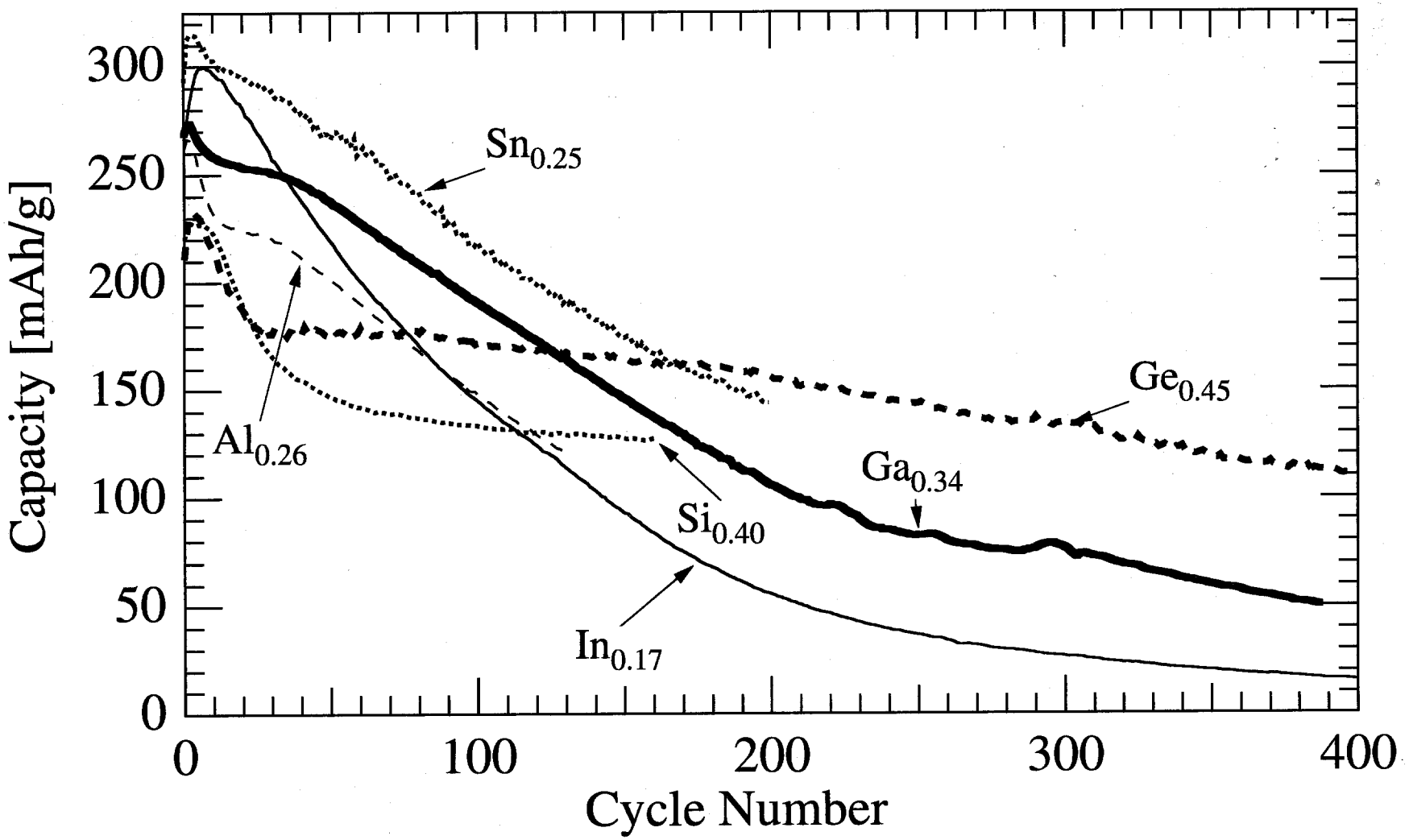

Figure VII-19 Cyclic lifetimes of $LaNi_{5-x}M_x$ alloys during electrochemical charge-discharge cycling.

3. Discussion

The goal of this thesis work is to determine the chemical effects of Ni-substitution on the reversible hydriding properties of $LaNi_5$, in particular its lifetime during electrochemical charge-discharge cycling. To separate the chemical from mechanical and microstructure effects, it was sometimes necessary to exclude data from the final analysis. For example, the alloy $Ge_{0.5}$ was not single phase. This would not have presented a problem in itself, but the small precipitates created effects such as smaller particle size and possibly increased lattice strain in the alloys, which would increase the surface area of the alloy and impact the cycling stability. As seen in Fig. 1, the $Ge_{0.5}$ alloy is less stable than the $Ge_{0.45}$ alloy during electrochemical cycling.

As mentioned above, several alloys ($Si_{0.2}$, $Al_{0.2}$, $Ge_{0.1}$) had plateau pressures greater than 1 atm, and this prevented accurate measurement of their capacities in the slightly pressurized cells used in these tests. An example of this can be seen in the $Ge_{0.1}$ curve in **Figure VII-18**. This alloy could not retain a charge higher than 30 mAh/g after the 20th cycle, when the cell O-ring seal was broken. Some solutes (Ge, Si) have large solubilities in the KOH electrolyte, thereby making the composition of the resultant alloys change during their cycling. It is possible that the faster decay of the $Ge_{0.5}$ trace of **Figure VII-18** is enhanced by a greater dissolution of Ge from the smaller alloy particles.

The cyclic lifetimes of the Sn_x, Ge_x, and M_x alloys were characterized with the exponential decay parameter δ of equation VII.3. To explore the relationship between the alloy capacity fade and alloy composition, solute chemistry, and alloy physical properties, δ was plotted *vs* a number of variables characterizing the alloy. **Figure VII-20** shows δ plotted *vs* solute composition x. We see that for the Sn_x and Ge_x alloys, δ has an almost linear dependence on composition, but the slopes of these correlations are different. Furthermore, the capacity fade parameter is lower for Ge-substituted alloys than for alloys with the same amount of Ni replaced by Sn. The characteristic

degradation constant for a state-of-the-art commercial MmB_5 alloy from Rhone-Poulenc, Inc., is ~0.0022, which could be achieved with solute compositions of $x_{Ge} = 0.36$ or $x_{Sn} = 0.5$.

The discontinuous volume expansion of the Ge_x alloys, seen in **Figure V-26**, increases only slightly for $x > 0.2$, but the capacity fade parameter continues to decrease linearly with composition. This implies that there are additional lifetime controlling effects present. Sn-substituted alloys are not included in the volume expansion data, but a plot of δ *vs* ΔV (**Figure VII-21**) supports this conclusion. These data seem rather scattered and there is not a clear correlation between the capacity fade parameter and alloy volume expansion.

Finally, **Figure VII-22** displays δ *vs* the average bond strength (heat of formation, ΔH) of La with the B ($= Ni_{1-x/5}M_{x/5}$) elements. As seen in **Figure VII-22b**, the relationship between δ and ΔH_{La-B} is linear for almost all of the M_x alloys. The alloys with faster capacity fade than would be expected from their ΔH_{La-B} have been labeled in **Figures VII-21** and **VII-22** for comparison.

Although it is true that MH lifetimes during charge/discharge cycling of alkaline rechargeable cells are affected by the alloy volume expansion upon hydrogen absorption, this alloy property is not adequate in predicting the exponential capacity fade of the alloys. Another important factor is the resistance of the lattice to the formation of microstructural defects, such as can be measured by diffraction peak broadening. There are two important aspects of the crystalline defects that form after hydrogen activation. First, the defects are evidence that the lattice is unstable and is beginning to decompose. Second, the presence of lattice defects enhances the diffusion of metal atoms necessary for phase transformation from the haucke phase structure. The bond strength of La to an average B ($= Ni_{1-x/5}M_{x/5}$) element serves as a more accurate predictor of the alloy capacity fade.

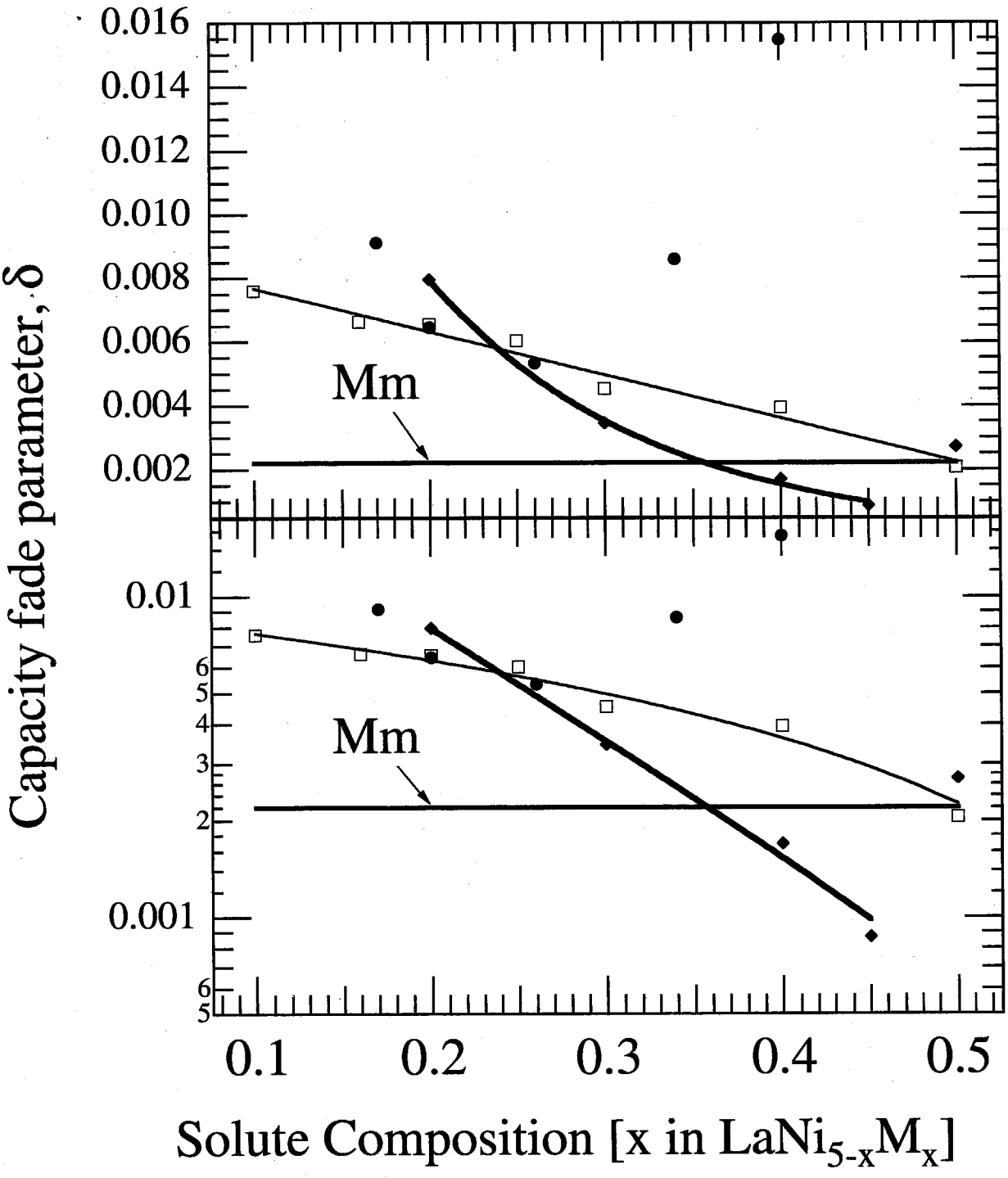

Figure VII-20 Linear and semi-log plots of δ *vs* substituted composition, x. { ◆ - Ge_x; □ - Sn_x; ● - M_x}

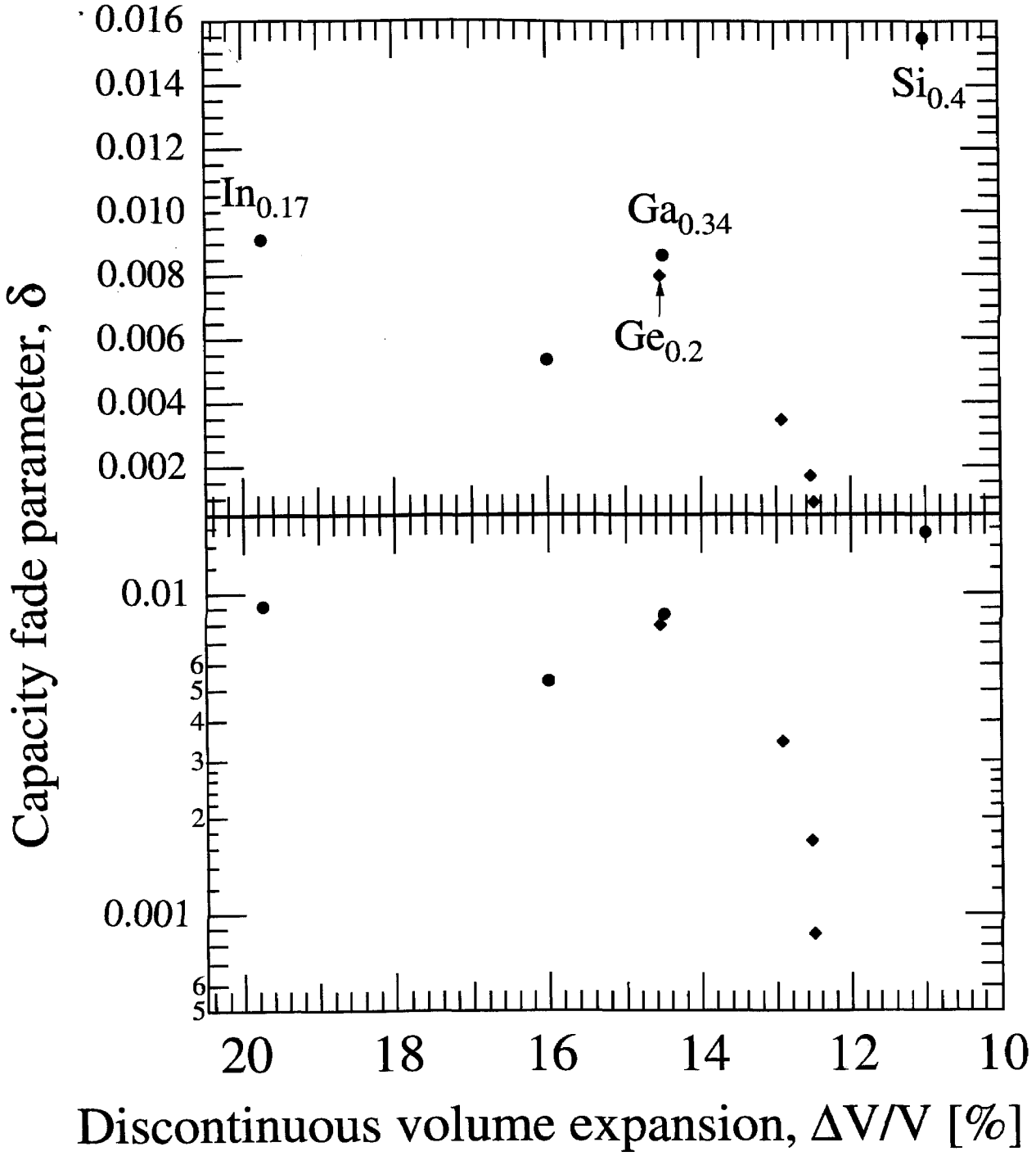

Figure VII-21 Linear and semi-log plots of δ *vs* discontinuous volume expansion of alloy. { ◆ - Ge_x; ● - M_x}

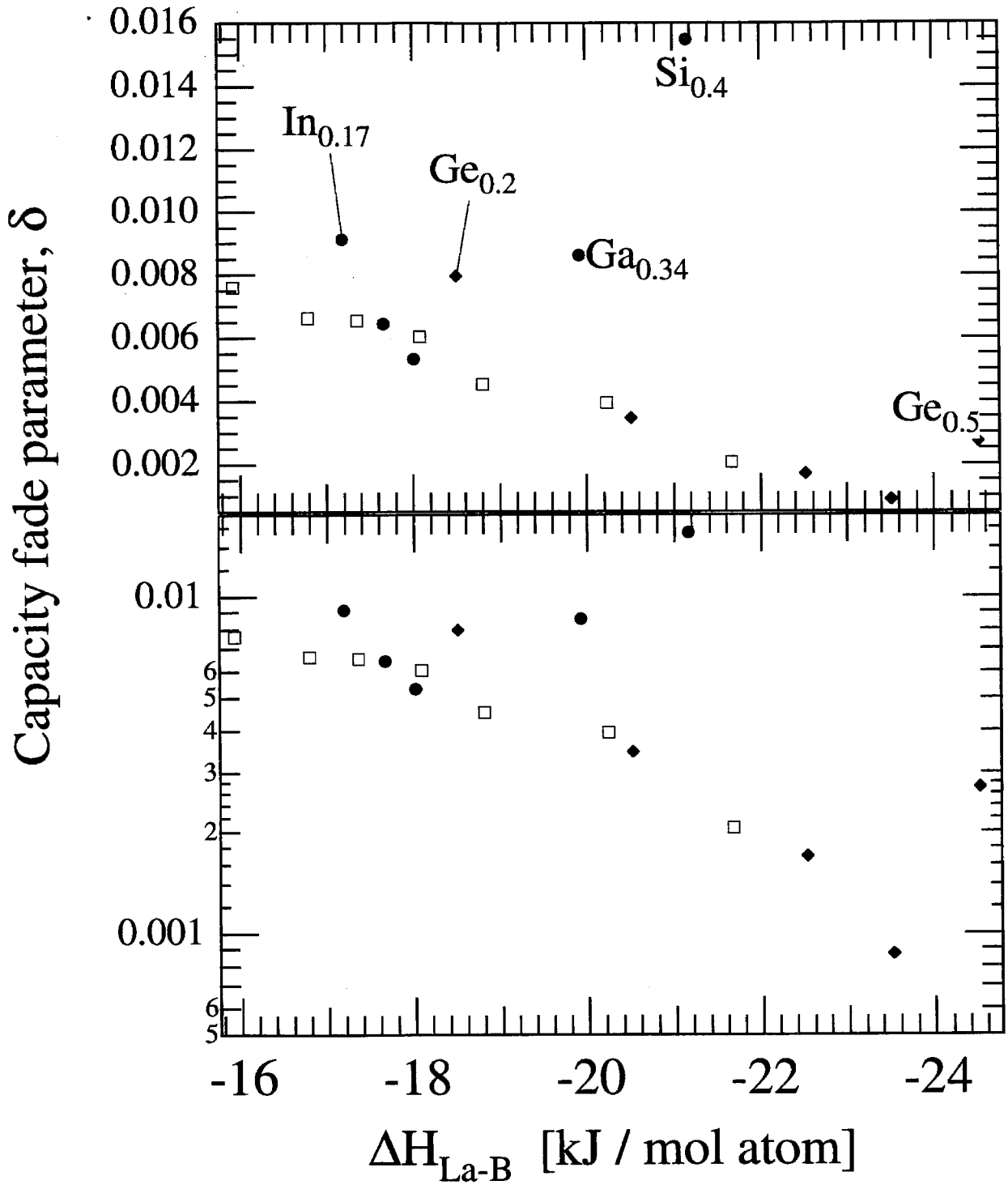

Figure VII-22 Linear and semi-log plots of δ *vs* the heat of formation of La with an average B element. { ◆ - Ge_x; □ - Sn_x; ● - M_x}

[1] S. Luo, W. Luo, J.D. Clewley, Ted B. Flanagan, and L.A. Wade, *J. Alloys Comp.*, **231** (1995): 467.

[2] K. Petrov, A.A. Rostami, A. Visintin, and S. Srinivasan, *J. Electrochem. Soc.*, **141** (1994): 1747.

[3] C.K. Witham, B. Fultz B.V. Ratnakumar, and R.C. Bowman, Jr., in *Hydrogen and Metal Hydride Batteries*, P.D. Bennett and T. Sakai, Ed., **PV 94-27**, p. 68, The Electrochem. Soc. Proceedings Series, Pennington, NJ (1994).

[4] A. Züttel, F. Meli, and L. Schlapbach, *J. Alloys Comp.*, **200** (1993): 157.

[5] Z.-P. Li, W.-Q. Lei, C.-P. Chen, J. Wu, and Qi-Dong Wang, *J. Less-Common Met.*, **172-174** (1991): 1260.

[6] G. Bronoël, J. Sarradin, M. Bonnemay, A. Percheron, J.C. Achard, and L. Schlapbach, *Int. J. Hydrogen Energy*, **1** (1976): 251.

[7] T. Sakai, K. Oguro, H. Miyamura, N. Kuriyama, A. Kato, H. Ishikawa, and C. Iwakura, *J. Less-Common Met.*, **159** (1990): 193.

[8] M.H.J. van Rijswick, in *Hydrides for Energy Storage*, eds. A.F. Andresen and A.J. Maeland (Pergamon, Oxford, 1978), p. 261.

[9] T. Sakai, M. Matsuoka, and C. Iwakura, in *Handbook on the Physics and Chemistry of Rare Earths*, K. A. Gschneidner, Jr., and L. Eyring, eds., Vol. **21**, Elsevier Science B. V., Amsterdam (1995), p. 133.

[10] J.J.G. Willems, *Philips J. of Research*, **39 (1)** (1984): 1.

[11] S. Wakao and Y. Yonemura, *J. Less-Common Met.*, **131** (1987): 311.

[12] H. Sawa, M. Ohta, H. Jakao, and S. Wakao, *Z. Phys. Chem. NF*, **164** (1989): 1527.

[13] Z.P. Li, Y.Q. Lei, B.H. Liu, J. Wu, and Q.D. Wang, *Phys. Chem.*, **183** (1994): 287.

[14] Y.Q. Lei, C.S. Wang, X.G. Yang, H. G. Pan, J. Wu, and Q.D. Wang, *J. Alloys Comp.*, **231** (1994): 611.

[15] M.P. Sridhar Kumar, K. Petrov. W. Zhang, A.A. Rostami, S. Srinivasan, G.D. Adzic, J.R. Hounson, J.J. Reilly, and H.S. Lim, *J. Electrochem. Soc.*, **142** (1995): 3424.

[16] A. Anani, A. Visintin, K. Petrov, and S. Srinivasan, *J. Power Sources,* **47** (1994): 261.

[17] M. Wasz, R.B. Schwarz, S. Srinivasan, and M.P.S. Kumar, in *Materials for Electrochemical Energy Storage and Conversion-Batteries, Capacitors, and Fuel Cells*, Symposium Proceedings of the Materials Research Society, MRS, Pittsburgh, PA (1996).

[18] F. Meli, A. Zuettel, and A. Schlapbach, *J. Alloys Comp.*, **1992**, 190, 17.

[19] H. Ishikawa, K. Oguro, A. Kato, H. Suzuki, and E. Ishii, *J. Less-Common Met.*, **107** (1985): 105; **120** (1986): 123.

[20] T. Sakai, H. Ishikawa, K. Oguro, C. Iwakura, and H. Yoneyama, *J. Electrochem. Soc.*, **134 (3)** (1987): 558.

[21] A.H. Boonstra and T.N.M. Bernards, *J. Less-Common Met.*, **161** (1990): 355.

VIII. Conclusions

By characterizing solutes from a relatively small region of the periodic table, I was able to find some trends in the physical properties of $LaNi_{5-x}M_x$ alloys and the substituting element. The solubilities of sp-metals for Ni in $LaNi_5$ is strongly dependent upon the valence state of the substituting element. The expansion of the $LaNi_5$ unit cell by solute substitution is governed by the solute's metallic radius. The total lattice expansion associated with the metal-to-hydride phase transition is suppressed by solute substitution, and the magnitude of that suppression is related to the heat of formation of the solute with La. There seems to be a critical substituted composition above which substituting Ge for Ni does not reduce the discrete volume expansion experienced upon hydride formation. In all cases, the discrete c-axis expansion is more suppressed than the discrete a-axis expansion. The total lattice expansion of the alloys is more isotropic.

The logarithmic relationship between the alloy plateau pressure and the unit cell volume of the metal is confirmed for Sn- and Ge-substituted alloys. However, Ge-substituted alloys have lower plateau pressures than Sn-substituted alloys with the same unit cell volume. This implies that there is a second order effect controlling the alloy plateau pressures.

The electrode charge transfer kinetics measured by DC micropolarization and AC impedance give similar results. The conflicting trends seen in G-substituted and Sn-substituted alloys make it difficult to ascribe changes in charge transfer resistance to any single phenomenon. A correlation was seen between surface area measured by XRD and the charge transfer resistance.

There is a definite trend between alloy stability during electrochemical cycling and the heat of formation of the solute element with La.

Table of solute properties

Solute (M)	Atomic Number	Radius [Å] (CN=12) [1]	$r_M - r_{Ni}$ [Å] (CN=12) [1]	ΔH^f_{La-M} (exp.) [2,3] [kJ/g-atom]	Electro-negativity [1]
Cr	24	1.282	0.036	N/A	2.15
Mn	25	1.307	0.061	N/A	1.92
Fe	26	1.274	0.028	N/A	1.87
Co	27	1.252	0.006	-12.7 ($La_2Co_{1.7}$)	1.92
Ni	28	1.246	(1.24)	-15.8 (LaNi)	1.93
Cu	29	1.278	0.032	-15.8 (LaCu)	1.82
Al	13	1.432	0.186	-49.9 (LaAl)	1.52
Si	14	1.322	0.076	-99.0 ($LaSi_2$)	1.83
Ga	31	1.353	0.107	-95.7 ($LaGa_2$)	1.80
Ge	32	1.378	0.132	-116.4 (LaGe)	1.90
In	49	1.666	0.420	-93.0 (LaIn)	1.82
Sn	50	1.631	0.385	-87.4 (La_5Sn_4)	1.65
La	57	1.877	0.631	N/A	1.117

[1] E. T. Teatum, K. A. Gschneidner, Jr., and J. T. Waber, LASL Report LA-4003 (1968).

[2] C. Colinet, et al in *Handbook on the Phys. and Chem. of the Rare Earths - Lanthanides/Actinides: Phys. II*, v. 19, eds. K.A. Gschneidner, Jr., et al. (Elsevier, Amsterdam, 1994) 479.

[3] Experimental heats of LaM_n or NiM_n compounds with $n \neq 1$ were scaled to LaM and NiM.